Superconducting Hybrids at the Quantum Spin Hall Edge

Dissertation zur Erlangung des
naturwissenschaftlichen Doktorgrades
der Julius-Maximilians-Universität Würzburg

vorgelegt von

Felix Janosch Peter Lundt

aus Werneck

Würzburg, 2020

Eingereicht am 9. April 2020

bei der Fakultät für Physik und Astronomie

1. Gutachter: Prof. Dr. Björn Trauzettel

2. Gutachter: Prof. Dr. Fakher Assaad

3. Gutachter: .....

der Dissertation

Vorsitzende(r): Prof. Dr. Matthias Bode

1. Prüfer: Prof. Dr. Björn Trauzettel

2. Prüfer: Prof. Dr. Fakher Assaad

3. Prüfer: Prof. Dr. Hartmut Buhmann

im Promotionskolloquium

Tag des Promotionskolloqiums: 9. Oktober 2020

Doktorurkunde ausgehändigt am: .....

Supraleitende Hybrid-Strukturen auf Basis von Quanten-Spin-Hall-Randzuständen

Felix Janosch Peter Lundt
Institut für Theoretische Physik und Astrophysik, Universität Würzburg

Dissertation zur Erlangung des naturwissenschaftlichen Doktorgrades
April 9, 2020

Zusammenfassung

Diese Dissertation behandelt Strukturen auf der Grundlage von Quanten-Spin-Hall-Isolatoren, in denen deren Randzustände mit supraleitender und magnetischer Ordnung in Verbindung gebracht werden. Quanten-Spin-Hall-Isolatoren sind Beispiele für Systeme in der Festkörperphysik, deren physikalische Eigenschaften auf die topologische Struktur der Energiebänder zurückzuführen sind. Eine bemerkenswerte Konsequenz daraus ist die Entstehung von besonderen Randzuständen an der Oberfläche. Im Fall der zweidimensionalen Quanten-Spin-Hall-Isolatoren sind diese eindimensional und bestehen aus leitenden, metallischen Zuständen von gegenläufigen Elektronen mit entgegengesetztem Spin – sogenannte helikale Randzuände. Sie bergen großes Potenzial für Anwendungen in der Spintronik, bei der Informationen nicht durch die Ladung, sondern den Spin von Elektronen übertragen werden, und als Plattform für Quantencomputer. Am Beginn der Dissertation werden eindimensionale topologische Supraleiter allgemeiner besprochen. Ausgehend von der Kitaev-Kette und einem kontinuierlichen Modell werden grundlegende Konzepte anschaulich eingeführt, insbesondere im Hinblick auf die topologische Unterscheidung von trivialer und nicht-trivialer Phase und dem Auftreten von Majorana-Zuständen an deren Enden. Letztere sind die entscheidenden Bausteine auf dem Weg zu geschützten Operationen für Quanten-Bits. Da Randzustände von Quanten-Spin-Hall-Isolatoren im Zusammenspiel mit s-Wellen-Supraleitung und Magnetismus eine Möglichkeit für die Realisierung eines solchen eindimensionalen topologischen Supraleiters ist, wird in der Folge untersucht, unter welchen Bedingungen Majorana-Zustände auftreten können. Es wird gezeigt, dass dies zwischen Gebieten geschieht, in denen die Randzustände entweder nur von Supraleitung oder von Supraleitung und Magnetismus beeinflusst werden. In Systemen mit mehr als einer supraleitenden Region spielt die Phasendifferenz dabei eine übergeordnete Rolle und kann sogar dazu benutzt werden, Majorana-Zustände zu manipulieren. Weiterhin behandelt die Dissertation die Auswirkungen der helikalen Randzustände auf anomale Korrelationsfunktionen, die von der Supraleitung induziert werden. Es zeigt sich, dass Helizität und Magnetismus deren Eigenschaften bereichern können und unkonventionelle, exotische Paarungs-Mechanismen auftreten. Zusätzlich wird ein Zusammenhang zu Majorana-Zuständen demonstriert. Abschließend wird eine mögliche thermoelektrische Anwendung eines hybriden Systems besprochen, die die besonderen supraleitenden Eigenschaften ausnutzt, um eine Temperaturdifferenz zur Erzeugung von Cooper-Paaren mit Spin-Polarisierung zu verwenden. Diese stellen im Rahmen der supraleitenden Spintronik vielversprechende Einheiten zur verlustarmen Übertragung von Informationen dar.

Superconducting hybrids at the quantum spin Hall edge

Felix Janosch Peter Lundt
Institute for Theoretical Physics and Astrophysics, University of Würzburg

Thesis submitted for a doctoral degree in natural sciences
April 9, 2020

Abstract

This Thesis explores hybrid structures on the basis of quantum spin Hall insulators, and in particular the interplay of their edge states and superconducting and magnetic order. Quantum spin Hall insulators are one example of topological condensed matter systems, where the topology of the bulk bands is the key for the understanding of their physical properties. A remarkable consequence is the appearance of states at the boundary of the system, a phenomenon coined bulk-boundary correspondence. In the case of the two-dimensional quantum spin Hall insulator, this is manifested by so-called helical edge states of counter-propagating electrons with opposite spins. They hold great promise, *e.g.,* for applications in spintronics – a paradigm for the transmission and manipulation of information based on spin instead of charge – and as a basis for quantum computers. The beginning of the Thesis consists of an introduction to one-dimensional topological superconductors, which illustrates basic concepts and ideas. In particular, this includes the topological distinction of phases and the accompanying appearance of Majorana modes at their ends. Owing to their topological origin, Majorana modes potentially are essential building-blocks for topological quantum computation, since they can be exploited for protected operations on quantum bits. The helical edge states of quantum spin Hall insulators in conjunction with s-wave superconductivity and magnetism are a suitable candidate for the realization of a one-dimensional topological superconductor. Consequently, this Thesis investigates the conditions in which Majorana modes can appear. Typically, this happens between regions subjected to either only superconductivity, or to both superconductivity and magnetism. If more than one superconductor is present, the phase difference is of paramount importance, and can even be used to manipulate and move Majorana modes. Furthermore, the Thesis addresses the effects of the helical edge states on the anomalous correlation functions characterizing proximity-induced superconductivity. It is found that helicity and magnetism profoundly enrich their physical structure and lead to unconventional, exotic pairing amplitudes. Strikingly, the nonlocal correlation functions can be connected to the Majorana bound states within the system. Finally, a possible thermoelectric device on the basis of hybrid systems at the quantum spin Hall edge is discussed. It utilizes the peculiar properties of the proximity-induced superconductivity in order to create spin-polarized Cooper pairs from a temperature bias. Cooper pairs with finite net spin are the cornerstone of superconducting spintronics and offer tremendous potential for efficient information technologies.

Contents

1 Introduction

Over the last couple of centuries, life on earth has been completely reshaped by science and technology. Physics, in particular, has long been a bridge between the two. For instance, the spread of steam-powered machines was accompanied by the development of thermodynamics, just as electrification came about at the same time as Maxwell laid out his theory of electromagnetism. It is probably impossible to tell when in the past technology drove physics and vice versa.

This interconnectedness is nicely illustrated by the example of the Hampson-Linde cycle, – a refrigeration cycle independently developed by William Hampson in the United Kingdom and Carl von Linde in Germany – which really is a child of both technological and scientific advancement in the late 19th century [1, 2]. It allowed the liquefaction of air, and was subsequently improved by H. Kamerlingh Onnes to liquefy helium [3]. This, in turn, opened up new ways to probe the behavior of metals at unprecedentedly low temperatures, and eventually led to the discovery of superconductivity in 1911, a completely new state of matter at the time and awarded a Nobel prize in 1913 [4]. This scientific achievement has of course found its way into current technological applications such as MRI machines and SQUIDs, but also holds future promise for transmission lines and even wind turbines [5–7]. However, superconductors also keep facilitating new scientific findings, of which the discovery of the Higgs Boson in 2012 at CERN is a prominent example [8].

Of course, the way in which physics and technology push each other forward is often unexpected and hard to predict. It might sometimes take a very long time to happen, or maybe it does not work as intended at all. However, it seems hard to dismiss that the bond is strong and fruitful, and that not trying to find synergy is foolish.

At present, there are at least two major challenges for technology as the basis of the global economy. First, the effects of global warming are becoming more and more evident each year, even in the moderate climate of Central Europe. Second, improvements in silicon-based information technology as one of the pillars of the growth of the economy today are getting more difficult to achieve, with the technology reaching an incredibly mature state. This is often framed as the end to Moore's law, which states that the number of transistors in an integrated circuit doubles every two years [9, 10]. In fact, these two problems are likely going to merge, since

electrification as well as the need for smart and efficient management of resources might demand extraordinary progress in information technology.

In this context, it is not surprising that one of the overarching goals for the global physics community, directly and indirectly, has become to push for new paradigms for information technology over the last decades. The topics covered in this thesis – including topological phases of matter, topological superconductivity and Majorana fermions, quantum spin Hall insulators and helical edge states, unconventional superconductivity, and quantum thermodynamics – have to a large extent been developed with these problems in mind, and the attention they receive is a direct consequence of the hope people have for potentially beneficial outcomes.

More specifically, this thesis is concerned with quantum spin Hall edge states, from more fundamental properties towards a more applied proposal for a device. The applications that are the closest related to this fall into the categories (superconducting) spintronics and (topological) quantum computation. The former holds the promise of more efficient and faster logic operations than in traditional transistor-based chips [11, 12], while the latter constitutes a whole new computing paradigm.

Quantum computation is an immensely exciting research area in itself and has been kick-started by Richard Feynman in 1982 [13], who realized that simulating quantum mechanical systems with a classical computer is utterly inefficient, while a computer operating under the laws of quantum mechanics is perfectly capable of the task [14]. However, it was only the discovery of the first powerful quantum algorithms – Shor's algorithm for factorizing large numbers in 1994 [15], and Grover's algorithm for searching an unordered list [16] – which really sparked the interest of a broader community and fueled the drive to realize such a machine. This quest culminated in Google claiming to have reached "quantum supremacy" just last year in 2019 [17], seemingly bringing a useful quantum computer within reach. This could be a huge stimulus for innovation and also drive much needed progress in, *e.g.,* material science and quantum chemistry [10].

In the remainder of the introduction, we briefly sketch the history and state of the art in the realization of quantum spin Hall insulators and, importantly, hybrid systems at the quantum spin Hall edge. We are going to explain below why this extension is necessary.

The discovery of quantum spin Hall insulators is part of a larger paradigm shift in condensed matter physics, which started with the study of topological phase transitions defying the standard Landau classification by symmetry breaking [18,19]. The experimental discovery of the quantum Hall effect in 1980 [20] and its explanation in terms of a topological invariant of the bulk bands [21] further confirmed that topology can be used to distinguish gapped phases even with the same symmetries, and that topologically distinct systems can have dramatically different properties. Importantly, two systems are topologically equivalent when their Hamiltonians can be smoothly deformed into one another without ever closing the gap in the spectrum. In the example of the quantum Hall effect, the topological invariant is a Chern number and is directly tied to the Hall conductance and the number of conducting, chiral states localized at the edge of the sample. This is the first example of the *bulk-boundary correspondence*, relating global, bulk properties to states localized at

interfaces with systems of different topology.

The quantum Hall effect was quickly used to accurately determine the fine structure constant [20], but widespread application is difficult due to the high magnetic fields required. It was Duncan Haldane who realized that in Graphene one could in principle build systems showing the quantum Hall effect, but without external magnetic field [22]. However, only in 2005 Charles Kane and Eugene Mele showed that two copies of the Haldane model can actually be realized in graphene if spin-orbit interaction is present [23, 24]. Interestingly, in this case the two spins experience opposite Hall conductances, such that states with opposite spins counterpropagate. It is this phenomenon that leads to the names *helical edge states* and quantum spin Hall insulator. Furthermore, the spin-momentum locking provides a very robust building block for spin transport and thus for spintronics.

Unfortunately, graphene has a rather small spin-orbit coupling such that the experimental detection of helical edge states in graphene is out of question. However, in the search for a semiconducting platform to mimic the physics behind the quantum spin Hall effect in Graphene, HgTe/CdTe quantum wells were theoretically identified as ideal candidates [25, 26] and subsequently shown to exhibit the quantum spin Hall effect [27–30]. Since then, the samples have been constantly improved and can now be turned into more complicated devices, *i.e.,* by including superconductivity [31–34]. Furthermore, there is an intense search for additional platforms for helical edge states, for instance InAs/GaSb quantum wells [35], bismuthene [36, 37], and monolayer transition metal-dichalgonides such as WTe_2 [38]. Note that the mechanism developed for graphene is partly resurrected in these latter two examples. Moreover, progress is made in inducing superconductivity and even magnetism into those systems [39–42].

The reason why the interplay of the edge states with superconductivity and ferromagnetism is important is because they can form new topological phases with interesting properties. In particular, it has been predicted that the boundary states are Majorana fermions, *i.e.,* particles described by a hermitian second-quantized creation/annihilation operator $\gamma = \gamma^\dagger$ which are therefore their own anti-particles [43–45]. They were originally proposed by Ettore Majorana in the 1930s as real solutions to the Dirac equation [46], but so far Majorana fermions do not seem to exist as elementary particles. In superconductors, however, one can hope to combine electrons and holes in equal-weight superpositions, where it might become possible to construct a charge conjugation invariant particle.

Due to the reduced dimensionality of the Majorana fermions as effective degrees of freedom at the boundary of a topological superconductor, they can exhibit exotic exchange statistics beyond the standard Bose-Einstein and Fermi-Dirac paradigm. This property is the cornerstone of the applicability of Majorana fermions for quantum computation [47–52].

In the main part of the thesis, we are going to explore hybrid systems on the basis of helical edge states, especially with respect to Majorana and Andreev bound states, unconventional superconductivity beyond standard BCS-theory, and superconducting spintronics. The thesis is organized as follows:

In Chapter 2, we give a short introduction in one-dimensional, spinless, superconducting systems and specifically consider the Kitaev chain and a related con-

tinuum model. We discuss the bulk-boundary correspondence and show how Majorana modes appear at the ends of topological domains. Furthermore, we explain how quantum spin Hall edge states and spin-orbit coupled nanowires relate to one-dimensional topological superconductors. Lastly, we motivate why Majorana modes are promising building blocks for topological quantum computers.

Chapter 3 focuses specifically the helical edge states of a quantum spin Hall insulator. Starting from general properties of helical edge states, we discuss in detail how bound states arise from elementary scattering processes in a variety of structures with superconducting and ferromagnetic regions. Of particular importance are conditions under which Majorana bound states are possible, and how they can be manipulated.

In Chapter 4, we study the influence of the helical nature of the edge states on superconducting, anomalous correlation functions. After giving a very brief introduction in superconductivity beyond BCS theory, we proceed to discuss how pairing amplitudes can be classified and contain information about the physics of a system. We apply these concepts to the helical edge and give detailed calculations of both local and nonlocal correlation functions. Finally, we study the relation of bound states and nonlocal pairings.

In Chapter 5, a thermoelectric device for the generation of equal-spin Cooper pairs on the basis of helical edge states is proposed. Building on the derivation of expressions for the charge current within scattering theory, we show how a temperature gradient can be used for a thermoelectric effect in which nonlocal spin-polarized Andreev processes dominate over normal transmission. Furthermore, we demonstrate that this translates in an enhancement of supercurrent, which constitutes a signature of the creation of equal-spin Cooper pairs. Lastly, we connect the thermoelectric effect to the results of Chapter 4 and show it to be a consequence of odd-frequency pairing.

We provide concluding remarks and a short outlook in the final Chapter 6.

2

The Kitaev chain & Majorana fermions

Contents

The goal of this introductory chapter is to familiarize ourselves with some of the basic concepts behind one-dimensional, topological, superconducting systems. To that end, we first discuss the Kitaev chain as a lattice model of a one-dimensional spinless superconductor in Section 2.1. We identify points in parameter space at which the gap in the spectrum closes and which therefore separate topologically distinct phases. Furthermore, we show that the topological phase is characterized by zero-energy Majorana states localized at the ends of an open chain. Next, we consider topological phases and the bulk-boundary correspondence of a continuum model of a one-dimensional spinless superconductor in Section 2.2, since it will be closer to the effective description of helical edge states. To make this connection explicit, we show in Section 2.3 how the physics of a one-dimensional spinless superconductor can be mimicked by helical edge states of a quantum spin Hall insulator and nanowires. Lastly, Section 2.4 connects Majoranas as representatives of non-Abelian anyons to quantum computation.

Of course, there is a large body of literature on the topic. Most broadly helpful for the matter discussed in this chapter are Refs. [45, 53, 54], but we point towards more specialized references over the course of the chapter.

2.1 The Kitaev chain

2.1.1 Spectrum and topological invariant

We begin this chapter with the Kitaev chain as a simple toy model in which Majorana fermions appear in a straightforward and illuminating fashion as a consequence of a topological invariant. Conceived by Alexei Kitaev in Ref. [47], it is a one-dimensional model of a spinless p-wave superconductor. With N the number of sites, its Hamiltonian reads (we set the lattice constant to one)

$$H = -\mu \sum_{j=1}^{N} \hat{c}_j^\dagger \hat{c}_j - \frac{1}{2} \sum_{j=1}^{N} \left(t\, \hat{c}_j^\dagger \hat{c}_{j+1} + t \hat{c}_{j+1}^\dagger \hat{c}_j \right) + \frac{1}{2} \sum_{j=1}^{N} \left(\Delta \mathrm{e}^{\mathrm{i}\phi}\, \hat{c}_j \hat{c}_{j+1} + \Delta \mathrm{e}^{-\mathrm{i}\phi}\, \hat{c}_{j+1}^\dagger \hat{c}_j^\dagger \right), \tag{2.1}$$

where the operator $\hat{c}_j^\dagger$ ($\hat{c}_j$) creates (annihilates) an electron at site j, μ is the chemical potential and t, Δ are positive parameters describing the nearest neighbor hopping and the p-wave pairing amplitude, respectively. The phase of the superconducting pairing is described by ϕ. We emphasize the fact that because of dealing with spinless fermions, this unusual pairing term effectively couples particles with the same spin. Due to the Pauli principle, electrons at adjacent sites are paired since they cannot occupy the same site. In contrast, a standard Bardeen-Cooper-Schrieffer (BCS) pairing term typically is local and couples electrons with opposite spin.

Note that with periodic boundary conditions, the sites 1 and N are considered to be adjacent to one-another such that the pairing and hopping terms in Eq. (2.1) also couple these sites.

We introduce the Fourier transforms of the fermionic creation/annihilation op-

erators in terms of the momentum k, which read

$$\begin{aligned} \hat{c}_k &= \frac{1}{\sqrt{N}} \sum_{j=1}^{N} \mathrm{e}^{\mathrm{i}kj} \hat{c}_j \\ \hat{c}_j &= \frac{1}{\sqrt{N}} \sum_{k=-\pi}^{\pi} \mathrm{e}^{-\mathrm{i}kj} \hat{c}_k, \end{aligned} \tag{2.2}$$

where we used periodicity to restrict the momentum to the interval $[-\pi, \pi]$.

The Hamiltonian can be recast in the form

$$H = \frac{1}{2} \sum_k \Psi_k^\dagger \, \mathcal{H}_{\mathrm{BdG}} \, \Psi_k, \tag{2.3}$$

where we introduced the Bogoliubov-de Gennes (BdG)-Hamiltonian

$$\mathcal{H}_{\mathrm{BdG}} = \begin{pmatrix} \epsilon_k & \tilde{\Delta}_k^* \\ \tilde{\Delta}_k & -\epsilon_k \end{pmatrix} \tag{2.4}$$

and the Nambu-spinor

$$\Psi_k^\dagger = \left(c_k^\dagger, c_{-k} \right). \tag{2.5}$$

We see that the BdG-Hamiltonian contains the standard kinetic term on the diagonal in a manifestly particle-hole symmetric way, whereas the superconducting pairing potential couples electrons and holes.

The standard tight-binding kinetic energy is given by $\epsilon_k = -t\cos(k) - \mu$, and $\tilde{\Delta}_k = -\mathrm{i}\Delta \mathrm{e}^{\mathrm{i}\phi} \sin(k)$ is the Fourier transform of the pairing. Note that the latter is odd in k and hence constitutes a triplet pairing function. Since we discuss spinless fermions, this is required by the Pauli principle. We will return to this point in depth in Chapter 4.

One can now straightforwardly diagonalize the BdG-Hamiltonian. The energy spectrum is determined by the eigenvalues $E_\pm$ of $\mathcal{H}_{\mathrm{BdG}}$, which read

$$E_\pm = \pm E_{\mathrm{bulk}} \qquad \text{with} \qquad E_{\mathrm{bulk}} = \sqrt{\epsilon_k^2 + \left|\tilde{\Delta}_k\right|^2}. \tag{2.6}$$

The corresponding eigenvectors $\varphi_\pm$ are found to be

$$\varphi_- = \begin{pmatrix} \cos\left(\frac{\theta_k}{2}\right) \\ \mathrm{i}\mathrm{e}^{\mathrm{i}\phi} \sin\left(\frac{\theta_k}{2}\right) \end{pmatrix} \qquad \text{and} \qquad \varphi_+ = \begin{pmatrix} \mathrm{i}\mathrm{e}^{-\mathrm{i}\phi} \sin\left(\frac{\theta_k}{2}\right) \\ \cos\left(\frac{\theta_k}{2}\right) \end{pmatrix}, \tag{2.7}$$

and we define the mixing angle θ_k via[1]

$$\cos(\theta_k) = \frac{\epsilon_k}{E_+}, \qquad \sin(\theta_k) = \frac{\Delta \sin(k)}{E_+}. \tag{2.8}$$

The eigenvectors define the unitary Bogoliubov transformation, which diagonalizes the Hamiltonian and provides a connection between the original fermions on the

[1]Note that in order to obtain θ_k from the definition in Eq. (2.8), only applying the inverse sine or cosine might not be enough. Since $\arcsin(x)$ and $\arccos(x)$ need to be injective functions, they map the interval $[-1, 1]$ only to $[-\pi/2, \pi/2]$ and $[0, \pi]$, respectively.

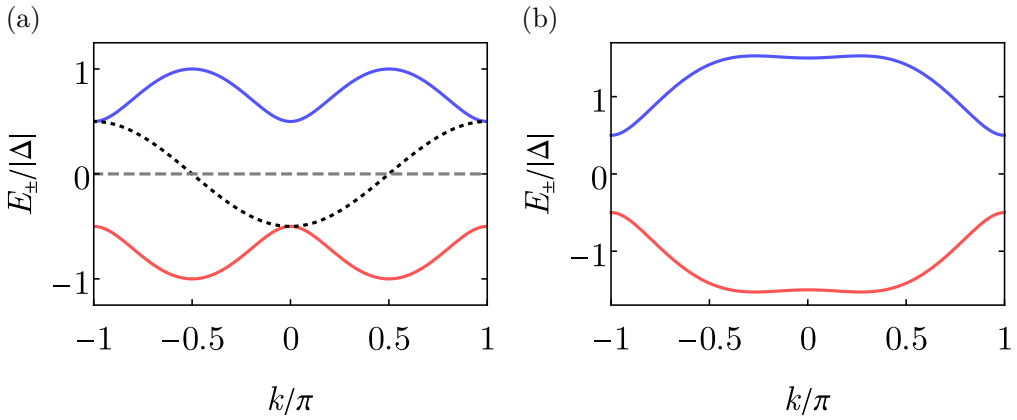

Figure 2.1: Energy spectrum of the Kitaev chain in (a) the topological phase and (b) the trivial phase. In (a), we choose $\mu = 0$ and $t = 0.5\Delta$. The horizontal dashed gray line indicates the chemical potential, while the dashed black line corresponds to the normal state dispersion $-t\cos(k)$. It touches the hole band (red line) at $k = 0$, but the electron band (blue line) at $k = \pm\pi$, which corresponds to the eigenstate changing its character from electron- to hole-like and back as k changes from $-\pi$ to π. In (b), we change the chemical potential to $\mu = \Delta$, such that it no longer intersects the dispersion $-t\cos(k)$. This is the key distinction between the two phases.

chain, described by $\hat{c}_k, \hat{c}_k^\dagger$, and the elementary fermionic excitations of the BdG-Hamiltonian, described by a new set of operators $\hat{a}_k, \hat{a}_k^\dagger$. Explicitly, the Bogoliubov transformation reads

$$\begin{pmatrix} \hat{a}_k \\ \hat{a}_{-k}^\dagger \end{pmatrix} = U_k \begin{pmatrix} \hat{c}_k \\ \hat{c}_{-k}^\dagger \end{pmatrix} \qquad \text{with} \qquad U_k = \left(\varphi_-, \varphi_+,\right), \tag{2.9}$$

such that

$$\hat{a}_k = \cos\left(\frac{\theta_k}{2}\right)\hat{c}_k + \mathrm{i}e^{-\mathrm{i}\phi}\sin\left(\frac{\theta_k}{2}\right)\hat{c}_{-k}^\dagger. \tag{2.10}$$

In essence, the coupling of electrons and holes through the superconducting pairing potential leads to new fermionic degrees of freedom, which arise by a rotation of the elementary electrons in particle-hole (or Nambu) space.

The diagonalized version of the BdG-Hamiltonian becomes

$$H = \sum_k E_{\mathrm{bulk}}(k)\,\hat{a}_k^\dagger \hat{a}_k. \tag{2.11}$$

The system is described by particles, created and annihilated by the operators $\hat{a}_k^\dagger, \hat{a}_k$, with energies $E_{\mathrm{bulk}}(k)$. The elementary excitations of the system are superpositions of electrons and holes. Having a closer look at $E_{\mathrm{bulk}}(k)$, we see that the coupling of electrons and holes leads to quasiparticles with an additional contribution $|\tilde{\Delta}_k|^2$ to their energies, which introduces a gap in the spectrum (see Fig. 2.1). Panel (a) corresponds to the topological strong pairing phase, while (b) is a representative of a topologically trivial system in the weak pairing phase. Below, we are going to show that the key difference is whether the chemical potential intersects the normal state dispersion.

The distinction between the two phases can be made by the topological structure of the BdG-Hamiltonian. As a first step, let us rewrite

$$\mathcal{H}_{\mathrm{BdG}} = \boldsymbol{h}(k) \cdot \hat{\boldsymbol{\tau}} \tag{2.12}$$

where $\hat{\boldsymbol{\tau}} = (\hat{\tau}_1, \hat{\tau}_2, \hat{\tau}_3)$ are the Pauli matrices acting in Nambu space. We can omit any contribution proportional to the unit matrix. For our standard form in Eq. (2.4), we can deduce

$$\boldsymbol{h}(k) = \left(\Delta \sin(\phi) \sin(k), -\Delta \cos(\phi) \sin(k), \epsilon_k\right)^T . \tag{2.13}$$

Notably, writing the Hamiltonian in this way admits an intuitive relation to the energy spectrum. Squaring gives

$$\mathcal{H}_{\mathrm{BdG}}^2 = |\boldsymbol{h}(k)|^2 \hat{\tau}_0, \tag{2.14}$$

which obviously has eigenvalues $\pm|\boldsymbol{h}(k)|^2$. Therefore, the eigenvalues of the BdG-Hamiltonian itself are simply given by the modulus of $\boldsymbol{h}(k)$ and one finds $|\boldsymbol{h}(k)| \equiv E_{\mathrm{bulk}}(k)$.

In the following, we can make a more general argument by considering more general vectors $\boldsymbol{h}(k)$. However, the particular structure of the BdG-Hamiltonian arising due to particle-hole symmetry poses an important constraint on $\boldsymbol{h}(k)$. The spinor Ψ_k satisfies

$$\left(\Psi_{-k}^\dagger\right)^{\mathrm{T}} = \hat{\tau}_1 \Psi_k \qquad \text{and} \qquad \left(\Psi_{-k}\right)^{\mathrm{T}} = \Psi_k^\dagger \hat{\tau}_1, \tag{2.15}$$

which allows us to rewrite the Hamiltonian according to

$$\begin{aligned}
H = \frac{1}{2}\sum_k \Psi_k^\dagger \, \boldsymbol{h}(k) \cdot \hat{\boldsymbol{\tau}} \, \Psi_k &= \frac{1}{2}\sum_k \Psi_k^\dagger \, \overbrace{(\hat{\tau}_1)^2}^{\mathbb{1}} \, \boldsymbol{h}(k) \cdot \hat{\boldsymbol{\tau}} \, \overbrace{(\hat{\tau}_1)^2}^{\mathbb{1}} \, \Psi_k \\
&= \frac{1}{2}\sum_k \left(\Psi_k^\dagger \, \hat{\tau}_1\right) \hat{\tau}_1 \, \boldsymbol{h}(k) \cdot \hat{\boldsymbol{\tau}} \, \hat{\tau}_1 \left(\hat{\tau}_1 \, \Psi_k\right) \\
&= \frac{1}{2}\sum_k \left(\Psi_{-k}\right)^{\mathrm{T}} \hat{\tau}_1 \, \boldsymbol{h}(k) \cdot \hat{\boldsymbol{\tau}} \, \hat{\tau}_1 \left(\Psi_{-k}^\dagger\right)^{\mathrm{T}} \\
&= \frac{1}{2}\sum_k \left(\Psi_k\right)^{\mathrm{T}} \left(\hat{\tau}_1 \left(\boldsymbol{h}(-k) \cdot \hat{\boldsymbol{\tau}}\right)^{\mathrm{T}} \hat{\tau}_1\right)^{\mathrm{T}} \left(\Psi_k^\dagger\right)^{\mathrm{T}} \\
&= -\frac{1}{2}\sum_k \left[\Psi_k^\dagger \, \hat{\tau}_1 \left(\boldsymbol{h}(-k) \cdot \hat{\boldsymbol{\tau}}\right)^{\mathrm{T}} \hat{\tau}_1 \, \Psi_k\right]^{\mathrm{T}} .
\end{aligned} \tag{2.16}$$

Resolving the product of transposed objects into the transpose of a product involves the anticommutation of fermionic creation/annihilation operators in the last step and thus picks up a minus sign. Note that we again ignore constant terms.

In order for the expressions after the first and last equal sign in Eq. (2.16) to be the same, we need to impose the relation

$$\boldsymbol{h}(k) = -\hat{\tau}_1 \left(h_1(-k)\hat{\tau}_1, -h_2(-k)\hat{\tau}_2, h_3(-k)\hat{\tau}_3\right) \hat{\tau}_1. \tag{2.17}$$

Using the fact that the Pauli matrices anticommute, which implies $\hat{\tau}_i \hat{\tau}_j \hat{\tau}_i = -\hat{\tau}_j$ for $i \neq j$, we therefore obtain the constraints

$$h_{1,2}(-k) = -h_{1,2}(k) \qquad \text{and} \qquad h_3(-k) = h_3(k) \tag{2.18}$$

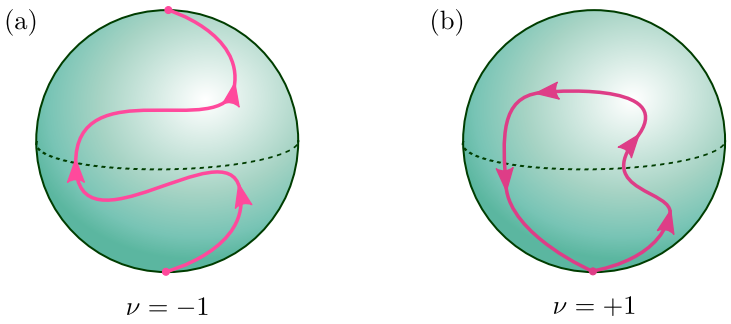

Figure 2.2: (a) Possible path of $\hat{\boldsymbol{h}}(k)$ in the topological phase if k is swept from 0 to π. The path is fixed to north and south pole (or vice versa) at $k = 0, \pi$, but can be smoothly deformed in between without changing the invariant ν. (b) Possible path of $\hat{\boldsymbol{h}}(k)$ in the trivial phase. The vector $\hat{\boldsymbol{h}}(k)$ points to the same pole at $k = 0, \pi$. Smoothly changing the path in between again leaves ν the same.

on the elements of the vector $\boldsymbol{h}(k)$. Eq. (2.18) means that $h_{1,2,3}(k)$ are purely even or odd functions of k, implying that we can restrict the further discussion to the interval $k \in [0, \pi]$. Furthermore, note that for periodic boundary conditions, the points $k = -\pi$ and $k = \pi$ can be identified with one-another. A direct consequence of this and Eq. (2.18) is the property

$$h_{1,2}(\pm\pi) = 0 \qquad \text{and} \qquad h_{1,2}(0) = 0, \tag{2.19}$$

since $h_{1,2}(-\pi) = h_{1,2}(\pi) = -h_{1,2}(\pi)$ and even more straightforwardly $h_{1,2}(0) = -h_{1,2}(0)$.

The important map for which we are going to define a topological invariant is given by

$$\begin{aligned} \hat{\boldsymbol{h}} : [0, \pi] &\mapsto \mathbb{S}^2 \\ k &\mapsto \hat{\boldsymbol{h}}(k) = \frac{\boldsymbol{h}(k)}{|\boldsymbol{h}(h)|} \end{aligned} \tag{2.20}$$

which takes the real numbers in $[0, \pi]$ to a point on the unit sphere. We aim to classify gapped systems, *i.e.,* $\boldsymbol{h}(k)$ and thus $\hat{\boldsymbol{h}}(k)$ is finite for all k.

Due to Eq. (2.19), the vector $\hat{\boldsymbol{h}}(k)$ must be parallel to the z-axis at $k = 0, \pi$ and point to either north or south pole. We can therefore write

$$\hat{\boldsymbol{h}}(0) = s_0 \, \hat{\boldsymbol{z}}, \qquad \hat{\boldsymbol{h}}(\pi) = s_\pi \, \hat{\boldsymbol{z}}, \tag{2.21}$$

where $\hat{\boldsymbol{z}}$ is the unit vector in the positive z-direction and $s_{0,\pi} = \mathrm{sgn}(\epsilon_{0,\pi}) = \pm 1$ are the signs fixing $\hat{\boldsymbol{h}}(0, \pi)$ to either the north or the south pole, given by the sign of the kinetic energy at the respective momenta.

As a result, as one maps $k \mapsto \hat{\boldsymbol{h}}(k)$ from $k = 0$ to $k = \pi$, the resulting points on the sphere can form two kinds of paths, which are topologically distinct. Either both start and end point are at the same pole and the path is closed, or start and end point are on opposing poles and the path is open (see Fig. 2.2). Note that neither do we need to specify which pole the starting and end point is, nor whether the open paths go from north to south pole or vice versa. There is always a unitary transformation

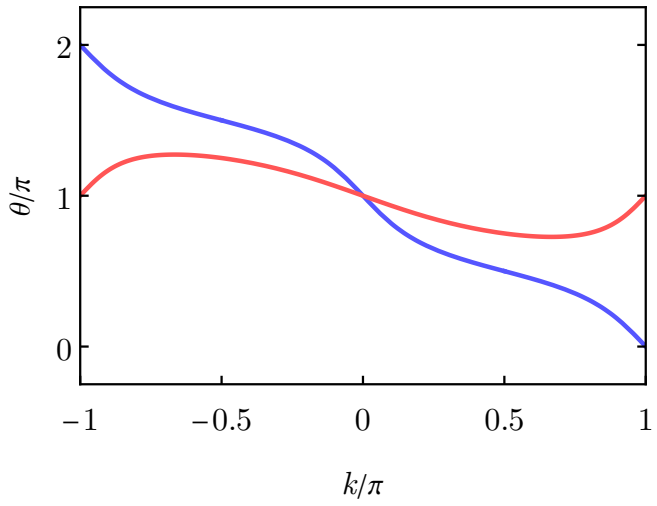

Figure 2.3: Plot of the mixing angle as one sweeps k across the Brillouin zone in the topological (blue line) and trivial regime (red line). We choose the same parameters as in Fig. 2.1. In the trivial regime, the angle stays within a small interval around $\theta = \pi$, whereas in the topological regime, the mixing angle wraps around the unit circle once as it moves continuously from 2π to 0 (these two points can be identified with one-another).

connecting the two respective cases, and the only meaningful invariant is whether or not the path is closed. Using the notation in Eq. (2.21), this is equivalent to $s_0 = s_\pi$ for a closed path, and $s_0 = -s_\pi$ for an open path, respectively. This can be formulated in a concise fashion by defining the $\mathbb{Z}_2$ invariant

$$\nu = s_0 s_\pi. \tag{2.22}$$

For closed maps from one pole back onto itself, we therefore have $\nu = +1$, whereas $\nu = -1$ for open paths connecting opposite poles. The fact that only the closure of the path is important corresponds to the product of s_0 and s_π being invariant, instead of the values of $s_{0,\pi}$ itself.

The physical intuition gained here is the following. First, $\nu = 1$ means that $\mathrm{sgn}(\epsilon_k)$ is the same at 0 and π. Then, there are no states at the Fermi level and we have a trivial insulator, since this situation is smoothly connected with the trivial vacuum $\mu \to -\infty$, where no states are occupied. However, if $\nu = -1$, there is one pair of states at the Fermi level and the pairing leads to a nontrivial insulator.

Another way of making a topological distinction between the phases is provided by the mixing angle θ_k [55]. We can think of $\cos(\theta_k) \equiv x$ and $\sin(\theta_k) \equiv y$ as x- and y-components of all points on a unit circle in $\mathbb{R}^2$ (which is equivalent to $\mathbb{S}^1$). The angle θ_k is thus the one-dimensional parameter marking the angular position of the point on the circle. As such it is 2π-periodic, and thus $\theta(k)$ represents a map from the unit circle onto the unit circle:

$$\begin{aligned} \theta : \mathbb{S}^1 &\mapsto \mathbb{S}^1 \\ k &\mapsto \theta(k). \end{aligned} \tag{2.23}$$

As we have seen before, the chain is in a topological phase if μ is within the band ϵ_k and trivial otherwise. In the trivial regime, where $\mu < -t$ ($\mu > t$), we readily see

that $x = \cos(\theta_k) = \epsilon_k/E_+$ is strictly positive (negative). By contrast, $y = \sin(\theta_k) = \Delta \sin(k)/E_+$ is negative for $-\pi \leq k < 0$ and positive for $0 < k \leq \pi$. Put together, sweeping k from $-\pi$ to π therefore traces θ_k on a path on the circle which stays in the first and fourth (second and third) quadrant, but will never wrap around the full circle. Note that this is a direct consequence of the chemical potential being outside the band, and therefore the absence of states at the Fermi level. In the topological regime for $-t < \mu < t$, however, the sign of $x = \cos(\theta_k)$ does change. Importantly, it does so when $-t\cos(k) = \mu$ and therefore *not* at $k = 0, \pi$, which is where $y = \sin(\theta_k)$ changes sign. This means that sweeping k across the Brillouin zone will definitely force θ_k through all quadrants. Since the signs of $x = \cos(\theta_k)$ and $y = \sin(\theta_k)$ change in an alternating fashion, it is actually guaranteed that θ_k performs a full turn around the circle. We illustrate this in Fig. 2.3.

2.1.2 Majorana fermions in the Kitaev chain

2.1.2.1 A short introduction

In 1937, Ettore Majorana discovered that the Dirac equation admits a real solution, with the remarkable consequence that it is invariant under the charge conjugation operator connecting particles and antiparticles [46]. A state with these properties would therefore describe a neutral spin-1/2 particle, which is its own antiparticle [56]. It has been coined *Majorana fermion* in honor of its discoverer.

Although Majorana himself speculated that Neutrinos might be their own antiparticles, the observation of lepton number conservation seemed to make a strong distinction between neutrinos and antineutrinos. More recently, however, the discovery of neutrino oscillations among their flavor eigenstates suggests that only the sum of lepton numbers over all three flavors can be conserved, thus opening a backdoor for Majorana fermions in the form of neutrinos as fundamental part of the standard model [57].

For the purposes of this thesis, however, we ignore the particle physics background to the Majorana fermion and turn to condensed matter realizations [58–61]. They rely on the simple idea that in superconductors, basic excitations are always superpositions of electrons and holes [62, 63]. However in conventional BCS superconductors the energy spectrum of excitations is gapped. Since charge-conjugation links states at energies $\pm E$, the only invariant energy $E = 0$ is forbidden by the superconducting gap. Moreover, since Cooper pairs in BCS superconductors are spin singlet states, the elementary excitations also have mixed spin, which further obstructs the construction of Majorana operators [54, 57, 64].

Remarkably, the rise of topological superconductivity has provided a way out. As we are going to see in the rest of the chapter for the example of a one-dimensional spinless superconductor, nontrivial topological properties of the bulk gap allow for mid-gap zero-energy states located at the edge by means of the so-called *bulk-boundary correspondence* [45, 59, 60, 65–67]. In rough terms, the second-quantized operators associated with these states have the form

$$\gamma_+ = \hat{c} + \hat{c}^\dagger, \qquad \gamma_- = -\mathrm{i}\hat{c} + \mathrm{i}\hat{c}^\dagger \tag{2.24}$$

and thus are hermitian, *i.e.,* they fulfill

$$\gamma_{\pm} = \gamma_{\pm}^{\dagger}. \tag{2.25}$$

This implies that creation and annihilation of these states are equivalent, and it is in this sense that they are their own antiparticles. Strictly speaking, as we will see shortly, they are not fermions since there is no well-defined occupation number associated with them. Therefore, states with operators fulfilling the constraint Eq. (2.25) should be called *Majorana modes* for clarity [67, 68]. However, the condensed matter literature is often quite loose in this regard and we adopt this convention after having clarified this point here.

By now, there is an abundance of physical systems which aim to realize topological superconductors with Majorana modes at their boundary. Early proposals based on vortices in $p + ip$ superconductors [69–73] could effectively realized by means of the proximity effect in two-dimensional electron gases [74] or at the surface of three-dimensional topological insulators [43]. However, more relevant to the material discussed in this thesis are end states of one-dimensional topological systems. Research in this direction was driven by Kitaev [47, 48] and the insight that the physics of the Kitaev chain can be realized using helical edge states [43, 44] and nanowires [75, 76] (see Section 2.3). Other one-dimensional examples are chains of magnetic adatoms on top of a Pb superconductor [77, 78] and helical hinge states of Bismuth films subjected to superconductivity and magnetism [79].

The most basic experimental signatures of Majorana modes is a zero-bias conductance peak of quantized value $2e^2/h$. Since the earliest report of experimental evidence for Majoranas in nanowires in 2012 in Ref. [80], advances in device fabrication have led to more robust results and conductance measurements closer to the theoretical prediction [81–88].

Furthermore, Majorana modes can be associated with transferring single electrons across Josephson junctions instead of Cooper pairs. A direct consequence of this is a doubling of the supercurrent period from 2π to 4π as a function of the phase difference across the junction, thus leading to a fractional Josephson effect [44,89,90]. Experimentally, this signature has been found in HgTe/CdTe and InAs/GaSb quantum wells [32, 33, 91, 92] as well as in semiconductor nanowires [81, 93].

2.1.2.2 Kitaev chain

Going back to the Kitaev chain as introduced in Section 2.1.1, Majorana fermions appear straightforwardly as a consequence of the nontrivial topology as edge states. In order to make them apparent, we need to move to the situation of an open chain with N sites. This corresponds to removing the hopping and pairing between the first and the N-th site in the Hamiltonian in Eq. (2.1), which yields

$$H = -\mu \sum_{j+1}^{N} \hat{c}_j^{\dagger}\hat{c}_j - \frac{1}{2}\sum_{j=1}^{N-1}\left(t\,\hat{c}_j^{\dagger}\hat{c}_{j+1} + t\hat{c}_{j+1}^{\dagger}\hat{c}_j\right) + \frac{1}{2}\sum_{j=1}^{N-1}\left(\Delta \mathrm{e}^{\mathrm{i}\phi}\,\hat{c}_j\hat{c}_{j+1} + \Delta \mathrm{e}^{-\mathrm{i}\phi}\,\hat{c}_{j+1}^{\dagger}\hat{c}_j^{\dagger}\right), \tag{2.26}$$

Next, we introduce Majorana operators through the definition

$$\gamma_{A,j} = \hat{c}_j \, \mathrm{e}^{\mathrm{i}\phi/2} + \hat{c}_j^\dagger \, \mathrm{e}^{-\mathrm{i}\phi/2} \tag{2.27a}$$

$$\gamma_{B,j} = \mathrm{i} \left(\hat{c}_j \, \mathrm{e}^{\mathrm{i}\phi/2} - \hat{c}_j^\dagger \, \mathrm{e}^{-\mathrm{i}\phi/2} \right). \tag{2.27b}$$

Given the fermionic anticommutation relations of the standard creation/annihilation operators $\hat{c}_j, \hat{c}_j^\dagger$, it is straightforward to verify that the Majorana operators from Eq. (2.27) fulfill the important relations

$$\{\gamma_{\alpha,i}, \gamma_{\alpha',j}\} = 2\delta_{i,j}\delta_{\alpha,\alpha'} \tag{2.28a}$$

$$\gamma_{\alpha,j}^\dagger = \gamma_{\alpha,j}. \tag{2.28b}$$

The former relation, Eq. (2.28a), constitutes the Clifford algebra obeyed by the Majorana operators, whereas the latter relation Eq. (2.28b) is a manifestation of Majoranas being their own antiparticles. One way to interpret Eq. (2.28b) is that the complex[2] fermionic operators $\hat{c}_j, \hat{c}_j^\dagger$ are split in their real and imaginary parts by Eq. (2.27). In other words, the fermions at each site are split into two Majoranas at the same site. An important consequence of Eq. (2.28) is the property

$$\gamma_{\alpha,j}^\dagger \gamma_{\alpha,j} = \gamma_{\alpha,j}\gamma_{\alpha,j} = \mathbb{1}. \tag{2.29}$$

This means that there is no well-defined occupation number associated with the Majorana operators.

The question to be addressed now is how the Hamiltonian Eq. (2.26) can be understood in terms of Majorana operators. To proceed, we invert Eq. (2.27) to find

$$c_j = \frac{\mathrm{e}^{-\mathrm{i}\phi/2}}{2} \left(\gamma_{B,j} + \mathrm{i}\gamma_{A,j} \right) \tag{2.30}$$

$$c_j^\dagger = \frac{\mathrm{e}^{\mathrm{i}\phi/2}}{2} \left(\gamma_{B,j} - \mathrm{i}\gamma_{A,j} \right), \tag{2.31}$$

which we can subsequently insert into the Hamiltonian Eq. (2.26). It is illustrative to note explicitly that

$$\hat{c}_i^\dagger \hat{c}_j = \frac{1}{4} \left[\gamma_{B,i}\gamma_{B,j} + \gamma_{A,i}\gamma_{A,j} + \mathrm{i} \left(\gamma_{B,i}\gamma_{A,j} - \gamma_{A,i}\gamma_{B,j} \right) \right], \tag{2.32}$$

which, using Eq. (2.28), leads to

$$\hat{c}_j^\dagger \hat{c}_j = \frac{1}{4} \left[\gamma_{B,j}^2 + \gamma_{A,j}^2 + \mathrm{i} \left(\gamma_{B,j}\gamma_{A,j} - \gamma_{A,j}\gamma_{B,j} \right) \right] = \frac{1}{2} \left(1 + \mathrm{i}\gamma_{B,j}\gamma_{A,j} \right) \tag{2.33}$$

and

$$\hat{c}_j^\dagger \hat{c}_{j+1} + \hat{c}_{j+1}^\dagger \hat{c}_j = \frac{\mathrm{i}}{2} \left(\gamma_{B,j}\gamma_{A,j+1} - \gamma_{A,j}\gamma_{B,j+1} \right), \tag{2.34}$$

where the terms of the form $\gamma_{\alpha,j}\gamma_{\alpha,j\pm1}$ must cancel each other in the Hamiltonian since they are anti-hermitian. From the pairing terms we obtain

$$\mathrm{e}^{\mathrm{i}\phi} \hat{c}_j \hat{c}_{j+1} + \mathrm{e}^{-\mathrm{i}\phi} \hat{c}_{j+1}^\dagger \hat{c}_j^\dagger = \frac{\mathrm{i}}{2} \left(\gamma_{B,j}\gamma_{A,j+1} + \gamma_{A,j}\gamma_{B,j+1} \right). \tag{2.35}$$

[2]Complex in the sense of non-hermitian, *i.e.,* not invariant under "conjugation". In the same way, the Majorana operators can be thought to be real.

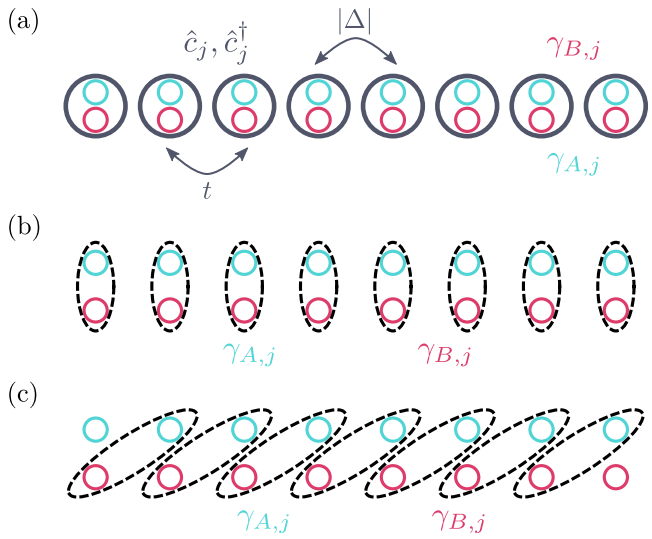

Figure 2.4: Schematic depiction of the Kitaev chain. (a) The chain in terms of electrons (gray circles) with indicated hopping t, pairing $|\Delta|$ and Majorana operators $\gamma_{A/B,j}$. (b) In the topologically trivial regime, Majoranas at the same sites are coupled more strongly than Majoranas at different sites. Consequently, they can pair and form normal fermions. (c) In the nontrivial regime, the coupling between Majoranas on neighboring sites is dominant. The resulting fermions are thus superpositions of Majoranas from adjacent sites. Clearly, as panel (c) shows, for open chains this leaves two Majoranas at the ends unpaired. They form a highly nonlocal fermionic state.

We thus see that the on-site terms give rise to a term coupling Majoranas at the same site (plus a constant term, Eq. (2.33)), whereas the hopping and pairing terms couple Majoranas at different sites (Eqs. (2.34) and (2.35)). Note that the latter two come with a relative sign.

After rewriting the terms making up the previous Hamiltonian in terms of Majorana operators, we can straightforwardly write

$$H = -\frac{\mu}{2}\sum_{j=1}^{N}(1 + \mathrm{i}\gamma_{B,j}\gamma_{A,j}) - \frac{\mathrm{i}}{4}\sum_{j=1}^{N-1}\Big[(\Delta + t)\,\gamma_{B,j}\gamma_{A,j+1} + (\Delta - t)\,\gamma_{A,j}\gamma_{B,j+1}\Big]. \quad (2.36)$$

The general Hamiltonian is rather complicated to analyze. However, since we have already seen that the system has a topologically nontrivial phase for finite Δ and $-t < \mu < t$ and a trivial phase otherwise, we will focus on special, tractable points within the phases.

For the trivial phase, we choose $\Delta = t = 0$ – *i.e.,* an inert chain of localized electrons with uniform onsite potential $\mu \neq 0$. Note that if $\mu < 0$, the ground state $|\mathrm{GS}\rangle$ will be the vacuum state $|0\rangle$ with occupation numbers $n_j = \hat{c}_j^\dagger \hat{c}_j |0\rangle = 0$, whereas for $\mu > 0 \quad \forall j$ the ground state will be the one with every fermion state filled, $|1\rangle$, *i.e.,* $n_j = \hat{c}_j^\dagger \hat{c}_j |1\rangle = |1\rangle \quad \forall j$. In either case the energy spectrum will have a gap, since creating an excited state by adding (for $|\mathrm{GS}\rangle = |0\rangle$) or removing (for $|\mathrm{GS}\rangle = |1\rangle$) a particle, respectively, will cost energy $|\mu|$. Notably, this is true regardless of where the particle is added, and therefore the trivial phase has no edge states. For completeness, note that we have to exclude the case $\mu = 0$, since then

the system would be gapless. In the Majorana formulation, for $\Delta = t = 0$ in the trivial phase the latter term in Eq. (2.36) vanishes and thus the Hamiltonian only couples Majoranas at the same site. This is of course a direct consequence of turning off all couplings of the original fermions to the nearest neighbors.

The topologically nontrivial phase is best understood for $\Delta = t \neq 0$ and $\mu = 0$. The Hamiltonian thus becomes

$$H = -\frac{\mathrm{i}t}{2} \sum_{j=1}^{N-1} \gamma_{B,j}\gamma_{A,j+1}, \tag{2.37}$$

meaning that the description boils down to a chain with a coupling of Majorana operators at *different sites*, *i.e.,* Majorana operators $\gamma_{B,j}$ are coupled with $\gamma_{A,j+1}$ at the next site. This has the crucial implication that the Majoranas $\gamma_{A,1}$ and $\gamma_{B,N}$ are not paired at all, since there are no partners available to these modes at the ends of the chain. In fact, $\gamma_{A,1}$ and $\gamma_{B,N}$ do not even enter the Hamiltonian in Eq. (2.37), which implies

$$[\gamma_{A,1}, H] = [\gamma_{B,N}, H] = 0 \tag{2.38}$$

by simply applying the anticommutation relations.

To see that this actually translates into a fermionic edge state, we define the operator

$$\hat{f} = \frac{1}{2}\left(\gamma_{B,N} + \mathrm{i}\gamma_{A,1}\right). \tag{2.39}$$

One can easily check that $\hat{f}$ does fulfill fermionic anticommutation relations [also compare with Eq. (2.30)]. Moreover, the fermion defined through the annihilation operator in Eq. (2.39) is highly nonlocal since it combines Majoranas at opposite ends of the chain.

Since the commutator is linear, $\hat{f}$ and $\hat{f}^\dagger$ also commute with the Hamiltonian, *i.e.,*

$$\left[\hat{f}, H\right] = \left[\hat{f}^\dagger, H\right] = 0. \tag{2.40}$$

As a result, the ground state will now be two-fold degenerate.

Let us first have a look at the bulk[3] of the chain, which still remains gapped. This can be made explicit by defining fermionic operators

$$\hat{d}_j = \frac{1}{2}\left(\gamma_{B,j} - \mathrm{i}\gamma_{A,j+1}\right). \tag{2.41}$$

A simple calculation shows that the Hamiltonian can be written in the form

$$H = t \sum_{j=1}^{N-1} \left(\hat{d}_j^\dagger \hat{d}_j - \frac{1}{2}\right), \tag{2.42}$$

which is the Hamiltonian of a chain of $N-1$ sites with onsite potential t, up to a constant. Clearly, the corresponding ground state $|\mathrm{GS}\rangle$ is just an empty chain with occupation numbers zero. Adding a particle creates an excited state, separated from the ground state by energy t.

[3]Bulk refers to all Majorana operators except for $\gamma_{A,1}$ and $\gamma_{B,N}$. Note that sites 1 and N then still partly belong to the bulk through $\gamma_{A,N}$ and $\gamma_{B,1}$.

In contrast, adding one fermion created by the operator $\hat{f}^\dagger$ costs zero energy, since the energy of the state $|1_{\hat{f}}\rangle \equiv \hat{f}^\dagger|\mathrm{GS}\rangle$ is

$$\langle 1_{\hat{f}}|H|1_{\hat{f}}\rangle = \langle 1_{\hat{f}}|H\,\hat{f}^\dagger|\mathrm{GS}\rangle = \langle 1_{\hat{f}}|\hat{f}^\dagger\,H|\mathrm{GS}\rangle = E_{\mathrm{GS}}\langle 1_{\hat{f}}|1_{\hat{f}}\rangle = E_{\mathrm{GS}}, \tag{2.43}$$

i.e., equal to the ground state energy. We thus conclude that the states $|\mathrm{GS}\rangle$ and $\hat{f}^\dagger|\mathrm{GS}\rangle$ form a basis of the low-energy (and in fact degenerate) subspace.

The physical properties of the Kitaev chain in the topological phase are rooted in the nontrivial topology associated with the bulk of the chain. At the boundary of the topological chain, an interface between a trivial and nontrivial phase arises. This interface binds a localized state within the gap. The mathematical reason behind is the *bulk-boundary correspondence*. Loosely speaking, there is no smooth way of interpolating across the boundary between distinct topological phases, and hence the gap has to close, *i.e.,* some subgap state must exist. At the special points above, this boundary was well illustrated by the different couplings of Majoranas in the two phases. Clearly, an open chain in the topological phase or an interface between a trivial and a topological region leave a single Majorana mode per interface unpaired, leading to zero-energy modes localized at the interfaces (*cf.* Fig. 2.4).

Strikingly, much of the behavior of the Majorana zero modes localized at the edges is stable even away from $\mu = 0$, precisely because it is a feature of the topology. In the topological phase, but for $\mu \neq 0$, Majorana operators of type A will be coupled to Majoranas of type B on the same site, as well as on neighboring sites on *both* sides. This has two important consequences:

(i) The edge modes will no longer simply be given by $\gamma_{A,1}, \gamma_{B,N}$. Introducing the shorthand γ_L (γ_R) for the mode localized at the left (right) end of the chain, the edge modes are given by superpositions of the form [47]

$$\begin{aligned} \gamma_L &= \sum_{j=1}^{N} \left(\alpha_{L,+}x_+^{-j} + \alpha_{L,-}x_-^{-j}\right)\gamma_{A,j} \\ \gamma_R &= \sum_{j=1}^{N} \left(\alpha_{R,+}x_+^{j} + \alpha_{R,-}x_-^{j}\right)\gamma_{B,j}, \end{aligned} \tag{2.44}$$

where $x_\pm = 2(t+\Delta)/(-\mu \pm \sqrt{\mu^2 - 4t^2 + 4\Delta^2})$ with $|x_\pm| > 1$, and coefficients $\alpha_{L/R,\pm}$ subject to boundary conditions. The weights of the mode γ_L (γ_R) are therefore decaying (growing) with j, as desired. Eq. (2.44) is valid in the thermodynamic limit $N \to \infty$, where $\gamma_{L,R}$ give rise to a truly zero-energy fermion via

$$\hat{f} = \frac{1}{2}\left(\gamma_R + \mathrm{i}\gamma_L\right). \tag{2.45}$$

(ii) For a finite chain, the different couplings between Majoranas for $\mu \neq 0$ will lead to a weak coupling between γ_L and γ_R and thus a splitting between the degenerate zero-energy states. The effective Hamiltonian takes the form

$$H_{\mathrm{eff}} = \frac{\mathrm{i}}{2}\epsilon\gamma_L\gamma_R \equiv \epsilon\left(\hat{f}^\dagger\hat{f} - \frac{1}{2}\right), \tag{2.46}$$

where the splitting energy scales as $\epsilon \propto \exp(-N/l_0)$. The length l_0 is determined by the larger value of $\ln(|x_\pm|)$, which is the larger localization length scale of the modes $\gamma_{L/R}$.

Note that both of the above points originate from the more complicated interplay of couplings away from the special case $\mu = 0$. First, they allow the edge modes, which are perfectly pinned to the boundary of the chain for $\mu = 0$, to interact and spread away from the edge. Not only does that lead to an overlap (although exponentially small) of the edge modes, the additional couplings also allow for a nonzero matrix element of the effective Hamiltonian coupling the two edge modes and therefore a splitting of the degeneracy. The distinction between an overlap of wave functions and a nonzero energy splitting will reappear throughout this thesis.

As a last remark, note that given a sufficiently long chain, *i.e.,* $N \cdot a \gg l_0$, the energy splitting and the delocalization of the zero modes can safely be ignored since they become negligible in comparison with all other relevant length and energy scales in the system.

2.2 Continuum model of a one-dimensional spinless superconductor

2.2.1 Phase diagram of the continuum model

More insight into the physics of spinless one-dimensional superconductors can be gained by considering a continuum model. As opposed to the Kitaev chain as a lattice model, where it was possible to define discrete Majorana operators at each site and study the coupling between them, the continuum model enables us to make a more precise connection between Majorana modes and boundaries of topological phases.

The normal state Hamiltonian in momentum space in this case can be written in the form

$$H = \int \frac{\mathrm{d}p}{2\pi} \left[\psi_p^\dagger \left(\frac{p^2}{2m} - \mu \right) \psi_p + p\,\Delta \left(\psi_p \psi_{-p} + \text{h.c.} \right) \right], \tag{2.47}$$

where $\psi_p^\dagger$ (ψ_p) creates (annihilates) a spinless fermion with momentum p. Furthermore, $\xi_p = p^2/2m - \mu$ is the normal state dispersion, with m the electron's mass and μ the chemical potential. The second term in Eq. (2.47) describes the effect of p-wave superconductivity. For simplicity, we choose $\Delta > 0$, implying that Δ is real.

To proceed, we bring H in a BdG-form, which reads

$$H = \frac{1}{2} \int \frac{\mathrm{d}p}{2\pi} \Psi_p^\dagger \, \mathcal{H}_{\text{BdG}} \, \Psi_p \tag{2.48}$$

with the Hamiltonian density

$$\mathcal{H}_{\text{BdG}} = \begin{pmatrix} \xi_p & p\,\Delta \\ p\,\Delta & -\xi_p \end{pmatrix} = \xi_p \, \hat{\tau}_3 + p\,\Delta \, \hat{\tau}_1. \tag{2.49}$$

In Eq. (2.48), we introduce the spinor $\Psi_p = (\psi_p, \psi_{-p}^\dagger)^{\mathrm{T}}$. By diagonalizing the BdG-Hamiltonian the spectrum can be easily found to be

$$E_\pm = \pm \sqrt{\xi_p^2 + \Delta^2 p^2}, \tag{2.50}$$

i.e., the system exhibits an energy gap unless the expression within the square root vanishes. Inspecting the two terms inside the square root, we see that in the presence of superconductivity ($\Delta \neq 0$) the gap can only close if $\mu = 0$ and only at zero momentum $p = 0$. As it turns out, the $\mu = 0$ line separates a trivial from a topological regime. Just as we saw for the Kitaev chain, in the trivial phase the chemical potential lies outside the band ($\mu < 0$), while in the topological phase the chemical potential is within the band ($\mu > 0$).

To make this connection more explicit, note that we can write

$$\mathcal{H}_{\mathrm{BdG}} = \boldsymbol{h} \cdot \hat{\boldsymbol{\tau}}, \tag{2.51}$$

with $\boldsymbol{h} = (h_1, h_2, h_3) = (p\,\Delta, 0, \xi_p)^{\mathrm{T}}$, which is analogous to the way we treated the BdG-Hamiltonian for the Kitaev chain in Section 2.1. As a consequence of the fact that $\boldsymbol{h}$ lies in the x, z-plane, by defining the unit vector $\hat{\boldsymbol{h}}(p) = \boldsymbol{h}(p)/|\boldsymbol{h}(p)|$ we obtain a map

$$\begin{aligned} \hat{\boldsymbol{h}} : \mathbb{R} &\mapsto \mathbb{S}^1 \\ p &\mapsto \hat{\boldsymbol{h}}(p) \end{aligned} \tag{2.52}$$

from the real numbers to the unit circle. The winding number associated with this mapping as one sweeps p from $-\infty$ to ∞ along the real axis distinguishes the two phases.

The argument follows similar lines as in Section 2.1. First note that h_1 linearly depends on p (remember $\Delta > 0$), which means $\hat{\boldsymbol{h}}$ points in negative x-direction for $p < 0$ and in positive x-direction for $p > 0$. Furthermore, in the limit $p \to \pm\infty$, the quadratic contribution to $h_3 = \xi_p$ dominates the linear behavior of h_1 and thus $\hat{\boldsymbol{h}}$ is parallel to the z-axis for $p \to \pm\infty$.

In the trivial phase, for $\mu < 0$, the chemical potential is outside the band and thus $\xi_p > 0 \quad \forall p$. Therefore, the vector $\hat{\boldsymbol{h}}$ always points in positive z-direction and is only slightly tilted away from the z-axis as $|p|$ grows away from zero. As explained above, at large p it comes back to the z-axis, such that $\hat{\boldsymbol{h}}$ as a whole traces an arc less than half the circumference of the unit circle.

In the nontrivial, topological phase, ξ_p switches sign at $p = \pm\sqrt{2m\mu}$. While the behavior for large $|p|$ is unaffected and $\hat{\boldsymbol{h}}$ points along the positive z-axis, h_3 is now negative for $|p| < \sqrt{2m\mu}$. Therefore, sweeping p from $-\infty$ to ∞ sends $\hat{\boldsymbol{h}}$ from the "north pole" in a counterclockwise fashion around the unit circle, such that it wraps around the unit circle one time.

2.2.2 Bulk-boundary correspondence

In this section, we show explicitly how an interface between a topological and a trivial region of a one-dimensional spinless superconductor gives rise to a boundary state.

We can construct such a domain wall by making the chemical potential position dependent. The trivial region is created by choosing $\mu < 0$ for $x < 0$ and, respectively, the nontrivial region by taking $\mu > 0$ for $x > 0$. The point $x = 0$ therefore separates the two regions and a domain wall is formed. A natural case to consider

is a profile for $\mu(x)$ which saturates at $|\mu(x)| \equiv \mu_\infty$ far away from $x = 0$ and is zero at $x = 0$, *i.e.,* $\mu(0) = 0$. This is achieved by taking

$$\mu(x) = \mu_\infty \tanh\left(\frac{x}{\lambda}\right), \tag{2.53}$$

for instance. In Eq. (2.53), λ is a parameter determining the length scale on which $\mu(x)$ transitions between $\pm|\mu_\infty|$, and μ_∞ fixes the energy scale for the chemical potential term.

If the spatial profile of the chemical potential is sufficiently smooth, *i.e.,* $\mu(x)$ varies relatively slowly, only small momenta will play a role[4]. This allows us to neglect the kinetic term in the Hamiltonian. Indeed, while the chemical potential term is of order μ_∞ and the pairing term is of order Δ/λ, the kinetic energy scales with $1/(\lambda^2 m)$. The kinetic energy is therefore small compared to the chemical potential and pairing terms if

$$1 \ll \mu_\infty \lambda^2 m \qquad \text{and} \qquad 1 \ll \Delta\lambda m, \tag{2.54}$$

which can be achieved by making λ large, or alternatively by taking $m \to \infty$.

As a consequence, near the interface the BdG-Hamiltonian can be written as

$$\mathcal{H}_{\text{BdG}} = -\mu(x)\hat{\tau}_3 + p\,\Delta\,\hat{\tau}_1 \tag{2.55}$$

Eq. (2.55) has the form of a massive Dirac equation, where the role of the mass is played by the term $-\mu(x)$. The dispersion relation of course follows directly from the general BdG-Hamiltonian in Eq. (2.49) and its spectrum in Eq. (2.50) by simplifying $\xi_p = \mu(x)$ and is thus given by $E_\pm = \pm\sqrt{(\mu(x))^2 + \Delta^2 p^2}$. Importantly, the mass term depends on position and changes sign at the domain wall. This situation is well-known in the context of high-energy physics and has been first studied by Jackiw and Rebbi in 1976 [94]. Their groundbreaking finding was that under very general circumstances, a particle obeying the Dirac equation coupled to a scalar field – which is just another name for a mass term – with a kink profile will develop a zero-energy bound state localized at the kink. This mode is called a soliton, because it appears alone and separated in energy from the continuum of states in the bulk bands.

In a sense, the appearance of the bound state is a topological feature of the mass profile. To see this, note that far away from the domain wall, $\mu(x)$ is practically constant and the spectrum is gapped. Importantly, the sign of $\mu(x)$ does not influence the spectrum itself, but the interpolation between masses with opposite signs requires a zero in the mass term, which is enough for a bound state to form. The existence of the bound state does not depend on the exact shape of the interpolation and thus is robust against small variations, as long as the signs of the asymptotic values $\lim_{x\to\pm\infty}\mu(x)$ remain fixed.

[4]It is helpful to think in terms of the Fourier decomposition of $\mu(x)$. Indeed, one finds

$$\mathcal{FT}\left[\mu_\infty \tanh(x/\lambda)\right](p) = \mathrm{i}\mu_\infty\sqrt{\frac{\pi}{2}}\,\frac{1}{\sinh\left(\lambda p\pi/2\right)},$$

which roughly decays exponentially on a scale $1/\lambda$.

To see that the Hamiltonian in Eq. (2.55) does have exactly one zero energy eigenstate, we make the ansatz

$$\phi_0(x) = \underbrace{\frac{1}{N_\mu}\, \mathrm{e}^{-\frac{1}{\Delta}\int_0^x \mathrm{d}x'\ \mu(x')}}_{:=\chi_0(x)} \underbrace{\begin{pmatrix} u_0 \\ v_0 \end{pmatrix}}_{:=|\psi_0\rangle}, \tag{2.56}$$

where $|\psi_0\rangle$ is a spinor still to be determined and N_μ is a normalization factor depending on the exact form of $\mu(x)$. Inserting the ansatz into the real space version of Eq. (2.55), where $p \to \hat{p} = -\mathrm{i}\partial_x$, we obtain

$$\mathcal{H}_{\mathrm{BdG}}\, \phi_0(x) = (-\hat{\tau}_3 + \mathrm{i}\hat{\tau}_1)\, \mu(x)\chi_0(x)|\psi_0\rangle. \tag{2.57}$$

For $\phi_0(x)$ to be a zero energy solution, it needs to fulfill $\mathcal{H}_{\mathrm{BdG}}\, \phi_0(x) = 0$, which allows us to determine the spinor $|\psi_0\rangle = (u_0, v_0)^{\mathrm{T}}$. We find

$$\begin{pmatrix} -1 & \mathrm{i} \\ \mathrm{i} & 1 \end{pmatrix} |\psi_0\rangle = 0 \qquad \text{or} \qquad \begin{aligned} -u_0 + \mathrm{i}v_0 &= 0 \\ \mathrm{i}u_0 + v_0 &= 0. \end{aligned} \tag{2.58}$$

Crucially, by multiplying the second equation on the right hand side of Eq. (2.58) with i, we readily see that there is only a single condition for the two components from the Hamiltonian, and of course another from normalization. Hence, up to a global phase, there is only a *single* zero-energy solution of the form of Eq. (2.56). In fact, Jackiw and Rebbi showed in their original paper that this ansatz together with the continuum states form a complete and normalized set of states. Hence, we conclude that $\phi_0(x)$ is the only zero-energy state present and is found to be

$$\phi_0(x) = \frac{1}{2}\, \chi_0(x) \begin{pmatrix} 1+\mathrm{i} \\ 1-\mathrm{i} \end{pmatrix}. \tag{2.59}$$

The reason why we chose $|\psi_0\rangle$ in this way will become apparent below.

Finally, any general wave function of the form $\phi(x) = (u, v)^{\mathrm{T}}$ solving the BdG-Hamiltonian allows us to find the associated second-quantized quasiparticle operator γ according to (see, *e.g.,* Ref. [95])

$$\gamma = \int \mathrm{d}x\, \phi^*(x)^{\mathrm{T}} \Psi(x), \tag{2.60}$$

where $\Psi(x) = (\psi(x), \psi(x)^\dagger)^{\mathrm{T}}$ is the real-space form of the spinor introduced in Eq. (2.49). Here, the operator corresponding to the zero-energy bound state is thus

$$\gamma = \frac{1}{\sqrt{2}} \int \mathrm{d}x\, u(x) \left[(1+\mathrm{i})\psi(x) + (1-\mathrm{i})\psi^\dagger(x)\right], \tag{2.61}$$

which has the important property

$$\gamma = \gamma^\dagger. \tag{2.62}$$

In summary, we found that there is a single bound state at the boundary between a topological and a trivial phase of a spinless one-dimensional superconductor. The associated quasiparticle operator is hermitian, and thus the quasiparticle is its own antiparticle. We have therefore shown that the edge state of a spinless, one-dimensional topological superconductor is a Majorana mode. The discussion in this section is a special case of the more general *index theorem* in mathematics due to Atiyah and Singer, which relates the topology of certain parameters of a differential equation (comparable to the mass term in our case) to solutions with particular properties (comparable to bound states) [57, 96, 97].

2.3 Physical realizations of the Kitaev chain

While the Kitaev chain is a convenient model to introduce and illustrate the general idea behind Majorana fermions in condensed matter systems, there are severe limitations to its direct applicability. The basic challenges of an experimental realization are connected with the assumption of spinless fermions in the Kitaev chain. Since electrons are spin one-half particles, they generally come in pairs of both spin polarizations. Ignoring possible intricacies of spin playing a role, we simply note that two fermionic states per site will lead to four Majoranas per site. Therefore, copying the Kitaev chain for each spin species will still leave two unpaired Majoranas at both ends of the chain, which can be recombined into one local fermion. Furthermore, in the Hamiltonian in Eq. (2.1), we assumed p-wave pairing in a one-dimensional electronic system, which is a rather exotic state of superconductivity. Realistic proposals will therefore have to eliminate one half of the spin-degrees of freedom from the problem, and also find a way to utilize standard s-wave singlet pairing.

2.3.1 Quantum spin Hall edge states

The striking consequence of the topological nature of the gap in quantum spin Hall systems is the emergence of edge states localized at the boundary to a topologically trivial region. Their defining properties are that they are counter-propagating and of opposite spin, *i.e.,* the direction of motion is locked to the spin projection. When the Fermi level is within the bulk gap, the edge states are the only low-energy degrees of freedom and can be modeled by the Hamiltonian

$$H_0 = \int \mathrm{d}x\, \Psi(x)^\dagger \left(v_\mathrm{F} \hat{p}\, \hat{\sigma}_3 - \mu\right) \Psi(x), \tag{2.63}$$

with the Fermi velocity v_F and the chemical potential μ. The spinor is defined as $\Psi(x) = (\psi_\uparrow(x), \psi_\downarrow(x))^\mathrm{T}$. Note how the peculiar structure of the kinetic term reflects the special physical properties of the edge states. The term linear in $\hat{p}$ leads to a linear dispersion with group velocity $\pm v_\mathrm{F}$. However, the Pauli matrix $\hat{\sigma}_3$ acting in spin space results in a relative sign of the kinetic terms of spin $\uparrow$ and $\downarrow$. As a consequence, the particular Hamiltonian in Eq. (2.63) describes rightmoving (leftmoving) spin-$\uparrow$ ($\downarrow$) electrons.

Importantly, by focusing on the edge states and their effective Hamiltonian, we are left with a single pair of fermionic states and thus avoid fermion doubling. One can hope to find a route to a topological superconducting phase by utilizing the spin-momentum locking of the edge states (which can be thought of as infinitely strong spin-orbit coupling (SOC)), the spin-polarizing effect of a magnetic field, and proximity induced s-wave singlet pairing. Note that the latter is naturally supported by the counterpropagating electrons of opposite spin we find at the helical edge. The effect of proximity induced s-wave singlet pairing can be modeled by adding the term

$$H_\Delta = \int \mathrm{d}x\, \Delta\, (\psi_\uparrow(x)\psi_\downarrow(x) + \mathrm{h.c.}) \tag{2.64}$$

to the Hamiltonian. Although H_Δ has a standard BCS-form, the physical consequences it has on the edge states go beyond s-wave singlet effects. We will discuss

this in depth in Chapter 4, but restrict ourselves in this chapter to what we need to connect quantum spin Hall insulator (QSHI) edge states to spinless superconductivity.

To see how these ingredients fit together, let us start without superconductivity and only including a Zeeman coupling into the edge states, which explicitly breaks time-reversal symmetry and introduces a gap in the spectrum (*cf.* Chapter 3 for more details). We thus consider the Hamiltonian

$$H' = H_0 + H_\mathrm{z}, \tag{2.65}$$

where the Zeeman term is given by

$$H_\mathrm{z} = b \int \mathrm{d}x\, \Psi^\dagger(x)\, \hat{\sigma}_1\, \Psi(x), \tag{2.66}$$

with b the strength of the magnetic field. We choose the field along the x-direction, but the precise orientation is not important as long as it lies in the plane perpendicular to the SOC. We can straightforwardly diagonalize the Hamiltonian and write it in the form

$$H' = \int \frac{\mathrm{d}k}{2\pi} \left(\psi_+^\dagger(k), \psi_-^\dagger(k)\right) \begin{pmatrix} \epsilon_+(k) & 0 \\ 0 & \epsilon_-(k) \end{pmatrix} \begin{pmatrix} \psi_+(k) \\ \psi_-(k) \end{pmatrix}, \tag{2.67}$$

where we have taken the Fourier transform and switched to momentum space. The operators $\psi_\pm(k)$ now annihilate particles in the two bands given by their dispersions $\epsilon_\pm(k) = -\mu \pm \sqrt{v_\mathrm{F}^2 k^2 + b^2}$. Note that the new operators $\psi_\pm$ are related to the previous operators by a unitary transformation ($UU^\dagger = 1$)

$$\begin{pmatrix} \psi_+(k) \\ \psi_-(k) \end{pmatrix} = U \begin{pmatrix} \psi_\uparrow(k) \\ \psi_\downarrow(k) \end{pmatrix}. \tag{2.68}$$

The new operators are thus superpositions of the field operators $\psi_\uparrow, \psi_\downarrow$, and consequently not eigenstates of $\hat{\sigma}_3$ anymore.

Next, we address the question how superconductivity affects the edge states. To do so, we invert Eq. (2.68) and write H_Δ in terms of $\psi_\pm$. We find

$$\begin{aligned} H_\Delta = \int \frac{\mathrm{d}k}{2\pi} \{ & \Delta_s(k) \left[\psi_-(-k)\psi_+(k) + \mathrm{h.c.}\right] \\ & + \Delta_p(k) \left[\psi_-(-k)\psi_-(k) + \psi_+(-k)\psi_+(k) + \mathrm{h.c.}\right] \}, \end{aligned} \tag{2.69}$$

with the effective pairings

$$\Delta_s(k) = -\frac{b\Delta}{\sqrt{v_\mathrm{F}^2 k^2 + b^2}} \qquad \text{and} \qquad \Delta_p(k) = -\frac{v_\mathrm{F} k \Delta}{2\sqrt{v_\mathrm{F}^2 k^2 + b^2}}. \tag{2.70}$$

Eq. (2.69) has a straightforward interpretation. The first term represents s-wave pairing (since Δ_s is even in k) which couples states in different bands. It is a remnant of the original s-wave singlet pairing and strongest at $k = 0$. Note that taking the limit $b \to 0$ in Eqs. (2.69) and (2.70) is problematic, since they were explicitly derived for a nonzero magnetic field. Nevertheless, the magnetic field intertwines with s-wave pairing in the following way. At $k = 0$, the spin of the

+ band points along the magnetic field in positive x-direction, whereas the spin of the − band points in negative x-direction. For k away from zero, the spin of the + (−)band rotates back to the projections without magnetic field, *i.e.,* ↑ for $k \to \infty$ and ↓ for $k \to -\infty$ (and vice versa for the − band). Therefore, only around $k = 0$ are the spins in different bands and at momenta k and $-k$ really anti-aligned. The region in momentum space where this is the case, and s-wave singlet pairing therefore possible, is larger for larger magnetic fields.

More important for the connection to the Kitaev chain, however, is the second term in Eq. (2.69). It describes pairing which couples states in the same band and opposite momenta, where, crucially, the pairing strength is an odd function of k. This is necessary since field operators with the same band index (as the only quantum number here) anticommute, rendering products such as $\psi_\pm(-k)\psi_\pm(k)$ odd in k. Were they coupled by s-wave pairing, the product of pairing and field operators would not survive the integration over all momenta. A p-wave pairing term, however, avoids this problem. Note that $\Delta_p(k)$ is zero at $k = 0$ by definition and saturates at $\pm\Delta/2$ for $k \to \pm\infty$. The physical mechanism how s-wave singlet pairing can mediate p-wave pairing is closely related to the behavior of the spin projections along the bands mentioned before. Away from $k = 0$, the spins within one band tend to be antiparallel, whereas they tend to be aligned with the magnetic field close to $k = 0$. Consequently, singlet pairing can couple states at momenta $\pm k$. The degree to which spins are parallel or antiparallel, respectively, depends on the momentum and the strength of the magnetic field.

Summarizing the considerations above, placing the chemical potential within one of the two bands is essentially enough to realize a spinless p-wave superconductor with only one pair of states at the Fermi level. For instance, in the limit $b \gg \Delta$, where the gap between the bands becomes very large, we can place μ close to the bottom of the upper band such that the lower band plays no role for the low-energy physics. Note that this means the chemical potential is of the order of the magnetic field strength, or more precisely $\mu \geq b$. Projecting the lower band away and focusing on small momenta, we can write

$$\epsilon_+(k) \approx -\mu_{\text{eff}} + \frac{k^2}{2m_{\text{eff}}} \tag{2.71}$$

with $\mu_{\text{eff}} = \mu - b$ and $m_{\text{eff}} = b/v_{\text{F}}^2$, as well as

$$\Delta_p(k) \approx \Delta_{\text{eff}}\, k \tag{2.72}$$

with $\Delta_{\text{eff}} = v_{\text{F}}\Delta/(2b)$. With these approximations and going back to real space, we thus obtain

$$H' + H_\Delta \approx \int \mathrm{d}x \left[\psi_+^\dagger(x) \left(\frac{\hat{p}^2}{2m_{\text{eff}}} - \mu_{\text{eff}}\right) \psi_+(x) + \Delta_{\text{eff}}\Big(\psi_+(x)\, \hat{p}\, \psi_+(x) + \text{h.c.}\Big)\right]. \tag{2.73}$$

We can readily identify the low-energy Hamiltonian of the helical edge states of a QSHI, proximity coupled with an s-wave superconductor and subject to a magnetic field, with the continuum model of a spinless p-wave superconductor. As noted before, the system is in a trivial phase if $\mu_{\text{eff}} < 0 \Leftrightarrow \mu < b$, *i.e.,* if the chemical potential is outside the upper band. The topological phase is realized if $\mu_{\text{eff}} > 0 \Leftrightarrow \mu > b$. This argument is only valid as long as $h \gg \Delta$.

In order to obtain a full phase diagram, let us go back to the original description in terms of the $\psi_{\uparrow,\downarrow}$ operators and consider the full Hamiltonian $H = H_0 + H_z + H_\Delta$. Bringing H in a BdG-form, it is straightforward to determine the excitation spectrum. One finds two positive eigenvalues

$$E_\pm(k) = \sqrt{b^2 + \Delta^2 + \mu^2 + k^2 v_F^2 \pm 2\sqrt{b^2\Delta^2 + b^2\mu^2 + \mu^2 k^2 v_F^2}} \tag{2.74}$$

and two negative ones with a minus sign in front of $E_\pm$, therefore the gap in the excitation spectrum vanishes if $E_\pm = 0$. This reveals that only E_- can be zero at $k = 0$. We have

$$E_\pm(k=0) = \sqrt{b^2 + \Delta^2 + \mu^2 - 2b\sqrt{\Delta^2 + \mu^2}} = \sqrt{\left(b - \sqrt{\Delta^2 + \mu^2}\right)^2}, \tag{2.75}$$

and arrive at the conclusion that the topological phase transition happens at the gap closing $b = \sqrt{\Delta^2 + \mu^2}$. Since we know that the topological phase requires $\mu > b$ for small Δ, we deduce that the system is in the topological regime if

$$\Delta^2 + \mu^2 > b^2. \tag{2.76}$$

Roughly speaking, the system is topological if the quasiparticle gap is dominated by superconductivity and trivial if the gap is largely due to the magnetic field. Curiously, this implies that the topologically nontrivial phase extends to the case of zero magnetic field, *i.e.,* $b = 0$.

2.3.2 Nanowires

The pursuit of an experimental detection of Majorana fermions in the laboratory received a major push, when two seminal works [75, 76] showed that the topological phase of the Kitaev chain can be mimicked by a nanowire. All the setup needs to have is sizable SOC intrinsic to the wire, as well as proximity to a magnetic field and a conventional s-wave superconductor. We are going to review the intricate interplay of these ingredients in the following and show how the physics of the Kitaev chain emerges under the right circumstances.

The lowest subband of such an electron-doped semiconducting wire, for instance InAs or InSb, can be modeled by the Hamiltonian

$$H = H_{\text{wire}} + H_\Delta, \tag{2.77}$$

where

$$H_{\text{wire}} = \int \mathrm{d}x \, \left(\psi_\uparrow^\dagger, \psi_\downarrow^\dagger\right) \left(\mathcal{H}_0 + \mathcal{H}_{\text{soc}} + \mathcal{H}_z\right) \begin{pmatrix}\psi_\uparrow \\ \psi_\downarrow\end{pmatrix}, \tag{2.78a}$$

with

$$\mathcal{H}_0 = \left(-\frac{\partial_x^2}{2m} - \mu\right)\hat{\sigma}_0, \tag{2.78b}$$

$$\mathcal{H}_{\text{soc}} = -\mathrm{i}\alpha\hat{\sigma}_2\partial_x, \tag{2.78c}$$

$$\mathcal{H}_z = b\hat{\sigma}_3, \tag{2.78d}$$

describe the spin-orbit coupled wire subjected to a magnetic field, and

$$H_\Delta = \int \mathrm{d}x\, \Delta \left(\psi_\uparrow \psi_\downarrow + \psi_\downarrow^\dagger \psi_\uparrow^\dagger\right) \tag{2.79}$$

describes the effect of the proximity induced s-wave pairing. Note that the Pauli matrices $\hat{\sigma}_i$ act in spin space. The field operator $\psi_\sigma^\dagger$ (ψ_σ) adds (removes) an electron with spin $\sigma =\uparrow,\downarrow$ to (from) the wire.

Let us set $\Delta = 0$ and discuss H_{wire} first. It contains a standard kinetic term $\mathcal{H}_0$ with effective mass m and chemical potential μ, a SOC term $\mathcal{H}_{\text{soc}}$ along the y-direction with coupling constant α, and finally the Zeeman term $\mathcal{H}_z$ coupling the electron spin to a magnetic field of strength b along the z-direction. We note that SOC and magnetic field have to be perpendicular, but only the relative angle between them is important. We choose to align the magnetic field with the spin quantization axis. The effect of the three terms in $\mathcal{H}_{\text{wire}}$ is as follows. Clearly, the kinetic term alone produces two degenerate dispersion relations in the form of parabolas, one for each spin. The Zeeman term lifts the spin-degeneracy by shifting up/down spins in opposite directions. Lastly, the SOC term is off-diagonal in spin space and therefore couples $\uparrow$ and $\downarrow$ spins. It aims to align the spins along the y-axis, although with a coupling strength that depends on momentum. Especially, the coupling changes sign at zero momentum.

On the basis of these general arguments, we can get a rough idea how nanowires can reproduce topological phases. Since using s-wave singlet pairing and magnetic fields is usually counterproductive, with the latter polarizing spin while the former necessarily requires opposite spins, it is not hard to see that SOC is of paramount importance. It provides a way of tilting the spins away from the quantization axis, such that there are now pairs of electrons with opposite components in the plane perpendicular to the SOC. Due to the spin-splitting by the magnetic field, the spin-degeneracy is automatically lifted. This turns out to be enough to create an effective p-wave pairing in an effectively spinless channel.

In order to illustrate the physics of the wire and to relate it to the Kitaev chain and the edge states of the quantum spin Hall insulator more concretely, we are going to consider two specific limits. In both cases, we assume that the pairing is smaller than the bigger of the two energy scales set by the magnetic field and SOC, *i.e.,* $\Delta \ll \max(b, \epsilon_{\text{soc}})$ with $\epsilon_{\text{soc}} = m\alpha^2$.

As a first step, let us rewrite the Hamiltonian in momentum space and in terms of Nambu spinors, thus bringing it in the form of a BdG-Hamiltonian. We find

$$H_{\text{wire}} = \frac{1}{2}\int \mathrm{d}x\, \Psi_p^\dagger\, \mathcal{H}_{\text{BdG}}\, \Psi_p, \tag{2.80}$$

where the BdG-Hamiltonian is given by the matrix

$$\mathcal{H}_{\text{BdG}} = \begin{pmatrix} \frac{p^2}{2m} - \mu + b & -\mathrm{i}p & 0 & \Delta \\ \mathrm{i}p & \frac{p^2}{2m} - \mu - b & \Delta & 0 \\ 0 & \Delta & -\frac{p^2}{2m} + \mu + b & \mathrm{i}p \\ \Delta & 0 & -\mathrm{i}p & -\frac{p^2}{2m} + \mu - b \end{pmatrix} \tag{2.81a}$$

or

$$\mathcal{H}_{\text{BdG}} = \hat{\tau}_3 \left[\left(\frac{p^2}{2m} - \mu\right)\hat{\sigma}_0 + \alpha\hat{\sigma}_2\right] - b\,\hat{\tau}_0\hat{\sigma}_3 + \Delta\,\hat{\tau}_1\hat{\sigma}_0 \tag{2.81b}$$

in short, with the spinor[5]

$$\Psi_p = \left(\psi_\uparrow(p), \psi_\downarrow(p), \psi_\downarrow^\dagger(p), -\psi_\uparrow^\dagger(p)\right). \tag{2.82}$$

In Eq. (2.82), $\psi_\sigma^\dagger(p)$ [$\psi_\sigma(p)$] creates [annihilates] an electron with spin σ and momentum p and we use the notation $\hat{\tau}_i$ for Pauli matrices in Nambu space.

2.3.2.1 Kitaev limit

In the Kitaev limit, the largest energy is the magnetic field and we assume $b \gg \epsilon_{\text{soc}}$. As a lowest order approximation, we can set the SOC to zero. Also setting $\Delta = 0$ for now, the eigenvalues of the matrix in Eq. (2.81) give the normal state dispersions $\epsilon_{p,\sigma} = \frac{p^2}{2m} - \mu + \text{sgn}(\sigma)b$, with $\sigma = \uparrow, \downarrow$ and $\text{sgn}(\sigma = \uparrow) = 1$ ($\text{sgn}(\sigma = \downarrow) = -1$). As mentioned before, we find two parabolas shifted up or down depending on the spin.

When the chemical potential is below the bottom of the spin-$\uparrow$ band, *i.e.,* $\mu < b$, there are either no states at the Fermi momentum for $\mu < -b$, or a single right- and left-moving mode both with spin $\downarrow$.

If the chemical potential is within the spin-$\downarrow$ band, but close to the bottom of it, the states in the spin-$\uparrow$ band play no role for the low-energy physics. We introduce the basis

$$|\text{e}\uparrow\rangle = (1,0,0,0)^{\text{T}}, \quad |\text{e}\downarrow\rangle = (0,1,0,0)^{\text{T}}, \quad |\text{h}\downarrow\rangle = (0,0,1,0)^{\text{T}}, \quad |\text{h}\uparrow\rangle = (0,0,0,1)^{\text{T}}, \tag{2.83}$$

of which only the spin-$\downarrow$ states $|e\downarrow\rangle$ and $|h\downarrow\rangle$ are important when considering the effect of superconductivity without SOC.

It is now easy to verify that spin-polarization prohibits superconducting pairing. All matrix elements of the pairing term with respect to $|\text{e}\downarrow\rangle$, $|\text{h}\downarrow\rangle$ are indeed zero, explicitly

$$\langle \text{e}\downarrow | \Delta\, \hat{\tau}_1\hat{\sigma}_0 | \text{e}\downarrow\rangle = \langle \text{e}\downarrow | \Delta\, \hat{\tau}_1\hat{\sigma}_0 | \text{h}\downarrow\rangle = \langle \text{h}\downarrow | \Delta\, \hat{\tau}_1\hat{\sigma}_0 | \text{e}\downarrow\rangle = \langle \text{h}\downarrow | \Delta\, \hat{\tau}_1\hat{\sigma}_0 | \text{h}\downarrow\rangle = 0. \tag{2.84}$$

Note that this also means that superconductivity cannot introduce a gap into the system at the Fermi level, *i.e.,* at band crossings at finite momenta. This is actually true even when the high-energy spin-$\uparrow$ states are taken into account, since the pairing not only requires opposite spins, but also needs to couple states at opposite momenta. However, finite Δ would slightly push the bands apart at $p = 0$.

Including SOC perturbatively to first order, the physical picture changes. The dispersion without superconductivity does not change, since the matrix elements of the states in Eq. (2.83) with an off-diagonal perturbation are zero. However, the first order correction of the eigenstates is nonzero, and the low-energy states to first order are then given by (up to normalization)

$$|\text{e}\downarrow^{(1)}\rangle = \left(\frac{\text{i}\alpha p}{2b}, 1, 0, 0\right)^{\text{T}}, \qquad |\text{h}\downarrow^{(1)}\rangle = \left(0, 0, 1, \frac{-\text{i}\alpha p}{2b}\right)^{\text{T}} \tag{2.85}$$

[5]Note the order and the sign in the last two components of the spinor, which looks unnecessary, but in fact allows a somewhat simpler spin structure in the anomalous part of the Hamiltonian. We will come back to this point in the discussion about superconducting correlations.

The low-energy states thus acquire a nonzero spin-↑ component. One can check that the particular superpositions arising in Eq. (2.85) are given by a large component still pointing in negative z-direction (corresponding to spin ↓), but additionally a small component pointing in positive (negative) y-direction for $|\mathrm{e}\downarrow\rangle$ ($|\mathrm{h}\downarrow\rangle$). The spins are therefore slightly tilted away from the z-axis. Hence, $|\mathrm{e}\downarrow\rangle$ and $|\mathrm{h}\downarrow\rangle$ now have *opposite* polarization along the y-direction. Note that the deviation from the z-axis is linear in the momentum, and inversely proportional to the magnetic field. This reflects the fact that a larger magnetic field increases the initial polarization along z.

To see how superconductivity now enters the low-energy physics, we calculate

$$\langle \mathrm{e}\downarrow^{(1)} | \Delta\, \hat{\tau}_1\hat{\sigma}_0 | \mathrm{h}\downarrow^{(1)}\rangle = -\frac{\mathrm{i}\Delta\alpha p}{b}, \qquad \langle \mathrm{h}\downarrow^{(1)} | \Delta\, \hat{\tau}_1\hat{\sigma}_0 | \mathrm{e}\downarrow^{(1)}\rangle = \frac{\mathrm{i}\Delta\alpha p}{b}, \tag{2.86a}$$

$$\langle \mathrm{e}\downarrow^{(1)} | \Delta\, \hat{\tau}_1\hat{\sigma}_0 | \mathrm{e}\downarrow^{(1)}\rangle = 0, \qquad \langle \mathrm{h}\downarrow^{(1)} | \Delta\, \hat{\tau}_1\hat{\sigma}_0 | \mathrm{h}\downarrow^{(1)}\rangle = 0. \tag{2.86b}$$

The resulting low-energy Hamiltonian in the basis $|\mathrm{e}\downarrow^{(1)}\rangle, |\mathrm{h}\downarrow^{(1)}\rangle$ is thus

$$H \simeq \left(\frac{p^2}{2m} - \mu'\right)\hat{\tau}_3 + \frac{\Delta\alpha p}{b}\hat{\tau}_2, \tag{2.87}$$

where we shifted the chemical potential $\mu' = \mu + b$. Comparing Eq. (2.87) with Eq. (2.4), we conclude that the low-energy physics of the wire in the Kitaev limit corresponds to the low momentum expansion of the BdG-Hamiltonian of the Kitaev chain.

2.3.2.2 QSHI limit

In this section, we are going to show how the physics of the spin-orbit coupled nanowire relates to the edge states of a QSHI. In the QSHI limit, we reverse the relationship between SOC and the magnetic field compared to the Kitaev limit and assume that $\epsilon_{\mathrm{soc}} \gg b$. Neglecting the Zeeman field at first, the Hamiltonian in Eq. (2.81) gives the normal state energies

$$\epsilon_p = \frac{1}{2m}\left(p + \mathrm{sgn}(\lambda)\, m\alpha\right)^2 - \mu - \frac{1}{2}m\alpha^2, \tag{2.88}$$

where $\lambda = \pm 1$ indicates the polarization of the spin of the eigenstates in y-direction, *i.e.,* along the SOC. The eigenstates read

$$|{\rightarrow}\rangle = \frac{1}{\sqrt{2}}\left(1, \mathrm{i}\right)^{\mathrm{T}}, \qquad |{\leftarrow}\rangle = \frac{1}{\sqrt{2}}\left(1, -\mathrm{i}\right)^{\mathrm{T}}, \tag{2.89}$$

where $\hat{\sigma}_2|{\rightarrow}\rangle = |{\rightarrow}\rangle$ and $\hat{\sigma}_2|{\leftarrow}\rangle = -|{\leftarrow}\rangle$, *i.e.,* $|{\rightarrow}\rangle$ ($|{\leftarrow}\rangle$) corresponds to $\lambda = 1$ ($\lambda = -1$). Thus, we find two bands in the form of shifted parabolas and a crossing at $p = 0$, and additionally with opposite polarization along the y-axis. In the following, we are interested in the question how a magnetic field and superconductivity can lift the zero-momentum crossing. For simplicity, we set $\mu = 0$ and therefore place the chemical potential in the middle of both magnetic and superconducting gap.

Since we focus on small momenta now, we neglect the kinetic energy term in Eq. (2.81). The $p \sim 0$ part of the Hamiltonian thus reads

$$\mathcal{H}_{\mathrm{BdG}} \simeq \alpha p\, \hat{\tau}_3\hat{\sigma}_2 + b\, \hat{\tau}_0\hat{\sigma}_3 + \Delta\, \hat{\tau}_1\hat{\sigma}_0, \tag{2.90}$$

which we readily identify as the model for QSHI edge states from Section 2.3.1 and Chapter 3, first rotated in spin-space about the x- and then about the y-axis by 90 degrees. Of course, this close relationship arises since around zero momentum the bands of the wire in the QSHI limit without magnetic field exactly mimic the spin-momentum locking of helical edge states.

Close to $p = 0$, the spectrum of the wire is therefore analogous to the helical edge and given by $\epsilon_p = \pm\sqrt{(\alpha p)^2 + (b \pm \Delta)^2}$. Note that the gap closes linearly for $b = \pm\Delta$, which signals a topological phase transition. In order to decide which is the trivial and which is the topological phase, we note that without closing the gap in the full spectrum (*i.e.,* not only around $p \approx 0$) one can increase the magnetic field from the QSHI limit with $|\Delta| < |b| < \epsilon_{\text{soc}}$ to the Kitaev limit discussed previously, where $|\Delta| < \epsilon_{\text{soc}} < b$. Thus, the case $|b| > |\Delta|$ phase of the QSHI limit is smoothly connected with the topological phase in the Kitaev limit, and thus topological itself. For nonzero μ, one finds the topological criterion $b > \sqrt{\Delta^2 + \mu^2}$ in the same fashion.

It is important to note that this is the reverse condition as in the QSHI case in Section 2.3.1. The physical reason for this is the fact that the quantum wire has a parabolic dispersion, *i.e.,* away from $p = 0$ the bands bend upwards. Loosely speaking, it can be thought of as a QSHI edge model for $p \simeq 0$ and an additional spinless superconductor at the outer wings of the dispersion for larger p. The wire therefore has one additional pair of states at the Fermi energy, which renders the $|\Delta| > |b|$ phase of the wire trivial since standard s-wave singlet pairing is always possible.

2.4 Quantum computation with Majorana fermions

In this section, we aim to sketch the connection between Majorana fermions and quantum computation, which is arguably the biggest promise and main motivation behind the realization of Majoranas in the laboratory.

While the goal of this section is to merely give a hint of how to utilize Majorana fermions for quantum computation, a more comprehensive discussion of this exciting line of research can be found in, *e.g.,* [48, 51, 52, 67, 68, 98–101].

2.4.1 Many-body ground state & non-Abelian statistics

The most fundamental building blocks of any quantum computer are qubits, which store information, and quantum gates, which manipulate qubits to perform computations. In this section, we consider how Majorana fermions can be used to construct qubits and perform operations on them, before we turn to the explicit relation of braiding and quantum gates in Section 2.4.2.

Fortunately, for a simple and accessible discussion we can turn to the Kitaev chain again, and similar ideas apply to almost all realizations of topological superconductors. We already have done most of the work in Section 2.1.2 and merely use the results in the context of quantum computation. We restrict ourselves to the special point $t = \Delta$, $\mu = 0$ within the topological region. Recall that the bulk of the chain corresponds to a chain of inert fermions $\hat{d}_j^\dagger, \hat{d}_j$. The bulk ground state

$|\mathrm{GS}\rangle$ with energy E_{GS} corresponds to all states j being empty, but is in fact two-fold degenerate due to the presence of the zero-energy fermion

$$\hat{f} = \frac{1}{2}\left(\gamma_{B,N} + \mathrm{i}\gamma_{A,1}\right), \tag{2.91}$$

where $\gamma_{B,N}$ and $\gamma_{A,1}$ are Majoranas located at opposite ends of the chain. As a consequence, $|\mathrm{GS}\rangle$ and $\hat{f}^\dagger|\mathrm{GS}\rangle$ span a degenerate ground state subspace.

The key insight due to Kitaev and his seminal work [48] was the realization that $|\mathrm{GS}\rangle$ and $\hat{f}^\dagger|\mathrm{GS}\rangle$ could be used as states forming a qubit. Assuming the Majoranas $\gamma_{B,N}$ and $\gamma_{A,1}$ are well-separated and isolated, their recombination into a single fermion means that the qubit is actually nonlocal. Crucially, using Majoranas for quantum computation offers the possibility to realize protected operations on these qubits. The reason for this is deeply rooted in the fact that in lower than three dimensions, exchanging particles can have more complicated effects than simply giving a factor of ± 1 as for bosons and fermions. In two dimensions, for instance, a particle adiabatically encircling another particle and finally returning to its starting point is associated with a winding number, since the traced out path cannot be smoothly contracted to a point without crossing the position of the other particle. Thus, the final state does not need to be the same as the initial one [51, 52, 68].

In general, there are two possibilities. The final state $|\psi_f\rangle$ can differ from the initial state $|\psi_i\rangle$ by an arbitrary phase 2λ, such that

$$|\psi_f\rangle = \mathrm{e}^{2\mathrm{i}\lambda}|\psi_i\rangle, \tag{2.92}$$

where λ is the phase associated with one exchange of positions, *i.e.,* "half" of one full encircling. Note that $\lambda = 0$ ($\lambda = \pi$) corresponds to the familiar case of bosons (fermions). If the phase is neither bosonic nor fermionic, the particle is said to obey *anyonic statistics*.

Even more exotic behavior, however, can occur when the ground state is actually a degenerate manifold spanned by ground states $|\psi_i^n\rangle$. The superscript in $|\psi_i^n\rangle$ labels the degenerate ground states. In this case, there is nothing that stops the adiabatic encircling operation from mixing the different ground states, such that the final state becomes a superposition of the form

$$|\psi_f\rangle = \sum_{m,n} U_{mn}\, c_n |\psi_i^n\rangle \equiv U|\psi_i\rangle, \tag{2.93}$$

with $|\psi_i\rangle = \sum_n c_n|\psi_i^n\rangle$ the initial state. The action of the encircling operation is thus represented by a unitary matrix U corresponding to a rotation in the ground state manifold. Intriguingly, the matrices associated with distinct exchanges do not need to commute, potentially leading to *non-Abelian statistics*. These rotations can therefore be exploited to realize unitary quantum gates. Note that since they only rely on the topological properties of the exchange protocol, but not on the local details of the exact path, they too offer the potential for topological protection.

As a last remark, while these considerations apply to two-dimensional systems directly, it is not immediately obvious how to realize exchanges with one-dimensional topological superconductors and zero-dimensional Majoranas at the ends. We are going to show one example at the end of the chapter.

2.4.2 Realizing quantum gates with Majorana fermions

2.4.2.1 Braid group representation

In this section, we first review Ivanov's seminal work on the relationship of non-Abelian statistics and braiding to Majorana modes bound to vortices in spinless $p+\mathrm{i}p$ superconductors. After that, we show in a simplified toy model how Majorana modes bound to the end of one-dimensional topological phases can exhibit similar behavior.

Let us first briefly introduce the basic physics of a spinless $p+\mathrm{i}p$ superconductor. A two-dimensional electron gas exhibiting this kind of superconducting order can be modeled by the Hamiltonian

$$H = \int \mathrm{d}^2\mathbf{r} \left\{ \psi^\dagger \left(-\frac{\boldsymbol{\nabla}^2}{2m} - \mu \right) \psi + \frac{\Delta}{2} \left[\mathrm{e}^{\mathrm{i}\phi} \psi \left(\partial_x + \mathrm{i}\partial_y \right) \psi + \mathrm{h.c.} \right] \right\}, \tag{2.94}$$

where $\psi(\mathbf{r})$ annihilates a particle with mass m at position $\mathbf{r} = (x, y)^{\mathrm{T}}$, μ is the chemical potential, and the order parameter is determined by its modulus $\Delta > 0$ and a phase ϕ. Note the structure of the derivatives within the pairing term, which gives the $p + \mathrm{i}p$ pairing phase its name.

We do not want to analyze this exotic superconducting state in any detail. However, by following a protocol very much like the one we discussed for the Kitaev chain, one can write Eq. (2.94) in a BdG-form and define a map from the two-dimensional momentum space to a unit sphere. Analogous to the 1D cases presented in earlier sections, it turns out that this mapping has a topological invariant, namely the number of times the mapping covers the unit sphere. Mathematically, the invariant is called a Chern number. Coincidentally, the $p + \mathrm{i}p$ superconductor is topological for $\mu > 0$, *i.e.,* when the chemical potential intersects the band.

The interesting feature for our purpose is that a vortex created by threading a magnetic flux through the two-dimensional bulk in the topological phase forms a small trivial region and therefore introduces a boundary between phases with different topological character. The bulk-boundary correspondence turns out to apply to this case as well, and the zero-energy edge state associated with it is a Majorana mode yet again.

As a last introductory remark, spinless $p + \mathrm{i}p$ superconductors could be realized at the surface of 3D topological insulators [43] or in conventional two-dimensional electron systems by utilizing SOC, ferromagnetism, and conventional s-wave superconductivity [74]. Additionally, there is an ongoing search for intrinsic $p + \mathrm{i}p$ superconductors, of which Sr_2Ru_4 is an exemplary candidate [73]. Finally, $p + \mathrm{i}p$ superconductors share defining features with the Moore-Read state in fractional quantum Hall systems [51, 69, 70].

With this basic introduction at hand, let us consider two vortices binding Majorana modes, which we label i and $i + 1$ for reasons becoming apparent later on, as shown in Fig. 2.5. We assume that the vortices remain well-separated, such that the overlap of Majoranas is negligible. Note that a vortex is associated with a twist of the superconducting phase of 2π when going around the vortex. Therefore, in order for the phase to be single-valued we introduce branch cuts (indicated by the dashed

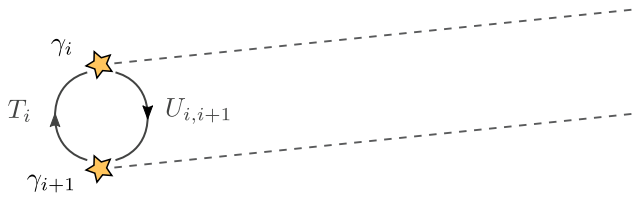

Figure 2.5: Schematic depiction of an elementary braiding operation T_i of two Majorana modes γ_i, γ_{i+1} bound to vortices, represented by yellow stars. Note that we define the braiding operator T_i to exchange the vortices in a clockwise fashion. The dashed lines indicate the branch cuts associated with the vortices.

lines), where the phase jumps by 2π. The operators γ_i fulfill the same defining algebra as the Majoranas we encountered in the Kitaev chain, *i.e.,* [compare with Eq. (2.28)]

$$\{\gamma_i, \gamma_j\} = 2\delta_{i,j}, \qquad \gamma_i^\dagger = \gamma_i. \tag{2.95}$$

Importantly, the locations of the vortices can be manipulated by moving the local pinning potentials. When a Majorana crosses the branch cut from another vortex, its associated operator changes in a nontrivial way. To see this, note that pairing terms such as $\Delta \mathrm{e}^{\mathrm{i}\phi}\psi\psi$ and $\Delta \mathrm{e}^{-\mathrm{i}\phi}\psi^\dagger\psi^\dagger$ are globally gauge invariant under the simultaneous transformations $\phi \to \phi + \theta$, $\psi \to e^{-\mathrm{i}\theta/2}\psi$ and $\psi^\dagger \to \mathrm{e}^{\mathrm{i}\theta/2}\psi^\dagger$ (we can omit spatial dependencies and derivatives for a global phase rotation). Thus, if Majoranas move across a branch cut and the phase of the order parameter changes by 2π, the fermion fields acquire a factor of -1. Consequently, the same is true for Majorana operators, since they are formed by a linear combination of creation and annihilation operators (*cf.* Eq. (2.27)).

We are now in the position to examine the effect of exchanging and braiding of a set of N Majorana modes. We refer to a braid if Majoranas are moved around and return to one of the initial positions of the Majoranas. Note that we use exchanging and braiding interchangeably. Importantly, braiding operations are *not* simply permutations, precisely because the statistics of Majorana modes is non-Abelian, so that braiding operations do not commute. We will return to this point shortly. Furthermore, for N vortices they form the so-called Braid group B_N, which is generated by elementary exchanges T_i of adjacent elements obeying ($i = 1, \ldots, N-1$)

$$\begin{aligned} T_i T_j &= T_j T_i \qquad |i-j| > 1 \\ T_i T_j T_i &= T_j T_i T_j \qquad |i-j| = 1. \end{aligned} \tag{2.96}$$

In our particular case, we choose the convention that T_i exchanges Majoranas γ_i and γ_{i+1} in a clockwise fashion. Of course, all other exchanges can be decomposed into a product of the generators T_i. Therefore it suffices to find a representation of the exchange of neighboring Majoranas.

Focusing on the situation in Fig. 2.5, we can read off the action of T_i on the operators γ_i and γ_{i+1}. Exchanging them as in a clockwise fashion moves γ_i to the position of the vortex hosting γ_{i+1}, crossing its branch cut in the process. At the same time, γ_{i+1} is moved to the position of γ_i without crossing any branch cuts.

Thus, the effect of T_i on γ_i and γ_{i+1} can be summarized as

$$T_i : \begin{cases} \gamma_i & \mapsto -\gamma_{i+1} \\ \gamma_{i+1} & \mapsto \gamma_i. \end{cases} \tag{2.97}$$

Ivanov's groundbreaking prediction was that there is a unique, unitary representation implementing the effect of T_i given by (up to a phase factor)

$$U_{i,i+1} = \exp\left(\frac{\pi}{4}\gamma_i\gamma_{i+1}\right) = \frac{1}{\sqrt{2}}\left(1 + \gamma_i\gamma_{i+1}\right), \tag{2.98}$$

[6]

such that

$$T_i(\gamma_{i/i+1}) = U_{i,i+1}\gamma_{i/i+1}U_{i,i+1}^\dagger = \mp\gamma_{i+1,i}. \tag{2.99}$$

Note that the inverse braiding operation is the counter-clockwise exchange, upon which γ_{i+1} acquires the minus sign, *i.e.,* $\gamma_{i+1} \to -\gamma_i$, while $\gamma_i \to \gamma_{i+1}$. Since the representation given in Eq. (2.97) is unitary, we obtain $T_i^{-1}(\gamma_{i/i+1}) = U_{i,i+1}^\dagger\gamma_{i/i+1}U_{i,i+1}$. Furthermore, since the braiding of the vortices essentially corresponds to the adiabatic time evolution of the operators, the effect of a braiding operation on a state is simply given by applying the unitary operators to the states themselves, *i.e.,* for some state $|\psi\rangle$ in the degenerate ground-state manifold

$$|\psi\rangle \mapsto U_{i,i+1}|\psi\rangle. \tag{2.100}$$

As a last remark, observe that $U_{i,i+1}$ as defined in Eq. (2.98) is even in Majorana operators and thus even in fermionic creation/annihilation operators. Hence, a braiding operation can never change the parity of the acted upon state. We will return to this restriction below.

2.4.2.2 Examples for braiding operators

Let us use the results of the previous section to explicitly discuss how systems of two and four vortices behave under braiding operations, and how to construct quantum gates from them.

Starting with two vortices binding Majoranas γ_1 and γ_2, there is of course only one fermionic degree of freedom. We construct it according to

$$\hat{c} = \frac{1}{2}\left(\gamma_1 + \mathrm{i}\gamma_2\right), \qquad \hat{c}^\dagger = \frac{1}{2}\left(\gamma_1 - \mathrm{i}\gamma_2\right). \tag{2.101}$$

From there, we obtain the basis $\{|0\rangle, |1\rangle\}$ with the states defined as

$$\hat{c}^\dagger|0\rangle = |1\rangle, \qquad \hat{c}|0\rangle = 0. \tag{2.102}$$

First, note that the two basis states are distinguished by their parity since

$$\hat{P}|0\rangle = -1, \qquad \hat{P}|1\rangle = 1 \tag{2.103}$$

[6] The latter equality follows from the series expansion of the exponential.

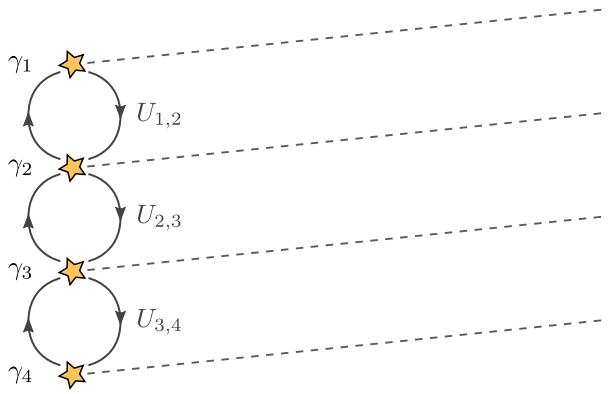

Figure 2.6: Schematic depiction of elementary braiding operations of four Majoranas $\gamma_{1,2,3,4}$ as an extension of Fig. 2.5.

with $\hat{P} = \mathrm{i}\gamma_1\gamma_2 = 2\hat{c}^\dagger\hat{c} - 1$. Therefore, braiding operations will never be able to mix the basis states and can only induce phase rotations. As a consequence, the single fermionic state stemming from two Majorana modes is insufficient to encode a qubit. This is related to the fact that for two vortices, there is only a single generator of the braid group, which reads

$$U_{1,2} = \exp\left(\frac{\pi}{4}\gamma_1\gamma_2\right) = \exp\left[\mathrm{i}\frac{\pi}{4}\left(1 - 2\hat{c}^\dagger\hat{c}\right)\right] \equiv \exp\left[\mathrm{i}\frac{\pi}{4}\hat{\sigma}_3\right] \tag{2.104}$$

where $\hat{\sigma}_3$ is a Pauli matrix in the space spanned by $\{|0\rangle,\ |1\rangle\}$. Braiding the pair of Majoranas therefore leads to a phase shift that depends on the parity of the state it acts on. This is clearly a unitary rotation and not just an overall phase shift.

Next, we extend the previous system by two more Majoranas, γ_3 and γ_4, as depicted in Fig. 2.6. For better comparability, we group the Majoranas in a pairwise fashion according to

$$\hat{c}_1 = \frac{1}{2}\left(\gamma_1 + \mathrm{i}\gamma_2\right) \qquad \text{and} \qquad \hat{c}_2 = \frac{1}{2}\left(\gamma_3 + \mathrm{i}\gamma_4\right). \tag{2.105}$$

Explicitly, the basis of the subspace is $\{|00\rangle, |11\rangle, |01\rangle, |10\rangle\}$, where the basis states are given by

$$|10\rangle = \hat{c}_1^\dagger|00\rangle, \qquad |01\rangle = \hat{c}_2^\dagger|00\rangle, \qquad |11\rangle = \hat{c}_1^\dagger\hat{c}_2^\dagger|00\rangle, \tag{2.106}$$

as well as the empty state with $\hat{c}_1|00\rangle = \hat{c}_2|00\rangle = 0$. Note that we grouped the basis according the parity of the states, which is even for $|00\rangle, |11\rangle$ and odd for $|01\rangle, |10\rangle$. There are now three elementary exchanges of adjacent Majoranas. Clearly, nothing changes about the action of $U_{1,2}$ on γ_1 and γ_2, apart from identifying $\hat{c}_1, \hat{c}_1^\dagger$ with $\hat{c}, \hat{c}^\dagger$ from before. Since braiding the first two Majoranas leaves γ_3 and γ_4 unchanged, we immediately have

$$\begin{aligned} U_{1,2} = \exp\left(\frac{\pi}{4}\gamma_1\gamma_2\right) = \frac{1}{\sqrt{2}}\left(1 + \gamma_1\gamma_2\right) = \frac{1}{\sqrt{2}}\left(1 + \mathrm{i} - 2\mathrm{i}\hat{c}_1^\dagger\hat{c}_1\right) \\ = \frac{1}{\sqrt{2}}\begin{pmatrix} 1+\mathrm{i} & 0 & 0 & 0 \\ 0 & 1-\mathrm{i} & 0 & 0 \\ 0 & 0 & 1+\mathrm{i} & 0 \\ 0 & 0 & 0 & 1-\mathrm{i} \end{pmatrix}, \end{aligned} \tag{2.107}$$

which is a generalization of the case of two Majoranas. We choose to write it in a slightly different form, since the second pair of Majoranas complicates the notation. Similarly, braiding γ_3 and γ_4 gives

$$U_{3,4} = \exp\left(\frac{\pi}{4}\gamma_3\gamma_4\right) = \frac{1}{\sqrt{2}}\left(1+\gamma_3\gamma_4\right) = \frac{1}{\sqrt{2}}\left(1+\mathrm{i}-2\mathrm{i}\hat{c}_2^\dagger\hat{c}_2\right) = \frac{1}{\sqrt{2}}\begin{pmatrix}1+\mathrm{i} & 0 & 0 & 0\\ 0 & 1-\mathrm{i} & 0 & 0\\ 0 & 0 & 1-\mathrm{i} & 0\\ 0 & 0 & 0 & 1+\mathrm{i}\end{pmatrix}, \tag{2.108}$$

which only differs from $U_{1,2}$ in that the relative phase shifts in the odd parity sectors are different.

The most interesting effect, however, is produced by braiding Majoranas contributing to different fermionic states, in our case this is achieved by the operator $U_{2,3}$. We obtain

$$U_{2,3} = \exp\left(\frac{\pi}{4}\gamma_2\gamma_3\right) = \frac{1}{\sqrt{2}}\left(1+\gamma_2\gamma_3\right) = \frac{1}{\sqrt{2}}\left[1+\mathrm{i}\left(\hat{c}_1^\dagger\hat{c}_2^\dagger-\hat{c}_1\hat{c}_2+\hat{c}_1^\dagger\hat{c}_2-\hat{c}_1\hat{c}_2^\dagger\right)\right] = \frac{1}{\sqrt{2}}\begin{pmatrix}1 & \mathrm{i} & 0 & 0\\ \mathrm{i} & 1 & 0 & 0\\ 0 & 0 & 1 & \mathrm{i}\\ 0 & 0 & \mathrm{i} & 1\end{pmatrix}. \tag{2.109}$$

Braiding γ_2 and γ_3 thus has the remarkable effect of mixing the basis states of the same parity. This becomes even more obvious if we consider exchanging γ_2 and γ_3 twice, which is implemented by the operator

$$(U_{2,3})^2 = \begin{pmatrix}0 & \mathrm{i} & 0 & 0\\ \mathrm{i} & 0 & 0 & 0\\ 0 & 0 & 0 & \mathrm{i}\\ 0 & 0 & \mathrm{i} & 0\end{pmatrix}, \tag{2.110}$$

which means that up to a phase, the states of equal parity are *interchanged* by repeating the braid. Note that this corresponds to transitions between $|01\rangle$ and $|10\rangle$, *i.e.,* a charge transfer between the first pair of vortices to the second, or between $|00\rangle$ and $|11\rangle$, *i.e.,* the addition or removal of two fermions (corresponding to a Cooper pair).

As a final remark, it is now easy to check that the braiding operations $U_{1,2}$ and $U_{2,3}$, as well as $U_{2,3}$ and $U_{3,4}$, respectively, do not commute. Hence, the outcome of a sequence of braids will depend on the order of the individual exchanges and is thus non-Abelian, distinguishing braiding of Majoranas from mere permutations of fermions or bosons.

2.4.2.3 Quantum gates

The results in the previous section demonstrate that braiding Majoranas does lead to nontrivial operations on a degenerate set of states. We now want to build on

this formalism to make the bridge to quantum information processing and quantum computing more explicit.

The fundamental building block of quantum computing is a *quantum bit*, or *qubit*, which is a two-level quantum system with states $|\bar{0}\rangle$ and $|\bar{1}\rangle$[7]. These states are the quantum analog of the possible values of classical bits, 0 and 1. Any possible operation on a qubit is then engineered by subjecting the qubit to precisely controlled physical manipulations, leading to a unitary time evolution generated by the Hamiltonian of the manipulation. Any operation on a single qubit is therefore given by a 2×2 unitary operator U, also called a quantum gate. In the following, we are going to relate the braiding operations to a few special representatives of single-qubit gates and discuss limitations of braiding for quantum computing applications. For a comprehensive introduction of Quantum Computation see the excellent text book by Nielsen and Chuang [102].

As a first step, we need to define a two-level system on which to operate. Note that the two states resulting from the fermionic level associated with a single pair of vortices are not sufficient, since they differ in parity and can never mix under braiding. Therefore, we turn to the four-vortex case, which results in four degenerate fermionic states, two even-parity and two odd-parity states, respectively. Possible choices for the qubit states are then[8]

$$|00\rangle \equiv |\bar{0}_e\rangle \qquad \text{and} \qquad |11\rangle \equiv |\bar{1}_e\rangle \tag{2.111a}$$

$$\text{or} \qquad |01\rangle \equiv |\bar{0}_o\rangle \qquad \text{and} \qquad |10\rangle \equiv |\bar{1}_o\rangle, \tag{2.111b}$$

where we introduce the subscript to distinguish between the qubit built from even- and odd-parity states.

With our construction of a qubit at hand, the first important set of gates to construct are the Pauli gates X, Y, Z, which simply correspond to the familiar Pauli matrices acting in the space of the qubit. The gates X and Z can be determined directly from the braiding operators. We find

$$\begin{pmatrix} Z_e & 0 \\ 0 & Z_o \end{pmatrix} = -\mathrm{i}\,(U_{1,2})^2 \tag{2.112}$$

and

$$\begin{pmatrix} X_e & 0 \\ 0 & X_o \end{pmatrix} = -\mathrm{i}\,(U_{2,3})^2\,, \tag{2.113}$$

implying that $Z_{e/o}$ and $X_{e/o}$ in both parity subspaces are derived from braiding Majoranas $\gamma_{1,2}$ and $\gamma_{2,3}$, respectively, up to a global phase shift which could for instance be absorbed in the definition of the qubit states. We can use this result to straightforwardly construct the third Pauli gate according to

$$\begin{pmatrix} Y_e & 0 \\ 0 & Y_o \end{pmatrix} = -\mathrm{i}\,(U_{2,3})^2\,(U_{1,2})^2\,, \tag{2.114}$$

[7] We add the bar in order to distinguish the qubit states from the states characterized by occupation numbers in the previous section.

[8] Of course it is only important to choose states of equal parity, the subsequent assignment to $|\bar{0}\rangle$, $|\bar{1}\rangle$ is arbitrary.

which also follows directly from the multiplicative property of Pauli matrices, *i.e.,* $\sigma_i\sigma_j = \mathrm{i}\epsilon_{ijk}\sigma_k$.

Furthermore, we can use the braiding operators to build the Hadamard (H) and phase gate (S), defined as

$$H = \frac{1}{\sqrt{2}}\begin{pmatrix}1 & 1\\ 1 & -1\end{pmatrix}, \qquad S = \begin{pmatrix}1 & 0\\ 0 & \mathrm{i}\end{pmatrix}. \tag{2.115}$$

We readily obtain

$$\begin{pmatrix}S_e & 0\\ 0 & S_o\end{pmatrix} = \mathrm{e}^{\mathrm{i}\frac{\pi}{4}}\,(U_{1,2})^{-1} \tag{2.116}$$

as well as

$$\begin{pmatrix}H_e & 0\\ 0 & H_0\end{pmatrix} = -\mathrm{i}\,U_{1,2}U_{2,3}U_{1,2} = \mathrm{i}U_{2,3}U_{1,2}U_{2,3}. \tag{2.117}$$

The quantum gates discussed in this section, together with the two-qubit CNOT-gate, are called Clifford gates. We do not show it here, but it is possible to construct the CNOT-gate on the basis of Majorana zero modes using auxiliary qubits and parity measurements [103]. Therefore, all Clifford gates can be constructed by braiding operators.

However, there are of course infinitely many possible unitary operations on a given number of qubits, which raises the question how significant the Clifford gates actually are for realizing a useful quantum computing task. Remarkably, one can show that there are discrete sets of gates that allow for an arbitrarily accurate approximation of any unitary operation on an arbitrary number of qubits, using only these gates. Such sets are called *universal* for quantum computing. It turns out that adding a single non-Clifford element elevates the Clifford gates to a universal set of gates[9], where the missing piece is the T-gate[10] defined as

$$T = \begin{pmatrix}1 & 0\\ 0 & \mathrm{e}^{\mathrm{i}\pi/4}\end{pmatrix}. \tag{2.118}$$

While this prevents braiding of Majoranas from being universal on its own [104,105], realizing quantum gates on the grounds of their non-Abelian statistics still holds great promise. The reason for this is the topological protection enjoyed by the braiding operations, which is rooted in the fact that a braid does not depend on specific details of the procedure, but the outcome is completely determined by the topology of it instead.

2.4.2.4 Explicit calculation of the braid operator for two Majoranas

To conclude the section, we now want to take a step back and have a closer look at how Majorana modes can be braided. Specifically, we want to connect the effect of

[9] Actually, the single-qubit Hadamard- and T-gate together with the CNOT-gate are enough for universality [102]. The Pauli gates are not needed at all, and the phase-gate is usually added because of its importance for quantum error-correction.

[10] The T-gate also goes by the name magic gate or, awkwardly, $\pi/8$-gate – the latter name referring to the possibility to write $T = \exp(-\mathrm{i}\pi/8)\,\mathrm{diag}[\exp(\mathrm{i}\pi/8), \exp(-\mathrm{i}\pi/8)]$.

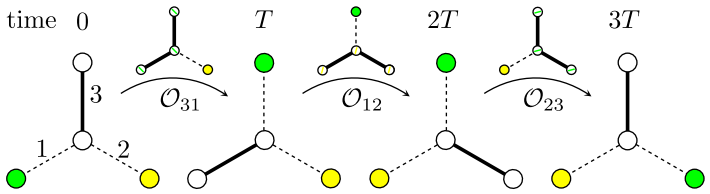

Figure 2.7: Schematic depiction of a braiding operation at a Y-junction formed by three topological superconductors, represented by numbered lines. The circles indicate Majorana modes located at the ends of the superconductors. Note that in the center, Majoranas from all three superconductors hybridize and form one true Majorana mode as well as one fermionic state, which we ignore. The dashing of the lines indicates whether the couplings Δ_i associated with the superconductors are zero (dashed) or finite (solid). At the ends of section with zero coupling, the Majorana modes remain at zero energy (indicated by colored circles). The figure shows the three stages at times $0, T, 2T, 3T$ of the braiding protocol at which only one of the couplings is finite. Additionally, the intermediate steps are indicated by operations $\mathcal{O}_{ij}$ during which the couplings are tuned. Figure without changes from Ref. [106], licensed under CC BY 4.0. Copyright IOP Publishing Ltd and Deutsche Physikalische Gesellschaft.

the braid operation on the Majorana operators, which we defined rather ad-hoc in Eq. (2.97), to the adiabatic time evolution of a quantum system. For completeness, we note that one can beautifully connect it to a non-Abelian Berry phase [54, 68, 101, 106].

For simplicity, we restrict ourselves to the explicit time evolution and to that end turn to a Y-junction of three one-dimensional spinless superconductors as depicted in Fig. 2.7. Interestingly, a similar setup can be used to construct a robust T-gate [107].

In the following, we will ignore the exact physical realization of the Y-junction and focus on the effective minimal model [54, 106]. It consists of four Majorana zero modes, three of which located at the outer ends of the wires, while the fourth one emerges through hybridization of the three inner ones. Since the wires are assumed to have a finite length, an outer Majorana γ_j is coupled to the central one with a coupling strength Δ_j (which is assumed to be adjustable), and we can describe the system with the Hamiltonian

$$H = \mathrm{i}\sum_{j=1}^{3} \Delta_j \gamma_0 \gamma_j = \mathrm{i}\bar{\Delta}\gamma_0\gamma_{\bar{\Delta}}, \tag{2.119}$$

with $\gamma_{\bar{\Delta}} = \sum_j \Delta_j \gamma_j / \bar{\Delta}$ where $\bar{\Delta} = \sqrt{\Delta_1^2 + \Delta_2^2 + \Delta_3^2}$. Eq. (2.119) thus describes the coupling between the central Majorana and a specific linear superposition of the outer ones, with a coupling given by $\bar{\Delta}$. The Majoranas γ_0 and $\gamma_{\bar{\Delta}}$ thus split and form levels at $\pm\bar{\Delta}$. However, one can construct linearly independent superpositions of the outer Majoranas γ, γ', which fulfill

$$\{\gamma_0, \gamma\} = \{\gamma_0, \gamma'\} = \{\gamma_{\bar{\Delta}}, \gamma\} = \{\gamma_{\bar{\Delta}}, \gamma'\} = \{\gamma, \gamma'\} = 0 \tag{2.120}$$

as well as $\gamma^2 = \gamma'^2 = 1$ and $\gamma^\dagger = \gamma$, $\gamma'^\dagger = \gamma'$. Thus, as long as $\bar{\Delta} \neq 0$, the system always features two true zero-energy Majoranas, which we can use to define

a fermionic state. Away from $\bar{\Delta} = 0$, the ground state will hence remain twofold degenerate.

Note that if only one of the couplings Δ_j is nonzero, the Hamiltonian only couples γ_0 and γ_j such that the zero modes are given by the two $\gamma_{k\neq j}$ and are localized at the end of the uncoupled wires. From this observation, we can develop the idea for a braiding operation. Specifically, let us start with $\Delta_3 \neq 0$ and $\Delta_1 = \Delta_2 = 0$, such that we have true zero-energy Majoranas γ_1 and γ_2. If we then tune to the point in parameter space, where $\Delta_3 = 0$ and $\Delta_1 \neq 0$ with $\Delta_2 = 0$ throughout (and avoiding $\bar{\Delta} = 0$), γ_2 would remain uncoupled and stay at zero energy and the end of wire 2. However, the available position of the other unpaired Majorana γ_1 moves to the end of wire 3, which is equivalent to γ_1 moving to the end of wire 3. With the end of wire 2 now being available, we can then switch on Δ_2 and tune Δ_1 back to zero, which moves Majorana 2 to the end of wire 1. Finally tuning back to the point $\Delta_3 \neq 0$ and $\Delta_1 = \Delta_2 = 0$ and thus completing one cycle, we move Majorana 1 to the end of wire 2. In effect, we have exchanged the positions of γ_1 and γ_2 and hence performed a braid.

This can be shown by explicitly calculating the time evolution of the Majorana operators in the Heisenberg representation. In every step of the above procedure, we transfer one Majorana $\gamma_{k'}$ to another position k by tuning Δ_k to zero and turning on $\Delta_{k'}$. We therefore evaluate

$$\dot{\gamma}_{k'}(t) = \mathrm{i}\,[H_{kk'}(t), \gamma_k(t)]\,, \tag{2.121}$$

where the time-dependent Hamiltonian would be

$$H(t) = \mathrm{i}\,[(1-\alpha(t))\,\Delta_k \gamma_0 \gamma_k + \alpha(t)\Delta_{k'}\gamma_0\gamma_{k'}] \tag{2.122}$$

and $\alpha(t)$ adiabatically interpolating between 0 at time $t = 0$ and 1 at time $t = T$. By using a nice analogy with the motion of a spin in an adiabatically varying magnetic field, one can show that (see [106, 108] for details)

$$\gamma_k(T) = -s_k s_{k'} \gamma_{k'}(0), \tag{2.123}$$

where $s_j = \operatorname{sgn}\Delta_j$. Applied to the first step above, we indeed find that $\gamma_3(0) \mapsto \gamma_3(T) = -s_k s_{k'}\gamma_1(0)$. This means that $\gamma_3(T)$, which is an instantaneous zero mode of $H(T)$ located at the end of wire 3, will be formed by the time-evolved operator corresponding to γ_1 at the beginning of the procedure.

All we have left to do is to combine the recipe in Eq. (2.123) to all three of the steps outlined above. For simplicity, let us assume that $\Delta_j > 0$. We then obtain

$$\begin{aligned} \gamma_1 &\to -\gamma_3, \quad & \gamma_2 &\to \gamma_2 & &\text{step 1} \\ -\gamma_3 &\to -\gamma_3, \quad & \gamma_2 &\to -\gamma_1 & &\text{step 2} \\ -\gamma_3 &\to \gamma_2, \quad & -\gamma_1 &\to -\gamma_1 & &\text{step 3,} \end{aligned} \tag{2.124}$$

such that the overall effect is summarized as

$$\gamma_1 \to \gamma_2, \quad \gamma_2 \to -\gamma_1. \tag{2.125}$$

Therefore, we can immediately identify the successive coupling/decoupling of pairs of Majoranas with the effect of an inverse elementary braid on the Majoranas bound

in vortices in Eq. (2.97). A similar protocol, in which γ_2 is parked at wire 3 whereas γ_1 jumps directly to wire 2, yields exactly the elementary braid in Eq. (2.97).

Note that since we only consider two unpaired Majoranas, the ground states have opposite parity and can therefore never mix in a Y-junction setup as the one we discussed. In order to go beyond the diagonal unitary operator associated with this, one would have to move to more complicated structures with more Majorana zero modes [68].

3

Majorana modes at the helical edge

Contents

In Chapter 2, we discuss how the effective theory of helical edge states realized in QSHIs relates to the continuum model of a spinless p-wave superconductor. We found that under the influence of s-wave singlet pairing and a magnetic field and as long as the induced gap is dominated by superconductivity, the spin-momentum locking of the edge states is able to mediate p-wave pairing, and the edge states correspond to the topological phase of the spinless p-wave superconductor. As such, we expect Majorana modes to appear at boundaries between a region with a superconducting gap and regions with topologically trivial gaps, for instance, a magnetic gap. In this chapter, we are first going to discuss helical edge states in more detail in order to provide a solid basis for the results in the following chapters. We then proceed to show explicitly how Majorana bound states (MBSs) and Andreev bound states (ABSs) arise and behave in hybrid systems at the helical edge.

The possibility of realizing Majorana modes at the boundary of topological insulators was first pointed out in a seminal paper by Fu and Kane [43]. This sparked a lot of interest in the community, and the connection to the helical edge states of two-dimensional quantum spin Hall insulators is the focus of Refs. [44, 109–116]. In particular, the material presented in this chapter is well-complemented and more importantly greatly extended in Refs. [95, 117–119].

In the following, we are going to focus on a single helical edge with specific regions subjected to either proximity induced superconductivity *or* a magnetic field (*e.g.,* by proximity to a ferromagnetic insulator). In this thesis, we therefore distinguish between (i) normal regions (N), – bare helical edge states described by $\mathcal{H}_0$ – (ii) superconducting regions (S), – helical edge states with proximity induced superconducting order described by $\mathcal{H}_0 + \mathcal{H}_\Delta$ – and (iii) ferromagnetic regions (F), – helical edge states subject to a magnetic field described by $\mathcal{H}_0 + \mathcal{H}_m$.

3.1 General properties of helical edge states

3.1.1 The Bogoliubov-de Gennes Hamiltonian

The Hamiltonian of the edge states including superconductivity and the magnetic field in the BdG-form is given by

$$H = \frac{1}{2}\int \mathrm{d}x\, \Psi(x)^\dagger\, \mathcal{H}_{\mathrm{BdG}}\, \Psi(x), \tag{3.1}$$

where the spinor is $\Psi(x) = (\psi_\uparrow(x), \psi_\downarrow(x), \psi_\downarrow^\dagger(x), -\psi_\uparrow^\dagger(x))^{\mathrm{T}}$. The BdG-Hamiltonian can be split into three parts according to

$$\mathcal{H}_{\mathrm{BdG}} = \mathcal{H}_0 + \mathcal{H}_\Delta + \mathcal{H}_m, \tag{3.2}$$

with the bare Hamiltonian density of the edge states

$$\mathcal{H}_0 = v_{\mathrm{F}}\hat{p}\,\hat{\tau}_3 \otimes \hat{\sigma}_3 - \mu\,\hat{\tau}_3 \otimes \hat{\sigma}_0, \tag{3.3}$$

the contribution from s-wave superconductivity

$$\mathcal{H}_\Delta = [\Delta_1\,\hat{\tau}_1 + \Delta_2\,\hat{\tau}_2] \otimes \hat{\sigma}_0 = [\Delta\cos\varphi\,\hat{\tau}_1 + \Delta\sin\varphi\,\hat{\tau}_2] \otimes \hat{\sigma}_0, \tag{3.4}$$

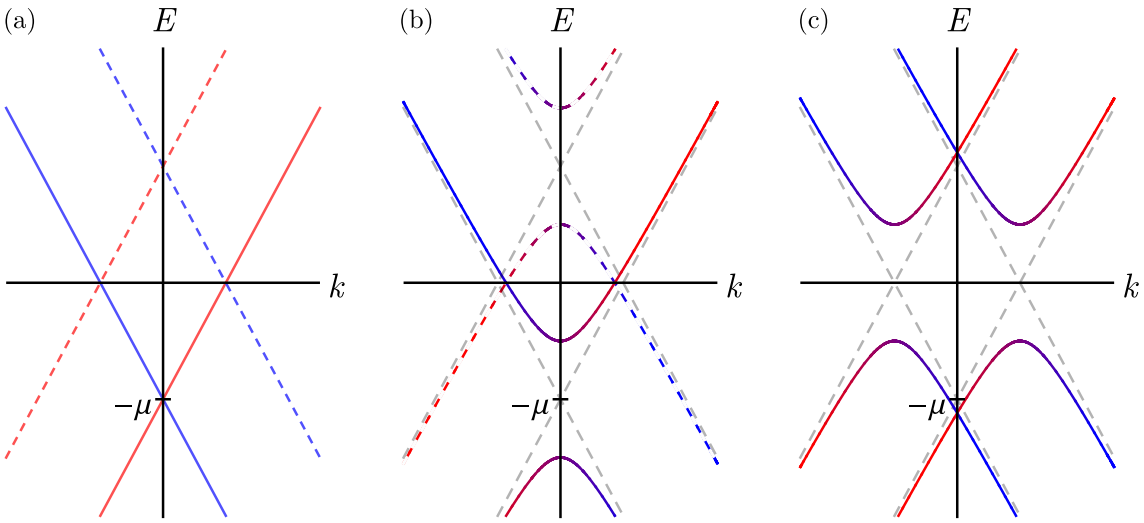

Figure 3.1: The spectrum of the BdG-Hamiltonian in (a) N, (b) F, and (c) S regions. In (a), solid (dashed) lines indicate electrons (holes), while red (blue) refers to spin-↑ rightmovers (spin-↓ leftmovers). Note that due to particle-hole symmetry, the spectra of electrons and holes are mirrored. If the helical edge states are coupled to a magnetic field, a gap opens in the spectrum [see (b)]. States with different spins hybridize such that the polarization of states within one band changes with k. The dashed gray lines correspond to the dispersion in N regions for better comparability. Panel (c) shows the gap opened by a proximity coupled superconductor, which hybridizes electron- and hole-states of opposite spins (as indicated by the colored transition). Since electron- and hole-blocks are now mixed, a distinction by using solid and dashed lines is no longer possible.

and the term stemming from the ferromagnet

$$\mathcal{H}_m = \hat{\tau}_0 \otimes \boldsymbol{m}(x) \cdot \hat{\boldsymbol{\sigma}} = \hat{\tau}_0 \otimes \left[m_\parallel \cos\lambda\, \hat{\sigma}_1 + m_\parallel \sin\lambda\, \hat{\sigma}_2 + m_z\, \hat{\sigma}_3 \right]. \tag{3.5}$$

As before, v_F is the Fermi velocity and μ the chemical potential. In Eq. (3.4), the two real parameters $\Delta_{1,2}$ can be parametrized in polar coordinates, where $\Delta = \sqrt{\Delta_1^2 + \Delta_2^2} > 0$ is the modulus of the (complex) superconducting order parameter and φ its phase. In Eq. (3.5), we parametrize the magnetic field by $m_\parallel > 0$ as the modulus and λ as the angle of the field in the x, y-plane (measured from the x-axis). The component in z-direction is denoted by m_z.

Note that the Pauli matrices $\hat{\sigma}_i$ act in spin space, while the Pauli matrices $\hat{\tau}_i$ act in Nambu (or particle-hole) space. For notational simplicity, we are going to drop the tensor product from now on and choose the basis above as a standard convention. Furthermore, we neglected the dependence on position of all parameters describing proximity induced superconductivity or magnetism, which we need to model heterostructures. The same applies to the chemical potential.

Before exploring the spectrum in detail, we note that the BdG-Hamiltonian in Eq. (3.1) features a duality of the spin and particle-hole degrees of freedom [109, 113, 118, 120, 121], since the structure of superconducting and magnetic terms in Eqs. (3.4) and (3.5) are the same. Thus, one can identify the Pauli matrices $\hat{\sigma}_i \leftrightarrow \hat{\tau}_i$ and the parameters $(\Delta, \varphi, \mu) \leftrightarrow (m_\parallel, \lambda, m_z)$.

Throughout this thesis, we adopt the convention $\hbar = v_\mathrm{F} = 1$ ubiquitously used in the literature. However, we might restore these constants for more clarity.

We show the spectrum of the BdG-Hamitonian for various cases in Fig. 3.1 and provide detailed expressions for eigenstates and eigenenergies in Appendix A. Without superconductivity and magnetism ($\Delta = 0$, $m_\parallel = 0$, $m_z = 0$), the helical edge consists of two counterpropagating modes with linear dispersion and group velocity v_F. Due to spin-momentum locking, they also have opposite spins. Throughout this thesis we adopt the convention that right movers have spin $\uparrow$, while leftmovers have spin $\downarrow$. Because of the description in the BdG-formalism and the corresponding introduction of holes, the spectrum is doubled (dashed lines for holes). Particle-hole symmetry ensures that electron and hole dispersions of the same spin are symmetric with respect to the point $E = 0, k = 0$.

Turning on a magnetic field in the x, y-plane (*i.e.,* $m_z = 0$) couples electrons of different spins and holes of different spins. Consequently, the crossing at $k = 0$ is lifted and the spectrum develops a gap of size $2m_\parallel$. Note that this only remains true for a ferromagnetic insulator, *i.e.,* as long as $|\mu| < m_\parallel$. A finite z-component shifts the electron- and hole-dispersions in opposite k-directions. For vanishing in plane field $m_\parallel = 0$, this is of course equivalent to pushing spin $\uparrow$ and $\downarrow$ dispersions up or down in energy, resulting in a crossing away from $k = 0$. We remark that the in-plane angle does not affect the spectrum, but enters in the eigenstates.

Finally, in a region with superconductivity the structure of the BdG-Hamiltonian in Eq. (3.4) reveals a coupling of electrons with spin $\uparrow$ ($\downarrow$) and holes with spin $\downarrow$ ($\uparrow$). Consequently, the resulting eigenstates are superpositions of those states and the spectrum develops an energy gap of 2Δ.

The important conclusion from this discussion is that both superconductivity and magnetism lead to a gap in the spectrum of the helical edge states. The eigenstates of the bare helical edge are simply propagating plane waves, whereas for energies below the corresponding gap they become evanescent waves whenever an order parameter (superconducting or magnetic) is present. Therefore, superconducting and ferromagnetic regions can act as barriers, which are able to trap bound states. In turn, the nature of these bound states is the focus of the remainder of the chapter.

3.1.2 Magnetism and time-reversal symmetry

At this point it is worth discussing the role played by time-reversal symmetry (TRS) for the helical edge states. In the absence of superconductivity and magnetism, the Fourier transformed Hamiltonian of the edge states can be written in the form

$$H = \int \frac{\mathrm{d}k}{2\pi} \left(\psi_\uparrow^\dagger, \psi_\downarrow^\dagger\right) \mathcal{H}_0(k) \left(\psi_\uparrow, \psi_\downarrow\right)^\mathrm{T}, \tag{3.6}$$

where

$$\mathcal{H}_0(k) = \begin{pmatrix} v_\mathrm{F}k - \mu & 0 \\ 0 & -v_\mathrm{F}k - \mu. \end{pmatrix} \tag{3.7}$$

The Hamiltonian is obviously block-diagonal, with energies $E_{\uparrow/\downarrow}(k) = \pm v_\mathrm{F}k - \mu$ and corresponding eigenstates $\varphi_\uparrow = (1, 0)^\mathrm{T}$ and $\varphi_\downarrow(0, 1)^\mathrm{T}$. The blocks are related by

time-reversal symmetry (TRS). For our case of spin-1/2 particles, the time-reversal operator is given by [53]

$$T = \mathrm{i}\hat{\sigma}_2 \cdot \mathrm{K}, \tag{3.8}$$

where $\hat{\sigma}_2$ acts in spin space and K denotes complex conjugation. Importantly, the time-reversal operator fulfills

$$T^2 = -\mathbb{1} \tag{3.9}$$

and is *antiunitary*. Following Ref. [122], this always implies that one can write $T = U \cdot \mathrm{K}$, with U a unitary matrix. Note that if $T^2 = -\mathbb{1}$, U needs to be antisymmetric $U^{\mathrm{T}} = -U$. All of these properties are of course fulfilled by the representation in Eq. (3.8).

It is now straightforward to check that the Hamiltonian of the helical edge states is time-reversal invariant and obeys

$$T\mathcal{H}_0(k)T^{-1} = \mathcal{H}_0(-k), \tag{3.10}$$

while the eigenstates are transformed into one-another under time-reversal, since

$$\varphi_\uparrow = T\varphi_\downarrow, \qquad \varphi_\downarrow = -T\varphi_\uparrow. \tag{3.11}$$

Due to the particularly simple structure of our Hamiltonian, the eigenstates are always orthogonal and, importantly, are not coupled by the Hamiltonian.

However, as long as time-reversal invariance (TRI) is present, even more complicated Hamiltonians share an important feature with our simple one. Let us consider a k-dependent Hamiltonian $\mathcal{H}(k)$ of a spin-1/2 particle with TRS, *i.e.,*

$$T\mathcal{H}(k)T^{-1} = \mathcal{H}(-k), \tag{3.12}$$

where $\mathcal{H}(k)$ is a matrix in spin space and $T^2 = -\mathbb{1}$. Given an eigenstate $|\phi(k)\rangle$ with energy E_k fulfilling

$$\mathcal{H}(k)|\phi(k)\rangle = E(k)|\phi(k)\rangle, \tag{3.13}$$

the time-reversed partner $T|\phi(k)\rangle$ is an eigenstate of $\mathcal{H}(-k)$ with energy E_k, since

$$\mathcal{H}(-k)\,T|\phi(k)\rangle = T\mathcal{H}(k)T^{-1}\,T|\phi(k)\rangle = TE_k|\phi(k)\rangle = E_k\,T|\phi(k)\rangle. \tag{3.14}$$

In other words, the spectrum of $T|\phi(k)\rangle$ can be obtained by flipping the dispersion of $|\phi(k)\rangle$ and taking $k \to -k$. Consequently, at $k = 0$ the spectrum is potentially degenerate, if $T|\phi(k)\rangle$ and $|\phi(k)\rangle$ are distinct states.

In order to check, we compute the overlap (we drop the momentum for simplicity) by explicitly using the representation of time-reversal operator and eigenstate in spin space. We find

$$\langle\phi|T|\phi\rangle = \sum_{i,j} \phi_i^*\, U_{ij}\mathrm{K}\, \phi_j = \sum_{i,j} \phi_i^*\ (-U_{ji})\, \phi_j^* = -\sum_{i,j} \phi_j^*\, U_{ji}\mathrm{K}\, \phi_i = -\langle\phi|T|\phi\rangle = 0, \tag{3.15}$$

where we have used the antisymmetry of U. Eigenstates related by time-reversal are therefore not only distinct, but orthogonal!

A similar calculation shows that the matrix element of time-reversed partners with respect to the Hamiltonian has the property $\langle T\phi|\mathcal{H}|\phi\rangle = -\langle T\phi|\mathcal{H}|\phi\rangle = 0$ and

thus vanishes. Hence, any scattering from one state to the other one is forbidden by TRS.

Applied to the case of helical edge states, we conclude that backscattering – *i.e.,* the transition from a right- to a leftmover or vice versa – is impossible, unless TRS is explicitly broken by a magnetic field.

Of course, this picture changes as soon as superconductors enter the game. In this case, the breaking of a $U(1)$-symmetry allows the coupling of counterpropagating electrons and holes and thus gives rise to the possibility of Andreev reflection.

3.1.3 Superconductivity and Majorana fermions

As a last precursor before moving to bound states, we review a few features of the BdG-Hamiltonian of the helical edge with regard to particle-hole symmetry following Refs. [54, 95, 123]. This will enable us to discuss Majorana bound states and their wave functions in a straightforward manner.

In a similar way as for the Kitaev chain in Section 2.1.1, there is a built-in redundancy in the spinor $\Psi(x) = (\psi_\uparrow(x), \psi_\downarrow(x), \psi_\downarrow^\dagger(x), -\psi_\uparrow^\dagger(x))^{\mathrm{T}}$, which can be expressed as

$$\Psi(x) = \mathcal{C}\,\Psi^\dagger(x), \tag{3.16}$$

where we introduce the charge conjugation operator

$$\mathcal{C} = \hat{\tau}_2\hat{\sigma}_2\,\mathrm{K}, \tag{3.17}$$

with K the operator of complex conjugation.

This implies that the BdG-Hamiltonian must fulfill the constraint

$$\hat{\tau}_2\hat{\sigma}_2\,(\mathcal{H}_{\mathrm{BdG}})^*\,\hat{\tau}_2\hat{\sigma}_2 = -\mathcal{H}_{\mathrm{BdG}}. \tag{3.18}$$

We can equivalently state the particle-hole symmetry of the BdG-Hamiltonian in the form

$$\mathcal{C}\,(\mathcal{H}_{\mathrm{BdG}})^*\,\mathcal{C}^{-1} = -\mathcal{H}_{\mathrm{BdG}}. \tag{3.19}$$

As a consequence, the BdG-Hamiltonian anticommutes with the charge conjugation operator, *i.e.,*

$$\{\mathcal{H}_{\mathrm{BdG}}, \mathcal{C}\} = 0. \tag{3.20}$$

We emphasize that this is not a physical symmetry, but merely a consequence of the doubling of degrees of freedom and thus required for consistency.

However, Eq. (3.19) has important consequences for the eigenspinors $\phi_{j,E_j}(x)$ of $\mathcal{H}_{\mathrm{BdG}}$, fulfilling the eigenvalue equation

$$\mathcal{H}_{\mathrm{BdG}}\phi_{j,E_j}(x) = E_j\phi_{j,E_j}(x), \tag{3.21}$$

where E_j is the energy of the eigenspinor. Eq. (3.21) is also called the Bogoliubov-de Gennes equation (BdG equation). The index j labels possibly degenerate states.

Due to Eq. (3.19), for every solution $\phi_{j,E_j}(x)$ with energy E_j, there is always a charge conjugated partner $\mathcal{C}\phi_{j,E_j}(x)$ which is an eigenstate of the BdG-equation at $-E_j$. It is helpful to introduce the notation

$$\mathcal{C}\phi_{j,E_j} = \phi_{j^c,-E_j} \tag{3.22}$$

for the charge conjugated spinor, where j^c is the label of the charge-conjugated partner state. We furthermore define the components of $\phi_{j,E_j}(x)$ as

$$\phi_{j,E_j}(x) = \left(u_{\uparrow,j,E_j}, u_{\downarrow,j,E_j}, v_{\downarrow,j,E_j}, v_{\uparrow,j,E_j}\right)^{\mathrm{T}}. \tag{3.23}$$

For simplicity, we are often going to drop the subscripts j, E_j.

Furthermore, since the BdG-Hamiltonian is hermitian, the eigenspinors fulfill the completeness relations

$$\int \mathrm{d}x\, \phi^\dagger_{i,E_i}(x)\phi_{j,E_j}(x) = \delta_{ij} \tag{3.24a}$$

and

$$\sum_j \phi_{j,E_j}(x)\phi^\dagger_{j,E_j}(y) = \mathbb{1}\,\delta(x-y). \tag{3.24b}$$

Using Eq. (3.24), the Hamiltonian can be diagonalized and brought into the form

$$H = \sum_j E_j \gamma_j^\dagger \gamma_j, \tag{3.25}$$

where the fermionic Bogoliubov (quasiparticle) operators are given by

$$\begin{aligned} \gamma_j &= \int \mathrm{d}x\, \left[\phi_{j,E_j}(x)\right]^\dagger\, \Psi(x), \\ \gamma_j^\dagger &= \int \mathrm{d}x\, \Psi^\dagger(x)\, \phi_{j,E_j}(x). \end{aligned} \tag{3.26}$$

Note that the sum over energies might need to be converted into an integral, if there is a continuum of states. Moreover, it will become useful to invert Eq. (3.26) and express the field operators in terms of the operators $\gamma_i, \gamma_i^\dagger$. One finds

$$\Psi(x) = \sum_{E_j>0} \left[\phi_{j,E_j}(x)\,\gamma_j + \mathcal{C}\phi_{j,E_j}\,\gamma_j^\dagger\right]. \tag{3.27}$$

By combining Eqs. (3.22) and (3.26), one can readily see that the Bogoliubov operators are also constrained according to

$$\gamma_{j^c,-E_j} = \gamma^\dagger_{j,E_j}, \tag{3.28}$$

i.e., creating a Bogoliubov particle at energy E_j in state j is equivalent to annihilating one at energy $-E_j$ in state j^c.

This last property has the important consequence of allowing for the existence of Majorana fermions, if the left and right hand side of Eq. (3.28) coincide. Note that this is only possible at zero energy, *i.e.,* if $E_j = 0$, *and* if the state is invariant under charge conjugation such that $j = j^c$.

Importantly, for any zero-energy quasiparticle with Bogoliubov operator $\gamma_{j,0}$ for which $j \neq j^c$, we can always construct new operators $\gamma_\pm$ in the form

$$\gamma_+ = \gamma_{j,0} + \gamma_{j^c,0}, \qquad \gamma_- = -\mathrm{i}\gamma_{j,0} + \mathrm{i}\gamma_{j^c,0}. \tag{3.29}$$

Both of these manifestly fulfill the Majorana condition

$$\gamma_\pm^\dagger = \gamma_\pm. \tag{3.30}$$

Equivalently, one can construct Majorana wave functions $\phi_\pm$ obeying

$$\mathcal{C}\phi_\pm = \phi_\pm \tag{3.31}$$

from the wave function $\phi_{j,0}$ associated with the operator $\gamma_{j,0}$. They have the form

$$\phi_+ = \phi_{j,0} + \mathcal{C}\phi_{j,0}, \qquad \phi_- = -\mathrm{i}\phi_{j,0} + \mathrm{i}\mathcal{C}\phi_{j,0}, \tag{3.32}$$

and one can straightforwardly show that following Eq. (3.26), they lead to second-quantized Majorana operators $\gamma_\pm = \gamma_\pm^\dagger$.

In conclusion, in order to find Majorana wave functions in hybrid systems at the helical edge, a good starting point is to look for any zero-energy solutions to the BdG-equation. The analysis in this section then provides a clear recipe to construct Majorana wave functions according to Eq. (3.32).

3.2 Bound states in single cavities

In the previous section, we discussed the effects of superconductivity and ferromagnetism on the entire helical edge, and established that S and F regions can act as barriers. As a next step, we consider heterostructures with two barriers (either two S or one S, one F) and discuss the emerging bound states.

3.2.1 Two superconducting barriers

We start with the case of two superconducting barriers. The basis of our discussion is very similar to one of the first problems in quantum mechanics any physics student has to solve: scattering off a step potential in one dimension. In order to make this connection, and since the procedure in this section is of great importance for the rest of the thesis, the discussion in this section is quite detailed. In future sections, we then skip a lot of analogous steps for brevity and clarity.

3.2.1.1 The NS-junction

The elementary building block for this section is the interface between a normal helical edge region (N) and a domain with proximity induced superconductivity (S) as depicted in Fig. 3.2 In the following, the chemical potential plays no role and is therefore set to zero.[1] For a single superconductor, the superconducting phase can be gauged away. However, anticipating cases with more than one superconducting region, we keep it in this section.

We choose the origin to be exactly at the interface, and model the system by a position dependent pair potential of the form $\Delta_1(x) = \theta(x)\Delta_0 \cos\varphi$ and $\Delta_2(x) = \theta(x)\Delta_0 \sin\varphi$, where $\Delta_0 > 0$ and $\theta(x)$ is the Heaviside step function. As a

[1] The reason for this can be seen in the explcit expressions in Appendix A and the fact that the chemical potential only leads to a shift of momenta which is the same within the $(u_\uparrow, v_\downarrow)^{\mathrm{T}}$- and $(u_\downarrow, v_\uparrow)^{\mathrm{T}}$-blocks, respectively. The blocks refer to components of solutions $\phi = (u_\uparrow, u_\downarrow, v_\downarrow, u_\uparrow)^{\mathrm{T}}$ to the BdG-equation, see main text.

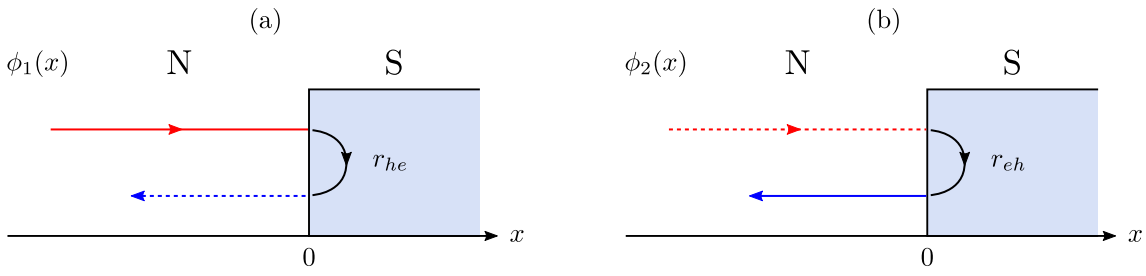

Figure 3.2: The two possible scattering states of an NS-junction below the gap. Solid (dashed) lines indicate electrons (holes), and red (blue) corresponds to spin-↑ (spin-↓) modes. The arrows indicate the direction of propagation. Additionally, the possible Andreev reflection processes are shown in black.

consequence, the Hamiltonian can be split in two parts. For $x < 0$, it corresponds to the free helical edge and the eigenstates are plane waves, wheras for $x > 0$ the spectrum acquires a gap. For energies below the gap, the eigenstates are evanescent waves. Note that there are two solutions exponentially decaying to the right (*i.e.,* for growing x), and two solutions exponentially growing to the right.

In the following, we discuss how the NS-interface affects solutions of the BdG-equation ($E < \Delta_0$)

$$\begin{pmatrix} v_\mathrm{F}\hat{p} & 0 & \theta(x)\Delta_0 \mathrm{e}^{-\mathrm{i}\varphi} & 0 \\ 0 & -v_\mathrm{F}\hat{p} & 0 & \theta(x)\Delta_0 \mathrm{e}^{-\mathrm{i}\varphi} \\ \theta(x)\Delta_0 \mathrm{e}^{\mathrm{i}\varphi} & 0 & -v_\mathrm{F}\hat{p} & 0 \\ 0 & \theta(x)\Delta_0 \mathrm{e}^{\mathrm{i}\varphi} & 0 & v_\mathrm{F}\hat{p} \end{pmatrix} \phi(x) = E\,\phi(x) \tag{3.33}$$

by determining the scattering matrix. In the basis we choose, the solutions ϕ are vectors of the form $\phi = (u_\uparrow, u_\downarrow, v_\downarrow, u_\uparrow)^\mathrm{T}$, *i.e.,* u_σ (v_σ) refers to electrons (holes) with spin $\sigma = \uparrow, \downarrow$.

Note that the Hamiltonian is constant for $x < 0$ and $x > 0$ and that within these regions, the eigenstates correspond to the ones discussed in Section 3.1. Hence, within both regions, any superposition of the corresponding eigenstates at the same energy is a solution to the BdG-Hamiltonian. Crucially, however, integrating the BdG-equation in Eq. (3.33) across the interface from $-\epsilon$ to ϵ ($\epsilon > 0$) and taking the limit $\epsilon \to 0$ implies that the solution $\phi(x)$ needs to be continuous at $x = 0$ due to the derivative in $\hat{p} = -\mathrm{i}\partial_x$. Therefore, the task at hand boils down to finding superpositions of the known eigenstates within each region which match at the interface. Furthermore, note that the coefficients in front of the χ_{e-}, χ_{h+} solutions in the superconductor need to be zero for normalizability.

To obtain the scattering matrix, one conveniently makes use of *scattering states*. In our particular system, there are two of them, namely

$$\phi_1(x) = \begin{cases} \mathrm{e}^{\mathrm{i}Ex/v_\mathrm{F}}\phi_{e+} + r_{ee}\,\mathrm{e}^{-\mathrm{i}Ex/v_\mathrm{F}}\phi_{e-} + r_{he}\,\mathrm{e}^{-\mathrm{i}Ex/v_\mathrm{F}}\phi_{h-} & x < 0 \\ C_e\,\mathrm{e}^{-\Omega(E)x}\chi_{e+} + D_e\,\mathrm{e}^{-\Omega(E)x}\chi_{h+} & x > 0 \end{cases} \tag{3.34a}$$

and

$$\phi_2(x) = \begin{cases} \mathrm{e}^{\mathrm{i}Ex/v_\mathrm{F}}\phi_{h+} + r_{hh}\,\mathrm{e}^{-\mathrm{i}Ex/v_\mathrm{F}}\phi_{h-} + r_{eh}\,\mathrm{e}^{-\mathrm{i}Ex/v_\mathrm{F}}\phi_{e-} & x<0 \\ C_h\,\mathrm{e}^{-\Omega(E)x}\chi_{h+} + D_h\,\mathrm{e}^{-\Omega(E)x}\chi_{e+} & x>0. \end{cases} \tag{3.34b}$$

They are constructed by adding one plane wave with amplitude 1 moving towards the interface (rightmoving electron for ϕ_1, rightmoving hole for ϕ_2) and a linear combination of all modes moving away from the interface. In our case, since we consider energies below the gap, there are no propagating modes on the superconducting side, but evanescent waves instead. This method works for arbitrarily complicated setups, but is particularly simple to explain for the case of an NS-junction.

The unknown coefficients in the linear superpositions are then determined by matching the ansatzes for $x>0$ and $x<0$ of ϕ_1 and ϕ_2, respectively. Note that we have four unknowns and four equations.

The coefficients are straightforwardly found to be

$$\begin{gathered} r_{he} = \mathrm{e}^{-\mathrm{i}\eta(E)+\mathrm{i}\varphi}, \qquad r_{eh} = \mathrm{e}^{-\mathrm{i}\eta(E)-\mathrm{i}\varphi}, \qquad r_{ee} = r_{hh} = 0 \\ C_e = \sqrt{2}\mathrm{e}^{-\mathrm{i}\eta(E)}, \qquad C_h = \sqrt{2}, \qquad D_e = D_h = 0. \end{gathered} \tag{3.35}$$

The physical interpretation of this result is striking. The two coefficients r_{he}, r_{eh} associated with an incoming electron (hole) but outgoing hole (electron) – known as *Andreev* reflections – are given by a complex phase, which depends on the energy and also contains the phase of the superconductor. In contrast, the coefficients r_{ee}, r_{hh} corresponding to normal reflection are zero. Since the absolute square of these coefficients is associated with a scattering probability, we conclude that the NS-interface on top of a helical edge induces *perfect* Andreev reflection [124]. Incoming electrons are turned into holes and vice versa, and acquire a phase shift of $-\eta(E)\pm\varphi$ in the process.

Notice the close connection of this result with the structure of the BdG-Hamiltonian in Eq. (3.33). It is essentially block-diagonal in the $(u_\uparrow, v_\downarrow)^\mathrm{T}$- and the $(u_\downarrow, v_\uparrow)$-blocks, respectively. Consequently, electrons with spin $\uparrow$ ($\downarrow$) are only coupled to holes with spin $\downarrow$ ($\uparrow$) in the former (latter). As a result, there is no way in which a rightmoving electron with spin $\uparrow$ approaching a superconductor can be scattered back as a leftmoving electron with spin $\downarrow$. The only possible scattering channel is Andreev reflection. Thus, the corresponding coefficient has modulus one. This is in contrast to conventional metal-superconductor interfaces, where an additional normal scattering potential can be associated with the interface and thus normal backscattering occurs [124–128].

A general solution to the BdG-equation in Eq. (3.33) can now be written as a linear combination of both scattering states in the form

$$\phi(x) = a_e\phi_1(x) + a_h\phi_2(x). \tag{3.36}$$

For $x<0$, this reads (keeping the coefficients $r^{ee/hh/eh/he}$ general for a moment)

$$\begin{gathered} \phi(x) = a_e\,\mathrm{e}^{\mathrm{i}Ex/v_\mathrm{F}}\phi_{e+} + a_h\,\mathrm{e}^{\mathrm{i}Ex/v_\mathrm{F}}\phi_{h+} \\ + (a_e r_{ee} + a_h r_{eh})\,\mathrm{e}^{-\mathrm{i}Ex/v_\mathrm{F}}\phi_{e-} + (a_e r_{he} + a_h r_{hh})\,\mathrm{e}^{-\mathrm{i}Ex/v_\mathrm{F}}\phi_{h-}. \end{gathered} \tag{3.37}$$

We can therefore read off a linear relationship between the amplitudes of all modes moving toward the interface (incoming, given by a_e, a_h) and the modes moving away from it (outgoing, named b_e, b_h). For our case of an NS-junction, it has the simple form

$$\begin{pmatrix} b_e \\ b_h \end{pmatrix} = \underbrace{\begin{pmatrix} 0 & r_{eh} \\ r_{he} & 0 \end{pmatrix}}_{S_{\mathrm{NS}}} \begin{pmatrix} a_e \\ a_h \end{pmatrix} = \begin{pmatrix} 0 & \mathrm{e}^{-\mathrm{i}\eta(E)-\mathrm{i}\varphi} \\ \mathrm{e}^{-\mathrm{i}\eta(E)+\mathrm{i}\varphi} & 0 \end{pmatrix} \begin{pmatrix} a_e \\ a_h \end{pmatrix}, \tag{3.38}$$

where we introduced the *scattering matrix* S_{NS}.

Note that for energies above the gap, the procedure would be similar. For the scattering states with particles coming in from the left, one would only have to replace the evanescent waves by the corresponding propagating ones. However, there would be additional scattering states for quasiparticles coming in from the *right*. Consequently, the scattering matrix would then be a 4×4-matrix coupling the amplitudes of two incoming modes per side and the two outgoing modes per side. Furthermore, the propagating modes on the S side would give rise to finite transmissions. True bound states are therefore not possible above the gap.

3.2.1.2 The SN-junction

In order to form a potential well out of two superconductors, we need to consider the mirror counterpart of the previous section, *i.e.,* an SN-junction. Of course, the calculation is analogous and equally simple, so we merely state the results here. The scattering matrix S_{SN} relating the incoming and outgoing modes in this case is given by

$$\begin{pmatrix} b_e \\ b_h \end{pmatrix} = \underbrace{\begin{pmatrix} 0 & r'_{eh} \\ r'_{he} & 0 \end{pmatrix}}_{S_{\mathrm{SN}}} \begin{pmatrix} a_e \\ a_h \end{pmatrix} = \begin{pmatrix} 0 & \mathrm{e}^{-\mathrm{i}\eta(E)-\mathrm{i}\varphi} \\ \mathrm{e}^{-\mathrm{i}\eta(E)+\mathrm{i}\varphi} & 0 \end{pmatrix} \begin{pmatrix} a_e \\ a_h \end{pmatrix}, \tag{3.39}$$

where we the prime distinguishes the coefficients from the previous case, and we again use the notation of $a_{e/h}$ ($b_{e/h}$) for incoming (outgoing) electrons or holes. Conveniently, the scattering matrices for both SN- and NS-junction have the same form.

3.2.1.3 Resonance condition for bound states

With the results from the previous sections at hand, we can now turn to the system depicted in Fig. 3.3. It consists of two semi-infinite S regions separated by a normal region of width d. For simplicity, we assume that the modulus of the superconducting gap is the same on both sides, whereas the phase can be different. The pair potential can then be written as $\Delta_1(x) = \theta(-x - d/2)\Delta_0 + \theta(x - d/2)\Delta_0 \cos\varphi$ and $\Delta_2(x) = \theta(x - d/2)\Delta_0 \sin\varphi$. The chemical potential does not influence the appearance of bound states, and we set it to zero as before.

There are several ways to find the conditions under which bound states arise. We start with the most straightforward way, and then use the results from the NS-junction to show more elegant ways. For notational simplicity, we set $v_F = 1$

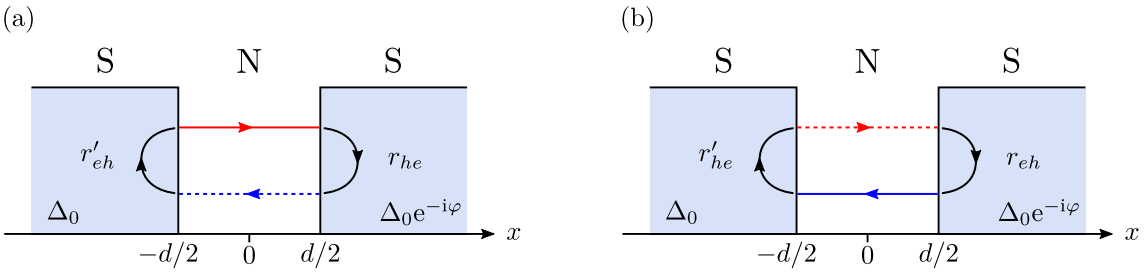

Figure 3.3: Schematic depiction of the two bound states in an SS-junction. Colors and dashing to distinguish electrons/holes with different spins as in Fig. 3.2.

from now on. Furthermore, let us first focus on the $(u_\uparrow, v_\downarrow)^{\mathrm{T}}$-block of a bound state wave function $\phi(x) = (u_\uparrow(x), u_\downarrow(x), v_\downarrow(x), u_\uparrow(x))^{\mathrm{T}}$, *i.e.,* the block which consists of rightmoving electrons and leftmoving holes in the N region of the junction.

A suitable ansatz for a bound state is then

$$\phi(x) = \begin{cases} A\,\mathrm{e}^{\Omega x}\chi_{h-} & x < -d/2 \\ B\,\mathrm{e}^{\mathrm{i}Ex}\phi_{e+} + C\,\mathrm{e}^{-\mathrm{i}Ex}\phi_{h-} & -d/2 < x < d/2 \\ D\,\mathrm{e}^{-\Omega x}\chi_{e+} & x > d/2. \end{cases} \tag{3.40}$$

In the central N region, it is a superposition of both possible modes, whereas the choice of eigenstates of the S regions is made such that the wave function decays to zero for $x \to \pm\infty$. As before, the wave function needs to be continuous at the interfaces at $x = \pm d/2$. After some straightforward algebra, matching the wave function leads to an equation of the form

$$\underbrace{\begin{pmatrix} -\frac{1}{\sqrt{2}}\mathrm{e}^{-\Omega d/2}\mathrm{e}^{-\mathrm{i}\eta} & \mathrm{e}^{-\mathrm{i}Ed/2} & & \\ -\frac{1}{\sqrt{2}}\mathrm{e}^{-\Omega d/2} & & \mathrm{e}^{\mathrm{i}Ed/2} & \\ & \mathrm{e}^{\mathrm{i}Ed/2} & & -\frac{1}{\sqrt{2}}\mathrm{e}^{-\Omega d/2}\mathrm{e}^{\mathrm{i}\eta}\mathrm{e}^{-\mathrm{i}\varphi} \\ & & \mathrm{e}^{-\mathrm{i}Ed/2} & -\frac{1}{\sqrt{2}}\mathrm{e}^{-\Omega d/2} \end{pmatrix}}_{M} \begin{pmatrix} A \\ B \\ C \\ D \end{pmatrix} = \begin{pmatrix} 0 \\ 0 \\ 0 \\ 0 \end{pmatrix}, \tag{3.41}$$

which only has a nontrivial solution if $\det M = 0$. Calculating the determinant, we see that it vanishes whenever the simple relation

$$\mathrm{e}^{2\mathrm{i}dE - 2\mathrm{i}\eta(E) + \mathrm{i}\varphi} - 1 = 0 \tag{3.42a}$$

holds, where we explicitly hint at the energy dependence of η (recall that $\eta(E) = \arccos(E)$). This condition can equivalently expressed as

$$Ed - \eta(E) + \varphi/2 = n\,\pi \tag{3.42b}$$

or

$$\sin\left(Ed - \eta(E) + \varphi/2\right) = 0. \tag{3.42c}$$

In conclusion, whenever Eq. (3.42a) is fulfilled, the ansatz in Eq. (3.40) leads to a well-defined wave function, provided the coefficients A, B, C, D are chosen such that the wave function is normalized.

The condition in Eq. (3.42a) has a straightforward and illuminating interpretation. As mentioned before, the bound state in Fig. 3.3 (a) consists of a rightmoving electron and a leftmoving hole, connected by two Andreev reflections. A bound state arises if this loop of traversing the cavity as electron, being converted into a hole, moving back towards the SN-interface as a hole, and finally being Andreev reflected again, happens phase coherently. The three terms in the exponential of Eq. (3.42a) directly correspond to the dynamic phase picked up during free motion across the normal region and the two Andreev reflections (compare with Sections 3.2.1.1 and 3.2.1.2!). Eq. (3.42a) thus corresponds to the condition that the total phase of one loop is equal to a multiple of 2π. This tracking of phases during a closed loop or a general scattering process can be a helpful tool to develop a sound physical picture.

In principle, we could now repeat the procedure outlined above for the remaining $(u_\downarrow(x), v_\uparrow(x))^{\mathrm{T}}$ block in order to find the resonance condition for the bound state in Fig. 3.3 (b). However, due to particle-hole symmetry, the ansatz in Eq. (3.40) is the charge-conjugated version of the ansatz in the $(u_\downarrow(x), v_\uparrow(x))^{\mathrm{T}}$ block at energy $-E$. Hence, sending $E \to -E$ in Eqs. (3.40)–(3.42) directly yields the condition for a bound state as shown in Fig. 3.3, which reads

$$\mathrm{e}^{2\mathrm{i}dE - 2\mathrm{i}\eta(E) - \mathrm{i}\varphi} - 1 = 0 \;\Leftrightarrow\; Ed - \eta(E) - \varphi/2 = n\,\pi \;\Leftrightarrow\; \sin\left(Ed - \eta(E) - \varphi/2\right) = 0. \tag{3.43}$$

Note that we used $\arccos(-x) = \pi - \arccos(x)$ and rearranged the conditions in order to bring them into this form, which corresponds to the other resonance conditions in Eq. (3.42) for $\varphi \to -\varphi$. Observe how this result is immediately apparent through the phase-tracking method. While the dynamical phases stay the same, the Andreev processes involved are now different and induce the change of sign in front of the superconducting phase φ.

In Fig. 3.4, we show solutions to the resonance conditions Eqs. (3.42) and (3.43) for two exemplary values of the junction width d.

3.2.1.4 The short and the long junction limit

There are two particularly illustrative cases worth discussing, namely the short and the long junction limit for which $d \to 0$ and $d \to \infty$, respectively. The most convenient resonance conditions for this analysis are the ones in the form

$$Ed - \eta(E) \pm \varphi/2 = n\,\pi. \tag{3.44}$$

In the short junction limit, we can solve for $\eta(E)$ and apply the cosine to both sides. Taking care of the range of $\eta(E) \in [0, \pi]$ and $\varphi \in [0, 2\pi]$, which restricts the index n, the resonance conditions then reduce to

$$E = \pm\Delta_0 \cos\left(\varphi/2\right), \tag{3.45}$$

where the $+$ $(-)$ corresponds to the $(u_\uparrow, v_\downarrow)^{\mathrm{T}}$ $[(u_\downarrow, v_\uparrow)^{\mathrm{T}}]$ block. We conclude that for $d = 0$, there is a single 4π-periodic pair of bound states, both of which touch the gap edges at $\varphi = 0, 2\pi$, but cross zero energy at $\varphi = \pi$ [also see Fig. 3.4 (a)]. This crossing is protected by fermion parity and leads to MBS, as we shall

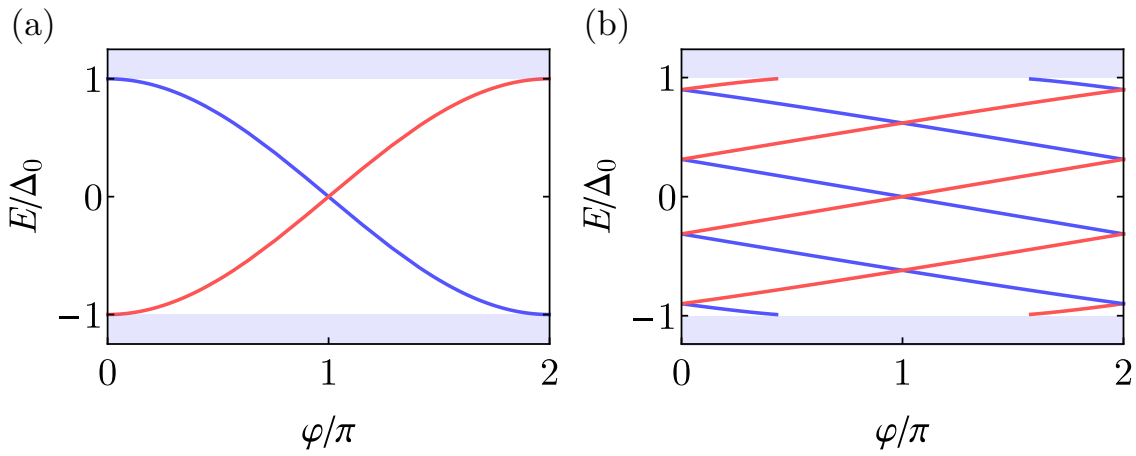

Figure 3.4: Plot of the spectrum of bound states in an SS-junction for $d = 0\xi_0$ (a) and $d = 2\xi_0$ (b), where $\xi_0 = \hbar v_\mathrm{F}/\Delta_0$ is the coherence length (we restore the constants $\hbar, v_\mathrm{F}$ for clarity). The blue [red] line corresponds to the bound state in Fig. 3.3 (a) [(b)] – *i.e.*, the $(u_\uparrow, v_\downarrow)^\mathrm{T}$ [$(u_\downarrow, v_\uparrow)^\mathrm{T}$] block. The blue areas indicate the continuum of states above the gap.

see below. The 4π-periodicity is a hallmark of topological superconductivity and the appearance of MBS. There has been substantial experimental and theoretical effort to find and understand the signatures of it in the properties of Josephson junctions [32, 33, 44, 89–92].

Increasing the distance d between the superconductors from zero to finite values activates the first term in Eq. (3.44), such that the range of the entire left hand side extends 2π. The physical consequence is the appearance of additional bound states, since the dynamical phase picked up during propagation becomes nonzero such that the entire phase shift of a closed loop can reach different multiples of 2π, depending on the energy. Also note that the new states at higher energies push the other ones down. For larger and larger d, the term $-\eta(E)$ becomes less relevant and the states will approach linear dependency on the phase, as can already be seen in Fig. 3.4 (b).

3.2.1.5 Deriving the resonance condition with scattering matrices

As simple and straightforward the condition for bound states can be derived from the wave function ansatz or the phase tracking method, these are not really practical in more complicated systems. Matching the wave function at the interfaces was simplified due to the simplicity of the Hamiltonian. The fact that there was only a single decaying solution in the outer S regions lead to a simple system of equations, the solutions of which were easy to determine. All of this is no longer true for more complicated systems and obtaining the resonance condition becomes significantly more tedious. Furthermore, calculating the phase picked up during a closed loop only gives a definite condition for bound states as long as there is only a single one.

Anticipating the need for a more elegant way of finding bound states, we are going to discuss how we can directly use the scattering matrices for the NS- and SN-junctions. At this stage, this does not really make a big difference, but will prove

to be useful later on.

As a first step, we note that in Fig. 3.3, we center the origin within the N region such that the interfaces are located at $x = \pm d/2$. However, the discussion in Sections 3.2.1.1 and 3.2.1.2 assumed the interfaces between N and S regions to be at $x = 0$. The scattering matrices within the SS-junction are thus phase-shifted, accounting for the translation needed to relate the scattering problems. One can think of these phases as the dynamical phases picked up by particles traveling an additional distance before reaching the interface.

Next, consider Fig. 3.3 and a suitable wave function in the $(u_\uparrow, v_\downarrow)^{\mathrm{T}}$-block at the origin. It consists of a rightmoving electron and a leftmoving hole. With respect to the right NS-interface, the $u_\uparrow(x = 0)$ component is an incoming mode, while the $u_\downarrow(x = 0)$ component is an outgoing mode. Consequently, they are related by an Andreev reflection coefficient $\tilde{r}_{he} = \mathrm{e}^{idE} r_{he}$ according to

$$v_\downarrow(0) = \tilde{r}_{he} u_\uparrow(0), \tag{3.46}$$

where r_{he} is the Andreev reflection coefficient for the NS-interface placed at the origin.

Accordingly, considering the opposite SN-interface at $x = -d/2$, the $u_\downarrow(0)$ component is the incoming one, whereas $u_\uparrow(0)$ amounts to an outgoing mode. They are related via the Andreev reflection coefficient $\tilde{r}'_{eh} = \mathrm{e}^{idE} r'_{eh}$ in the form

$$u_\uparrow(0) = \tilde{r}'_{eh} v_\downarrow(0), \tag{3.47}$$

where r'_{eh} is the corresponding reflection from the SN-interface at the origin.

Combining the two conditions from the two elementary scattering events in Eqs. (3.46) and (3.47) leads to

$$(\tilde{r}_{he}\tilde{r}'_{eh} - 1)\, v_\downarrow(0) = 0 \quad \Leftrightarrow \quad \mathrm{e}^{2\mathrm{i}dE}\, r_{he}\, r'_{eh} - 1 = 0. \tag{3.48}$$

Inserting the expressions for r_{he} and r'_{eh} into Eq. (3.48) then immediately reproduces the resonance condition in Eq. (3.42) [note that the phase in the left S region is zero and φ in the right one]. In an analogous way one can combine the scattering coefficients for the $u_\downarrow, v_\uparrow$-block, which of course leads back to Eq. (3.43).

In more complicated setups, there could for instance be an additional scattering region in the center of the structure. In this case, an equivalent process will amount to a combination of scattering matrices relating wave functions with multiple components, but the underlying idea remains the same. One uses the fact that the wave functions within the system must be related by the elementary scattering processes, in order to derive a compatibility relation in the same spirit as Eq. (3.48). For arbitrary wave functions, it will only be fulfilled for definite energies, for which the appropriate combination of scattering coefficients (or matrices in general) amounts to multiplying with 1 (applying the identity operator). An example of this is the SFS-system discussed in Section 3.3.2

3.2.1.6 Majorana bound states

After establishing the spectrum of bound states within the SS-junction, we can now proceed to discuss the appearance of MBS in the system. It turns out that most of

the work is already done. Using the resonance conditions in Eq. (3.44) derived in Section 3.2.1.3, one can easily see that there is always a bound state at $E = 0$ in both blocks if the phase difference is $\varphi = \pi$. The bound state in the $(u_\uparrow, v_\downarrow)^{\mathrm{T}}$-block is easily obtained by inserting the explicit expressions for the eigenstates within the different regions in the ansatz Eq. (3.40) for $E = 0$ and $\varphi = \pi$. Furthermore, without loss of generality we set $A = 1$, and and the other coefficients B, C, D follow from Eq. (3.41). The wave function at zero energy then acquires the form

$$\phi_1(x) = \chi_0 \cdot \begin{cases} \mathrm{e}^{\Delta_0(x+d/2)} & x < -d/2 \\ 1 & -d/2 < x < d/2 \\ \mathrm{e}^{-\Delta_0(x-d/2)} & x > d/2, \end{cases} \tag{3.49}$$

where we use the spinor $\chi_0 = (-\mathrm{i}, 0, 1, 0)^{\mathrm{T}}$. It is constant in the N region, and exponentially decays into the superconductors for $|x| > d/2$.

Instead of repeating the same steps for the solution in the other block, we recall that the two blocks are actually related through charge conjugation, provided $E \to -E$. However, since we discuss a zero energy bound state, charge conjugation directly yields the bound state in the other block via

$$\phi_2 = \mathcal{C}\phi_1, \tag{3.50}$$

with the charge conjugation operator $\mathcal{C} = \hat{\tau}_2\hat{\sigma}_2\,\mathrm{K}$ as defined in Eq. (3.17).

Finally, using the fundamental properties of the BdG-Hamiltonian of the helical edge from Section 3.1.3, we know that any zero-energy solution can be decomposed into two Majorana wave functions. Hence, we find

$$\phi_+ = \phi_1 + \mathcal{C}\phi_1 \qquad \text{and} \qquad \phi_- = -\mathrm{i}\,\phi_1 + \mathrm{i}\,\mathcal{C}\phi_1, \tag{3.51}$$

which satisfy the Majorana condition in Eq. (3.31) by definition. Note that since $\phi_2 = \mathcal{C}\phi_1$ and $\mathcal{C}^2 = \mathbb{1}$, decomposing ϕ_2 in an analogous way leads to the *same* Majorana wave functions.

We conclude this section by noting that the presence of zero-energy Majorana wave functions can be understood in terms of the Jackiw-Rebbi model of a massive Dirac Hamiltonian with a mass kink similar to Section 2.2.2. To see this, consider the Hamiltonian in the $(u_\uparrow, v_\downarrow)^{\mathrm{T}}$-block, which for phase difference $\varphi = \pi$ reads

$$\begin{pmatrix} v_{\mathrm{F}}\hat{p} & \Delta(x) \\ \Delta^*(x) & -v_{\mathrm{F}}\hat{p} \end{pmatrix} = v_{\mathrm{F}}\hat{p}\,\hat{\tau}_3 + \mathrm{sgn}(x)\Delta_0\,\hat{\tau}_1 \tag{3.52}$$

and thus has a form similar to Eq. (2.55).

3.2.2 Superconducting and ferromagnetic barrier

The previous section equips us with the tools to discuss the case of one S and one F barrier more efficiently. However, we take a similar approach and start with an NF- and FN-interface as a precursor.

3.2.2.1 The NF- and FN-junction

In line with the discussion above, we model the NF-junction by taking $m_1(x) = \theta(x)m_\parallel \cos\lambda$ and $m_2(x) = \theta(x)m_\parallel \sin\lambda$. Furthermore, note that the BdG-equation takes the form

$$\begin{pmatrix} v_{\mathrm{F}}\hat{p}-\mu & \theta(x)m_\parallel \mathrm{e}^{-\mathrm{i}\lambda} & 0 & 0 \\ \theta(x)m_\parallel \mathrm{e}^{\mathrm{i}\lambda} & -v_{\mathrm{F}}\hat{p}-\mu & 0 & 0 \\ 0 & 0 & -v_{\mathrm{F}}\hat{p}+\mu & \theta(x)m_\parallel \mathrm{e}^{-\mathrm{i}\lambda} \\ 0 & 0 & \theta(x)m_\parallel \mathrm{e}^{\mathrm{i}\lambda} & v_{\mathrm{F}}\hat{p}+\mu \end{pmatrix} \phi(x) = E\,\phi(x). \quad (3.53)$$

First, since the chemical potential affects the size of the gap in the spectrum within the F region, we do need to take it into account here. Interestingly, due to the duality between magnetism and superconductivity, in Eq. (3.53) the component m_z plays the same role as the chemical potential in the cases of NS- and SN-junctions (*cf.* Sections 3.2.1.1 and 3.2.1.2). It merely leads to unimportant phase factors and is therefore set to zero. Secondly, apart from the chemical potential, Eq. (3.53) has the same block-diagonal structure as Eq. (3.33) in the $(u_\uparrow, u_\downarrow)^{\mathrm{T}}$- and $(v_\downarrow, v_\uparrow)^{\mathrm{T}}$-blocks, *i.e.,* in the electron- and hole sectors. This is also reflected in the similarity of the eigenstates, see Appendix A. Hence, as long as we keep track of the chemical potential, we know that we can adapt the results from the previous section. These properties are a manifestation of the superconductor-magnetism duality of the BdG-Hamiltonian.

Solving the scattering problem then leads to the scattering coefficients

$$r_{ee} = \mathrm{e}^{-\mathrm{i}\rho_e(E)+\mathrm{i}\lambda}, \qquad r_{hh} = \mathrm{e}^{-\mathrm{i}\rho_h(E)-\mathrm{i}\lambda}, \qquad r_{he} = r_{eh} = 0, \quad (3.54)$$

where r_{ee}, r_{hh} (r_{he}, r_{he}) are the normal (Andreev) reflections within the electron and hole blocks (in the blocks familiar from the previous section). Furthermore, we restrict ourselves to energies below the gap. In conclusion, using the same notation for incoming and outgoing modes as before, the scattering matrix for the NF-junction can be expressed as

$$\begin{pmatrix} b_e \\ b_h \end{pmatrix} = \underbrace{\begin{pmatrix} r_{ee} & 0 \\ 0 & r_{hh} \end{pmatrix}}_{S_{\mathrm{NF}}} \begin{pmatrix} a_e \\ a_h \end{pmatrix}. \quad (3.55)$$

Similarly, just as in the previous SN- and NS-junctions, the scattering coefficients in the FN-junction have the same form and read

$$r'_{ee} = \mathrm{e}^{-\mathrm{i}\rho_e(E)+\mathrm{i}\lambda}, \qquad r'_{hh} = \mathrm{e}^{-\mathrm{i}\rho_h(E)-\mathrm{i}\lambda}, \qquad r_{he} = r_{eh} = 0. \quad (3.56)$$

Clearly, the scattering matrices are also equal, *i.e.,* $S_{\mathrm{NF}} = S_{\mathrm{FN}}$.

3.2.2.2 Resonance condition for bound states

With the elementary scattering coefficients for junctions involving ferromagnets at hand, we can proceed to determine a resonance condition for a bound state between an S and an F barrier. Without loss of generality, we choose to place the superconductor to the left and the ferromagnet to the right, see Fig. 3.5. The schematic

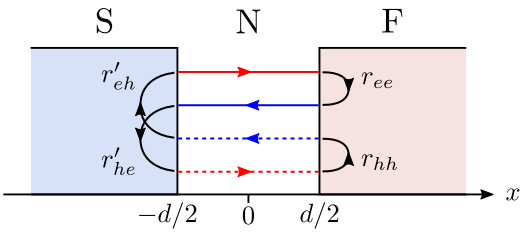

Figure 3.5: Sketch of an SF-junction and the formation of bound states. As before, red (blue) lines refer to spin-↑ (-↓), while red (blue) lines indicate electrons (holes).

depiction of the system already reveals a striking difference to the SS-case. The combined Hamiltonian of superconductivity and magnetism at the helical edge does no longer decouple into blocks, which manifests itself in the fact that a full loop between S- and F-barrier requires all four solutions in the normal region. A suitable ansatz for a bound state wave function is thus much more complicated, since both solutions exponentially decaying away from the N region are required within S and F. Accordingly, the ansatz in the interior N region needs to comprise all four propagating modes.

As a consequence, instead of matching the full ansatz at the interfaces at $x = \pm d/2$ and deriving the bound state condition from there, we take advantage of the two other approaches outlined in Section 3.2.1.5.

First, we note that there is only a single way of completing a full loop involving all possible scatterings at the barriers. Hence, tracking the phase picked up in the process yields the correct resonance condition. The loop consists of four crossings of the internal N regions, each of which contributes a phase factor $\mathrm{e}^{\mathrm{i}Ed}$. Following Sections 3.2.1.2 and 3.2.2.1, the two Andreev reflections amount to a phase factor of the form $\mathrm{e}^{-2\mathrm{i}\eta(E)}$. Note that the phase dependencies of both Andreev reflections cancel. Moreover, the two normal reflections off the ferromagnet yield $\mathrm{e}^{-\mathrm{i}\rho_e(E)-\mathrm{i}\rho_h(E)}$, where the dependence on the in-plane angle cancels in the same fashion. Put together, we find the resonance condition

$$4Ed - 2\eta(E) - \rho_e(E) - \rho_h(E) = 2\pi\, n, \tag{3.57}$$

with $n \in \mathbb{Z}$.

Furthermore, we note that making use of the scattering matrices S_{SN} and S_{NF} and taking into account the phase shift due to the translation of the interfaces as before, we can write down conditions on any solution $\phi(x = 0)$ of the BdG-equation as before. From the SN-interface we have

$$\begin{pmatrix} u_\uparrow(0) \\ v_\uparrow(0) \end{pmatrix} = \tilde{S}_{\mathrm{SN}} \begin{pmatrix} u_\downarrow(0) \\ v_\downarrow(0) \end{pmatrix}, \tag{3.58}$$

while the NF-interface leads to

$$\begin{pmatrix} u_\downarrow(0) \\ v_\downarrow(0) \end{pmatrix} = \tilde{S}_{\mathrm{NF}} \begin{pmatrix} u_\uparrow(0) \\ v_\uparrow(0) \end{pmatrix}. \tag{3.59}$$

The scattering matrices are given by

$$\tilde{S}_{\mathrm{SN}} = \begin{pmatrix} 0 & \tilde{r}'_{eh} \\ \tilde{r}'_{he} & 0 \end{pmatrix} \quad \text{and} \quad \tilde{S}_{\mathrm{NF}} = \begin{pmatrix} \tilde{r}_{ee} & 0 \\ 0 & \tilde{r}_{hh} \end{pmatrix}, \tag{3.60}$$

where the tilde expresses the phase shift as $\tilde{r}_{\alpha\beta} = \mathrm{e}^{\mathrm{i}Ed} r_{\alpha\beta}$ and accordingly $\tilde{r}'_{\alpha\beta} = \mathrm{e}^{\mathrm{i}Ed} r'_{\alpha\beta}$.

One can combine Eqs. (3.58) and (3.59) into the condition

$$\left(\tilde{S}_{\mathrm{SN}}\tilde{S}_{\mathrm{NF}} - \mathbb{1}\right)\begin{pmatrix} u_\uparrow(0) \\ v_\uparrow(0) \end{pmatrix} = 0, \tag{3.61}$$

such that the system has a bound state if

$$\det\left(\tilde{S}_{\mathrm{SN}}\tilde{S}_{\mathrm{NF}} - \mathbb{1}\right) = 0. \tag{3.62}$$

It is straightforward to show that Eq. (3.62) is equivalent to

$$\tilde{r}'_{eh}\tilde{r}_{hh}\tilde{r}'_{he}\tilde{r}_{ee} - 1 = 0, \tag{3.63}$$

and that Eq. (3.63) is equivalent to Eq. (3.57).

Remarkably, the resonance condition Eq. (3.57) only depends on the width of the normal region d, the induced superconducting gap Δ_0, as well as the parameters determining the magnetic gap, *i.e.,* the in-plane component of the magnetic field $m_\parallel$ and the chemical potential μ. Hence, there is no easily accessible way of tweaking the appearance of bound states as there was with the phase difference in the SS-junction.

Additonally, observe that if there is an energy E for which the resonance condition Eq. (3.57) is fulfilled, it also holds for $-E$ due to $\eta(-E) = \pi - \eta(E)$ and $\rho_e(-E) = \pi - \rho_h(E)$. As a direct consequence, there is always a bound state at $E = 0$. Note that for a junction without N region, *i.e.,* $d = 0$, the zero energy bound state is the only one possible, while for finite width d, more bound states may arise due to the additional winding of the phase during propagation.

3.2.2.3 Majorana bound state

In this section, we discuss how the fact that the resonance condition is always fulfilled at $E = 0$ relates to MBSs. First, we remark that there is only one way to complete the loop in the SF-junction, in contrast to the SS-case. This is already a hint that the state at zero energy is special and can not be decomposed in two Majorana wave functions in the same way as before.

In the following, since we are only interested in the zero energy state, we discuss a junction with $d = 0$. Furthermore, let us consider the SF-junction for $\mu = 0$ and $\lambda = \varphi = 0$, such that $\Delta_1(x), m_1(x) > 0$ and $\Delta_2(x) = m_2(x) = 0$. The Hamiltonian thus has the form

$$\begin{aligned}\mathcal{H}_{\mathrm{BdG}} &= \begin{pmatrix} v_{\mathrm{F}}\hat{p} & m_1(x) & \Delta_1(x) & 0 \\ m_1(x) & -v_{\mathrm{F}}\hat{p} & 0 & \Delta_1(x) \\ \Delta_1(x) & 0 & -v_{\mathrm{F}}\hat{p} & m_1(x) \\ 0 & \Delta_1(x) & m_1(x) & v_{\mathrm{F}}\hat{p} \end{pmatrix} \\ &= v_{\mathrm{F}}\hat{p}\,\hat{\tau}_3\hat{\sigma}_3 + m_1(x)\,\hat{\tau}_0\hat{\sigma}_1 + \Delta_1(x)\,\hat{\tau}_1\hat{\sigma}_0.\end{aligned} \tag{3.64}$$

We can perform a unitary rotation with $U = \exp(\mathrm{i}\hat{\tau}_2\hat{\sigma}_1\pi/4)$, leading to

$$\begin{aligned} U\mathcal{H}_{\mathrm{BdG}}U^\dagger &= v_{\mathrm{F}}\hat{p}\,\hat{\tau}_3\hat{\sigma}_3 + m_1(x)\,\hat{\tau}_0\hat{\sigma}_1 + \Delta_1(x)\,\hat{\tau}_3\hat{\sigma}_1 \\ &= \begin{pmatrix} v_{\mathrm{F}}\hat{p}\,\hat{\sigma}_3 + [m_1(x)+\Delta_1(x)]\;\hat{\sigma}_1 & 0 \\ 0 & -v_{\mathrm{F}}\hat{p}\,\hat{\sigma}_3 + [m_1(x)-\Delta_1(x)]\;\hat{\sigma}_1 \end{pmatrix}. \end{aligned} \tag{3.65}$$

We can identify the two blocks of Eq. (3.65) as two uncoupled Jackiw-Rebbi models with masses $M_1(x) = m_1(x) + \Delta_1(x)$ and $M_2(x) = m_1(x) - \Delta_1(x)$. Hence, for our choice of parameters, the system consists of one massive Dirac equation with a mass kink and one massive Dirac equation without mass kink, since $M_1 \geq 0\,\forall x$, while $M_2(x) < 0$ for $x < 0$ and $M_2(x)$ for $x > 0$. Consequently, we expect a zero energy state localized at the mass kink.

In order to explicitly determine the wave function of a solution at zero energy, we use the explicit form of the eigenstates within S and F regions (see Appendix A). We also reinstate the chemical potential, since it does influence the size of the gap and subsequently the following results. We make the ansatz [129]

$$\phi(x) = \begin{cases} A\,\mathrm{e}^{\Delta_0 x - \mathrm{i}\mu x}\chi_{e-} + B\,\mathrm{e}^{\Delta_0 x + \mathrm{i}\mu x}\chi_{h-} & x < 0 \\ C\,\mathrm{e}^{-\bar{m}x}\zeta_{e+} + D\,\mathrm{e}^{-\bar{m}x}\zeta_{h+} & x < 0, \end{cases} \tag{3.66}$$

where $\bar{m} = \kappa_{e/h}(0) = \sqrt{m_\parallel^2 - \mu^2}$. Matching the wave function at $x = 0$ leads to a relation between the coefficients A, B, C, D. The final solution, up to a normalization constant, can be expressed as

$$\phi(x) = \theta(-x)\,\mathrm{e}^{\Delta_0 x}\begin{pmatrix} c_1c_2\,\mathrm{e}^{\mathrm{i}\mu x} \\ c_1c_2^*\,\mathrm{e}^{-\mathrm{i}\mu x} \\ c_1^*c_2\,\mathrm{e}^{+\mathrm{i}\mu x} \\ -c_1^*c_2^*\,\mathrm{e}^{-\mathrm{i}\mu x} \end{pmatrix} + \theta(x)\,\mathrm{e}^{-\bar{m}x}\begin{pmatrix} c_1c_2 \\ c_1c_2^* \\ c_1^*c_2 \\ -c_1^*c_2^* \end{pmatrix}, \tag{3.67}$$

where we introduced the shorthands $c_1 = (1 - \mathrm{i})$ and $c_2 = \mathrm{e}^{\mathrm{i}\rho_e(0)/2}$.

Note that the ansatz in Eq. (3.66) required four coefficients, and that the wave function matching produces four equations. Hence, up to a global factor there is only one distinct solution. Except for a proper normalization constant, the wave function in Eq. (3.67) is chosen such that it explicitly fulfills the Majorana requirement $\phi(x) = \mathcal{C}\phi(x)$. Note that this directly implies that applying the decomposition in Section 3.1.3 yields $\phi_+ = \phi + \mathcal{C}\phi \propto \phi$ and $\phi_- = -\mathrm{i}\phi + \mathrm{i}\mathcal{C}\phi = 0$. In conclusion, the SF-junction discussed in this section binds exactly one MBS.

3.2.2.4 Differential conductance signatures

One of the smoking-gun experimental signatures for the appearance of MBS is a characteristic peak in the differential conductance originating from resonant tunneling into the bound state. Arguably, a conductance peak in a nanowire setup much like the ones we discussed in Chapter 2 was the basis for the claim of successful realization of MBS in Ref. [80] and subsequent works [82, 83, 86, 87]. Importantly, however, the peak should also be quantized at a value of $G = 2e^2/h$, *i.e.,* exactly the conductance of two quantum channels. It took substantial effort to improve

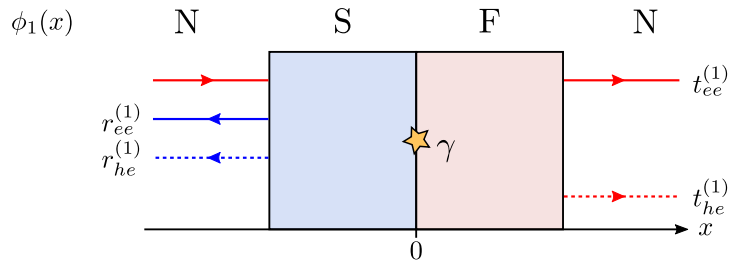

Figure 3.6: Schematic sketch of an SF-junction with finite barriers, such that the system outside the S- and F-regions is described by the BdG-Hamiltonian $\mathcal{H}_0$ of the bare helical edge. The color and dashing distinguish the modes as in Fig. 3.5. For clarity, we indicate the scattering state ϕ_1 corresponding to an electron coming in from the left, including all outgoing modes together with the scattering coefficients.

the experiments enough in order to actually achieve a properly quantized conductance peak. The transport properties of a system on the basis of QSHI edge states hosting a single MBS are thus of great importance as well and were studied in Refs. [44, 95, 129].

For our case at of an MBS bound between an S- and an F-region, the simplest way to make the state accessible for electrical probing is to make the width of superconducting and ferromagnetic regions finite, see Fig. 3.6 and Ref. [129]. For simplicity, we ignore phase difference and in-plane angle of the magnetic field and take the distance between S and F region to zero, such that there are no higher energy ABSs. We therefore model the system by taking $\Delta_1(x) = \Delta_0\theta(x+L_\mathrm{S})\theta(-x)$ and $m_1(x) = m_0\theta(x)\theta(-x+L_F)$, with $\Delta_0, m_0 > 0$ and $\Delta_2 = m_2 = 0$. As before, the z-component of the magnetic field plays no role and is neglected as well.

The now finite widths of the barriers does not change the appearance of a state localized at the SF interface at zero energy. Clearly the Hamiltonian is the same within the S and F regions, so that the wave function $\phi(x)$ from Eq. (3.67) is still valid in the interval $[-L_\mathrm{S}, L_\mathrm{F}]$. Outside of this region, the Hamiltonian is diagonal. As a result, matching the previous solutions to a linear combination of the eigenstates in the outer N regions is trivially possible.

In order to determine the differential conductance at zero energy, we need to solve the scattering problem of the SF-junction. The scattering states are constructed in a similar fashion as in the simple cases in Section 3.2.1. Note that due to the N regions on the very left and right of the junction, there are four possibilities of injecting particles and hence four scattering states ϕ_j, $j = 1, 2, 3, 4$, corresponding to (i) an incoming electron from the left ($j = 1$), (ii) an incoming hole from the left ($j = 2$), (iii) an incoming electron from the right ($j = 3$), (iv) an incoming hole from the right ($j = 4$).

Furthermore, the physics of the SF-junction, where superconducting and magnetic order are combined, is richer than in systems with only S or F regions. This is simply due to the fact that the BdG-Hamiltonian is no longer block diagonal, which opens up new scattering channels compared with purely S- or F-systems. In more graphical terms, notice for instance how a subsequent scattering of a rightmoving electron off the NF- and then off the SN-interface turns it into a rightmoving hole.

As a consequence, incoming electrons from either direction can either be reflected as an electron (normal reflection) or as a hole (Andreev reflection), or be transmitted as an electron (electron cotunneling (EC)) or as a hole (crossed Andreev reflection (CAR)).

For completeness, we give the asymptotic form of the scattering states at zero energy outside the S- and F-regions, *i.e.,* for $x < -L_\mathrm{S}$ and $x > L_\mathrm{F}$. In the leftmost region, they read

$$\begin{aligned}
\phi_1(x) &= \left(\mathrm{e}^{\mathrm{i}\mu x}, r_{ee}^{(1)}\,\mathrm{e}^{-\mathrm{i}\mu x}, r_{he}^{(1)}\,\mathrm{e}^{\mathrm{i}\mu x}, 0\right)^T \\
\phi_2(x) &= \left(0, r_{eh}^{(2)}\,\mathrm{e}^{-\mathrm{i}\mu x}, r_{hh}^{(2)}\,\mathrm{e}^{\mathrm{i}\mu x}, \mathrm{e}^{-\mathrm{i}\mu x}\right)^T \\
\phi_3(x) &= \left(0, t_{ee}^{(3)}\,\mathrm{e}^{-\mathrm{i}\mu x}, t_{he}^{(3)}\,\mathrm{e}^{\mathrm{i}\mu x}, 0\right)^T \\
\phi_4(x) &= \left(0, t_{eh}^{(4)}\,\mathrm{e}^{-\mathrm{i}\mu x}, t_{hh}^{(4)}\,\mathrm{e}^{\mathrm{i}\mu x}, 0\right)^T,
\end{aligned} \tag{3.68}$$

and in the rightmost region, we find

$$\begin{aligned}
\phi_1(x) &= \left(t_{ee}^{(1)}\,\mathrm{e}^{\mathrm{i}\mu x}, 0, 0, t_{he}^{(1)}\,\mathrm{e}^{-\mathrm{i}\mu x}\right)^T \\
\phi_2(x) &= \left(t_{eh}^{(2)}\,\mathrm{e}^{\mathrm{i}\mu x}, 0, 0, t_{hh}^{(2)}\,\mathrm{e}^{-\mathrm{i}\mu x}\right)^T \\
\phi_3(x) &= \left(r_{ee}^{(3)}\,\mathrm{e}^{\mathrm{i}\mu x}, \mathrm{e}^{-\mathrm{i}\mu x}, 0, r_{he}^{(3)}\,\mathrm{e}^{-\mathrm{i}\mu x}\right)^T \\
\phi_4(x) &= \left(r_{eh}^{(4)}\,\mathrm{e}^{\mathrm{i}\mu x}, 0, \mathrm{e}^{\mathrm{i}\mu x}, r_{hh}^{(4)}\,\mathrm{e}^{-\mathrm{i}\mu x}\right)^T.
\end{aligned} \tag{3.69}$$

The scattering coefficients denote reflections (transmissions) of an injected particle of type β into a particle of type α as $r_{\alpha\beta}^{(i)}$ ($t_{\alpha\beta}^{(i)}$). The superscript refers to the scattering state.

In the following, we focus on the case of strong barriers in order to have a well-localized MBS. This is achieved by choosing large values for $m_0 L_\mathrm{F}$ and $\Delta_0 L_\mathrm{S}$, *cf.* Eq. (3.67). As a consequence, we expect negligible transmissions away from resonances, such that the scattering properties are captured well by the reflection coefficients. The local differential conductances G_LL and G_RR, defined as

$$G_\mathrm{LL} := (\partial I_\mathrm{L}/\partial V_\mathrm{L})_{V_\mathrm{L}=0} \qquad \text{and} \qquad G_\mathrm{RR} := (\partial I_\mathrm{R}/\partial V_\mathrm{R})_{V_\mathrm{R}=0} \tag{3.70}$$

where $I_\mathrm{L,R}$, $V_\mathrm{L,R}$ are the currents and voltages in the left and right lead, are related to the scattering coefficients at zero energy by the well-known Blonder-Tinkham-Klapwijk (BTK)-formula [125]

$$\begin{aligned}
G_\mathrm{LL} &= \frac{e^2}{h}\left[1 - |r_{ee}^{(1)}|^2 + |r_{he}^{(1)}|^2\right] = \frac{e^2}{h}\left[1 - |r_{hh}^{(2)}|^2 + |r_{eh}^{(2)}|^2\right] \\
G_\mathrm{RR} &= \frac{e^2}{h}\left[1 - |r_{ee}^{(3)}|^2 + |r_{he}^{(3)}|^2\right] = \frac{e^2}{h}\left[1 - |r_{hh}^{(4)}|^2 + |r_{eh}^{(4)}|^2\right]
\end{aligned}. \tag{3.71}$$

Determining the scattering coefficients $r_{\alpha\beta}^{(j)}, t_{\alpha\beta}^{(j)}$ amounts to matching the scattering states $\phi_j(x)$ at the interfaces $x = -L_\mathrm{S}, 0, L_\mathrm{F}$ and solving the resulting linear system of equations. Note that in the intererior of the S and F domains, the scattering states are given by a superposition of all four corresponding eigenstates. The explicit solutions are lengthy and not very illuminating, so we restrict ourselves to

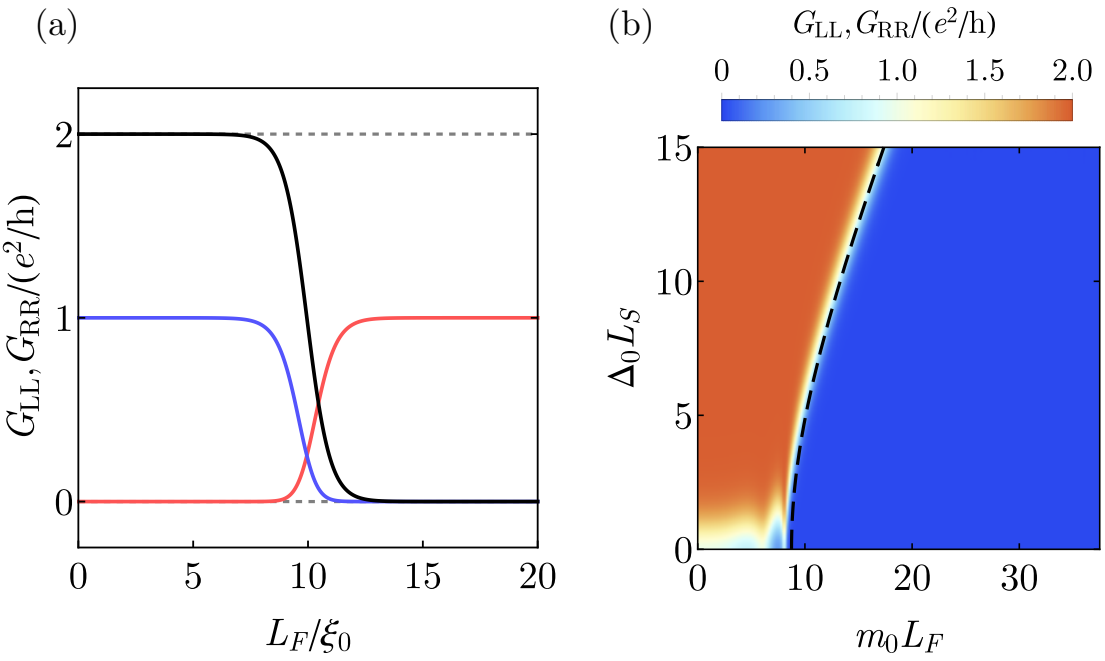

Figure 3.7: Plot of the differential conductances at zero energy. In panel (a), we show the Andreev reflection amplitudes $|r_{he}^{(1)}|^2, |r_{he}^{(3)}|^2$ (blue), the normal reflection amplitude $|r_{ee}^{(1)}|^2, |r_{ee}^{(3)}|^2$ (red), and the resulting local conductances $G_{\rm LL}, G_{\rm RR}$ (black) as a function of the thickness of the F region, which essentially varies the effective magnetic gap. We choose $L_S = 10\xi_0$, $m_0 = \Delta_0$, $\mu = 3.5\Delta_0$, with ξ_0 the coherence length. In panel (b) we show a density plot of the local conductances as a function of both the effective superconducting and the effective magnetic gap. The transition coincides with the black dashed line where $m_0^2 L_{\rm F}^2 - \mu^2 L_{\rm F}^2 = \Delta_0^2 L_{\rm S}^2$. As before, $\mu = 3.5\Delta_0$.

numerical results in this section. However, we remark that the case of a finite F region and a semi-infinite S region was solved analytically in Ref. [95]. Their result of perfect Andreev reflection at zero energy is approached for our system for $\Delta_0 L_{\rm S} \to \infty$.

Indeed, our results can be summarized as shown in Fig. 3.7. For strong barriers, we find that all Andreev reflection amplitudes approach unity, *i.e.*, $|r_{eh}^{(i)}|^2, |r_{he}^{(i)}|^2 \to 1$, if the superconducting barrier dominates and the condition

$$\Delta_0^2 L_{\rm S}^2 > m_0^2 L_{\rm F}^2 - \mu_2 L_{\rm F}^2 \tag{3.72}$$

is fulfilled, in agreement with Ref. [95]. Note that almost perfect Andreev reflection necessarily implies negligible normal reflection, due to unitarity of the scattering matrix. Accordingly, the local conductances tend to the expected value as $G_{\rm LL} = G_{\rm RR} \sim 2e^2/h$.

However, in the opposite case for a stronger magnetic barrier, where

$$m_0^2 L_{\rm F}^2 - \mu^2 L_{\rm F}^2 > \Delta_0^2 L_{\rm S}^2, \tag{3.73}$$

normal reflection amplitudes are close to one, $|r_{ee}^{(i)}|^2, |r_{hh}^{(i)}|^2 \to 1$, while Andreev

reflections go to zero. As a consequence, the local conductances also vanish and we find $G_{\mathrm{LL}} = G_{\mathrm{RR}} \sim 0$.

In conclusion, there is a transition between conductance values of $2e^2/h$ and 0 whenever the gaps become comparable, *i.e.,* $m_0^2 L_{\mathrm{F}}^2 - \mu^2 L_{\mathrm{F}}^2 \approx \Delta_0^2 L_{\mathrm{S}}^2$. However, in our case this does *not* signal the appearance of a protected zero-energy bound state, since we have shown above that the MBS is *always* present for any configuration.

To resolve this apparent contradiction, we introduce yet another way of solving the scattering problem in terms of *transfer matrices*. To that end, we rewrite the BdG-equation at zero energy, $\mathcal{H}_{\mathrm{BdG}}\phi(x) = 0$, in the form

$$\partial_x \phi(x) = \mathrm{i} h(x) \phi(x), \tag{3.74}$$

where we essentially ordered the derivatives from the momentum operator on one side and everything else on the other. Hence, the matrix $h(x)$ is given by

$$h(x) = \mu \hat{\tau}_0 \hat{\sigma}_3 - \mathrm{i} m_1(x) \hat{\tau}_3 \hat{\sigma}_2 - \mathrm{i}\Delta_1(x) \hat{\tau}_2 \hat{\sigma}_3. \tag{3.75}$$

In analogy of the formal solution to the Schrödinger equation, Eq. (3.74) can be solved by introducing a unitary "position evolution" operator $U(x, x')$. It relates solutions according to

$$\phi(x) = U(x, x')\, \phi(x') \tag{3.76}$$

and is defined as

$$U(x, x') = S_{\leftarrow} \mathrm{e}^{\mathrm{i} \int_x^{x'} \mathrm{d}\xi \; h(\xi),} \tag{3.77}$$

where $S_{\leftarrow}$ is the spatial ordering operator [130–134], which orders according to increasing spatial argument from right to left(hence the arrow). The matrix $U(x, x')$ can be regarded as a transfer matrix, because following Eq. (3.76) it relates wave functions at different positions, *i.e.,* left and right of a scattering region. This is in contrast to the scattering matrix, which sorts into in- and outgoing modes and thus mixes left and right. However, both matrices essentially link the same coefficients in a linear way, so there is a one-to-one correspondence between the two. The convenient property of transfer matrices is, that they can easily be combined by repeatingly applying Eq. (3.76).

In order to solve the scattering problem of interest to us, we therefore need to solve the equation

$$U(L_{\mathrm{F}}, -L_{\mathrm{S}})\, \phi(-L_{\mathrm{S}}) = \phi(L_{\mathrm{F}}), \tag{3.78}$$

and thus all relevant information is contained in the matrix $U(L_{\mathrm{F}}, -L_{\mathrm{S}})$.

By evaluating Eq. (3.77) and using that $h(x)$ is constant within S and F region, we find

$$U(L_{\mathrm{F}}, -L_{\mathrm{S}}) = \exp\left[\mathrm{i} L_{\mathrm{F}} \left(\mu \hat{\tau}_0 \hat{\sigma}_3 - \mathrm{i} m_0 \hat{\tau}_3 \hat{\sigma}_2\right)\right] \exp\left[\mathrm{i} L_{\mathrm{S}} \left(\mu \hat{\tau}_0 \hat{\sigma}_3 - \mathrm{i}\Delta_0 \hat{\tau}_2 \hat{\sigma}_3\right)\right]. \tag{3.79}$$

To proceed, we first note that we can simply decompose the latter exponential into a product, since $[\hat{\tau}_0 \hat{\sigma}_3, \hat{\tau}_2 \hat{\sigma}_3] = 0$ such that the terms commute.[2] Furthermore, the term from the chemical potential within the superconductor $\exp(\mathrm{i} L_{\mathrm{S}} \mu \hat{\tau}_0 \hat{\sigma}_3)$ is diagonal and unitary, *i.e.,* its entries are mere phase factors. Hence, this term does not change the important properties and is therefore ignored.

[2] Recall the Baker-Campbell-Hausdorff formula

$$\mathrm{e}^X \mathrm{e}^Y = \mathrm{e}^{X+Y+\frac{1}{2}[X,Y]+\ldots} \tag{3.80}$$

Next, since additionally $[\hat{\tau}_3\hat{\sigma}_2, \hat{\tau}_2\hat{\sigma}_3] = 0$, the term containing the pairing potential can safely be joined into the exponential stemming from the F region. Upon gauging away the term $\exp(\mathrm{i}L_\mathrm{S}\mu\hat{\tau}_0\hat{\sigma}_3)$ and a little rewriting, we find the effective propagator

$$U(L_\mathrm{F}, -L_\mathrm{S}) = \exp\left[\mathrm{i}(L_\mathrm{S}+L_\mathrm{F})\left[\frac{L_\mathrm{F}}{L_\mathrm{S}+L_\mathrm{F}}\left(\mu\hat{\tau}_0\hat{\sigma}_3 - \mathrm{i}m_0\hat{\tau}_3\hat{\sigma}_2\right) - \mathrm{i}\frac{L_\mathrm{S}}{L_\mathrm{S}+L_\mathrm{F}}\Delta_0\hat{\tau}_2\hat{\sigma}_3\right]\right]. \tag{3.81}$$

As a result we can conclude that the order, and in fact the exact position, of the barriers do not matter at zero energy (additional phases due to propagation vanish at $E = 0$). Specifically, one can identify Eq. (3.81) as the propagator of a system with chemical potential $\tilde{\mu} = L_\mathrm{F}\mu/(L_\mathrm{S}+L_\mathrm{F})$, where a magnetic field with $\tilde{m} = L_\mathrm{F}m/(L_\mathrm{S}+L_\mathrm{F})$ and proximity induced superconductivity with pair potential $\tilde{\Delta} = L_\mathrm{S}\Delta_0/(L_\mathrm{S}+L_\mathrm{F})$ are superimposed between $x = -L_\mathrm{S}$ and $x = L_\mathrm{F}$.

This insight is important, since there is a connection between helical edge states and the small momentum sector of a nanowire with SOC subjected to s-wave superconductivity and a magnetic field along the direction of the wire, as indirectly alluded to in Section 2.3. In the latter system, we saw that there was a topological phase transition at $\tilde{m}^2 = \tilde{\Delta}^2 + \tilde{\mu}^2$, which coincides with the location of the transition in the conductances. Our propagator, and by extension the scattering coefficients, therefore capture the behavior of a transition in a different system. The connection to the appearance of a bound state is therefore *not* a direct one, mathematically expressed by the possibility of manipulating the exponentials in the propagator freely.

3.3 Tunable hybridization in double cavities

To conclude this chapter, we now proceed to an extension of the SS-junction discussed in Section 3.2.1 by inserting an additional, finite S- or F-barrier between the two semi-infinite outer S regions. We are interested in the question how the bound states in such a double cavity are related to the bound states in single cavities, and in particular if and how Majorana bound states can still arise. Since the systems now become increasingly complex, we will not be able to provide as detailed analytical steps as before. However, the results from the previous sections together with numerical solutions will convey a compelling physical picture.

3.3.1 Three superconducting barriers

3.3.1.1 Bound state condition and spectrum

We start by considering an SSS-junction, see Fig. 3.8. For simplicity, we assume that the pair potential has the same modulus in each S region. Furthermore, the chemical potential plays no role and is therefore set to zero.

We use the phase of the leftmost S region as reference and set $\varphi_\mathrm{L} = 0$. Instead of working with the phases $\varphi_\mathrm{M}, \varphi_\mathrm{R}$ directly, it will be more convenient to use the phase differences across the LM-cavity $\varphi_1 := \varphi_\mathrm{M} - \varphi_\mathrm{L}$ and across the RM-cavity $\varphi_2 := \varphi_\mathrm{R} - \varphi_\mathrm{M}$ instead.

for noncommutative X, Y, where ... stands for higher nested commutators.

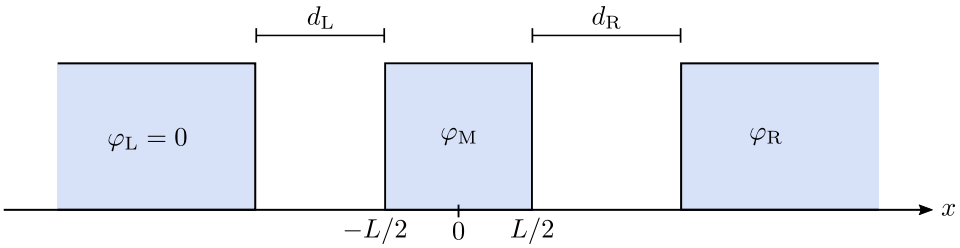

Figure 3.8: Sketch of a triple superconductor SSS-junction. We assume the outer S regions to be semi-infinite and thus extending to $x \to \pm\infty$. Furthermore, for simplicity we choose the modulus of the pairing potentials to be Δ_0 in all S regions and set the phase in the left S region to zero. The other parameters are $d_\mathrm{L} = d_\mathrm{R} = \xi_0$, $L = 1.5\xi_0$, where $\xi_0 = \hbar v_\mathrm{F}/\Delta_0$ the coherence length as before.

Again, just as in every system with only N and S regions, the problem decomposes into the $(u_\uparrow, v_\downarrow)^\mathrm{T}$- and $(u_\downarrow, v_\uparrow)$-blocks, which considerably simplifies the discussion. As before, we first focus on the former of the two blocks.

As a first step, we need to tackle the central S region, since we are subsequently going to be able to use our previous results for the outer SN- and NS-interfaces. Thus, we need to solve the scattering problem of a single S region, which is of course a special case of the SF-case of Section 3.2.2.4, we can use the same asymptotic form of the scattering states as in Eqs. (3.68) and (3.69) for the regions left and right of the barrier. The only difference is that in the absence of a magnetic domain, there are only Andreev reflections and EC. Matching the wave functions at the interfaces at $x = \pm L/2$ straightforwardly leads to the scattering matrix, and we shall only state the solutions we are going to need in the following. The ingoing and outgoing amplitudes are related by

$$\begin{pmatrix} b_e \\ b_h \end{pmatrix} = \underbrace{\begin{pmatrix} t_{ee}^{(1)} & r_{eh}^{(4)} \\ r_{he}^{(1)} & t_{hh}^{(4)} \end{pmatrix}}_{S_\mathrm{M}} \begin{pmatrix} a_e \\ a_h \end{pmatrix}, \tag{3.82}$$

where b_e (b_h) is the outgoing electron (hole) amplitudes on the right (left), a_e (a_h) is the incoming electron (hole) amplitude from the left (right), and S_M is the scattering matrix within the $(u_\uparrow, v_\downarrow)^\mathrm{T}$-block. The coefficients are given by

$$\begin{aligned} r_{he}^{(1)} &= -\mathrm{i}\mathrm{e}^{-\mathrm{i}LE+\mathrm{i}\varphi_\mathrm{M}} \frac{\sinh(L\Omega)}{\sinh(\mathrm{i}\eta + L\Omega)}, \qquad r_{eh}^{(4)} = -\mathrm{i}\mathrm{e}^{-\mathrm{i}LE-\mathrm{i}\varphi_\mathrm{M}} \frac{\sinh(L\Omega)}{\sinh(\mathrm{i}\eta + L\Omega)} \\ t_{ee}^{(1)} &= t_{hh}^{(4)} = \mathrm{i}\mathrm{e}^{-\mathrm{i}LE} \frac{\sin(\eta)}{\sinh(\mathrm{i}\eta + L\Omega)}. \end{aligned} \tag{3.83}$$

Next, we note that the outer interfaces between intermediate normal regions and superconductors are essentially shifted SN- and NS-interfaces. Building on previous sections, we can summarize their effect in the equation

$$\begin{pmatrix} a_e \\ a_h \end{pmatrix} = \underbrace{\begin{pmatrix} 0 & \mathrm{e}^{-\mathrm{i}\eta}\mathrm{e}^{\mathrm{i}E(L+2d_\mathrm{L})} \\ \mathrm{e}^{-\mathrm{i}\eta+\mathrm{i}\varphi_\mathrm{R}}\mathrm{e}^{\mathrm{i}E(L+2d_\mathrm{R})} & 0 \end{pmatrix}}_{S_\mathrm{A}} \begin{pmatrix} b_e \\ b_h \end{pmatrix}. \tag{3.84}$$

Note that the role of incoming and outgoing modes is reversed here. The first exponential in both nonzero elements of S_A stem from the Andreev reflection itself, whereas the second exponential is the phase shift due to the location of the interfaces.

Combining Eqs. (3.83) and (3.84) then yields the consistency condition

$$\det\left(S_\mathrm{M} S_\mathrm{A} - \mathbb{1}\right) = 0. \tag{3.85}$$

In an analogous way, for the $(u_\downarrow, v_\uparrow)^\mathrm{T}$-block one can derive a similar resonance condition. As before, particle-hole symmetry ensures that they are closely related and bound states always appear in pairs at energies $\pm E$.

Remarkably, in both blocks one can simplify the left hand side of Eq. (3.85) quite a lot. After some algebra, we arrive at an equation of the form [118]

$$D_1 + D_2 + \left(\mathrm{e}^{2\Omega L} - 1\right) D_2 = 0, \tag{3.86}$$

where

$$D_1 + D_2 = \sin(\eta) \sin\left[2E(d_\mathrm{L} + d_\mathrm{R}) - \eta \pm \frac{\varphi_1 + \varphi_2}{2}\right], \tag{3.87a}$$

$$D_2 = \sin\left[E d_\mathrm{L} - \eta \pm \frac{\varphi_1}{2}\right] \sin\left[E d_\mathrm{R} - \eta \pm \frac{\varphi_2}{2}\right]. \tag{3.87b}$$

The $+$ $(-)$ sign refers to the $(u_\uparrow, v_\downarrow)^\mathrm{T}$- $((u_\downarrow, v_\uparrow)^\mathrm{T}$-) block. Comparing with Section 3.2.1, we thus find a remarkably simple interpretation of the resonance condition for the SSS-junction in Eqs. (3.86) and (3.87). The term $D_1 + D_2$ is equivalent to a resonance condition of an SS-junction with width $d_\mathrm{L} + d_\mathrm{R}$, corresponding to the total width of both normal regions in the SSS-system. Furthermore, D_2 is a product of resonance conditions of two separate SS-junctions with respective widths d_L, d_R and phase differences φ_1 and φ_2. Eq. (3.86) therefore interpolates between the case of one big SS-junction for $L = 0$ and two uncoupled SS-junctions for $L \to \infty$. Hence, we can think of the SSS-junction as two cavities hosting bound states, where the finite central S region enables them to leak into the other cavity and acquire a delocalized character, expressed through the term D_2.

The resonance condition can be solved numerically. In Fig. 3.9, we show two spectra for a symmetric system, in which we fix the phase difference across the left cavity to be $\varphi_1 = \pi$ (left panel) and $\varphi_1 = \pi/2$ (right panel), and vary the phase difference across the right cavity from $\varphi_2 = 0$ to 2π.

In the first case, where $\varphi_1 = \pi$, the decomposition in separate SS-cavities would lead one to expect a zero energy state in the left cavity, and a state with a dispersion similar to Fig. 3.4. If they are brought together in an SSS-junction, however, Fig. 3.9 reveals hybridization around $\varphi_2 = \pi$, where bound states in both cavities have equivalent energies. In particular, in single SS-cavities we would have zero-energy states and hence Majoranas in both of them. Evidently, the close proximity of two such systems leads to hybridization and thus prevents true zero-energy states from forming. Note that at $\varphi_2 = 0, 2\pi$, a zero-energy bound state localized primarily in the left cavity is possible (see below).

If $\varphi_1 = \pi/2$, the hypothetically isolated right cavity still hosts a state dispersing as in Fig. 3.4, whereas the bound states in the left cavity now move to a finite

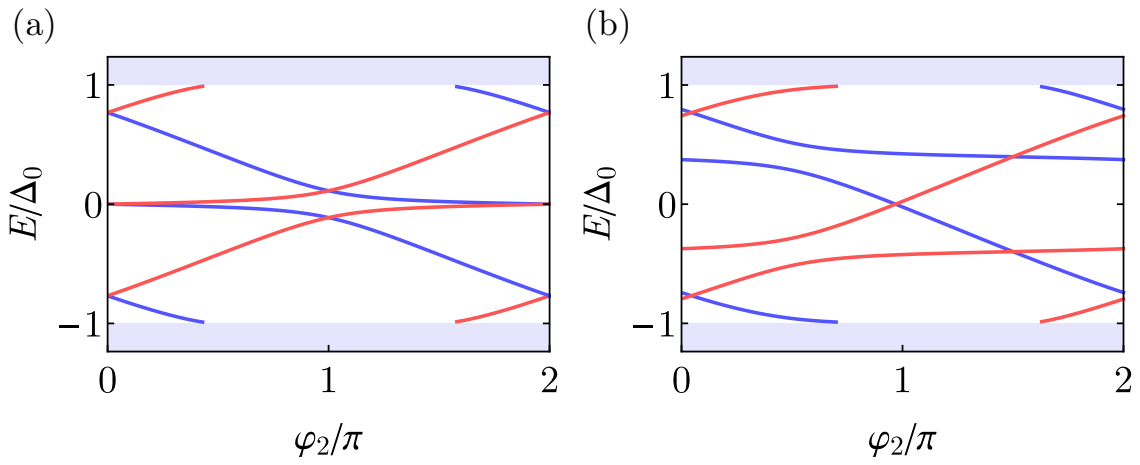

Figure 3.9: Plot of the bound state spectrum as a function of φ_2 for the SSS-junction with parameters as in Fig. 3.8, where $\varphi_1 = \pi$ in panel (a) and $\varphi_1 = \pi/2$ in panel (b), with the parameters as in Fig. 3.8. As in the case of the SS-junction, the blue [red] line corresponds to the bound state in the $(u_\uparrow, v_\downarrow)^{\mathrm{T}}$ $[(u_\downarrow, v_\uparrow)^{\mathrm{T}}]$ block.

energy. The spectrum in Fig. 3.9 shows avoided crossings around $\varphi_2 = \varphi_1$ due to hybridization. However, at phase differences $\varphi_2 = 2\pi - \varphi_1$ the crossings persist, even though the spectrum in both constituent SS-cavities is be the same. This is because of the fact that at this phase configuration, the states at the same energies belong to the two distinct sub-blocks of the Hamiltonian – in contrast to the $\varphi_1 = \varphi_2$ case – and thus never have a finite matrix element between them.

3.3.1.2 Majorana wave functions

From Eqs. (3.86) and (3.87) we can easily identify two situations in which $E = 0$ solves the resonance condition. The first is realized when $\varphi_1 = \pi$ and $\phi_2 = 0$, such that $\varphi_1 + \varphi_2 = \pi$, *cf.* Fig. 3.9. In this case, the first factor in Eq. (3.87b) corresponds to an SS-junction with phase difference π, which we know has a zero energy solution. As a consequence, this factor becomes zero. The same is true for Eq. (3.87a). Consequently, it is easy to see that Eq. (3.86) is also fulfilled. The other possibility is $\varphi_1 = 0$ and $\varphi_2 = \pi$, for which an analogous argument can be made.

One can interpret these configurations in the following way. For states at zero energy, neighboring superconducting regions with the same phase can be thought of as being one larger S region, since at $E = 0$ there is neither scattering nor phase propagation within the additional N region. Hence, the two possibilities outlined above correspond to SS-junctions with semi-infinite S regions and phase difference π, and we know from Section 3.2.1 that such a system hosts two Majorana modes localized between the superconductors. Therefore, we expect a similar state to arise in the SSS-case, where the Majorana states should be localized in the cavity between different superconducting phases. Note that one can again apply the Jackiw-Rebbi argument that we have a massive Dirac equation with a mass kink, where the mass kink corresponds to a phase difference of π.

Interestingly, it is not possible to place two mass kinks next to each other and still

obtain bound states at zero energy. Indeed, it is easy to see that for $\varphi_1 = \varphi_2 = \pi$, $D_1 + D_2 \neq 0$ in Eq. (3.87a), if $E = 0$ and as long as $L \neq 0$.

It is straightforward to write down the zero-energy wave functions for these two configurations hosting bound states at $E = 0$. Here, we take a symmetric system with $d_\mathrm{L} = d_\mathrm{R} \equiv d$, since the appearance of bound states does not depend on the widths and the explicit expressions are easier to compare. For $\varphi_1 = \pi$, $\varphi_2 = 0$, we find (with $\chi_0 = (-\mathrm{i}, 0, 1, 0)^\mathrm{T}$ as before and up to a normalization constant)

$$\phi_1^\mathrm{L}(x) = \chi_0 \cdot \begin{cases} \mathrm{e}^{\Delta_0 x} & x < -(d + L/2) \\ \mathrm{e}^{-(d+L/2)\Delta_0} & -(d + L/2) < x < L/2 \\ \mathrm{e}^{-(d+L)\Delta_0 - \Delta_0 x} & -L/2 < x < L/2 \\ \mathrm{e}^{-(d+3L/2)\Delta_0} & L/2 < x < d + L/2 \\ \mathrm{e}^{-\Delta_0 L - \Delta_0 x} & x > d + L/2, \end{cases} \tag{3.88}$$

which clearly has the highest weight in the left normal region, and is exponentially suppressed in the right cavity by a factor of $\exp(-L\Delta_0)$. The superscript indicates where the wave function is localized, while the subscript refers to the $(u_\uparrow, v_\downarrow)^\mathrm{T}$-block as before.

It is worth mentioning that within the central S region, there could in principle be another contribution from the exponentially growing solution to the BdG-equation within the superconductor. However, due to the phase difference of π, it is actually orthogonal to the spinor in the leftmost S region. In other words, at phase difference π between two S regions, the decaying and growing solutions within them become aligned. Together with the boundary condition that the wave function needs to decay away from the outmost SN-/NS-interfaces, this is what gives rise to the localization of the zero-energy states.

Furthermore, notice the strong similarity to the solution in the SS-case, which underlines the picture of the SSS-junction effectively reducing to the SS-junction.

Similarly, the zero-energy solution for $\varphi_1 = 0$, $\varphi_2 = \pi$ reads

$$\phi_1^\mathrm{R}(x) = \chi_0 \cdot \begin{cases} e^{-\Delta_0 L + \Delta_0 x} & x < -(d + L/2) \\ e^{-(d+3L/2)\Delta_0} & -(d + L/2) < x < L/2 \\ e^{-(d+L)\Delta_0 + \Delta_0 x} & -L/2 < x < L/2 \\ e^{-(d+L/2)\Delta_0} & L/2 < x < d + L/2 \\ e^{-\Delta_0 x} & x > d + L/2. \end{cases} \tag{3.89}$$

As expected, the zero-energy state is localized in the right cavity, but is otherwise completely analogous to ϕ_1^L.

As a final step, we can decompose the solutions $\phi_1^{\mathrm{L/R}}$ into two Majorana wave functions $\phi_+^{\mathrm{L/R}} = \phi_1^{\mathrm{L/R}} + \mathcal{C}\phi_1^{\mathrm{L/R}}$ and $\phi_-^{\mathrm{L/R}} = -\mathrm{i}\,\phi_1^{\mathrm{L/R}} + \mathrm{i}\,\mathcal{C}\phi_1^{\mathrm{L/R}}$. However, since the exponentials are real, they can be straightforwardly obtained from the wave functions $\phi_1^{\mathrm{L/R}}$ by replacing $\chi_0 \to \chi_0 + \mathcal{C}\chi_0, -\mathrm{i}\chi_0 + \mathrm{i}\mathcal{C}\chi_0$. Consequently, the spatial dependence of the Majorana states is completely determined by the wave functions $\phi_1^{\mathrm{L/R}}$. Crucially, this also implies that the two Majorana wave functions are always on top of each other and can never be separated.

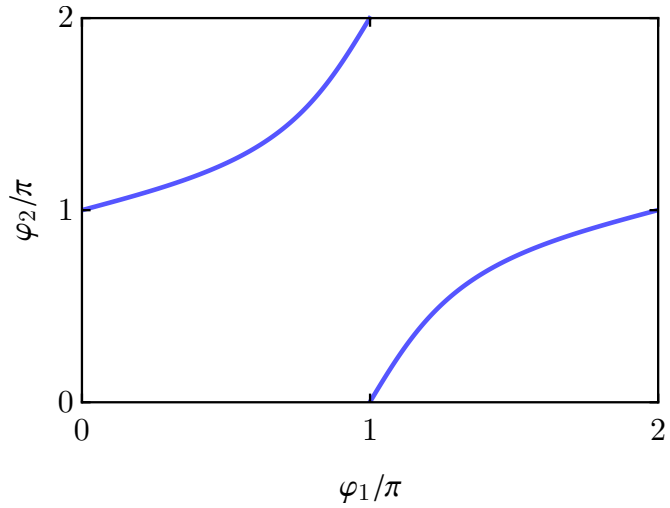

Figure 3.10: Plot of all values for $\varphi_{1,2}$ solving the resonance conditions for the SSS-junction at zero energy, with the same parameters as before.

We conclude this section by noting that the zero-energy bound states for the special cases above are connected by a continuum of configurations φ_1, φ_2, which also host bound states at $E = 0$. Specifically, in Fig. 3.10 we plot all pairs φ_1, φ_2, for which the resonance condition Eq. (3.86) is fulfilled at $E = 0$. Clearly, the cases discussed above correspond to the start and end points of the two branches in Fig. 3.10, respectively (note that we can identify 0 and 2π). Remarkably, by tuning the phases φ_1 and φ_2 along this trajectory, it appears to be possible to tune the wave functions in such a way that they shift their localization from one cavity to another. In Ref. [119] this feature combined with the effect of an additional ferromagnetic barrier (see Section 3.3.2 below) is used to move a single Majorana mode in a controlled fashion. By including a second edge and a quantum point contact connecting the edges, the authors develop a braiding protocol for Majorana modes in a QSHI.

3.3.2 Alternating superconducting and ferromagnetic barriers

3.3.2.1 Bound state condition

In the last part of the chapter, we turn to a system with semi-infinite outer superconductors and a finite F region between the two. Our interest is again focused on the appearance of bound states. Specifically, we expect MBS and ABS from both constituent SF- and FS-cavities to hybridize. Note that in Section 3.2.2 we saw that a single interface of a superconducting and a ferromagnetic region binds only one MBS. Thus, one important question is whether the proximity of two such states affects the localization of the MBS. For completeness, we note that due to the superconductivity-magnetism duality the SFS-system discussed below has similar features as an FSF setup, which is the focus of Ref. [118].

Since there are only two superconductors in this setup, we choose the phase of

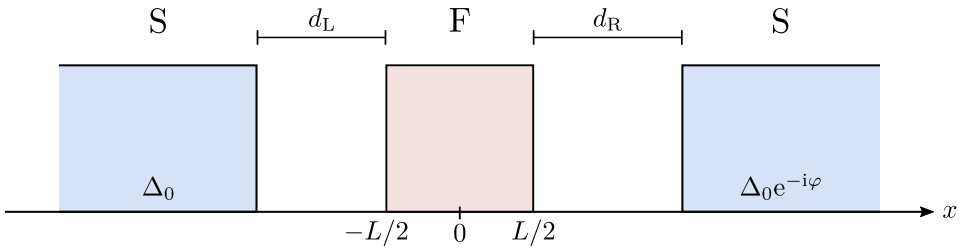

Figure 3.11: Sketch of an SFS-system with semi-infinite outer S barriers. Throughout the section, we choose $d \equiv d_\mathrm{L} = d_\mathrm{R} = 1.5\xi_0$, $L = 0.75\xi_0$, $m_\parallel = 1.5\Delta_0$, $m_z = 0$, $\lambda = 0$.

the left one to be zero and use φ to describe the phase difference. Conversely, since there is only a single F region, due to the duality between S and F regions we are free to choose $\lambda = 0$ for the in-plane angle of the magnetic field. Futhermore, we remark that the z-component of the magnetic field can be absorbed in the phase difference φ by a gauge transformation of the BdG-Hamiltonian of the form [95, 131, 132, 135]

$$\mathcal{H}_\mathrm{BdG} \to U^\dagger \mathcal{H}_\mathrm{BdG} U, \qquad U = \mathrm{e}^{-\mathrm{i}\hat{\tau}_3 \tilde{m}_z(x)/v_\mathrm{F}}, \tag{3.90}$$

where $\tilde{m}_z(x) = \int_{x_\mathrm{F}}^{x} \mathrm{d}x'\, m_z(x')$ and x_F is an arbitrary point within the F region. Hence, $\tilde{m}_z(x)$ is a nonzero constant outside the F region and a linear function within it. The derivative in the BdG-Hamiltonian acting on U thus cancels the m_z term. Furthermore, the pairing term in the BdG-Hamiltonian does not commute with U due to the $\hat{\tau}_3$ matrix. Performing the transformation of the pairing term shows that the gauge transformation shifts the phase difference according to $\phi \to \varphi' = \varphi - 2m_z L$. In the following, we will use φ' as the key parameter to tune the system.

Finally, for simplicity, we put the chemical potential to zero as well. While the effect of the chemical potential outside the F region again only leads to phase shifts, within the F region it actually changes the size of the gap for electrons and holes (*cf.* Section 3.2.2). A few details are lost by choosing $\mu = 0$, but make the development of a physical picture significantly easier. For more details we refer the reader to Ref. [95, 119]. We also restrict ourselves to cases when the magnetic gap is larger than the superconducting gap, *i.e.,* $m_\parallel > \Delta_0$, such that the bound states never have a propagating solution within the F region.

In order to obtain a condition for bound state energies, we follow the same recipe as for the SSS-junction. However, note that the problem is now more complicated since the BdG-Hamiltonian can no longer be decomposed into blocks. The central F region alone, however, still has the block-diagonal structure in Nambu space. Consequently, the scattering problem associated with the F region has the form

$$\begin{pmatrix} b_e^\mathrm{L} \\ b_h^\mathrm{L} \\ b_e^\mathrm{R} \\ b_h^\mathrm{R} \end{pmatrix} = \underbrace{\begin{pmatrix} \hat{R} & \hat{T}' \\ \hat{T} & \hat{R}' \end{pmatrix}}_{S_\mathrm{F}} \begin{pmatrix} a_e^\mathrm{L} \\ a_h^\mathrm{L} \\ a_e^\mathrm{R} \\ a_h^\mathrm{R} \end{pmatrix}, \tag{3.91}$$

where $\hat{R}, \hat{R}', \hat{T}, \hat{T}'$ are 2×2-matrices representing reflection and transmission within the blocks connecting the left and right sides of the F region. Explicitly, in terms of

the scattering coefficients they are given by

$$\hat{R} = \begin{pmatrix} r_{ee}^{(1)} & 0 \\ 0 & r_{hh}^{(2)} \end{pmatrix}, \hat{R}' = \begin{pmatrix} r_{ee}^{(3)} & 0 \\ 0 & r_{hh}^{(4)} \end{pmatrix}, \hat{T} = \begin{pmatrix} t_{ee}^{(1)} & 0 \\ 0 & t_{hh}^{(2)} \end{pmatrix}, \hat{T}' = \begin{pmatrix} t_{ee}^{(3)} & 0 \\ 0 & t_{hh}^{(4)} \end{pmatrix}. \tag{3.92}$$

All coefficients mixing electrons and holes vanish due to the form of the BdG-Hamiltonian of the F region. For completeness, the expressions for the coefficients read

$$\begin{aligned} r_{ee}^{(1)} = r_{hh}^{(2)} = r_{ee}^{(3)} = r_{hh}^{(4)} &= -\mathrm{i}\mathrm{e}^{-\mathrm{i}LE} \frac{\sinh(L\kappa)}{\sinh(\mathrm{i}\rho_0 + L\kappa)} \\ t_{ee}^{(1)} = t_{hh}^{(2)} = t_{ee}^{(3)} = t_{hh}^{(4)} &= \mathrm{i}\mathrm{e}^{-\mathrm{i}LE} \frac{\sin(\rho_0)}{\sinh(\mathrm{i}\rho_0 + L\kappa)}, \end{aligned} \tag{3.93}$$

where $\rho_0 \equiv \rho(\mu = 0) = \rho_h(\mu = 0)$. Note that they are particularly simple because of our choice of parameters. Additional phase factors would arise for finite λ, m_z.

Including the outer SN- and NS-interfaces is a straightforward extension of Section 3.3.1.1, since we need to include both blocks. We find

$$\begin{pmatrix} a_e^{\mathrm{L}} \\ a_h^{\mathrm{L}} \\ a_e^{\mathrm{R}} \\ a_h^{\mathrm{R}} \end{pmatrix} = \underbrace{\begin{pmatrix} \hat{R}_{\mathrm{A}}^{\mathrm{L}} & 0 \\ 0 & \hat{R}_{\mathrm{A}}^{\mathrm{R}} \end{pmatrix}}_{S_{\mathrm{A}}} \begin{pmatrix} b_e^{\mathrm{L}} \\ b_h^{\mathrm{L}} \\ b_e^{\mathrm{R}} \\ b_h^{\mathrm{R}} \end{pmatrix}, \tag{3.94}$$

where $\hat{R}_{\mathrm{A}}^{\mathrm{L/R}}$ encode the perfect Andreev reflection of modes at the left SN- and the right NS-interface. They explicitly read

$$\begin{aligned} \hat{R}_{\mathrm{A}}^{\mathrm{L}} &= \begin{pmatrix} 0 & r_{eh}^{\mathrm{L}} \\ r_{he}^{\mathrm{L}} & \end{pmatrix} = \begin{pmatrix} 0 & \mathrm{e}^{-\mathrm{i}\eta}\mathrm{e}^{\mathrm{i}E(L+2d_{\mathrm{L}})} \\ \mathrm{e}^{-\mathrm{i}\eta}\mathrm{e}^{\mathrm{i}E(L+2d_{\mathrm{L}})} & 0 \end{pmatrix} \\ \hat{R}_{\mathrm{A}}^{\mathrm{R}} &= \begin{pmatrix} 0 & r_{eh}^{\mathrm{R}} \\ r_{he}^{\mathrm{R}} & \end{pmatrix} = \begin{pmatrix} 0 & \mathrm{e}^{-\mathrm{i}\eta+\mathrm{i}\varphi}\mathrm{e}^{\mathrm{i}E(L+2d_{\mathrm{R}})} \\ \mathrm{e}^{-\mathrm{i}\eta-\mathrm{i}\varphi}\mathrm{e}^{\mathrm{i}E(L+2d_{\mathrm{R}})} & 0 \end{pmatrix}. \end{aligned} \tag{3.95}$$

The condition for bound states can then be readily obtained by combining Eqs. (3.91) and (3.94). In terms of the scattering matrices, we arrive at

$$\det\left(S_{\mathrm{F}} S_{\mathrm{A}} - \mathbb{1}\right) = 0. \tag{3.96}$$

Upon inserting the scattering coefficients from Eqs. (3.91) and (3.92) and Eqs. (3.94) and (3.95), we can write the resonance condition in the form

$$1 - \Sigma = 0, \tag{3.97}$$

where

$$\Sigma = \Sigma_1^{\mathrm{L}} + \Sigma_1^{\mathrm{R}} - \Sigma_1^{\mathrm{L}}\Sigma_1^{\mathrm{R}} + \Sigma_2^{\uparrow} + \Sigma_2^{\downarrow} - \Sigma_2^{\uparrow}\Sigma_2^{\downarrow} + \Sigma_3^{e} + \Sigma_3^{h}. \tag{3.98}$$

Each of the terms in Eq. (3.98) corresponds to a specific closed loop with the SFS-junction, see also Fig. 3.12. They are given by

$$\begin{aligned} \Sigma_1^{\mathrm{L}} &= r_{ee}^{(1)} r_{he}^{\mathrm{L}} r_{hh}^{(2)} r_{eh}^{\mathrm{L}}, & \Sigma_1^{\mathrm{R}} &= r_{ee}^{(3)} r_{he}^{\mathrm{R}} r_{hh}^{(4)} r_{eh}^{\mathrm{R}}, \\ \Sigma_2^{\uparrow} &= t_{ee}^{(1)} r_{he}^{\mathrm{R}} t_{hh}^{(4)} r_{eh}^{\mathrm{L}}, & \Sigma_2^{\downarrow} &= t_{hh}^{(2)} r_{eh}^{\mathrm{R}} t_{ee}^{(3)} r_{he}^{\mathrm{L}}, \\ \Sigma_3^{e} &= t_{ee}^{(1)} r_{he}^{\mathrm{R}} r_{hh}^{(4)} r_{eh}^{\mathrm{R}} t_{ee}^{(3)} r_{he}^{\mathrm{L}} r_{hh}^{(2)} r_{eh}^{\mathrm{L}}, & \Sigma_3^{h} &= t_{hh}^{(2)} r_{he}^{\mathrm{R}} r_{ee}^{(3)} r_{he}^{\mathrm{R}} t_{hh}^{(2)} r_{eh}^{\mathrm{L}} r_{ee}^{(1)} r_{he}^{\mathrm{L}}. \end{aligned} \tag{3.99}$$

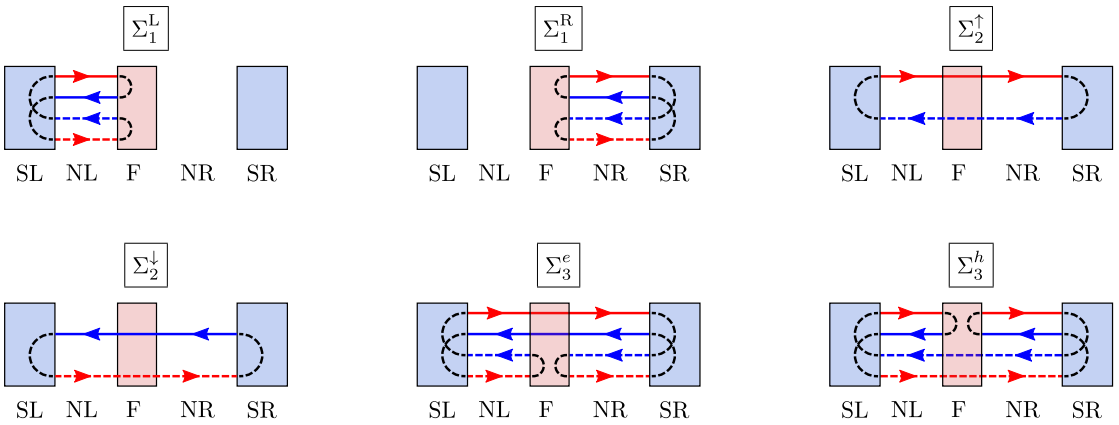

Figure 3.12: Sketch of the bound state interpretation of the self-energies. As before, red (blue) lines correspond to spin ↑ (spin ↓) modes, while solid lines refer to eelctrons (holes). Adapted from Ref. [136], copyright (2020) by The American Physical Society.

In conclusion, while it was fairly straightforward to derive a condition for bound states with the methods developed in this chapter, the connection to the constituent closed loops is rather complicated and of not much use analytically. However, we can use Eq. (3.96) or, alternatively, Eq. (3.98) to numerically obtain the spectrum of the system.

3.3.2.2 Spectrum and Majorana bound states

For the remainder of the section, we focus on a symmetric system with equal widths of the intermediate normal regions for simplicity, *i.e.*, $d_{\mathrm{L}} = d_{\mathrm{R}} \equiv d$. With the resonance condition Eq. (3.96) at hand, we plot the resulting bound state energies as a function of the phase difference φ in Fig. 3.13. Since the SFS-structure can be thought of as an SS-junction with inserted F-region, it is particularly interesting to compare with Fig. 3.4. Notably, the presence of a time-reversal breaking magnetic field lifts the degeneracies at $\varphi = 0, 2\pi$ and thus disconnects the bound states. However, the crossings at $\varphi = \pi$ are preserved and hence are the signatures of Majoranas relying on their 4π-periodic levels. Furthermore, we remark that the degeneracy of ABS scan be lifted by, *e.g.*, asymmetry in the setup [95, 118, 119].

Knowing that there is a zero-energy bound state at $\varphi = \pi$, it is interesting to find out where it is localized, and especially where the MBS wave functions are localized. Straightforwardly, we can make the ansatz for the wave function of the form

$$\phi(x) = \begin{cases} a_1 \mathrm{e}^{\Delta_0 x}\chi_{e-} + a_2 \mathrm{e}^{\Delta_0 x}\chi_{h-} & x < -(d + L/2) \\ b_1\phi_{e+} + b_2\phi_{e-} + b_3\phi_{h-} + b_4\phi_{h+} & -(d + L/2) < x < L/2 \\ c_1 \mathrm{e}^{-m_\parallel x}\zeta_{e+} + c_2 \mathrm{e}^{m_\parallel x}\zeta_{e-} + c_3 \mathrm{e}^{m_\parallel x}\zeta_{h-} + c_4 \mathrm{e}^{-m_\parallel x}\zeta_{h+} & -L/2 < x < L/2 \\ d_1\phi_{e+} + d_2\phi_{e-} + d_3\phi_{h-} + d_4\phi_{h+} & L/2 < x < d + L/2 \\ e_1 \mathrm{e}^{-\Delta_0 x}\chi_{e+} + e_2 \mathrm{e}^{-\Delta_0 x}\chi_{h+} & x > d + L/2, \end{cases} \tag{3.100}$$

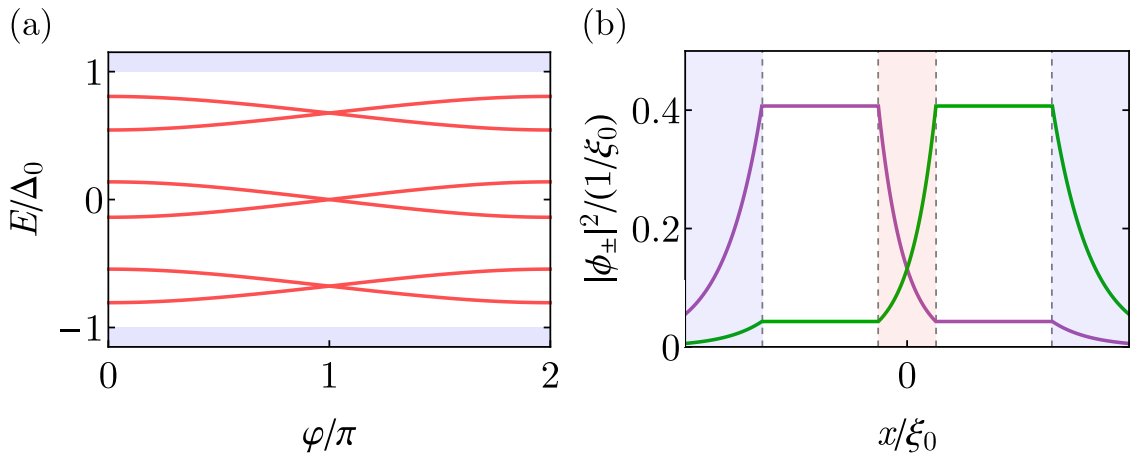

Figure 3.13: Plot of the bound state spectrum [panel (a)] and zero-energy wave function [panel (b)] of the SFS-junction, with parameters as defined in Fig. 3.11. In (a), the shaded blue area indicates the continuum of states above the gap. In (b), the shaded red (blue) regions refer to the F (S) regions in the system to visualize the localization of the bound states.

where we of course need the zero-energy expressions for the eigenstates $\phi_{\alpha\pm}, \chi_{\alpha\pm}, \zeta_{\alpha\pm}$.

Matching the wave function at the interfaces, we can determine the coefficients a_j, b_j, c_j, d_j. In Fig. 3.13, we plot the norm of the normalized resulting wave function, as well as the normalized Majorana wave functions $\phi_+ = \phi + \mathcal{C}\phi$ and $\phi_- = -\mathrm{i}\phi + \mathrm{i}\mathcal{C}\phi$. We find that the ferromagnetic region between two semi-infinite S regions is enough to split the two MBS and localize them on opposite sides of the F region.

This can also be understood in terms of the Jackiw-Rebbi form of the BdG-Hamiltonian, which we derived in Eq. (3.65) for the SF-junction. For a phase difference of $\varphi = \pi$, the pairing potential within the left S region is still $\Delta_0\hat{\tau}_1\hat{\sigma}_0$, while within the right S region it is $-\Delta_0\hat{\tau}_1\hat{\sigma}_0$. In terms of the masses $M_1(x) = m(x) + \Delta(x)$, $M_2(x) = m(x) - \Delta(x)$, we see that M_1 now shows a sign change between the F and the right S region, while M_2 has a mass kink between the left S and the F region. Hence, the system can be understood as two Jackiw-Rebbi models with mass kinks located in the gapless normal regions within the two cavities. This is consistent with the localization of the two Majorana wave functions shown in Fig. 3.13.

4

Unconventional superconductivity in helical edge states

Contents

In Chapter 2, we noted on several occasions that the symmetry properties of the proximity induced superconducting order parameter are intimately connected to the appearance of topological phases. For the model of the Kitaev chain, for instance, we assumed a spinless p-wave superconductor, whose order parameter transforms trivially under spin rotation, since it has no spin structure, and non-trivially under orbital rotations. One major obstacle for the realization of topological phases is precisely the need to effectively engineer such a pairing phase in spinful systems, especially in light of the fact that most superconductors available for practical purposes show s-wave singlet pairing. In this section, we turn this point around and start with the helical edge and proximity induced s-wave singlet pairing, in which we now know how to realize Majorana bound states. From there, we take a closer look at how the spin-momentum locking and proximity to magnetism affects superconducting correlations in the system.

As a disclaimer, for most of this chapter we are ignoring any details related to the proximity effect, which is to say that we are not interested in self-consistency equations and bulk properties. The exception is Section 4.1.1. Furthermore, we do not consider any effect superconducting correlations might have on the parent superconductor, a phenomenon called *inverse proximity effect*.

4.1 Correlation functions & symmetry classification

4.1.1 Generalized BCS-theory

In order to relate this chapter to the well-known framework of the standard BCS-theory of superconductivity and introduce important notation and concepts, we first give a generalized mean-field formulation of it to go beyond the standard s-wave singlet case. We follow Ref. [137] and point towards Refs. [138–141] for more and complementary information.

The first step to take is simply to allow a more general microscopic interaction in the Hamiltonian, writing the latter as (we use the letter $s =\uparrow,\downarrow$ to denote spin, and $\boldsymbol{k}$ for momenta in 3D)

$$H = \sum_{\boldsymbol{k},s} \xi_{\boldsymbol{k}} \hat{c}^\dagger_{\boldsymbol{k}s} \hat{c}_{\boldsymbol{k}s} + \frac{1}{2} \sum_{\boldsymbol{k},\boldsymbol{k}'} \sum_{s_1,s_2,s_3,s_4} V_{\boldsymbol{k},\boldsymbol{k}';s_1s_2s_3s_4}\, \hat{c}^\dagger_{\boldsymbol{k}s_1} \hat{c}^\dagger_{-\boldsymbol{k}s_2} \hat{c}_{-\boldsymbol{k}'s_3} \hat{c}_{\boldsymbol{k}'s_4}. \tag{4.1}$$

Note that the scattering only involves pairs of electrons, whose total momentum vanishes. The matrix elements are given by

$$V_{\boldsymbol{k},\boldsymbol{k}';s_1s_2s_3s_4} = \left\langle -\boldsymbol{k}, s_1; \boldsymbol{k}, s_2 \middle| \hat{V} \middle| -\boldsymbol{k}', s_3; \boldsymbol{k}', s_4 \right\rangle \tag{4.2}$$

and must fulfill

$$V_{\boldsymbol{k},\boldsymbol{k}';s_1s_2s_3s_4} = -V_{-\boldsymbol{k},\boldsymbol{k}';s_2s_1s_3s_4} = -V_{\boldsymbol{k},-\boldsymbol{k}';s_1s_2s_4s_3} = V_{-\boldsymbol{k},-\boldsymbol{k}';s_2s_1s_4s_3} \tag{4.3}$$

because of the fermionic anticommutation relations of the creation/annihilation operators $\hat{c}^\dagger_{\boldsymbol{k}s}, \hat{c}_{\boldsymbol{k}'s'}$.

The mean-field Hamiltonian is obtained using

$$b_{\boldsymbol{k},ss'} = \langle \hat{c}_{-\boldsymbol{k}s} \hat{c}_{\boldsymbol{k}s'} \rangle, \tag{4.4}$$

which differs from the standard BCS choice in that it has a spin structure, instead of simply pairing states with opposite spins yielding a singlet state. The quantity $b_{\boldsymbol{k},ss'}$ can be interpreted as the Cooper pair wave function. Assuming small fluctuations around the mean-field defined in Eq. (4.4), the Hamiltonian becomes

$$H_{\mathrm{MF}} = \sum_{\boldsymbol{k},s} \xi_{\boldsymbol{k}} \hat{c}^\dagger_{\boldsymbol{k}s} \hat{c}_{\boldsymbol{k}s} + \frac{1}{2} \sum_{\boldsymbol{k}} \sum_{s_1,s_2} \left[\Delta_{\boldsymbol{k},s_1s_2}\, \hat{c}^\dagger_{\boldsymbol{k}s_1} \hat{c}^\dagger_{-\boldsymbol{k}s_2} + \Delta^*_{\boldsymbol{k},s_1s_2}\, \hat{c}_{\boldsymbol{k}s_1} \hat{c}_{-\boldsymbol{k}s_2} \right] + K. \tag{4.5}$$

The constant term K quadratic in $b_{\boldsymbol{k},s_1s_2}$ is disregarded in the following. The generalized gap $\Delta_{\boldsymbol{k},ss'}$ is then determined by the self-consistent equations

$$\begin{aligned} \Delta_{\boldsymbol{k},ss'} &= -\sum_{\boldsymbol{k}'} \sum_{s_3,s_4} V_{\boldsymbol{k},\boldsymbol{k}';ss's_3s_4}\, b_{\boldsymbol{k},s_3s_4}, \\ \Delta^*_{\boldsymbol{k},ss'} &= -\sum_{\boldsymbol{k}'} \sum_{s_3,s_4} V_{\boldsymbol{k},\boldsymbol{k}';ss's_1s_2}\, b^*_{\boldsymbol{k},s_2s_1}. \end{aligned} \tag{4.6}$$

We see that the more general spin structure of the Cooper pair wave function in Eq. (4.4) translates into a gap function with matrix structure in spin space, which can be written as

$$\hat{\Delta}_{\boldsymbol{k}} = \begin{pmatrix} \Delta_{\boldsymbol{k},\uparrow\uparrow} & \Delta_{\boldsymbol{k},\uparrow\downarrow} \\ \Delta_{\boldsymbol{k},\downarrow\uparrow} & \Delta_{\boldsymbol{k},\downarrow\downarrow} \end{pmatrix}. \tag{4.7}$$

The anticommutation relations of the creation/annihilation operators also influence the properties of the gap function, much like they lead to the properties of the interaction matrix elements in Eq. (4.3). Separating the momentum- and spin-dependent parts of the wave function, *i.e.*, $b_{\boldsymbol{k},s_1s_2} = \phi(\boldsymbol{k})\xi_{s_1s_2}$, we note that we can distinguish the cases of even parity and spin singlet, for which

$$\phi(\boldsymbol{k}) = \phi(-\boldsymbol{k}) \Leftrightarrow \chi_{ss'} = \frac{1}{\sqrt{2}} \left(|\uparrow\downarrow\rangle - |\downarrow\uparrow\rangle \right), \tag{4.8}$$

and odd parity and spin triplet, reading

$$\phi(\boldsymbol{k}) = -\phi(-\boldsymbol{k}) \Leftrightarrow \chi_{ss'} = \begin{cases} |\uparrow\uparrow\rangle \\ \frac{1}{\sqrt{2}} \left(|\uparrow\downarrow\rangle + |\downarrow\uparrow\rangle \right) \\ |\downarrow\downarrow\rangle. \end{cases} \tag{4.9}$$

Note that the former case in Eq. (4.8) corresponds to conventional BCS-theory, whereas the latter case in Eq. (4.9) only arises for the more general interaction.

In the even parity, singlet case, the gap function fulfills

$$\Delta^s_{\boldsymbol{k},s_1s_2} = -\Delta^s_{\boldsymbol{k},s_2s_1} = \Delta^s_{-\boldsymbol{k},s_1s_2} = -\Delta^s_{-\boldsymbol{k},s_2s_1}, \tag{4.10}$$

while the odd parity, triplet gap function obeys

$$\Delta^t_{\boldsymbol{k},s_1s_2} = \Delta^t_{\boldsymbol{k},s_2s_1} = -\Delta^t_{-\boldsymbol{k},s_1s_2} = -\Delta^t_{-\boldsymbol{k},s_2s_1}. \tag{4.11}$$

In conclusion, the singlet gap function $\Delta^s_{\boldsymbol{k},s_1s_2}$ acquires a minus sign if the spin indices are exchanged, but is insensitive to $\boldsymbol{k} \to -\boldsymbol{k}$, while the opposite is true for the triplet gap function $\Delta^t_{\boldsymbol{k},s_1s_2}$. Importantly, note that both gap functions are odd under the simultaneous $s_1 \leftrightarrow s_2$, $\boldsymbol{k} \to -\boldsymbol{k}$, which can be summarized as

$$\hat{\Delta}^{s/t}_{\boldsymbol{k}} = -\left(\hat{\Delta}^{s/t}_{-\boldsymbol{k}} \right)^{\mathrm{T}}. \tag{4.12}$$

It is now useful to parametrize these two cases. In the conventional BCS case of even parity, singlet pairing, this can be achieved by a single scalar function $\psi(\boldsymbol{k})$, *i.e.,*

$$\hat{\Delta}^s_{\boldsymbol{k}} = \begin{pmatrix} \Delta^s_{\boldsymbol{k},\uparrow\uparrow} & \Delta^s_{\boldsymbol{k},\uparrow\downarrow} \\ \Delta^s_{\boldsymbol{k},\downarrow\uparrow} & \Delta^s_{\boldsymbol{k},\downarrow\downarrow} \end{pmatrix} = \mathrm{i}\hat{\sigma}_2\psi(\boldsymbol{k}), \tag{4.13}$$

where $\hat{\sigma}_2$ is the Pauli matrix acting in spin space. Since there are three possible spin configurations in the triplet case, we need three functions of the momentum $d_i(\boldsymbol{k})$ with $d_i(\boldsymbol{k}) = -d_i(-\boldsymbol{k})$ and $i = 1, 2, 3$. The triplet gap function then reads

$$\begin{aligned} \hat{\Delta}^t_{\boldsymbol{k}} &= \begin{pmatrix} \Delta^t_{\boldsymbol{k},\uparrow\uparrow} & \Delta^t_{\boldsymbol{k},\uparrow\downarrow} \\ \Delta^t_{\boldsymbol{k},\downarrow\uparrow} & \Delta^t_{\boldsymbol{k},\downarrow\downarrow} \end{pmatrix} \\ &= \begin{pmatrix} -d_1(\boldsymbol{k}) + \mathrm{i}d_2(\boldsymbol{k}) & d_3(\boldsymbol{k}) \\ d_3(\boldsymbol{k}) & d_1(\boldsymbol{k}) + \mathrm{i}d_2(\boldsymbol{k}) \end{pmatrix} = \mathrm{i}\left(\boldsymbol{d}(\boldsymbol{k}) \cdot \hat{\boldsymbol{\sigma}}\right) \hat{\sigma}_2. \end{aligned} \tag{4.14}$$

Note that the notation in terms of the Pauli matrix $\hat{\sigma}_2$ is a common choice, so we shall adapt it as well. Furthermore, it can also be helpful to think of $\hat{\Delta}^{s/t}$ as a vector in the Hilbert space of the two spins with basis $\{|\uparrow\uparrow\rangle, |\uparrow\downarrow\rangle, |\downarrow\uparrow\rangle, |\downarrow\downarrow\rangle\}$.

In conclusion, a straightforward generalization of standard BCS-theory shows nicely, how the spin structure and the orbital character of the pairing are interrelated. In particular, we recovered the widely used equivalency of spin singlet and even parity, as well as spin triplet and odd parity.

As a last remark, we note that one can calculate the spin expectation value of Cooper pairs according to [142]

$$\langle \hat{\boldsymbol{S}} \rangle = \mathrm{Tr}\left[\hat{\Delta}^{s/t}_{\boldsymbol{k}} \left(\hat{\Delta}^{s/t}_{\boldsymbol{k}}\right)^\dagger \hat{\boldsymbol{S}}\right], \tag{4.15}$$

where $\hat{\boldsymbol{S}} = \hat{\boldsymbol{\sigma}} \otimes \hat{\sigma}_0 + \hat{\sigma}_0 \otimes \hat{\boldsymbol{\sigma}}$. Using Eqs. (4.13) and (4.14), one can show that

$$\hat{\Delta}^s_{\boldsymbol{k}} \left(\hat{\Delta}^s_{\boldsymbol{k}}\right)^\dagger = |\psi(\boldsymbol{k})|^2 \, \hat{\sigma}_0 \tag{4.16}$$

and

$$\hat{\Delta}^t_{\boldsymbol{k}} \left(\hat{\Delta}^t_{\boldsymbol{k}}\right)^\dagger = |\boldsymbol{d}(\boldsymbol{k})|^2 \, \hat{\sigma}_0 + \mathrm{i}\left(\boldsymbol{d}(\boldsymbol{k}) \times \boldsymbol{d}^*(\boldsymbol{k})\right) \cdot \hat{\boldsymbol{\sigma}}. \tag{4.17}$$

Therefore, since the Pauli matrices are traceless, we immediately see that singlet pairing does not lead to any spin expectation value. In the triplet case, if the vector $\boldsymbol{d}$ is real the second term in Eq. (4.17) vanishes, and the spin expectation value is zero as well. However, if $\boldsymbol{d}$ is complex, the quantity

$$\boldsymbol{q}(\boldsymbol{k}) = \mathrm{i}\, \boldsymbol{d}(\boldsymbol{k}) \times \boldsymbol{d}^*(\boldsymbol{k}) \tag{4.18}$$

can be finite. These pairing states are called *non-unitary* and, remarkably, lead to a finite spin expectation value. In fact, the spin polarization is proportional to $\boldsymbol{q}(\boldsymbol{k})$.

4.1.2 Classification of correlation functions

The goal of this chapter is to discuss the effects of an s-wave order parameter on the (anomalous) correlation functions at the helical edge. While some of the concepts from Section 4.1.1 are still going to be of use, in this section we will adapt them in

order to be able to move on to the helical edge. Good references presenting these methods include Refs. [143–145] and references therein.

The key mathematical object to consider is the Nambu-Gor'kov Green function [146]

$$\begin{aligned}\mathcal{G}_{\sigma\sigma'}(\boldsymbol{r}_1,\boldsymbol{r}_2;t_1,t_2) &= -\Big\langle \mathcal{T}\Psi_\sigma(\boldsymbol{r}_1,t_1)\Psi^\dagger_{\sigma'}(\boldsymbol{r}_2,t_2)\Big\rangle \\ &= -\begin{pmatrix} \langle \mathcal{T}\psi_\sigma(\boldsymbol{r}_1,t_1)\psi^\dagger_{\sigma'}(\boldsymbol{r}_2,t_2)\rangle & \langle \mathcal{T}\psi_\sigma(\boldsymbol{r}_1,t_1)\psi_{\sigma'}(\boldsymbol{r}_2,t_2)\rangle \\ \langle \mathcal{T}\psi^\dagger_\sigma(\boldsymbol{r}_1,t_1)\psi^\dagger_{\sigma'}(\boldsymbol{r}_2,t_2)\rangle & \langle \mathcal{T}\psi^\dagger_\sigma(\boldsymbol{r}_1,t_1)\psi_{\sigma'}(\boldsymbol{r}_2,t_2)\rangle \end{pmatrix}\end{aligned} \tag{4.19}$$

where the Nambu spinor is defined as $\Psi_{\sigma'}(\boldsymbol{r}_2,t_2) = (\psi_{\sigma'}(\boldsymbol{r}_2,t_2),\psi^\dagger_{\sigma'}(\boldsymbol{r}_2,t_2))^{\mathrm{T}}$. The field operator $\psi_\sigma(\boldsymbol{r}_1,t_1)$ [$\psi^\dagger_\sigma(\boldsymbol{r}_1,t_1)$] annihilates [creates] a particle with spin σ at position $\boldsymbol{r}_1$ and time t_1. In principle, there could be more indices, *e.g.,* representing a band.

While the diagonal elements of the Nambu-Gor'kov Green function describe regular electron and hole propagation, the off-diagonal elements correspond to the creation/annihilation of Cooper pairs when two electrons are added to or removed from the condensate. Note the close relation between the off-diagonal terms and the Cooper pair wave function introduced in Eq. (4.4) in the previous section, which is a momentum space, equal-time version of the Nambu-Gor'kov Green function. This, in turn, also connects the self-consistency equation of the gap function to the Nambu-Gor'kov Green function.

In the following, we focus the discussion on the element

$$f_{\sigma\sigma'}(\boldsymbol{r}_1,\boldsymbol{r}_2;t_1,t_2) = \langle \mathcal{T}\psi_\sigma(\boldsymbol{r}_1,t_1)\psi_{\sigma'}(\boldsymbol{r}_2,t_2)\rangle. \tag{4.20}$$

In order to analyze the symmetry content of the function $f_{\sigma\sigma'}(\boldsymbol{r}_1,\boldsymbol{r}_2;t_1,t_2)$, we first need to restrict ourselves to equal times $t_2 = t_1$. Only then the field operators have a well-defined anticommutation relation. This leads to the crucial result, that the anomalous Green function needs to fulfill

$$f_{\sigma\sigma'}(\boldsymbol{r}_1,\boldsymbol{r}_2;t_1,t_1) = -f_{\sigma'\sigma}(\boldsymbol{r}_2,\boldsymbol{r}_1;t_1,t_1). \tag{4.21}$$

In other words, upon exchanging the spin indices σ,σ' and electron positions $\boldsymbol{r}_1,\boldsymbol{r}_2$, the anomalous Green function needs to acquire a sign. Evidently, this is similar to the Cooper pair wave function discussed in the previous section. Note that the mere permutation of indices is not equivalent to the action of time-reversal or parity operator, both of which involve complex conjugation. This would actually amount to a conversion of $f_{\sigma\sigma'}(\boldsymbol{r}_1,\boldsymbol{r}_2;t_1,t_2)$ into the correlator $\langle \mathcal{T}\psi^\dagger_\sigma(\boldsymbol{r}_1,t_1)\psi^\dagger_{\sigma'}(\boldsymbol{r}_2,t_2)\rangle$.

Following Eq. (4.21), one possibility to fulfill the constraint is a conventional BCS superconductor, which obeys

$$f_{\sigma\sigma'}(\boldsymbol{r}_1,\boldsymbol{r}_2;t_1,t_1) = f_{\sigma\sigma'}(\boldsymbol{r}_2,\boldsymbol{r}_1;t_1,t_1), \qquad f_{\sigma\sigma'}(\boldsymbol{r}_1,\boldsymbol{r}_2;t_1,t_1) = -f_{\sigma'\sigma}(\boldsymbol{r}_1,\boldsymbol{r}_2;t_1,t_1), \tag{4.22}$$

i.e., it is odd under the exchange of spin indices (*i.e.,* singlet), but even if the coordinates are exchanged. Importantly, Eq. (4.21) is also satisfied if

$$f_{\sigma\sigma'}(\boldsymbol{r}_1,\boldsymbol{r}_2;t_1,t_1) = -f_{\sigma\sigma'}(\boldsymbol{r}_2,\boldsymbol{r}_1;t_1,t_1), \qquad f_{\sigma\sigma'}(\boldsymbol{r}_1,\boldsymbol{r}_2;t_1,t_1) = f_{\sigma'\sigma}(\boldsymbol{r}_1,\boldsymbol{r}_2;t_1,t_1), \tag{4.23}$$

corresponding to a triplet correlation function even under the exchange of spin indices, but odd under the permutation of coordinates.

Henceforth, we shall refer to BCS superconductors in general, and these symmetry relations in particular, as *conventional*. All other instances are coined *unconventional*. The precise connection to the previous section is made by introducing center of mass and relative coordinates, followed by taking the Fourier transform over the relative coordinate.

We take a different direction by introducing time coordinates t, T according to

$$t = t_1 - t_2, \quad T = (t_1 + t_2)/2, \tag{4.24}$$

i.e., t is the time difference between both time arguments and T represents a global time coordinate. Since we discuss static problems without any explicit time dependence, the correlation functions should not depend on T. We will thus drop this coordinate for simplicity.

We therefore replace the correlation function in terms of t and replace

$$f_{\sigma\sigma'}(\boldsymbol{r}_1, \boldsymbol{r}_2; t_1, t_2) \to f_{\sigma\sigma'}(\boldsymbol{r}_1, \boldsymbol{r}_2; t). \tag{4.25}$$

Then, we can rephrase Eq. (4.21) in terms of the relative time in the form

$$f_{\sigma\sigma'}(\boldsymbol{r}_1, \boldsymbol{r}_2; 0) = -f_{\sigma'\sigma}(\boldsymbol{r}_2, \boldsymbol{r}_1; 0). \tag{4.26}$$

This looks like a trivial reformulation of the same property. However, writing the correlation function in terms of the Fourier transform $f_{\sigma\sigma'}(\boldsymbol{r}_1, \boldsymbol{r}_2; E)$ depending on the energy E yields

$$f_{\sigma\sigma'}(\boldsymbol{r}_1, \boldsymbol{r}_2; t) = \int_{-\infty}^{\infty} \mathrm{d}E\, \mathrm{e}^{\mathrm{i}Et} f_{\sigma\sigma'}(\boldsymbol{r}_1, \boldsymbol{r}_2; E). \tag{4.27}$$

Inserting Eq. (4.27) into Eq. (4.26) thus leads to

$$\int_{-\infty}^{\infty} \mathrm{d}E\, f_{\sigma\sigma'}(\boldsymbol{r}_1, \boldsymbol{r}_2; E) = -\int_{-\infty}^{\infty} \mathrm{d}E\, f_{\sigma'\sigma}(\boldsymbol{r}_2, \boldsymbol{r}_1; E). \tag{4.28}$$

This constraint is fulfilled if the correlation function is odd under the exchange of positions and spins as before, *i.e.,* if

$$f_{\sigma\sigma'}(\boldsymbol{r}_1, \boldsymbol{r}_2; E) = -f_{\sigma'\sigma}(\boldsymbol{r}_2, \boldsymbol{r}_1; E). \tag{4.29}$$

Arriving here is of course not surprising, and basically corresponds to the line of argumentation from before. Remarkably, however, there is a second way of satisfying Eq. (4.28), which is the relation

$$f_{\sigma\sigma'}(\boldsymbol{r}_1, \boldsymbol{r}_2; E) = -f_{\sigma'\sigma}(\boldsymbol{r}_2, \boldsymbol{r}_1; -E). \tag{4.30}$$

Eq. (4.30) suggests that the equal time constraint Eq. (4.26) can also be fulfilled if the Fourier transformed correlation function is odd *in energy* and satisfies

$$f_{\sigma\sigma'}(\boldsymbol{r}_1, \boldsymbol{r}_2; E) = -f_{\sigma\sigma'}(\boldsymbol{r}_1, \boldsymbol{r}_2; -E), \tag{4.31}$$

$E \to -E$	$\sigma \leftrightarrow \sigma'$	$\boldsymbol{r}_1 \leftrightarrow \boldsymbol{r}_2$	class
$+$	$-$	$+$	ESE
$-$	$-$	$-$	OSO
$+$	$+$	$-$	ETO
$-$	$+$	$+$	OTE

Table 4.1: Classification scheme for anomalous correlation functions. They can be either even (+) or odd (−) under the exchange of spins $\sigma \leftrightarrow \sigma'$ or positions $\boldsymbol{r}_1 \leftrightarrow \boldsymbol{r}_2$, or upon taking $E \to -E$. In the class nomenclature, the first letter refers to even- (E) or oddness (O) under $E \to -E$ in the frequency domain, the second letter labels singlet (S, odd under $\sigma \leftrightarrow \sigma'$) and triplet (T, even under $\sigma \leftrightarrow \sigma'$), and the third letter labels even- (E) or oddness (O) under $\boldsymbol{r}_1 \leftrightarrow \boldsymbol{r}_2$.

i.e., the sign arises due to the sign change of E[1]. This type of pairing is called *odd-frequency superconductivity* and has first been proposed by Berezinskii in the context of liquid ^{3}He [147]. For more recent reviews on this subject, see Refs. [145,148,149].

It is worth pointing out that due to Eq. (4.27), the oddness of $f_{\sigma\sigma'}(\boldsymbol{r}_1, \boldsymbol{r}_2; E)$ implies that the time correlation function is odd in its time argument, *i.e.,* it fulfills

$$f_{\sigma\sigma'}(\boldsymbol{r}_1, \boldsymbol{r}_2; t) = -f_{\sigma\sigma'}(\boldsymbol{r}_1, \boldsymbol{r}_2; -t). \tag{4.32}$$

In terms of the original coordinates t_1, t_2 we see that odd-frequency superconductivity amounts to a correlation function which is odd under the exchange of its time arguments. Note that this necessarily implies that the equal-time correlation function vanishes, which trivially also fulfills Eq. (4.21).

As a last step before we can move on to the helical edge, we note that so far we discussed time-ordered correlation functions, which might not be the most convenient choice. However, we note that one can go through similar arguments for Matsubara Green functions. This leads to the equivalent requirement on the anomalous part of the Matsubara Green function $f^{\mathrm{M}}_{\sigma\sigma'}(\boldsymbol{r}_1, \boldsymbol{r}_2; \mathrm{i}\omega_n)$ of the form

$$f^{\mathrm{M}}_{\sigma\sigma'}(\boldsymbol{r}_1, \boldsymbol{r}_2; \mathrm{i}\omega_n) = -f^{\mathrm{M}}_{\sigma'\sigma}(\boldsymbol{r}_2, \boldsymbol{r}_1; -\mathrm{i}\omega_n), \tag{4.33}$$

where $\omega_n = (2n+1)\pi/\beta$ are the Matsubara frequencies.

This intermediate step is of importance to us, since the real-time retarded and advanced Green functions $f^{R/A}_{\sigma\sigma'}(\boldsymbol{r}_1, \boldsymbol{r}_2; E)$ are obtained via analytical continuation according to

$$\lim_{\mathrm{i}\omega_n \to E \pm \mathrm{i}\delta} f^{\mathrm{M}}_{\sigma\sigma'}(\boldsymbol{r}_1, \boldsymbol{r}_2; \mathrm{i}\omega_n) = f^{R/A}_{\sigma\sigma'}(\boldsymbol{r}_1, \boldsymbol{r}_2; E), \tag{4.34}$$

where $\delta \to 0$ is understood. By using the definition of retarded and advanced Green functions in Eq. (4.34) and the property of the Matsubara Green function in Eq. (4.33), it is straightforward to show that retarded and advanced Green functions fulfill

$$f^{\mathrm{R}}_{\sigma\sigma'}(\boldsymbol{r}_1, \boldsymbol{r}_2; E) = -f^{\mathrm{A}}_{\sigma'\sigma}(\boldsymbol{r}_2, \boldsymbol{r}_1; -E). \tag{4.35}$$

For retarded and advanced Green functions, the oddness under exchanging spins, coordinates and times (or taking $E \to -E$) thus transforms them into one-another.

[1]Note that $f_{\sigma\sigma'}(\boldsymbol{r}_1, \boldsymbol{r}_2; E)$ then must be either even under the exchanges of spins and positions, or odd under both the exchange of spins and positions.

Note that even-frequency superconductivity implies

$$f^{\mathrm{R}}_{\sigma\sigma'}(\boldsymbol{r}_1,\boldsymbol{r}_2;E) = f^{\mathrm{A}}_{\sigma\sigma'}(\boldsymbol{r}_1,\boldsymbol{r}_2;-E), \tag{4.36}$$

while odd-frequency superconductivity is present if

$$f^{\mathrm{R}}_{\sigma\sigma'}(\boldsymbol{r}_1,\boldsymbol{r}_2;E) = -f^{\mathrm{A}}_{\sigma\sigma'}(\boldsymbol{r}_1,\boldsymbol{r}_2;-E). \tag{4.37}$$

We summarize the different possibilities in Table 4.1.

4.2 Correlation functions at the helical edge

In this section, we summarize the most important aspects with regard to correlation functions at the helical edge. The goal is to introduce notation and conventions, as well as explain how Green functions can be calculated. We follow the formalism developed in Refs. [117, 150–152].

4.2.1 Retarded Green function from scattering states

The cornerstone for the discussion in the following sections is the retarded Green function, which can be defined in terms of the Nambu spinor according to

$$G^{\mathrm{R}}(x,x';t,t') = -\mathrm{i}\theta(t-t')\Big\langle\Big\{\Psi(x,t),\Psi^\dagger(x',t')\Big\}\Big\rangle, \tag{4.38}$$

where the spinor reads $\Psi(x,t) = (\psi_\uparrow,\psi_\downarrow,\psi^\dagger_\downarrow,-\psi^\dagger_\uparrow)^{\mathrm{T}}$ as before. It is more convenient to work with its Fourier transform

$$G^{\mathrm{R}}(x,x',E) = \int_{-\infty}^{\infty}\mathrm{d}t\;\mathrm{e}^{\mathrm{i}(E+\mathrm{i}0^+)(t-t')}\,G^{\mathrm{R}}(x,x';t,t'), \tag{4.39}$$

where we moved to the relative time coordinate and neglect the global time coordinate, as before. Importantly, $G^{\mathrm{R}}(x,x',E)$ fulfills the equations of motion

$$[E-\mathcal{H}_{\mathrm{BdG}}(x)]\;G^{\mathrm{R}}(x,x',E) = \delta(x-x'), \tag{4.40a}$$

$$G^{\mathrm{R}}(x,x',E)\;[E-\mathcal{H}_{\mathrm{BdG}}(x)] = \delta(x-x'), \tag{4.40b}$$

where $\mathcal{H}_{\mathrm{BdG}}$ is the BdG-Hamiltonian of the helical edge states discussed in Section 3.1. The second equation of motion Eq. (4.40b) can be justified by noting that one can think of the Green function to be the inverse of the linear operator $E-\mathcal{H}_{\mathrm{BdG}}$. Furthermore, by taking the transpose Eq. (4.40b) can be rewritten in the form

$$\Big[E-\mathcal{H}^{\mathrm{T}}_{\mathrm{BdG}}(x)\Big]\;\Big(G^{\mathrm{R}}(x,x',E)\Big)^{\mathrm{T}} = \delta(x-x'). \tag{4.41}$$

Upon integration of Eq. (4.40a) from $-\epsilon$ to ϵ (subsequently $\epsilon\to 0$), the derivative contained in $\mathcal{H}_{\mathrm{BdG}}$ together with the delta-function on the left hand side of the equation of motion leads to the boundary condition

$$\lim_{\epsilon\to 0}\Big[G^{\mathrm{R}}(x'+\epsilon,x',E) - G^{\mathrm{R}}(x'-\epsilon,x',E)\Big] = \frac{1}{\mathrm{i}v_{\mathrm{F}}}\hat{\tau}_3\hat{\sigma}_3, \tag{4.42}$$

i.e., the retarded Green function has a discontinuity.

The boundary condition together with the equations of motion Eqs. (4.40a) and (4.41) justify the commonly used ansatz for the retarded Green function

$$G^{\mathrm{R}}(x,x',E) = \begin{cases} \sum_{i,j=1}^{4} \alpha_{ij}\phi_i(x)\tilde{\phi}_j(x') & x < x' \\ \sum_{i,j=1}^{4} \beta_{ij}\phi_i(x)\tilde{\phi}_j(x') & x > x', \end{cases} \tag{4.43}$$

where $\phi_i(x)$ and $\tilde{\phi}_j(x')$ are scattering state solutions to the BdG-equations

$$\mathcal{H}_{\mathrm{BdG}}\phi_i(x) = E\phi_i(x), \qquad \mathcal{H}^{\mathrm{T}}_{\mathrm{BdG}}\tilde{\phi}^{\mathrm{T}}_i(x) = E\tilde{\phi}^{\mathrm{T}}_i(x). \tag{4.44}$$

It is easy to verify that this ansatz indeed satisfies the equations of motion.

Finally, one can impose outgoing boundary conditions on the retarded Green function, which allows us to setting almost all α_{ij}, β_{ij} to zero. The final ansatz for the retarded Green function $G^{\mathrm{R}}(x,x',E)$ in terms of scattering states reads

$$G^{\mathrm{R}}(x,x',E) = \begin{cases} \alpha_{31}\phi_3(x)\tilde{\phi}_1(x') + \alpha_{32}\phi_3(x)\tilde{\phi}_2(x') \\ \qquad + \alpha_{41}\phi_4(x)\tilde{\phi}_1(x') + \alpha_{42}\phi_4(x)\tilde{\phi}_2(x') & x < x' \\ \beta_{13}\phi_1(x)\tilde{\phi}_3(x') + \beta_{23}\phi_1(x)\tilde{\phi}_4(x') \\ \qquad + \beta_{14}\phi_2(x)\tilde{\phi}_3(x') + \beta_{24}\phi_2(x)\tilde{\phi}_4(x') & x > x'. \end{cases} \tag{4.45}$$

Note that the scattering states $\phi_i(x), \tilde{\phi}_j(x')$ can be straightforwardly determined in the same fashion as in Chapter 3. The remaining unknown coefficients α_{ij}, β_{ij} from Eq. (4.45) can then be obtained by utilizing the boundary condition Eq. (4.42), which we demonstrate in more detail below.

4.2.2 Nambu space structure & advanced Green function

Once we calculated the retarded Green function from the scattering states following Section 4.2.1, we can proceed to analyze its symmetries.

To that end, let us introduce a few definitions first. The retarded Green function $G^{\mathrm{R}}(x,x',E)$ is, by definition, a matrix in Nambu and spin space. We can specify its blocks using

$$G^{\mathrm{R}}(x,x',E) = \begin{pmatrix} G^{\mathrm{R}}_{ee}(x,x',E) & G^{\mathrm{R}}_{eh}(x,x',E) \\ G^{\mathrm{R}}_{he}(x,x',E) & G^{\mathrm{R}}_{hh}(x,x',E) \end{pmatrix}. \tag{4.46}$$

The blocks G^{R}_{ee} and G^{R}_{hh} are the normal contributions to the retarded Green functions, which would also be present without superconductivity. In contrast, the *anomalous* blocks G^{R}_{eh} and G^{R}_{he} carry information about Andreev scattering and Cooper pairs, since they connect electrons and holes, and only emerge in the presence of superconductors.

We can further decompose the spin components of the individual blocks, which gives

$$\begin{aligned} G^{\mathrm{R}}_{ee} &= \begin{pmatrix} [G^{\mathrm{R}}_{ee}]_{\uparrow\uparrow} & [G^{\mathrm{R}}_{ee}]_{\uparrow\downarrow} \\ [G^{\mathrm{R}}_{ee}]_{\downarrow\uparrow} & [G^{\mathrm{R}}_{ee}]_{\downarrow\downarrow} \end{pmatrix}, \quad G^{\mathrm{R}}_{hh} = \begin{pmatrix} [G^{\mathrm{R}}_{hh}]_{\downarrow\downarrow} & [G^{\mathrm{R}}_{hh}]_{\downarrow\uparrow} \\ [G^{\mathrm{R}}_{hh}]_{\uparrow\downarrow} & [G^{\mathrm{R}}_{hh}]_{\uparrow\uparrow} \end{pmatrix}, \\ G^{\mathrm{R}}_{eh} &= \begin{pmatrix} [G^{\mathrm{R}}_{eh}]_{\uparrow\downarrow} & [G^{\mathrm{R}}_{eh}]_{\uparrow\uparrow} \\ [G^{\mathrm{R}}_{eh}]_{\downarrow\downarrow} & [G^{\mathrm{R}}_{eh}]_{\downarrow\uparrow} \end{pmatrix}, \quad G^{\mathrm{R}}_{he} = \begin{pmatrix} [G^{\mathrm{R}}_{he}]_{\downarrow\uparrow} & [G^{\mathrm{R}}_{he}]_{\downarrow\downarrow} \\ [G^{\mathrm{R}}_{he}]_{\uparrow\uparrow} & [G^{\mathrm{R}}_{he}]_{\uparrow\downarrow} \end{pmatrix}, \end{aligned} \tag{4.47}$$

where we suppressed the arguments of the spin components for brevity.

Since we ultimately seek to characterize the symmetry properties of the Green function, it is useful to explicitly extract the spin structure. To that end, we parametrize the anomalous part G^{R}_{eh} according to

$$G^{\mathrm{R}}_{eh}(x,x',E) = f^{\mathrm{R}}_0(x,x',E) + \sum_i f^{\mathrm{R}}_i(x,x',E)\hat{\sigma}_i. \tag{4.48}$$

Here, f^{R}_0 is the singlet component, whereas the functions f^{R}_i denote the vector specifying the triplet components. Note that our choice of basis in the Nambu spinor contained a minus sign in the hole sector, which might make some signs look suspicious.

The spin structure of the other anomalous block follows due to particle-hole symmetry. Since the retarded Green function is closely related to the Hamiltonian, it also shares its particle-hole symmetry. Using the charge conjugation operator $\mathcal{C} = \hat{\tau}_2\hat{\sigma}_2\,\mathrm{K}$, the retarded Green function fulfills

$$\mathcal{C}G^{\mathrm{R}}(x,x',E)\mathcal{C}^\dagger = -G^{\mathrm{R}}(x,x',-E). \tag{4.49}$$

We can use Eq. (4.49) to relate the blocks within the retarded Green function. Explicitly, we find

$$G^{\mathrm{R}}_{ee}(x,x',-E) = -\hat{\sigma}_2 G^{\mathrm{R}}_{hh}(x,x',E)^*\hat{\sigma}_2, \tag{4.50a}$$
$$G^{\mathrm{R}}_{eh}(x,x',-E) = \hat{\sigma}_2 G^{\mathrm{R}}_{he}(x,x',E)^*\hat{\sigma}_2, \tag{4.50b}$$

which means that the blocks G^{R}_{ee} and G^{R}_{eh} are sufficient to determine the entire retarded Green function.

As a last step, we note that the advanced Green function is related to the retarded Green function via the relation

$$G^{\mathrm{A}}(x,x',E) = \left(G^{\mathrm{R}}(x',x,E)\right)^\dagger. \tag{4.51}$$

Hence, we can use the retarded Green function to find the advanced one. The decomposition of G^{A} into electron-hole blocks and into spin components is analogous to the structure of G^{R}. As a result, we can straightforwardly obtain the spin functions from the advanced Green function f^{A}_0 (singlet) and f^{A}_i (triplet).

With the tools summarized in this section at hand, we are now able to classify the pairing characterized by the electron-hole block of retarded and advanced Green function according to Eq. (4.35). Since the singlet (triplet) components are necessarily odd (even) with respect to the exchange of spin indices, the functions $f^{\mathrm{R/A}}_{j=0,1,2,3}(x,x',E)$ fulfill

$$f^{\mathrm{R}}_0(x,x',E) = f^{\mathrm{A}}_0(x',x,-E), \qquad f^{\mathrm{R}}_{1,2,3}(x,x',E) = -f^{\mathrm{A}}_{1,2,3}(x',x,-E) \tag{4.52}$$

in order to keep the global antisymmetry. We classify the singlet into the ESE/OSO classes according to

$$\begin{aligned} &\text{ESE}: && f^{\mathrm{R}}_0(x,x',E) = f^{\mathrm{R}}_0(x',x,E), && f^{\mathrm{R}}_0(x,x',E) = f^{\mathrm{A}}_0(x,x',-E) \\ &\text{OSO}: && f^{\mathrm{R}}_0(x,x',E) = -f^{\mathrm{R}}_0(x',x,E), && f^{\mathrm{R}}_0(x,x',E) = -f^{\mathrm{A}}_0(x,x',-E), \end{aligned} \tag{4.53}$$

and the triplet into ETO/OTE following

$$\begin{aligned} \text{ETO}: \quad & f^{\mathrm{R}}_{1,2,3}(x,x',E) = -f^{\mathrm{R}}_{1,2,3}(x',x,E), \quad f^{\mathrm{R}}_{1,2,3}(x,x',E) = f^{\mathrm{A}}_{0}(x,x',-E) \\ \text{OTE}: \quad & f^{\mathrm{R}}_{1,2,3}(x,x',E) = f^{\mathrm{R}}_{1,2,3}(x',x,E), \qquad f^{\mathrm{R}}_{0}(x,x',E) = -f^{\mathrm{A}}_{1,2,3}(x,x',-E). \end{aligned} \tag{4.54}$$

4.3 Anomalous Green function at the helical edge

We can now proceed to explicitly calculate the retarded Green function for hybrid systems at the helical edge. To connect the symmetry classification of the pairing amplitudes to the previous chapter, we specifically discuss an SFS-system as in Section 3.3.2, with the only difference being that it has finite outer S barriers. In particular, except for the widths of the S regions we choose the same parameters as before.

The reason why we move to a setup with finite barriers is the close connection of the (retarded) Green function and the scattering coefficients [153]. In particular, the main focus of this section are nonlocal pairings and their connection to crossed Andreev reflection as well as Majorana and Andreev bound states. However, note that finite barriers imply that bound states turn in to quasi-bound state resonances. For completeness, we remark that local pairings have been studied in Refs. [117,154].

Although we will focus on a specific setup, some of the following results apply to generic scattering regions at the helical edge, since all details are hidden in the scattering coefficients. As a useful first step, we present expressions for the anomalous Green function when both positions fall within the same lead (*i.e.,* left or right of all barriers) before moving to nonlocal Green functions. We remark that keeping the positions outside of the heterostructure simplifies the expressions significantly, since we are able to use the asymptotic form of the scattering states. Note that we number the scattering states in the same way as in Section 3.2.2.4, *i.e.,* scattering state 1 (2) corresponds to an incoming electron (hole) from the left, wheras scattering state 3 (4) refers to an incoming electron (hole) from the right. In this chapter, the reflection (transmission) coefficients are labeled as r_i^α (t_i^α), where $i = 1,2,3,4$ refers to the scattering state and $\alpha = e,h$ to the outgoing particle type. For instance, r_1^h refers to the Andreev reflection of an electron from the left being backscattered as a hole. Extending the analysis to Green functions within the heterostructure is more involved, but can be straightforwardly done numerically.

4.3.1 Retarded Green function

4.3.1.1 Left lead

We start by discussing the form of the retarded Green function if both spatial arguments are placed within the left lead. Note that in that case scattering states $\phi_{1,2}, \tilde{\phi}_{1,2}$ contain normalized incoming modes as well as reflected ones, while $\phi_{3,4}, \tilde{\phi}_{3,4}$ only contain transmitted modes. The structure of the retarded Green function thus only depends on the explicit form of the scattering states, which is determined by the scattering processes allowed. Therefore, the most general case for us is a junction

containing both S and F regions, but the results trivially generalize to systems with only S or F barriers by setting the corresponding scattering coefficients to zero.

The retarded Green function is then obtained by inserting the ansatz in the form of Eq. (4.45) into the boundary condition in Eq. (4.42). This yields an equation of the form

$$\mathbf{C}_0 + \mathbf{C}_1\,\mathrm{e}^{-2\mathrm{i}k_e x} + \mathbf{C}_2\,\mathrm{e}^{-2\mathrm{i}k_h x} + \mathbf{C}_3\,\mathrm{e}^{\mathrm{i}(k_e-k_h)x} + \mathbf{C}_4\,\mathrm{e}^{-\mathrm{i}(k_e-k_h)x} + \mathbf{C}_5\,\mathrm{e}^{-\mathrm{i}(k_e+k_h)x} = \frac{1}{\mathrm{i}v_\mathrm{F}}\hat{\tau}_3\hat{\sigma}_3, \tag{4.55}$$

where $k_{e/h} = E \pm \mu$ and the $\mathbf{C}_i$ are 4×4-matrices whose elements consist of all contributions from the ansatz Eq. (4.45) which do not depend on position. Eq. (4.55) is fulfilled for arbitrary choice of x, x' if

$$\begin{aligned}\mathbf{C}_0 &= \frac{1}{\mathrm{i}v_F}\,\sigma_3\tau_3\\ \mathbf{C}_1 = \mathbf{C}_2 &= \mathbf{C}_3 = \mathbf{C}_4 = \mathbf{C}_5 = \mathbf{0}_{4\times 4}.\end{aligned}$$

Solving all these equations leads to expressions for the coefficients α_{ij}, β_{ij}. Additionally, some equations lead to relations between the scattering coefficients present in $\phi_i(x)$ and $\tilde{\phi}_j(x)$. One finds

$$\begin{aligned}\alpha_{31} &= -\frac{t_4^h}{\mathrm{i}v_\mathrm{F}(t_4^e t_3^h - t_3^e t_4^h)} & \alpha_{41} &= \frac{t_3^h}{\mathrm{i}v_\mathrm{F}(t_4^e t_3^h - t_3^e t_4^h)}\\ \alpha_{32} &= \frac{t_4^e}{\mathrm{i}v_\mathrm{F}(t_4^e t_3^h - t_3^e t_4^h)} & \alpha_{42} &= -\frac{t_3^e}{\mathrm{i}v_\mathrm{F}(t_4^e t_3^h - t_3^e t_4^h)}\\ \beta_{13} &= -\frac{\tilde{t}_4^h}{\mathrm{i}v_\mathrm{F}(\tilde{t}_4^e \tilde{t}_3^h - \tilde{t}_3^e \tilde{t}_4^h)} & \beta_{14} &= \frac{\tilde{t}_3^h}{\mathrm{i}v_\mathrm{F}(\tilde{t}_4^e \tilde{t}_3^h - \tilde{t}_3^e \tilde{t}_4^h)}\\ \beta_{23} &= \frac{\tilde{t}_4^e}{\mathrm{i}v_\mathrm{F}(\tilde{t}_4^e \tilde{t}_3^h - \tilde{t}_3^e \tilde{t}_4^h)} & \beta_{24} &= -\frac{\tilde{t}_3^e}{\mathrm{i}v_\mathrm{F}(\tilde{t}_4^e \tilde{t}_3^h - \tilde{t}_3^e \tilde{t}_4^h)}\end{aligned} \tag{4.56}$$

and

$$r_1^e = \tilde{r}_1^e, \qquad r_2^h = \tilde{r}_2^h, \qquad r_2^e = \tilde{r}_1^h, \qquad r_1^h = \tilde{r}_2^e. \tag{4.57}$$

Eqs. (4.56) and (4.57) are enough to simplify the general ansatz for the retarded Green function. One can combine both lines in the ansatz Eq. (4.45) in one compact expression. The blocks of the retarded Green function are of the form

$$G_{ee}^\mathrm{R}(x,x',E) = \frac{1}{\mathrm{i}v_\mathrm{F}}\begin{pmatrix}\theta(x-x')\,\mathrm{e}^{\mathrm{i}k_e(x-x')} & 0\\ \mathrm{e}^{-\mathrm{i}k_e(x+x')}\,r_1^e & \theta(x'-x)\,\mathrm{e}^{-\mathrm{i}k_e(x-x')}\end{pmatrix} \tag{4.58a}$$

$$G_{eh}^\mathrm{R}(x,x',E) = \frac{1}{\mathrm{i}v_\mathrm{F}}\begin{pmatrix}0 & 0\\ 0 & \mathrm{e}^{-(\mathrm{i}k_e x + \mathrm{i}k_h x')}\,r_2^e\end{pmatrix} \tag{4.58b}$$

$$G_{he}^\mathrm{R}(x,x',E) = \frac{1}{\mathrm{i}v_\mathrm{F}}\begin{pmatrix}\mathrm{e}^{-(\mathrm{i}k_h x + \mathrm{i}k_e x')}\,r_1^h & 0\\ 0 & 0\end{pmatrix} \tag{4.58c}$$

$$G_{hh}^\mathrm{R}(x,x',E) = \frac{1}{\mathrm{i}v_\mathrm{F}}\begin{pmatrix}\theta(x'-x)\,\mathrm{e}^{-\mathrm{i}k_h(x-x')} & \mathrm{e}^{-\mathrm{i}k_h(x+x')}r_2^h\\ 0 & \theta(x-x')\,\mathrm{e}^{\mathrm{i}k_h(x-x')}\end{pmatrix}. \tag{4.58d}$$

The diagonal terms of G_{ee}^R, corresponding to the diagonal elements of Eqs. (4.58a) and (4.58d), contain a step function to account for the discontinuity. Physically,

this feature corresponds to the helical nature of the edge states. The diagonals are associated with mere propagation of a specific particle with a given spin. Due to helicity, motion is only possible in one direction for each spin projection. Note that the positions x, x' can be thought of as corresponding to two times t, t'. Hence, the $\uparrow\uparrow$-component of G^{R}_{ee}, for instance, is only finite if the "later" position x is larger, *i.e.,* further to the right, than x'.

Furthermore, the offdiagonal terms in Eq. (4.58) correspond to a reflection process, which turns a rightmover into a leftmover of opposite spin. It is worth pointing out that the offdiagonal matrix elements of the retared Green function in Eq. (4.58) are proportional to the associated scattering coefficient.

4.3.1.2 Right lead

Following the same steps as in the previous section, one can calculate the retarded Green function if both spatial arguments are within the right lead. Note that in this case the states $\phi_{3,4}, \tilde{\phi}_{3,4}$ are composed of incoming and reflected modes, while $\phi_{1,2}, \tilde{\phi}_{1,2}$ only contribute transmitted modes. The system of equations resulting from the boundary condition is solved for

$$\begin{aligned}
\alpha_{31} &= -\frac{\tilde{t}^h_2}{\mathrm{i}v_{\mathrm{F}}(\tilde{t}^e_2\tilde{t}^h_1 - \tilde{t}^e_1\tilde{t}^h_2)} & \alpha_{41} &= \frac{\tilde{t}^e_2}{\mathrm{i}v_{\mathrm{F}}(\tilde{t}^e_2\tilde{t}^h_1 - \tilde{t}^e_1\tilde{t}^h_2)} \\
\alpha_{32} &= \frac{\tilde{t}^h_1}{\mathrm{i}v_{\mathrm{F}}(\tilde{t}^e_2\tilde{t}^h_1 - \tilde{t}^e_1\tilde{t}^h_2)} & \alpha_{42} &= -\frac{\tilde{t}^e_1}{\mathrm{i}v_{\mathrm{F}}(\tilde{t}^e_2\tilde{t}^h_1 - \tilde{t}^e_1\tilde{t}^h_2)} \\
\beta_{13} &= -\frac{t^h_2}{\mathrm{i}v_{\mathrm{F}}(t^e_2t^h_1 - t^e_1t^h_2)} & \beta_{14} &= \frac{t^e_2}{\mathrm{i}v_{\mathrm{F}}(t^e_2t^h_1 - t^e_1t^h_2)} \\
\beta_{23} &= \frac{t^h_1}{\mathrm{i}v_{\mathrm{F}}(t^e_2t^h_1 - t^e_1t^h_2)} & \beta_{24} &= -\frac{t^e_1}{\mathrm{i}v_{\mathrm{F}}(t^e_2t^h_1 - t^e_1t^h_2)},
\end{aligned} \tag{4.59}$$

and

$$r^e_4 = \tilde{r}^h_3, \qquad r^h_3 = \tilde{r}^e_4, \qquad r^e_3 = \tilde{r}^e_3, \qquad r^h_4 = \tilde{r}^h_4. \tag{4.60}$$

The retarded Green function is then readily obtained and reads

$$G^{\mathrm{R}}_{ee}(x,x',E) = \frac{1}{\mathrm{i}v_{\mathrm{F}}}\begin{pmatrix} \theta(x-x')\,\mathrm{e}^{\mathrm{i}k_e(x-x')} & \mathrm{e}^{\mathrm{i}k_e(x+x')}\,r^e_3 \\ 0 & \theta(x'-x)\,\mathrm{e}^{-\mathrm{i}k_e(x-x')} \end{pmatrix} \tag{4.61a}$$

$$G^{\mathrm{R}}_{eh}(x,x',E) = \frac{1}{\mathrm{i}v_{\mathrm{F}}}\begin{pmatrix} \mathrm{e}^{\mathrm{i}k_ex+\mathrm{i}k_hx'}\,r^e_4 & 0 \\ 0 & 0 \end{pmatrix} \tag{4.61b}$$

$$G^{\mathrm{R}}_{he}(x,x',E) = \frac{1}{\mathrm{i}v_{\mathrm{F}}}\begin{pmatrix} 0 & 0 \\ 0 & \mathrm{e}^{\mathrm{i}k_hx+\mathrm{i}k_ex'}\,r^h_3 \end{pmatrix} \tag{4.61c}$$

$$G^{\mathrm{R}}_{hh}(x,x',E) = \frac{1}{\mathrm{i}v_{\mathrm{F}}}\begin{pmatrix} \theta(x'-x)\,\mathrm{e}^{-\mathrm{i}k_h(x-x')} & 0 \\ \mathrm{e}^{\mathrm{i}k_h(x+x')}\,r^h_4 & \theta(x-x')\,\mathrm{e}^{\mathrm{i}k_h(x-x')} \end{pmatrix}. \tag{4.61d}$$

4.3.1.3 Nonlocal retarded Green function

The nonlocal retarded Green function where both spatial arguments are placed in opposite leads cannot be obtained in an analogous fashion. This is because the

boundary condition Eq. (4.42) relates the two pieces in the ansatz for the retarded Green function if their spatial arguments are equal, which is impossible for nonlocal correlations by definition.

However, note that the coefficients α_{ij}, β_{ij} are constants which do not depend on position. Therefore, we can use the solutions either from solving the boundary condition in the left or the right lead, *i.e.,* Eq. (4.56) or Eq. (4.59). More specifically, since the coefficients also cannot depend on where the boundary condition is solved, the solutions in Eqs. (4.56) and (4.59) need to be equal. This implies further relations between tilded and non-tilded coefficients, reading

$$\begin{aligned} t_1^e &= \tilde{t}_3^e, & t_3^e &= \tilde{t}_1^e, & t_2^e &= \tilde{t}_3^h, & t_4^e &= \tilde{t}_1^h, \\ t_1^h &= \tilde{t}_4^e, & t_3^h &= \tilde{t}_2^e, & t_2^h &= \tilde{t}_4^h, & t_4^h &= \tilde{t}_2^h. \end{aligned} \tag{4.62}$$

The ansatz for the nonlocal retarded Green function with spatial arguments in opposite leads then assumes a simple form using Eqs. (4.57), (4.60) and (4.62) and either the solutions for α_{ij}, β_{ij} from Eqs. (4.56) and (4.59). For $x < x'$, which corresponds to a propagation from the right to the left lead, we find

$$G^{\mathrm{R},<}(x,x',E) = \frac{1}{\mathrm{i}v_\mathrm{F}} \begin{pmatrix} 0 & 0 & 0 & 0 \\ 0 & \mathrm{e}^{-\mathrm{i}k_e(x-x')}\, t_3^e & \mathrm{e}^{-\mathrm{i}k_e x + \mathrm{i}k_h x'}\, t_4^e & 0 \\ 0 & \mathrm{e}^{-\mathrm{i}k_h x + \mathrm{i}k_e x'}\, t_3^h & \mathrm{e}^{-\mathrm{i}k_h(x-x')}\, t_4^h & 0 \\ 0 & 0 & 0 & 0 \end{pmatrix} \tag{4.63a}$$

whereas for $x > x'$, *i.e.,* propagation from left to right lead, one has

$$G^{\mathrm{R},>}(x,x',E) = \frac{1}{\mathrm{i}v_\mathrm{F}} \begin{pmatrix} \mathrm{e}^{\mathrm{i}k_e(x-x')}\, t_1^e & 0 & 0 & \mathrm{e}^{\mathrm{i}k_e x - \mathrm{i}k_h x'}\, t_2^e \\ 0 & 0 & 0 & 0 \\ 0 & 0 & 0 & 0 \\ \mathrm{e}^{\mathrm{i}k_h x - \mathrm{i}k_e x'}\, t_1^h & 0 & 0 & \mathrm{e}^{\mathrm{i}k_h(x-x')}\, t_2^h \end{pmatrix}. \tag{4.63b}$$

We introduce a superscript $<,>$ to distinguish these two cases. Note that these are still retarded Green functions and should not be confused with lesser and greater Green functions familiar from the Keldysh formalism.

As before, observe how the entries in Eq. (4.63) are proportional to the corresponding scattering coefficient. In particular, we see that $G^{\mathrm{R},<}(x,x',E)$ only contains processes connecting electrons and holes with spin $\downarrow$, in agreement with our convention for the helical edge states. Accordingly, the only nonzero elements of $G^{\mathrm{R},>}(x,x',E)$ are between electrons and holes with spin $\uparrow$. Note that, essentially, we have explicitly derived the Fisher-Lee relation for the system at hand [153].

4.3.2 Symmetry classification

4.3.2.1 Local anomalous Green function

It is now straightforward to show that unconventional superconductivity is inevitable in hybrid junctions on the basis of helical edge states. We start by discussing the local retarded Green functions from Sections 4.3.1.1 and 4.3.1.2.

In the left lead, the only nonzero element of the anomalous retarded Green function $G^{\mathrm{R}}_{eh}(x,x',E)$ reads

$$[G^{\mathrm{R}}_{eh}]_{\downarrow\uparrow}(x,x',E) = \frac{1}{\mathrm{i}v_{\mathrm{F}}}\,\mathrm{e}^{-(\mathrm{i}k_e x+\mathrm{i}k_h x')}\,r^e_2, \tag{4.64}$$

corresponding to the Andreev reflection of an spin $\uparrow$ hole into a spin $\downarrow$ electron. Clearly, since the $\uparrow\downarrow$-element of $G^{\mathrm{R}}_{eh}(x,x',E)$ is zero due to helicity, the decomposition in spin space according to Eq. (4.48) results in

$$f^{\mathrm{R}}_0(x,x',E) = -f^{\mathrm{R}}_3(x,x',E) = \frac{1}{2\mathrm{i}v_{\mathrm{F}}}\,\mathrm{e}^{-(\mathrm{i}k_e x+\mathrm{i}k_h x')}\,r^e_2. \tag{4.65}$$

This means that helicity necessarily implies local spin singlet and triplet pairing of equal amplitude, and therefore an inevitable emergence of unconventional superconductivity. A similar argument can be made for the anomalous Green function in the right lead.

For the sake of brevity, we refer the reader to Refs. [117, 154] for a more detailed symmetry analysis of local pairing amplitudes, especially with respect to even- and odd-frequency pairing.

4.3.2.2 Nonlocal anomalous Green function

Focussing on the anomalous part $G^{\mathrm{R}}_{eh}(x,x',E)$ of the nonlocal retarded Green functions, *i.e.,* the upper right block of Eqs. (4.63a) and (4.63b), we extract

$$[G^{\mathrm{R},<}_{eh}]_{\downarrow\downarrow}(x,x',E) = \frac{1}{\mathrm{i}v_{\mathrm{F}}}\,\mathrm{e}^{-\mathrm{i}k_e x+\mathrm{i}k_h x'}\,t^e_4 \tag{4.66a}$$

and

$$[G^{\mathrm{R},>}_{eh}]_{\uparrow\uparrow}(x,x',E) = \frac{1}{\mathrm{i}v_{\mathrm{F}}}\,\mathrm{e}^{\mathrm{i}k_e x-\mathrm{i}k_h x'}\,t^e_2. \tag{4.66b}$$

They are clearly proportional to the crossed Andreev reflection of a hole injected from the right [Eq. (4.66a)] and left [Eq. (4.66b)], respectively. Notably, the nonlocal, anomalous retarded Green function only has equal-spin components and is therefore manifestly a triplet correlation function. Note that this is clearly a consequence of helicity together with *both* proximity induced superconductivity (converting electrons and holes into each other) and magnetism (allowing spins to mix). Hence, nonlocal anomalous correlation functions in heterostructures at the helical edge are always unconventional and go beyond the singlet superconducting order provided by the "parent" superconductor.

However, categorizing the pairing amplitude into the ETO and OTE symmetry classes by analyzing the even- or oddness under $x \leftrightarrow x'$ and $E \to -E$ is not straightforward. To see this, let us introduce the equal-spin triplet components of the anomalous Green function defined as

$$f^{\mathrm{R},\gtrless}_{\pm}(x,x',E) = f^{\mathrm{R},\gtrless}_1(x,x',E) \mp f^{\mathrm{R},\gtrless}_2(x,x',E), \tag{4.67}$$

which is only another variable name for the equal-spin elements in Eq. (4.66) [$+$ $(-)$ refers to $\uparrow\uparrow$ $(\downarrow\downarrow)$]. In order to classify the pairing according to Eq. (4.54), we

would either need to compare the pairings $f_{\pm}^{\mathrm{R},\gtrless}(x,x',E)$ under the exchange $x \leftrightarrow x'$, or compare $f_{\pm}^{\mathrm{R},\gtrless}(x,x',E)$ with the associated pairing function from the advanced Green function $f_{\pm}^{\mathrm{A},\gtrless}(x,x',-E)$. Both of these comparisons are not well defined.

First, the pairings do not have a partner in the same spin channel under $x \leftrightarrow x'$ because of helicity, since propagation from left to right (right to left) is tied to spin $\uparrow$ ($\downarrow$).

Strikingly, the same is true for comparing retarded and advanced Green functions: while the retarded Green function corresponds to an expectation value with respect to a positive relative time between the two field operators, see the definition in Eq. (4.38), the advanced Green function correlates events with a negative relative time. Thus, in our helical system, the nonlocal advanced Green function $G^{\mathrm{A}}(x,x',E)$ in the spin $\uparrow$ channel will only be nonzero if $x < x'$, *i.e.,*

$$[G_{eh}^{\mathrm{A},<}]_{\uparrow\uparrow} \neq 0, \qquad [G_{eh}^{\mathrm{A},>}]_{\uparrow\uparrow} = 0. \tag{4.68}$$

Of course, this can be checked straightforwardly by using the relation between retarded and advanced Green functions, see Eq. (4.51). In conclusion, the advanced Green function which would be the partner to, for instance, $f_{+}^{\mathrm{R},>}$ is zero. The same argument can be made for the other nonzero pairings.

In order to resolve this issue, we now construct an antisymmetric correlation function which is manifestly odd under the exchange of spins, positions, and the transformation $E \to -E$. To that end, we combine the general relation between retarded and advanced Green function in Eq. (4.51) with particle-hole symmetry, as shown in Eqs. (4.49) and (4.50). This leads to the relation

$$[G_{eh}^{\mathrm{A}}]_{\sigma\sigma'}(x,x',E) = -[G_{eh}^{\mathrm{R}}]_{\sigma'\sigma}(x',x,E) \tag{4.69}$$

between elements in the electron-hole block of interest.

To see why this is useful, we explicitly construct the scalar spin-singlet and pseudovector spin-triplet components

$$f_{\mu}^{\mathrm{R}}(x,x',E) = \begin{cases} f_0^{\mathrm{R}}(x,x',E) \equiv [G_{eh}^{\mathrm{R}}]_{\uparrow\downarrow}(x,x',E) - [G_{eh}^{\mathrm{R}}]_{\downarrow\uparrow}(x,x',E) \\ f_3^{\mathrm{R}}(x,x',E) \equiv [G_{eh}^{\mathrm{R}}]_{\uparrow\downarrow}(x,x',E) + [G_{eh}^{\mathrm{R}}]_{\downarrow\uparrow}(x,x',E) \\ f_{+}^{\mathrm{R}}(x,x',E) \equiv [G_{eh}^{\mathrm{R}}]_{\uparrow\uparrow}(x,x',E) \\ f_{+}^{\mathrm{R}}(x,x',E) \equiv [G_{eh}^{\mathrm{R}}]_{\downarrow\downarrow}(x,x',E), \end{cases} \tag{4.70}$$

where the index $\mu = 0, 3, \pm$ denotes the spin channel. Furthermore, we introduce the exchange of spin indices by introducing indices with a bar $\bar{\mu}$, such that

$$f_{\bar{\mu}}^{\mathrm{R}}(x,x',E) = (-f_0^{\mathrm{R}}(x,x',E), f_j^{\mathrm{R}}(x,x',E)) \tag{4.71}$$

with $j = 3, \pm$.

Next, we furthermore symmetrize with respect to positions and define

$$f_{\pm,\mu}^{\mathrm{R}}(x,x',E) = f_{\mu}^{\mathrm{R}}(x,x',E) \pm f_{\mu}^{\mathrm{R}}(x',x,E). \tag{4.72}$$

Note that so far we only repeated the problem described above, since the last symmetrization step is again problematic for nonlocal pairing amplitudes.

However, one can perform the same construction for the advanced anomalous Green function G^{A}_{eh}, leading to amplitudes $f^{\mathrm{A}}_{\pm,\mu}$. Due to the relation to the retarded Green function in Eq. (4.69), they obey

$$\begin{aligned} f^{\mathrm{A}}_{\pm,\mu}(x,x',E) = f^{\mathrm{A}}_{\mu}(x,x',E) \pm f^{\mathrm{A}}_{\mu}(x',x,E) &= -f^{\mathrm{A}}_{\bar{\mu}}(x,x',-E) \mp f^{\mathrm{A}}_{\bar{\mu}}(x',x,-E) \\ &= \mp f^{\mathrm{R}}_{\pm,\bar{\mu}}(x,x',-E). \end{aligned} \tag{4.73}$$

It is now easy to see that the correlation function $F(x,x',E) = G^{\mathrm{R}}_{eh}(x,x',E) + G^{\mathrm{A}}_{eh}(x,x',E)$ is antisymmetric under the exchange of spins and positions and $E \to -E$, *i.e.,*

$$[F(x,x',E)]_{\sigma\sigma'} = -[F(x',x,-E)]_{\sigma'\sigma}. \tag{4.74}$$

Furthermore, one can construct its components $f_{\pm,\mu}(x,x',E)$ symmetrized with respect to positions and spins in the same fashion as retarded and advanced Green functions. Importantly, they fulfill

$$f_{\pm,0}(x,x',E) = \pm f_{\pm,0}(x,x',-E) \tag{4.75a}$$

$$f_{\pm,j}(x,x',E) = \mp f_{\pm,j}(x,x',-E), \tag{4.75b}$$

with $j = 3,\pm$. The first line Eq. (4.75a) clearly shows that the singlet even (odd) in spatial coordinates is also even (odd) in frequency and thus defines the singlet ESE and OSO classes. Eq. (4.75b) tells us that the triplet even (odd) in positions is odd (even) in frequency, giving rise to the triplet OTE and ETO pairing classes.

4.4 Nonlocal pairing in SFS-hybrid junctions

In this section, we put the technical definitions of the previous sections to use and explicitly calculate nonlocal pairing amplitudes in an SFS-heterostructure based on helical edge states. In particular, we compare them with resonances due to Majorana and Andreev quasi-bound states. For completeness, we note that the relation between local pairing amplitudes, in particular odd-freqency pairing, and Majorana bound states has been explored in Refs. [117, 154–161].

First, following the previous section we can write down an expression for the nonlocal pairing amplitude between left and right lead. As explained above, due to helicity they need to be spin-polarized. Using the result from Eq. (4.66), we find [introducing spatial coordinates x_{L} (x_{R}) in the left (right) lead]

$$f_{\pm,+}(x_{\mathrm{R}},x_{\mathrm{L}},E) = \frac{1}{\mathrm{i}v_{\mathrm{F}}}\,\mathrm{e}^{\mathrm{i}\mu(x_{\mathrm{L}}+x_{\mathrm{R}})}\left[\mathrm{e}^{-\mathrm{i}E(x_{\mathrm{L}}-x_{\mathrm{R}})}t^{e}_{2}(E) \mp \mathrm{e}^{\mathrm{i}E(x_{\mathrm{L}}-x_{\mathrm{R}})}t^{e}_{2}(-E)\right] \tag{4.76a}$$

in the spin $\uparrow\uparrow$-channel and

$$f_{\pm,-}(x_{\mathrm{R}},x_{\mathrm{L}},E) = \mp\frac{1}{\mathrm{i}v_{\mathrm{F}}}\,\mathrm{e}^{-\mathrm{i}\mu(x_{\mathrm{L}}+x_{\mathrm{R}})}\left[\mathrm{e}^{\mathrm{i}E(x_{\mathrm{L}}-x_{\mathrm{R}})}t^{e}_{4}(E) \mp \mathrm{e}^{-\mathrm{i}E(x_{\mathrm{L}}-x_{\mathrm{R}})}t^{e}_{4}(-E)\right] \tag{4.76b}$$

in the spin $\downarrow\downarrow$-channel. The latter is now nonzero because of the symmetrization procedure, even though we fixed the coordinates in opposite leads.

As mentioned before, we discuss a system as in Section 3.3.2 and Fig. 3.11 with finite S barriers. We take the widths of left (SL) and right (SR) superconductors

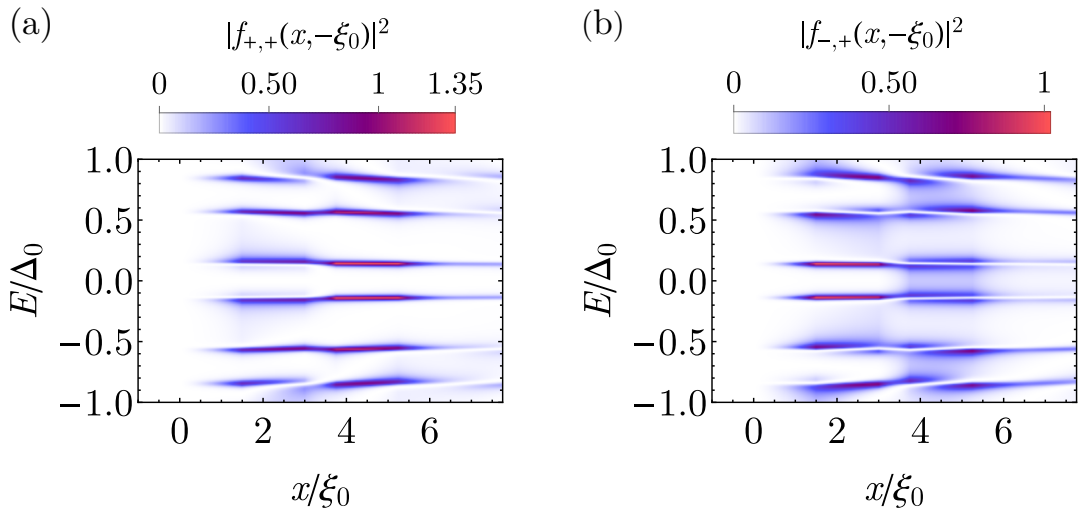

Figure 4.1: Density plot of the squared moduli of the nonlocal triplet pairings in the $\uparrow\uparrow$ channel as a function of position and energy. As explained in the main text, one spatial argument is fixed at $x = -\xi_0$ in the left lead, while the other is swept across the junction. We show the odd-frequency pairing $f_{+,+}$ in the OTE-class in panel (a), and the even-frequency pairing $f_{-,+}$ in the ETO-class in panel (b). The widths of left (SL) and right (SR) superconductors are chosen to be $d_{\mathrm{SL}} = d_{\mathrm{SR}} = 1.5\xi_0$, and the phase difference is $\varphi = 0$. Note that by the convention in this section, the left superconducting region is confined to $[0, 1.5\xi_0]$ and the right S region to $[5.25\xi_0, 6.75\xi_0]$.

to be $d_{\mathrm{SL}} = d_{\mathrm{SR}} = 1.5\xi_0$, with ξ_0 the coherence length. For convenience, we shift the origin to the interface of the left lead and the left superconductor and start the analysis at phase difference $\varphi = 0$.

For brevity, we focus on $f_{\pm,+}$ and thus the spin $\uparrow\uparrow$-channel, but an analogous analysis can be done for $f_{\pm,-}$.

In order to see the nonlocal amplitudes unfold, we take the following approach. First, in Fig. 4.1 we fix one spatial argument in the left lead, one coherence length ξ_0 away from the left superconductor, and sweep the other one across the junction. We furthermore plot the pairings as a function of energy, with the odd- (even-)frequency pairing to the left (right). Clearly, the nonlocal amplitudes build up within the left superconducting barrier and show rich behavior within the junction (in Fig. 4.3, we show cuts of the density plots and sketch the different regions for better illustration). Due to the interplay of superconductors and ferromagnet, CAR across the junction is possible such that the pairing amplitude remains finite when the variable spatial argument is within the right lead.

Interestingly, both OTE [panel (a)] and ETO [panel (b)] pairings seem to be enhanced at energies associated with quasi-bound state resonances. To make this connection explicit, we calculate the local density of states (LDOS) $\rho(E, x)$ from the retarded Green function according to

$$\rho(E, x) = -\frac{1}{\pi} \operatorname{Im}\left[\operatorname{Tr}\left(G^R(x, x, E)\right)\right]. \tag{4.77}$$

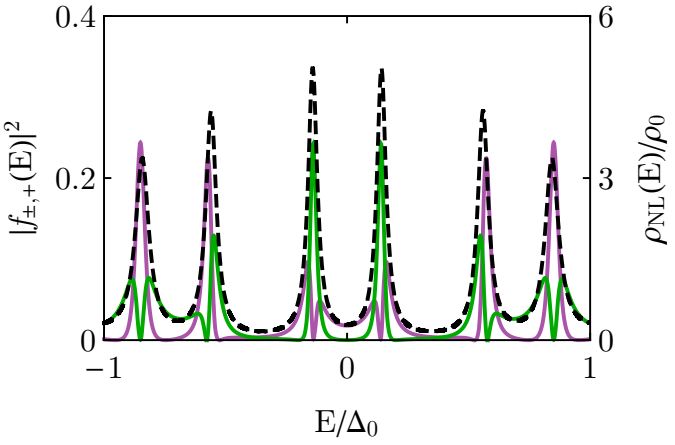

Figure 4.2: Cut of the absolute square of the nonlocal OTE amplitude $f_{+,+}$ (green) and ETO amplitude $f_{-,+}$ (purple) from Fig. 4.1 at the interface of right superconductor and right lead at $x = 6.75\xi_0$. Additionally, in dashed black we plot the local density of states ρ_{NL} within the left intermediate N region, normalized to the constant value in the leads.

We focus on the LDOS within the NL region $\rho_{\mathrm{NL}}(E) = \rho(E, x_{\mathrm{NL}})$, since we know from the previous chapter that bound states are trapped between S and F barriers. In Fig. 4.2 we compare the LDOS within NL and cuts of the pairings in Fig. 4.1 along the interface between the right superconductor and the right lead. Evidently, the pairing is enhance for quasi-bound state resonances. Furthermore, we see that the low-energy resonances associated with hybridized MBSs in an SFS-system with semi-infinite outer superconductors are dominated by the odd-frequency pairing component, while the higher energy Andreev resonances are more mixed. The connection between odd-frequency pairing and Majorana bound states is the main result of Ref. [118]. Note that these pairings can equivalently be evaluated using Eq. (4.76).

To analyze the difference between the Majorana- and Andreev-induced pairings in more detail, we show cuts along the energies of LDOS-peaks in Fig. 4.3. Interestingly, there seems to be a qualitative difference, since at $E \approx 0.141\Delta_0$ (left panel) the behavior is more stable and less oscillatory than at $E \approx 0.843\Delta_0$ (right panel). Furthermore, note that the odd-frequency component for the lower energy peak only starts to dominate the even-frequency pairing to the right of the ferromagnet.

As a last step, we discuss how the established behavior of nonlocal odd- and even-frequency pairing changes when the phase difference between the superconductors is varied and thus the hybridization of the bound states changes. Thus, in Fig. 4.4 we show the phase dependence of the nonlocal pairing between left lead and superconductor-right lead interface as in Fig. 4.2. Moreover, we add the energies of the LDOS-peaks as a dashed line. We find that except around $\varphi = \pi$, the low-energy Majorana quasi-bound states are always dominated by odd-frequency pairing, whereas the even-frequency component shows a dip at these resonant energies. The picture at the ABS-energies is less clear and both pairings can have roughly comparable magnitude (just as in Fig. 4.2), but overall the ETO pairing appears to be the dominating one.

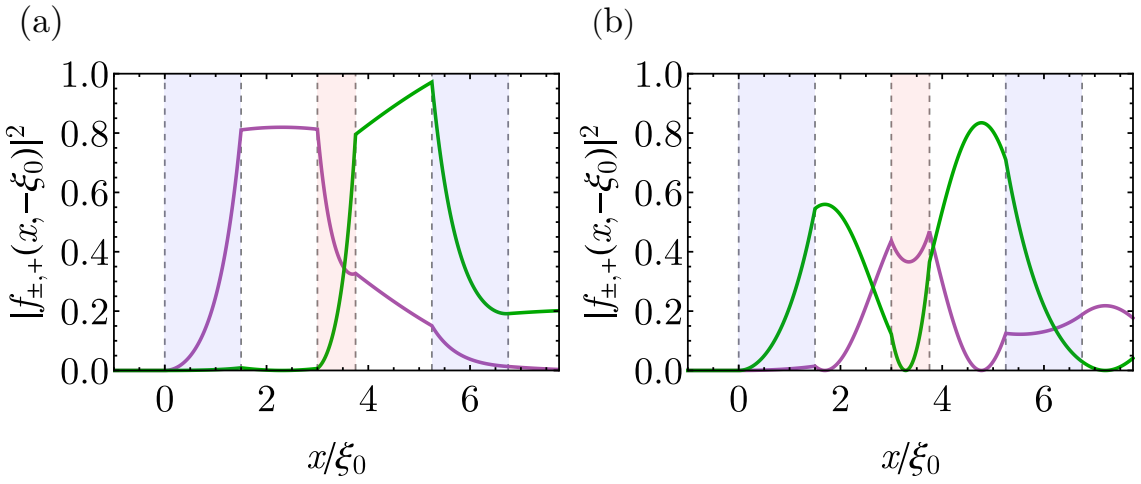

Figure 4.3: Cuts of nonlocal OTE amplitude $f_{+,+}$ (green) and ETO amplitude $f_{-,+}$ (purple) from Fig. 4.1 along the energies $E = 0.141\Delta_0$ [panel (a)] and $E = 0.843\Delta_0$ [panel (b)] associated with quasi-bound state resonances.

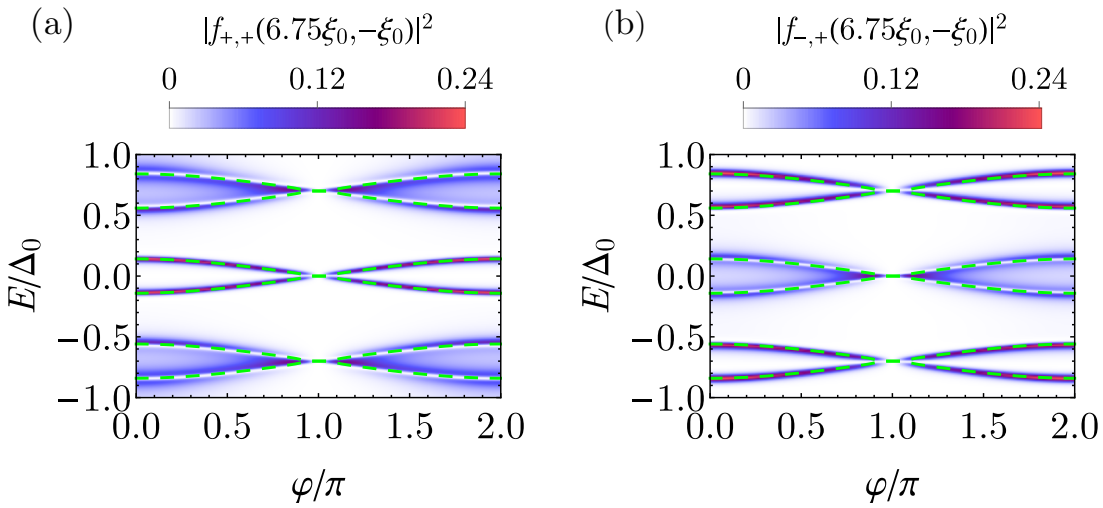

Figure 4.4: Plot of the nonlocal OTE [panel (a)] and ETO [panel (b)] pairings between $x' = -\xi_0$ and the right S-right lead interface at $x = 6.75\xi_0$ as a function of energy and phase difference φ, compared to the maxima of the LDOS ρ_{NL} shown by the dashed green line.

5

Thermoelectric generation of equal-spin Cooper pairs

Contents

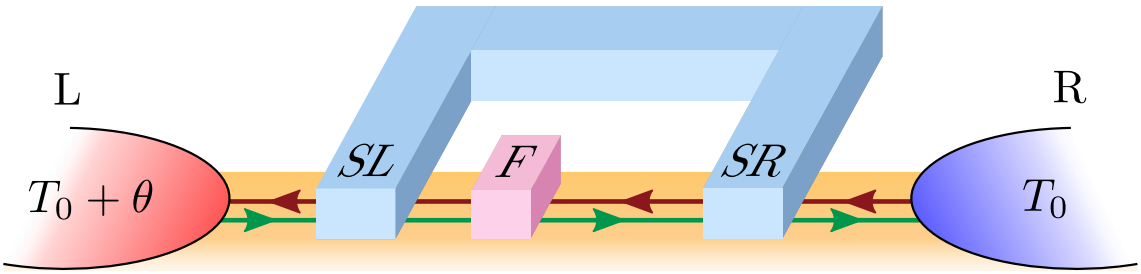

Figure 5.1: Schematic depiction of the proposed device. We consider an SFS-system proximity coupled to helical edge states, where spin $\uparrow$ ($\downarrow$) electrons represented by the green (brown) arrow travel to the right (left). The edge states connect a left (L) and a right (R) reservoir at chemical potential $\mu = 0$ and temperatures $T_0 + \theta$ and T_0, respectively. Here, $\mu = 0$ and T_0 are chemical potential and temperature of the superconductors, see main text. Note that we model the temperature dependence of the pairing potential according to $\Delta(T) = \Delta_0 \tanh\left(1.74\sqrt{\frac{T_c}{T} - 1}\right)$ such that Δ_0 corresponds to the zero-temperature value. The latter also defines a length scale via the coherence length $\xi_0 = \hbar v_\mathrm{F}/\Delta_0$. Throughout the chapter, we take the widths of the superconducting barriers to be $d_{SL} = d_{SR} = \xi_0$, the widths of the normal regions are $d_{NL} = 0.4\xi_0$, $d_{NR} = 0.9\xi_0$, and the ferromagnetic region $d_F = 0.6\xi_0$, unless specified otherwise. Furthermore, our standard convention is $T_c = \Delta_0$, $T_0 = T_c/2$, $\theta = T_c/4$ and $\varphi = \pi/2$. Note that for most of the chapter, we set $\hbar = v_\mathrm{F} = k_\mathrm{B} = 1$ where k_B is the Boltzmann constant. Adapted from Ref. [136], copyright (2020) by The American Physical Society.

One of the promises of the study of unconventional superconductivity is the field of superconducting spintronics, which aims to utilize triplet superconductivity and Cooper pairs with finite net spin for future information technology [12,143,162,163]. Typically, one uses hybrid junctions out of standard s-wave superconductors and ferromagnets to carefully manipulate the singlet pairing from the bulk superconductor and turn it into a triplet amplitude. This requires a high level of control over nanoscale magnetic building blocks.

Furthermore, S-F structures are known to be excellent thermoelectrics. Usually, superconducting materials by themselves show very small thermoelectric signatures, since particle-hole symmetry forces transport to be symmetric with respect to the Fermi surface. In conjunction with magnetic fields, however, the density of states in the superconductors can become spin-split. Together with a spin-filtering transport mechanism, the electron-hole coupling in the superconductor can actually be exploited to create asymmetric transport [164–176].

In this chapter, we present a synthesis of these two research areas. We employ an SFS-system and helical edge states as a spin filter, to allow for nonlocal CAR processes. Following Chapter 4, these are associated with a spin-polarized anomalous Green function and thus spin-polarized Cooper pairs. In the following, we first show that the system as depicted in Fig. 5.1 shows a thermoelectric effect which is in fact dominated by nonlocal CAR events. Subsequently, we present evidence that the equal-spin Cooper pairs responsible for the thermoelectric effect also induce enhanced supercurrents. We therefore propose a device which turns a temperature

difference into triplet Cooper pairs and possibly even spin-polarized supercurrent. This chapter builds on similar ideas in different settings, *i.e.,* thermoelectric effects in Andreev interferometers [177, 178] and in Cooper pair-splitters [179–182].

We remark that the idea pursued in this chapter brings us close to the field of *quantum thermodynamics*, which studies how temperature, heat, entropy and other quantities familiar from classical thermodynamics translate into quantum systems. This is especially interesting with respect to possible nanoscale devices converting heat into useful work (heat engine) or using electrical power to direct heat flow from cold to warm baths (refrigeration), for instance. For a comprehensive introduction into the topic, we refer the reader to the superb reviews [183–188] and references therein.

5.1 Current operators and average current

5.1.1 Current operators

We start the discussion by deriving the charge current operator. To that end, we need to consider the charge density $n(x)$ given by

$$n(x) = e\left(n_\uparrow + n_\downarrow\right) = e\left(\psi_\uparrow^\dagger \psi_\uparrow + \psi_\downarrow^\dagger \psi_\downarrow\right). \tag{5.1}$$

The time evolution of the charge density is determined by the commutator of $n(x)$ and the Hamiltonian H according to (we set $\hbar = 1$)

$$\partial_t n(x) = \mathrm{i}\left[H, n(x)\right], \tag{5.2}$$

where we write the Hamiltonian in the standard, non-BCS fashion as

$$H = H_0 + H_\Delta + H_m, \tag{5.3}$$

with the normal part

$$H_0 = \int \mathrm{d}x\, \left[\psi_\uparrow^\dagger(x)\left(-\mathrm{i}v_\mathrm{F}\partial_x - \mu\right)\psi_\uparrow(x) + \psi_\downarrow^\dagger(x)\left(\mathrm{i}v_\mathrm{F}\partial_x - \mu\right)\psi_\downarrow(x)\right], \tag{5.4}$$

the term describing proximity induced s-wave superconductivity

$$H_\Delta = \int \mathrm{d}x\, \left[\Delta(x)\mathrm{e}^{\mathrm{i}\varphi}\psi_\downarrow(x)\psi_\uparrow(x) + \Delta(x)\mathrm{e}^{-\mathrm{i}\varphi}\psi_\uparrow^\dagger(x)\psi_\downarrow^\dagger(x)\right], \tag{5.5}$$

and finally the contribution from the ferromagnetic regions

$$H_m = \int \mathrm{d}x\, \left(\psi_\uparrow^\dagger(x), \psi_\downarrow^\dagger(x)\right) \boldsymbol{m}(x)\cdot\hat{\boldsymbol{\sigma}} \begin{pmatrix}\psi_\uparrow(x)\\ \psi_\downarrow(x)\end{pmatrix}. \tag{5.6}$$

It is instructive to evaluate the commutator for each contribution to H separately. To that end, we make use of the relation

$$[AB, CD] = -AC\left\{D, B\right\} + A\left\{C, B\right\}D - C\left\{D, A\right\}B + \left\{C, A\right\}DB \tag{5.7}$$

where $\{A, B\} = AB + BA$ denotes the anticommutator, as well as standard fermionic anticommutation rules

$$\left\{\psi_\sigma(x), \psi^\dagger_{\sigma'}(y)\right\} = \delta_{\sigma\sigma'}\delta(x-y). \tag{5.8}$$

We then find

$$\begin{aligned}[H_0, n_\sigma(x)] &= \mathrm{i}ev_\mathrm{F}\,\mathrm{sgn}(\sigma)\left(\psi^\dagger_\sigma(x)\partial_x\psi_\sigma(x) + (\partial_x\psi^\dagger_\sigma(x))\psi_\sigma(x)\right) \\ &= \mathrm{i}ev_\mathrm{F}\,\mathrm{sgn}(\sigma)\partial_x\left(n_\sigma(x)\right),\end{aligned} \tag{5.9}$$

where $\mathrm{sgn}(\uparrow) = +1$, $\mathrm{sgn}(\downarrow) = -1$. Note that the chemical potential does not influence the commutator at all.

From the superconductor, one obtains the result

$$[H_\Delta, n_\uparrow + n_\downarrow] = -e\Delta\mathrm{e}^{\mathrm{i}\varphi}\left(\psi_\uparrow\psi_\downarrow - \psi_\downarrow\psi_\uparrow\right) - e\Delta\mathrm{e}^{-\mathrm{i}\varphi}\left(\psi^\dagger_\uparrow\psi^\dagger_\downarrow - \psi^\dagger_\downarrow\psi^\dagger_\uparrow\right), \tag{5.10}$$

where we omitted the position dependence for clarity.

Crucially, the contribution from the ferromagnetic part vanishes,

$$[H_m, n_\uparrow + n_\downarrow] = 0, \tag{5.11}$$

since it neither contains a derivative as H_0, nor an anomalous term as the superconductor, such that the individual anticommutators can readily be shown to cancel.

With these commutators at hand, we can write out the continuity equation for the charge current in the form

$$\partial_t n(x) + \partial_x\hat{I}(x) + S = 0, \tag{5.12}$$

where the charge current operator[1] due to particle propagation is

$$\hat{I}(x) = -v_\mathrm{F}\left[n_\uparrow(x) - n_\downarrow(x)\right] = -ev_\mathrm{F}\left[\psi^\dagger_\uparrow\psi_\uparrow - \psi^\dagger_\downarrow\psi_\downarrow\right], \tag{5.13}$$

and the source term stemming from the superconductor reads

$$S = \mathrm{i}e\Delta\left[\mathrm{e}^{\mathrm{i}\varphi}\left(\psi_\uparrow\psi_\downarrow - \psi_\downarrow\psi_\uparrow\right) + \mathrm{e}^{-\mathrm{i}\varphi}\left(\psi^\dagger_\uparrow\psi^\dagger_\downarrow - \psi^\dagger_\downarrow\psi^\dagger_\uparrow\right)\right]. \tag{5.14}$$

Hence, the current operator $\hat{I}$ in Eq. (5.13) simply counts the difference between left- and rightmovers. The source term arises since the pairing term H_Δ breaks charge conservation by allowing for Cooper pairs to be added or removed from the condensate. Note that Δ in Eq. (5.14) is the modulus and the phase dependence is explicitly written out in the bracket. Note that the supercurrent is obtained from the source term via

$$\hat{I}_\mathrm{S}(x) = \int \mathrm{d}x'\, S(x). \tag{5.15}$$

[1] We explicitly signal the operator nature here to avoid confusion with the charge current averages later on.

5.1.2 Average currents

The expressions for the charge- and supercurrent in Eq. (5.13) and Eqs. (5.14) and (5.15) are not immediately useful. The reason why we cannot simply take the average right away is that the field operators $\psi_\sigma^\dagger, \psi_\sigma$ are not the appropriate basis. Thus, the average should instead be taken with respect to fermionic quasiparticles[2] diagonalizing the Hamiltonian, which we introduced in Section 3.1.3.

Furthermore, note that we assume scattering within the heterostructure to be elastic. Hence, equilibration only takes place within the reservoirs, and particles carry information about the reservoir they originate from with them until they reach another one. For this reason, a natural basis for the evaluation of the average current are the scattering states.

For this section, we adopt the following convention. Scattering state $\phi_{E,1}$ ($\phi_{E,2}$) corresponds to an electron (hole) coming in from the left at energy E, whereas scattering state $\phi_{E,3}$ ($\phi_{E,4}$) is associated with an electron (hole) at energy E coming in from the right. The components of the scattering states are written as $\phi_{E,j} = (u_{\uparrow,j}(E), u_{\downarrow,j}(E), v_{\downarrow,j}(E), v_{\uparrow,j}(E))^{\mathrm{T}}$. Additionally, we set $v_{\mathrm{F}} = 1$ in the following.

Note that in our description of proximity induced superconductivity at the helical edge, there is no quasiparticle[3] injection from or escape into the parent bulk superconductor. Accordingly, the only contributions to the charge current are the standard particle current as well as the supercurrent contribution from the Cooper pair condensate.

We start by rewriting the current operator to properly take advantage of the Nambu formalism. For our purposes we need to express the current operator in a particle-hole symmetric fashion in terms of the Nambu spinors

$$\begin{aligned}
\hat{I}(x) &= -e\left(\psi_\uparrow^\dagger\psi_\uparrow - \psi_\downarrow^\dagger\psi_\downarrow\right) \\
&= -\frac{1}{2}e\left(\psi_\uparrow^\dagger\psi_\uparrow - \psi_\uparrow\psi_\uparrow^\dagger - \psi_\downarrow^\dagger\psi_\downarrow + \psi_\downarrow\psi_\downarrow^\dagger\right) \\
&= -\frac{1}{2}e\left(\psi_\uparrow^\dagger, \psi_\downarrow^\dagger, \psi_\downarrow, -\psi_\uparrow\right)\begin{pmatrix}1 & 0 & 0 & 0\\ 0 & -1 & 0 & 0\\ 0 & 0 & 1 & 0\\ 0 & 0 & 0 & -1\end{pmatrix}\begin{pmatrix}\psi_\uparrow\\ \psi_\downarrow\\ \psi_\downarrow^\dagger\\ -\psi_\uparrow^\dagger\end{pmatrix} \\
&= -\frac{1}{2}e\ \Psi^\dagger\left[\hat{\tau}_0\,\hat{\sigma}_3\right]\Psi\,.
\end{aligned} \tag{5.16}$$

This expression now corresponds to the common physical interpretation of holes contributing to the current, but with opposite sign. This rewriting is not strictly necessary. However, the symmetrized expression gives a result which is easier to deal with and can be connected to the Anantram-Datta formula in Ref. [189].

Before inserting the relation between field operators and Bogoliubov quasiparticle operators from Eq. (3.27) in Section 3.1.3, note that there are four scattering states but only two independent fermionic degrees of freedom: The field operators $\psi_\uparrow, \psi_\downarrow$ representing spin up/down electrons, and two Bogoliubov operators γ_i, γ_j. This is

[2] In this specific instance, quasiparticle refers to the solution of the effective BdG-Hamiltonian of the helical edge states with proximity induced superconductivity.

[3] Here we really do refer to the quasiparticles in the parent superconductor.

ensured by particle-hole constraint on the BdG formalism. It guarantees that for every solution $\phi_{E,j}$ there is a charge conjugated one $\mathcal{C}\phi_{E,j} = \phi_{-E,j^c}$. Equivalently, this means that the creation operator $\gamma^\dagger_{E,j}$ has a partner annihilation operator via $\gamma^\dagger_{E,j} = \gamma_{-E,j^c}$.

One way forward is thus to choose two scattering states and eliminate the charge conjugated ones. We then end up with two Bogoliubov quasiparticles and can treat them as ordinary fermions. If we kept four Bogoliubov operators, we would end up with ambiguous cross terms such as $\langle \gamma_{E,i}\gamma_{E',j}\rangle$, which should be zero for $i \neq j$. If they are, however, related by charge conjugation, i.e. $i = j^c$, this is no longer the case.

Let us make this explicit for our particular problem. For now, our interest is solely in the asymptotic form of the scattering states in the left and right leads and we set any details within the system aside. The states have asymptotic forms reading (we introduce an additional superscript in order to specify the lead)

$$\begin{aligned}
\phi^{\mathrm{L}}_{E,1}(x) &= \begin{pmatrix} \mathrm{e}^{\mathrm{i}k_e x} \\ s^{ee}_{LL}\,\mathrm{e}^{-\mathrm{i}k_e x} \\ s^{he}_{LL}\,\mathrm{e}^{-\mathrm{i}k_h x} \\ 0 \end{pmatrix}, \quad \phi^{\mathrm{L}}_{E,2}(x) = \begin{pmatrix} 0 \\ s^{eh}_{LL}\,e^{-\mathrm{i}k_e x} \\ s^{hh}_{LL}\,\mathrm{e}^{-\mathrm{i}k_h x} \\ \mathrm{e}^{\mathrm{i}k_h x} \end{pmatrix}, \\
\phi^{\mathrm{L}}_{E,3}(x) &= \begin{pmatrix} 0 \\ s^{ee}_{LR}\,\mathrm{e}^{-\mathrm{i}k_e x} \\ s^{he}_{LR}\,\mathrm{e}^{-\mathrm{i}k_h x} \\ 0 \end{pmatrix}, \quad \phi^{\mathrm{L}}_{E,4}(x) = \begin{pmatrix} 0 \\ s^{eh}_{RL}\,\mathrm{e}^{-\mathrm{i}k_e x} \\ s^{hh}_{RL}\,\mathrm{e}^{-\mathrm{i}k_h x} \\ 0 \end{pmatrix}
\end{aligned} \tag{5.17a}$$

in the left lead and

$$\begin{aligned}
\phi^{\mathrm{R}}_{E,1}(x) &= \begin{pmatrix} s^{ee}_{RL}\,\mathrm{e}^{\mathrm{i}k_e x} \\ 0 \\ 0 \\ s^{he}_{RL}\,\mathrm{e}^{\mathrm{i}k_h x} \end{pmatrix}, \quad \phi^{\mathrm{R}}_{E,2}(x) = \begin{pmatrix} s^{eh}_{RL}\,\mathrm{e}^{\mathrm{i}k_e x} \\ 0 \\ 0 \\ s^{hh}_{RL}\,\mathrm{e}^{\mathrm{i}k_h x} \end{pmatrix}, \\
\phi^{\mathrm{R}}_{E,3}(x) &= \begin{pmatrix} s^{ee}_{RR}\,\mathrm{e}^{\mathrm{i}k_e x} \\ \mathrm{e}^{-\mathrm{i}k_e x} \\ 0 \\ s^{he}_{RR}\,\mathrm{e}^{\mathrm{i}k_e x} \end{pmatrix}, \quad \phi^{\mathrm{R}}_{E,4}(x) = \begin{pmatrix} s^{eh}_{RR}\,\mathrm{e}^{\mathrm{i}k_e x} \\ 0 \\ \mathrm{e}^{-\mathrm{i}k_h x} \\ s^{hh}_{RR}\,\mathrm{e}^{\mathrm{i}k_h x} \end{pmatrix}
\end{aligned} \tag{5.17b}$$

in the right lead. The momenta are given by $k_{e/h} = E \pm \mu$. In Eq. (5.17), $s^{\alpha\beta}_{ij}$ is the scattering coefficient associated with a particle of type β coming in from lead j to be scattered into a particle of type α exiting the system in lead i. Note that the scattering coefficients are solely determined by the asymptotic form of the scattering states in the leads in Eq. (5.17), since inside the system they are given by completely general superpositions of eigenstates in the intermediate regions. Therefore, the linear equations that produce the scattering coefficients for the different scattering states really only differ where the leads are involved.

This observation is crucial. Note that we can link scattering states 1 and 2 as well as 3 and 4, respectively, by observing that

$$\phi_{E,2}(x) = -\mathcal{C}\left[\phi_{-E,1}(x)\right] \qquad \text{and} \qquad \phi_{E,4}(x) = \mathcal{C}\left[\phi_{-E,3}(x)\right], \tag{5.18}$$

if

$$s_{iL}^{\bar{\alpha}\bar{\beta}}(E) = -[s_{iL}^{\alpha\beta}(-E)]^* \qquad \text{and} \qquad s_{iR}^{\bar{\alpha}\bar{\beta}}(E) = [s_{iR}^{\alpha\beta}(-E)]^*\,, \tag{5.19}$$

where $\bar{\alpha} = h/e$ if $\alpha = e/h$. The additional sign for scattering states 1 and 2 is due to the choice of basis and the convention that the incoming current is always represented by an amplitude of +1. The point of this exercise is the conclusion that

$$\phi_{E,2} = -\phi_{E,1^c} \qquad \text{and} \qquad \phi_{E,4} = \phi_{E,3^c}\,, \tag{5.20}$$

indicating that we can express the scattering states 2 and 4 through the scattering states 1 and 3.

Recall from Section 3.1.3 that the quasiparticle operators can be expressed as

$$\gamma_{E,j} = \int \mathrm{d}x\, \left[\phi_{E,j}^*(x)\right]^T \Psi(x) = \int \mathrm{d}x\, \left[u_{\uparrow,j}^*\psi_\uparrow + u_{\downarrow,j}^*\psi_\downarrow + v_{\downarrow,j}^*\psi_\downarrow^\dagger - v_{\uparrow,j}^*\psi_\uparrow^\dagger\right] \tag{5.21}$$

and

$$\gamma_{E,j}^\dagger = \int \mathrm{d}x\, \left[\phi_{E,j}(x)\right]^T \Psi^\dagger(x) = \int \mathrm{d}x\, \left[-v_{\uparrow,j}\psi_\uparrow + v_{\downarrow,j}\psi_\downarrow + u_{\downarrow,j}\psi_\downarrow^\dagger + u_{\uparrow,j}\psi_\uparrow^\dagger\right]. \tag{5.22}$$

Using the notation $\mathcal{C}\phi_{E,j} = \phi_{-E,j^c}$, this directly implies

$$\gamma_{E,j}^\dagger = \gamma_{-E,j^c} \tag{5.23}$$

and also, combining Eqs. (5.20) and (5.23),

$$\gamma_{E,2} = -\gamma_{-E,1}^\dagger \qquad \text{and} \qquad \gamma_{E,4} = \gamma_{-E,3}^\dagger. \tag{5.24}$$

With that, we can rewrite the field operators by making use of the relations between the components $u_{\sigma,i}, v_{\sigma',j}$ that Eq. (5.18) implies. More specifically

$$\begin{aligned} &\left[u_{\uparrow,2}\gamma_{E,2} - v_{\uparrow,2}^*\gamma_{E,2}^\dagger + u_{\uparrow,4}\gamma_{E,4} - v_{\uparrow,4}^*\gamma_{E,4}^\dagger\right] \\ &= \left[-v_{\uparrow,1}^*(-E)\,\gamma_{-E,1}^\dagger + u_{\uparrow,1}(-E)\gamma_{-E,1} - v_{\uparrow,3}^*(-E)\gamma_{-E,3}^\dagger + u_{\uparrow,3}(-E)\gamma_{-E,3}\right] \end{aligned} \tag{5.25a}$$

$$\begin{aligned} &\left[u_{\downarrow,2}\gamma_{E,2} + v_{\downarrow,2}^*\gamma_{E,2}^\dagger + u_{\downarrow,4}\gamma_{E,4} + v_{\downarrow,4}^*\gamma_{E,4}^\dagger\right] \\ &= \left[v_{\downarrow,1}^*(-E)\,\gamma_{-E,1}^\dagger + u_{\downarrow,1}(-E)\gamma_{-E,1} + v_{\downarrow,3}^*(-E)\gamma_{-E,3}^\dagger + u_{\downarrow,3}(-E)\gamma_{-E,3}\right], \end{aligned} \tag{5.25b}$$

where we have explicitly reinstated the energy dependence of the components after the equal sign to emphasize the sign reversal. We see that substituting the terms from scattering states 2 and 4 by using particle-hole symmetry leads to expressions that are equivalent to the contributions from states 1 and 3 to the field operators (*cf.* Eq. (3.27) in Section 3.1.3) , but with a sign in the energy dependence.

Explicitly, inserting Eqs. (5.25a) and (5.25b) into a continuum-version of the definition of the field operators in Section 3.1.3 gives

$$\psi_\uparrow = \int_{-\infty}^{\infty} \frac{\mathrm{d}E}{\sqrt{2\pi}}\, \left[u_{\uparrow,1}(E)\gamma_{E,1} - v_{\uparrow,1}^*(E)\gamma_{E,1}^\dagger + u_{\uparrow,3}(E)\gamma_{E,3} - v_{\uparrow,3}^*(E)\gamma_{E,3}^\dagger\right] \tag{5.26a}$$

$$\psi_\downarrow = \int_{-\infty}^{\infty} \frac{\mathrm{d}E}{\sqrt{2\pi}}\, \left[u_{\downarrow,1}(E)\gamma_{E,1} + v_{\downarrow,1}^*(E)\gamma_{E,1}^\dagger + u_{\downarrow,3}(E)\gamma_{E,3} + v_{\downarrow,3}^*(E)\gamma_{E,3}^\dagger\right], \tag{5.26b}$$

where we now integrate over *all* energies.

Importantly, the quasiparticle operators in Eq. (5.26) fulfill

$$\begin{aligned}
\langle \gamma^\dagger_{E,i}\gamma_{E',j}\rangle &= \delta_{i,j}\,\delta(E-E')\,f^i_e(E)\\
&= \delta_{i,j}\,\delta(E-E')\,f_0(E,T_i,\mu_i),\\
\langle \gamma_{E,i}\gamma^\dagger_{E',j}\rangle &= \delta_{i,j}\,\delta(E-E')\,\Big(1-f^i_e(E)\Big)\\
&= \delta_{i,j}\,\delta(E-E')\,f^i_h(-E),\\
\langle \gamma_{E,i}\gamma_{E',j}\rangle &= \langle \gamma^\dagger_{E,i}\gamma^\dagger_{E',j}\rangle = 0\,,
\end{aligned} \tag{5.27}$$

where $f^i_e(E,T_i,\mu_i) \equiv f_0(E,T_i,\mu_i) = (\exp((E-\mu_i)/k_BT_i)+1)^{-1}$ is the usual (electronic) Fermi distribution function, $f^i_h(E) \equiv f_0(E,T_i,-\mu_i) = (\exp((E+\mu_i)/k_BT_i)+1)^{-1}$ is the hole distribution function, and T_i and μ_i are temperature and chemical potential in lead i, respectively. Note that the Bogoliubov quasiparticles create orthogonal states since we removed the redundancy, and hence the factor of $\delta_{i,j}$ where $i,j \in \{1,3\}$.

With the help of Eqs. (5.26) and (5.27), we can now finally calculate the expectation value of the current operators derived in the previous section. For the particle contribution, we find

$$\begin{aligned}
\langle \hat{I}(x)\rangle = \frac{1}{2}\frac{e}{h}\sum_{i=1,3}\int_{-\infty}^{\infty}\mathrm{d}E\ \Big[\ & |u_{\uparrow,i}|^2\,f^i_e(E) + |v_{\uparrow,i}|^2\,f^i_h(-E)\\
& - |u_{\uparrow,i}|^2\,f^i_h(-E) - |v_{\uparrow,i}|^2\,f^i_e(E)\\
& - |u_{\downarrow,i}|^2\,f^i_e(E) - |v_{\downarrow,i}|^2\,f^i_h(-E)\\
& + |u_{\downarrow,i}|^2\,f^i_h(-E) + |v_{\downarrow,i}|^2\,f^i_e(E)\Big]\,,
\end{aligned} \tag{5.28}$$

where we omit the energy and position dependence of the components for brevity and restored Planck's constant h. Eq. (5.28) allows us to calculate the particle current contribution at every position x within the junction.

The average supercurrent is given by

$$I_\mathrm{S} = \int \mathrm{d}x'\langle S(x)\rangle, \tag{5.29}$$

where the average of the source term can be evaluated with the help of Eqs. (5.26) and (5.27). We obtain

$$\begin{aligned}
\langle S(x)\rangle = -2e\Delta\sum_{j=1,3}\int_{-\infty}^{\infty}\mathrm{d}E\\
\Big\{\Big[\mathrm{Im}\left(\mathrm{e}^{-\mathrm{i}\varphi}u^*_{\uparrow,j}v_{\downarrow,j}\right) + \mathrm{Im}\left(\mathrm{e}^{-\mathrm{i}\varphi}u^*_{\downarrow,j}v_{\uparrow,j}\right)\Big]\,f^j_e(E)\\
-\Big[\mathrm{Im}\left(\mathrm{e}^{-\mathrm{i}\varphi}v_{\uparrow,j}u^*_{\downarrow,j}\right) + \mathrm{Im}\left(\mathrm{e}^{-\mathrm{i}\varphi}v_{\downarrow,j}u^*_{\uparrow,j}\right)\Big]\,f^j_h(-E)\Big\}\,.
\end{aligned} \tag{5.30}$$

The supercurrent in the left or right superconductor is then given by taking the integral in Eq. (5.29) over the respective regions.

5.2 Nonlocal thermoelectric current dominated by Andreev processes

5.2.1 The setup and average current

The stage is now set to apply the expression for the average particle contribution to the current. The setup we have in mind is rather specific, however, we are going to see why it is chosen this way.

In essence, we want to make use of the fact that the nonlocal pairing can only happen in the equal-spin channel and thus probe the transmission probabilities. Doing so by a temperature bias allows us to favor CAR over EC. We choose to apply the bias to the left of the system and calculate the current in the right lead. Explicitly, we are going to see that this amounts to realizing equilibrium between the S regions and the right reservoir, but to keep the left reservoir at a higher temperature.

The current in the right lead is obtained from Eq. (5.28) by taking $x \to \infty$, which is equivalent to using the asymptotic form of the scattering states in Eq. (5.17b). Furthermore, we need to include a global sign in order to comply with the convention that positive current flows out of a reservoir. In the system of interest here, this amounts to an effective reversal of direction with respect to the current derived in Eq. (5.28). We obtain

$$\begin{aligned} I_R = \frac{1}{2}\frac{e}{h}\int_{-\infty}^{\infty} \mathrm{d}E \; \Big[& \left(1 - |s^{ee}_{RR}(E)|^2 + |s^{he}_{RR}(E)|^2\right) f^R_e(E) \\ & + \left(-1 + |s^{ee}_{RR}(E)|^2 - |s^{he}_{RR}(E)|^2\right) f^R_h(-E) \\ & + \left(-|s^{ee}_{RL}(E)|^2 + |s^{he}_{RL}(E)|^2\right) f^L_e(E) \\ & + \left(|s^{ee}_{RL}(E)|^2 - |s^{he}_{RL}(E)|^2\right) f^L_h(-E)\Big] . \end{aligned} \tag{5.31}$$

By using the particle-hole symmetry of the scattering coefficients in Eq. (5.19) and taking $E \to -E$ in the terms proportional to $f^i_h(-E)$, the average current in the right lead acquires the form

$$\begin{aligned} I_R = \frac{1}{2}\frac{e}{h}\int_{-\infty}^{\infty} \mathrm{d}E \; \Big[& \left(1 - |s^{ee}_{RR}(E)|^2 + |s^{he}_{RR}(E)|^2\right) f^R_e(E) \\ & + \left(-1 + |s^{hh}_{RR}(E)|^2 - |s^{eh}_{RR}(E)|^2\right) f^R_h(E) \\ & + \left(-|s^{ee}_{RL}(E)|^2 + |s^{he}_{RL}(E)|^2\right) f^L_e(E) \\ & + \left(|s^{hh}_{RL}(E)|^2 - |s^{eh}_{RL}(E)|^2\right) f^L_h(E)\Big] . \end{aligned} \tag{5.32}$$

This is manifestly in the form familiar from the seminal paper by Anantram and Datta [189]. The first two lines in Eq. (5.32) can be interpreted as the contribution from electrons and holes injected from the right, while the following lines are associated with transmission processes from electron and hole injection from the left.

More insight can be gained by recalling that due to the unitarity of the scattering matrix, we have

$$\sum_{j,\alpha} |s_{ij}^{\beta\alpha}|^2 = 1 \qquad \text{and} \qquad \sum_{i,\beta} |s_{ij}^{\beta\alpha}|^2 = 1, \tag{5.33}$$

from which the explicit relations

$$|s_{LL}^{ee}|^2 + |s_{LL}^{eh}|^2 + |s_{LR}^{ee}| + |s_{LR}^{eh}| - 1 = |s_{LL}^{hh}|^2 + |s_{LL}^{he}|^2 + |s_{LR}^{hh}| + |s_{LR}^{he}| - 1 = 0 \tag{5.34}$$

follow.

Therefore, we can formally add zero to Eq. (5.32) and append the terms

$$\begin{aligned} \int_{-\infty}^{\infty} \mathrm{d}E \, \Big[&\Big(|s_{LL}^{ee}|^2 + |s_{LL}^{eh}|^2 + |s_{LR}^{ee}| + |s_{LR}^{eh}| - 1 \Big) \, f^S \\ &- \Big(|s_{LL}^{hh}|^2 + |s_{LL}^{he}|^2 + |s_{LR}^{hh}| + |s_{LR}^{he}| - 1 \Big) \, f^S \Big] , \end{aligned} \tag{5.35}$$

where we choose f^S to be the equilibrium Fermi function in the superconductor, i.e. $f^S \equiv f_0(E, T_S, 0) = f_e^S = f_h^S$ so that electrons and holes obey the same distribution function. Regrouping the terms inside the sum in Eq. (5.35) gives

$$\begin{aligned} -f^S \, \Big[&\Big(1 - |s_{LL}^{ee}|^2 + |s_{LL}^{he}|^2 \Big) + \Big(-|s_{LR}^{ee}| + |s_{LR}^{he}| \Big) \\ &- \Big(1 - |s_{LL}^{hh}|^2 + |s_{LL}^{eh}|^2 \Big) \Big(-|s_{LR}^{hh}| + |s_{LR}^{eh}| \Big) \Big] , \end{aligned} \tag{5.36}$$

and adding them to Eq. (5.32) finally yields

$$\begin{aligned} I_R = \frac{1}{2} \frac{e}{h} \int_{-\infty}^{\infty} \mathrm{d}E \, \Big[&\Big(1 - |s_{RR}^{ee}|^2 + |s_{RR}^{he}|^2 \Big) \Big(f_e^R - f^S \Big) \\ &- \Big(1 - |s_{RR}^{hh}|^2 + |s_{RR}^{eh}|^2 \Big) \Big(f_h^R - f^S \Big) \\ &+ \Big(-|s_{RL}^{ee}|^2 + |s_{RL}^{he}|^2 \Big) \Big(f_e^L - f^S \Big) \\ &- \Big(-|s_{RL}^{hh}|^2 + |s_{RL}^{eh}|^2 \Big) \Big(f_h^L - f^S \Big) \Big] . \end{aligned} \tag{5.37}$$

By noticing that $(f_\alpha^j - f^S)(E) = -(f_{\bar{\alpha}}^j - f^S)(-E)$ and $|s_{ij}^{\alpha\beta}(E)| = |s_{ij}^{\bar{\alpha}\bar{\beta}}(-E)|$ due to particle-hole symmetry, with $\bar{\alpha} = h, e$ if $\alpha = e, h$, the terms for hole injection in Eq. (5.37) can be folded back onto the terms for electron injection. We thus end up with

$$I_R = \frac{e}{h} \int_{-\infty}^{\infty} \mathrm{d}E \, \Big[\Big(1 - |s_{RR}^{ee}|^2 + |s_{RR}^{he}|^2 \Big) \Big(f_e^R - f^S \Big) + \Big(-|s_{RL}^{ee}|^2 + |s_{RL}^{he}|^2 \Big) \Big(f_e^L - f^S \Big) \Big] . \tag{5.38}$$

In Eq. (5.38), the first term is due to local reflections of particles injected from reservoir R, while the second term corresponds to the nonlocal contribution from transmitted particles, which have been injected from the left. One can readily see that the current is solely due to nonlocal processes as soon as the right reservoir is at equilibrium with the superconductors, *i.e.,* $T_\mathrm{R} = T_\mathrm{S} = T_0$ and $\mu_\mathrm{R} = \mu_\mathrm{S} = 0$. Furthermore, since our objective is a purely thermoelectric effect, we also set $\mu_\mathrm{L} = 0$ such that there is no voltage bias between the reservoirs. We introduce the temperature difference θ as the new key variable and parametrize the temperature of the left reservoir as $T_\mathrm{L} = T_0 + \theta$.

As a result, the nonlocal current $I^{\mathrm{R}} = I_{\mathrm{R}}^{ee} + I_{\mathrm{R}}^{he}$ can be separated in a normal part

$$I_{\mathrm{R}}^{ee} = -I_0 \int_{-\infty}^{\infty} \frac{\mathrm{d}E}{\Delta_0} T_{\mathrm{RL}}^{ee}(E)\, \delta f(E) \tag{5.39a}$$

and an Andreev contribution

$$I_{\mathrm{R}}^{he} = I_0 \int_{-\infty}^{\infty} \frac{\mathrm{d}E}{\Delta_0} T_{\mathrm{RL}}^{he}(E)\, \delta f(E), \tag{5.39b}$$

where we define $T_{\mathrm{RL}}^{\alpha\beta} = |s_{\mathrm{RL}}^{\alpha\beta}|^2$ to simplify the notation slightly. Furthermore, we made the integrand dimensionless by introducing $I_0 = e\Delta_0/h$ and the abbreviation $\delta f(E) = f_e^{\mathrm{L}}(E, T_0 + \theta, 0) - f^{\mathrm{S}}(E, T_0, 0)$.

Eq. (5.39b) represents the connection between the thermally induced charge current and unconventional superconductivity. To see this, recall Section 4.3.2.2, where we showed that nonlocal CAR processes are closely related to the spin-polarized, triplet component of the anomalous Green function. Since the latter can be interpreted as a Cooper pair wave function, one can interpret nonlocal CAR events as a signature of unconventional superconductivity. We are going to explore the consequences for the supercurrent in Section 5.4 and relate the thermoelectric effect to odd-frequency superconductivity in Section 5.5.

Importantly, δf is odd in energy and thus fulfills

$$\delta f(-E) = -\delta f(E). \tag{5.40}$$

Note that this is in stark contrast to a voltage bias V between two reservoirs at the same temperature. Indeed, the difference of Fermi functions in that case would be even and obey

$$f_0(E, T, V/2) - f_0(E, T, -V/2) = f_0(-E, T, V/2) - f_0(-E, T, -V/2). \tag{5.41}$$

Note that the terms in Eq. (5.35) are equivalent to contributions which arise by using the well-known formula from Ref. [189] if a superconducting reservoir with quasiparticle injection is included. Accordingly, setting the scattering coefficients into/out of the superconductor to zero is effectively equivalent to the sum rules Eq. (5.34) and adding zeros as in Eq. (5.35). Strikingly, this means that Eq. (5.38) holds even in the presence of quasiparticle exchange with the bulk superconductor. In that case, however, the scattering amplitudes connecting reservoirs L and R would no longer add up to unity.

5.2.2 Characterization of the effect

The result of the previous section in Eq. (5.39) makes it clear what we are looking for. Since CAR is typically weaker than EC, the only way to have the Andreev contribution dominate the normal one is by making CAR more asymmetric than EC.

Apart from a temperature difference between the leads, there are three crucial requirements for this peculiar thermoelectric effect: (i) phase difference $\varphi \neq n\pi$, with $n \in \mathbb{Z}$; (ii) base temperature $T_0 \approx T_c/2$; (iii) an asymmetry in the junction,

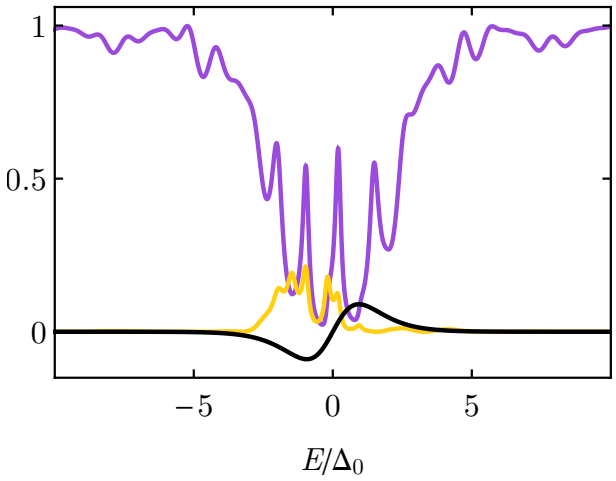

Figure 5.2: Plot of the EC amplitude $T^{ee}_{\mathrm{RL}}(E)$ (purple) and CAR amplitude $T^{he}_{\mathrm{RL}}(E)$ (yellow) together with the difference of Fermi functions $\delta f(E)$ (black) as functions of energy, where the parameters are set to their standard values given in Fig. 5.1. Adapted from Ref. [136], copyright (2020) by The American Physical Society.

most easily achieved by unequal widths of the N regions, such that $d_{\mathrm{NL}} \neq d_{\mathrm{NR}}$. In the following, we will first explore the influence of these parameters on the nonlocal current and state the explanation for it. In the following section, we are going to provide a detailed derivation for it.

We start by plotting the normal and crossed Andreev transmission probabilities together with δf in Fig. 5.2 for a representative set of parameters (see caption, these values will be used throughout the chapter unless explicitly stated otherwise), most notably $\varphi = \pi/2$ and with temperatures $T_0 = T_c/2$ and $\theta = T_c/2$. Just by bare inspection of the plot we see that the CAR probability is far more asymmetric in energy. On the relevant energy scale which will mainly contribute to the integral, set by T and θ, the EC amplitude is close to being symmetric, and we expect the EC contribution to the nonlocal charge current to be small. In contrast, the CAR probability has an asymmetry that matches the integration window very well.

We show the resulting nonlocal currents as a function of the temperature gradient θ in Fig. 5.3 (a), with the other parameters the same as in Fig. 5.2. First, at $\theta = 0$ the reservoirs are in equilibrium and there is of course no current. Increasing the temperature difference leads to a finite charge current, which indeed is hugely dominated by the CAR contribution. While this is true for both $\theta > 0$ and $\theta < 0$, we are going to restrict the discussion to the former case and positive temperature differences in the following.

Next, Fig. 5.3 (b) depicts the behavior of the currents in dependence of the phase difference φ. They show a Josephson-like sinusoidal behavior, and strikingly, the CAR contribution is dominating the charge current for all values of φ. The phase difference is revealed as an ideal parameter to tune the magnitude and sign of the effect. Note that the currents even vanish for $\varphi = n\pi$ with $n \in \mathbb{Z}$, such that the phase difference can be used to switch the effect off entirely.

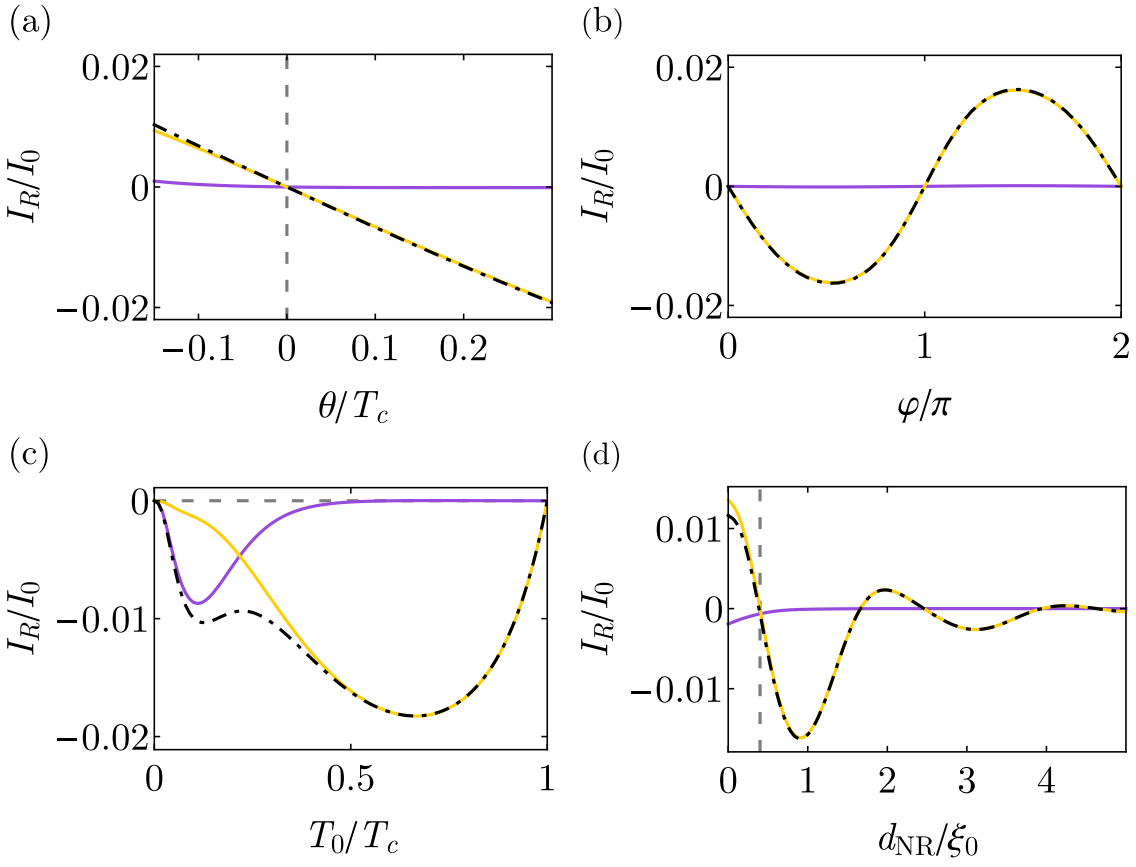

Figure 5.3: Plots of the contributions to the nonlocal charge current as a function of (a) the temperature difference θ, (b) the phase difference across the junction φ, (c) the base temperature T_0, and (d) the width of the right intermediate normal region d_{NR}. Corresponding to the colors in Fig. 5.2, the normal contribution I_{R}^{ee} (Andreev contribution I_{R}^{he}) is shown in purple (yellow). The total nonlocal current I_R is represented by the black dashed line. Panels (a)–(c) are adapted from Ref. [136], copyright (2020) by The American Physical Society.

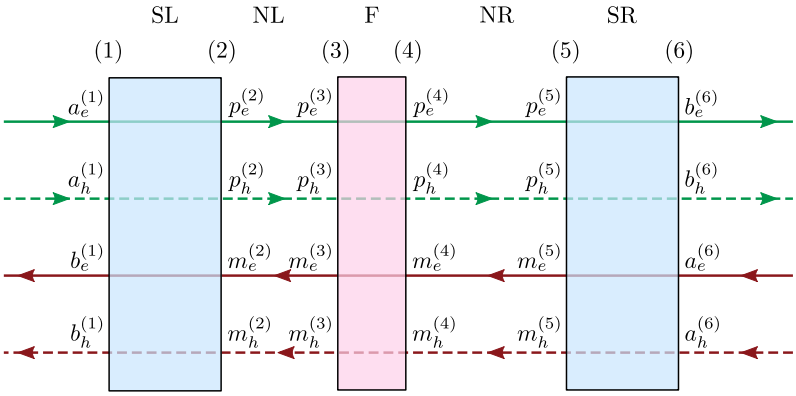

Figure 5.4: Schematic depiction of the wave function amplitudes $a_\alpha^{(i)}, b_\alpha^{(i)}, p_\alpha^{(i)}, m_\alpha^{(i)}$ at the interfaces across the system. The shaded blue (pink) areas correspond to the superconducting (ferromagnetic) barriers. Solid green (brown) arrows indicate rightmoving modes with spin $\uparrow$ (leftmoving modes with spin $\downarrow$), while solid (dashed) lines refer to electrons (holes). Adapted from the supplemental material of Ref. [136], copyright (2020) by The American Physical Society.

The influence of the base temperature T_0 at $\theta = T_0/4$ fixed is shown in Fig. 5.3 (c). The thermoelectrically produced charge current is largest for T_0 close to $T_c/2$. Furthermore, only for $T_0 \gtrsim T_c/2$ does the Andreev contribution dominate. This is due to the fact that for these temperatures the asymmetry of the CAR amplitude fits well to the difference of Fermi functions δf. For lower base temperatures, the maximum and minimum of δf move closer to $E = 0$ and also pick up the asymmetry of the EC probability.

Lastly, in Fig. 5.3 (d) we plot the nonlocal charge current as a function of the width of the right N region d_{NR}. First, note that at $d_{\mathrm{NR}} = d_{\mathrm{NL}}$ (dashed vertical line) the Andreev contribution vanishes. Except for a few special points, an asymmetric choice for d_{NR} leads to a finite Andreev contribution dominating the current. We also see that increasing d_{NR} suppresses I_{R}^{ee}. This is because a wider N region leads to denser quasi-bound state resonances and thus more peaks in the normal transmission, which results in an even more pronounced averaging out of the normal contribution to the current.

5.3 Mechanism of the effect

The previous section clearly shows that an Andreev dominated nonlocal electric current can be achieved rather generically for a wide range of parameters. Furthermore, the phase difference φ between the superconductors is an ideal candidate to tune the effect. In particular, as we have seen it seems as if suppressing the normal contribution is guaranteed as long as the base temperature is large enough so that the integration window averages over the subgap resonances. In contrast, the nonlocal Andreev current is very sensitive to the phase difference and the widths of the intermediate normal regions. This suggests that the underlying physics is different. In this section, we first present an illustrative solution to the scattering problem in our

SFS-heterostructure which provides some insight into the mechanism. Afterwards, we show that the constraint from particle-hole symmetry on that solution is enough to account for almost all signatures discussed in Section 5.2.2.

5.3.1 Solving the scattering problem

The method we employ here is similar to the way we obtained resonance conditions for bound states by combining scattering matrices for pieces of the full scattering problem. Note that throughout this section, we use $t_{ij}^{\alpha\beta}$ with $i \neq j$ for transmissions and $r_{ii}^{\alpha\beta}$ for reflection coefficients in order to make it easier to distinguish them.

We adopt the convention illustrated in Fig. 5.4. within the junction, the amplitudes of modes associated with right-(left-)moving particles and holes are denoted $p_{e/h}^{(i)}$ ($m_{e/h}^{(i)}$), where (i) refers to the number of the interface for clarity.

The outmost SN-interfaces connect the modes within the system to the asymptotic components corresponding to the incoming and outgoing amplitudes. In line with previous sections, they are labeled $a_{e/h}^{(i)}$ and $b_{e/h}^{(i)}$, respectively. The full scattering matrix of the system then relates them according to

$$\begin{pmatrix} b_e^{(1)} \\ b_h^{(1)} \\ b_e^{(6)} \\ b_h^{(6)} \end{pmatrix} = S \begin{pmatrix} a_e^{(1)} \\ a_h^{(1)} \\ a_e^{(6)} \\ a_h^{(6)} \end{pmatrix}, \tag{5.42}$$

with

$$S = \begin{pmatrix} R & T' \\ T & R' \end{pmatrix} \tag{5.43a}$$

and

$$R = \begin{pmatrix} r_{\mathrm{LL}}^{ee} & r_{\mathrm{LL}}^{eh} \\ r_{\mathrm{LL}}^{he} & r_{\mathrm{LL}}^{hh} \end{pmatrix}, R' = \begin{pmatrix} r_{\mathrm{RR}}^{ee} & r_{\mathrm{RR}}^{eh} \\ r_{\mathrm{RR}}^{he} & r_{\mathrm{RR}}^{hh} \end{pmatrix}, T = \begin{pmatrix} t_{\mathrm{RL}}^{ee} & t_{\mathrm{RL}}^{eh} \\ t_{\mathrm{RL}}^{he} & t_{\mathrm{RL}}^{hh} \end{pmatrix}, T' = \begin{pmatrix} t_{\mathrm{LR}}^{ee} & t_{\mathrm{LR}}^{eh} \\ t_{\mathrm{LR}}^{he} & t_{\mathrm{LR}}^{hh} \end{pmatrix}. \tag{5.43b}$$

In a similar fashion, we can connect the modes within the structure by the scattering matrices of the individual barriers. In contrast to Chapter 3, however, we want the scattering coefficients of the individual S and F barriers to not contain the phase shift due to a translation of the barriers. The solutions to the BdG-Hamiltonian within the N regions are given by (note that we set $\mu = 0$)

$$\phi_+^e(x) = \mathrm{e}^{\mathrm{i}Ex} \begin{pmatrix} 1 \\ 0 \\ 0 \\ 0 \end{pmatrix}, \phi_-^e(x) = \mathrm{e}^{-\mathrm{i}Ex} \begin{pmatrix} 0 \\ 1 \\ 0 \\ 0 \end{pmatrix}, \phi_-^h(x) = \mathrm{e}^{-\mathrm{i}Ex} \begin{pmatrix} 0 \\ 0 \\ 1 \\ 0 \end{pmatrix}, \phi_+^h(x) = \mathrm{e}^{\mathrm{i}Ex} \begin{pmatrix} 0 \\ 0 \\ 0 \\ 1 \end{pmatrix}, \tag{5.44}$$

where $+$ ($-$) corresponds to right-(left-)moving electrons (e) or holes (h). Therefore, we need to build the scattering matrix between interfaces (i) and $(i+1)$ from the solutions $\phi_\pm^\alpha(x - x_{(j)})$ and $\phi_\pm^\alpha(x - x_{(j+1)})$, where $x_{(j)}$ is the position of the j-th interface. Note that this convention also means that the normal regions acquire a scattering matrix whose elements merely reflect a phase factor describing propagation. This

factor was contained within the scattering matrix of the barriers in Chapter 3. The relations between left- and rightmoving modes inside the junction then read

$$\begin{pmatrix} b_e^{(1)} \\ b_h^{(1)} \\ p_e^{(2)} \\ p_h^{(2)} \end{pmatrix} = S_{\mathrm{SL}} \begin{pmatrix} a_e^{(1)} \\ a_h^{(1)} \\ m_e^{(2)} \\ m_h^{(2)} \end{pmatrix} \quad \text{with} \quad S_{\mathrm{SL}} = \begin{pmatrix} 0 & r^{eh}_{\mathrm{SL}(11)} & t^{ee}_{\mathrm{SL}(12)} & 0 \\ r^{he}_{\mathrm{SL}(11)} & 0 & 0 & t^{hh}_{\mathrm{SL}(12)} \\ t^{ee}_{\mathrm{SL}(21)} & 0 & 0 & r^{eh}_{\mathrm{SL}(22)} \\ 0 & t^{hh}_{\mathrm{SL}(21)} & r^{he}_{\mathrm{SL}(22)} & 0 \end{pmatrix}, \tag{5.45a}$$

$$\begin{pmatrix} m_e^{(2)} \\ m_h^{(2)} \\ p_e^{(3)} \\ p_h^{(3)} \end{pmatrix} = S_{\mathrm{NL}} \begin{pmatrix} p_e^{(2)} \\ p_h^{(2)} \\ m_e^{(3)} \\ m_h^{(3)} \end{pmatrix} \quad \text{with} \quad S_{\mathrm{NL}} = \begin{pmatrix} 0 & 0 & t^{ee}_{\mathrm{NL}(23)} & 0 \\ 0 & 0 & 0 & t^{hh}_{\mathrm{NL}(23)} \\ t^{ee}_{\mathrm{NL}(32)} & 0 & 0 & 0 \\ 0 & t^{hh}_{\mathrm{NL}(32)} & 0 & 0 \end{pmatrix}, \tag{5.45b}$$

$$\begin{pmatrix} m_e^{(3)} \\ m_h^{(3)} \\ p_e^{(4)} \\ p_h^{(4)} \end{pmatrix} = S_{\mathrm{F}} \begin{pmatrix} p_e^{(3)} \\ p_h^{(3)} \\ m_e^{(4)} \\ m_h^{(4)} \end{pmatrix} \quad \text{with} \quad S_{\mathrm{F}} = \begin{pmatrix} r^{ee}_{\mathrm{F}(33)} & 0 & t^{ee}_{\mathrm{F}(34)} & 0 \\ 0 & r^{hh}_{\mathrm{F}(33)} & 0 & t^{hh}_{\mathrm{F}(34)} \\ t^{ee}_{\mathrm{F}(43)} & 0 & r^{ee}_{\mathrm{F}(44)} & 0 \\ 0 & t^{hh}_{\mathrm{F}(43)} & 0 & r^{hh}_{\mathrm{F}(44)} \end{pmatrix}, \tag{5.45c}$$

$$\begin{pmatrix} m_e^{(4)} \\ m_h^{(4)} \\ p_e^{(5)} \\ p_h^{(5)} \end{pmatrix} = S_{\mathrm{NR}} \begin{pmatrix} p_e^{(4)} \\ p_h^{(4)} \\ m_e^{(5)} \\ m_h^{(5)} \end{pmatrix} \quad \text{with} \quad S_{\mathrm{NR}} = \begin{pmatrix} 0 & 0 & t^{ee}_{\mathrm{NR}(45)} & 0 \\ 0 & 0 & 0 & t^{hh}_{\mathrm{NR}(45)} \\ t^{ee}_{\mathrm{NR}(54)} & 0 & 0 & 0 \\ 0 & t^{hh}_{\mathrm{NR}(54)} & 0 & 0 \end{pmatrix}, \tag{5.45d}$$

$$\begin{pmatrix} m_e^{(5)} \\ m_h^{(5)} \\ b_e^{(6)} \\ b_h^{(6)} \end{pmatrix} = S_{\mathrm{SR}} \begin{pmatrix} p_e^{(5)} \\ p_h^{(5)} \\ a_e^{(6)} \\ a_h^{(6)} \end{pmatrix} \quad \text{with} \quad S_{\mathrm{SR}} = \begin{pmatrix} 0 & r^{eh}_{\mathrm{SR}(55)} & t^{ee}_{\mathrm{SR}(56)} & 0 \\ r^{he}_{\mathrm{SR}(55)} & 0 & 0 & t^{hh}_{\mathrm{SR}(56)} \\ t^{ee}_{\mathrm{SR}(65)} & 0 & 0 & r^{eh}_{\mathrm{SR}(66)} \\ 0 & t^{hh}_{\mathrm{SR}(65)} & r^{he}_{\mathrm{SR}(66)} & 0 \end{pmatrix}. \tag{5.45e}$$

Note that there are 16 equations in Eqs. (5.45a)–(5.45e) which do not involve the outgoing amplitudes $b_\alpha^{(i)}$. These can be used to solve for the coefficients $p_\alpha^{(i)}$, $m_\alpha^{(i)}$ which are then going to be given in terms of $a_\alpha^{(i)}$. As a last step, one can plug these solutions back into the four equations in Eqs. (5.45a) and (5.45e) for the outgoing coefficients $b_\alpha^{(i)}$. They are then directly given in terms of the incoming coefficients $a_\alpha^{(j)}$, such that we can read off the global scattering matrix elements of S in Eq. (5.42).

The CAR coefficient is given in the form

$$t^{he}_{\mathrm{RL}} = \frac{t_1 + t_2}{1 - \boldsymbol{\Sigma}} = (t_1 + t_2) \sum_{n=0}^{\infty} \boldsymbol{\Sigma}^n, \tag{5.46}$$

where we rediscover the self-energies from Fig. 3.12 in Section 3.3.2 given by

$$\boldsymbol{\Sigma} = \Sigma_1^{\mathrm{L}} + \Sigma_1^{\mathrm{R}} - \Sigma_1^{\mathrm{L}}\Sigma_1^{\mathrm{R}} + \Sigma_2^{\uparrow} + \Sigma_2^{\downarrow} - \Sigma_2^{\uparrow}\Sigma_2^{\downarrow} + \Sigma_3^{e} + \Sigma_3^{h} \tag{5.47}$$

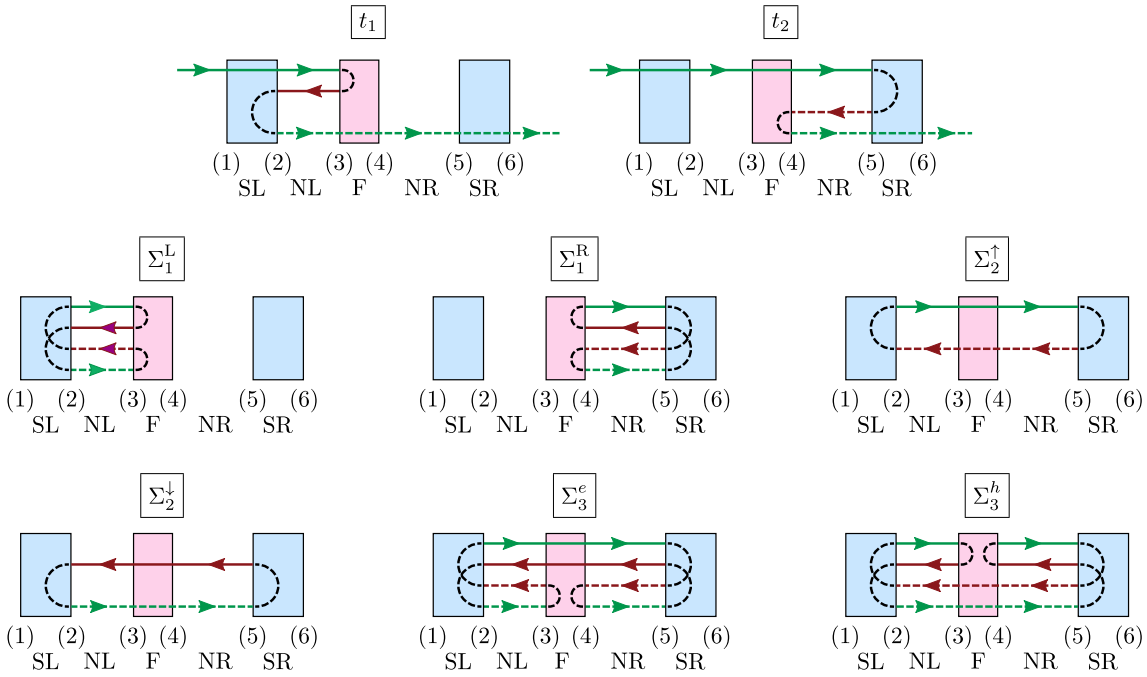

Figure 5.5: Sketch of the contributions to the crossed Andreev reflection coefficient t^{he}_{RL}. The shaded areas and arrows follow the same convention as Fig. 5.4. As explained in the main text, $t_{1,2}$ are the lowest order transmissions involving the smallest possible number of reflections and transmissions through the S and F barriers. The self-energies $\Sigma_1^{\mathrm{L/R}}$, $\sigma_2^{\uparrow/\downarrow}$ and $\Sigma_3^{e/h}$ correspond to closed loops within the heterostructures, closely related to bound states. Figure taken from Ref. [136], copyright (2020) by The American Physical Society.

and shown again in Fig. 5.5, together with the two lowest order processes t_1 and t_2. Note that we here use a different convention regarding the scattering coefficients and explicitly keep track of the phases picked up during propagation, such that the expressions for the self-energies take a slightly different form in terms of the scattering coefficients in this chapter. However, the result stays the same.

Strikingly, Eq. (5.46) implies a straightforward interpretation of the CAR coefficient. It is the sum of two terms t_1 and t_2 corresponding to the lowest order processes contributing to CAR (also see Fig. 5.5), with the additional insertion of all possible closed loops labeled $\Sigma_1^{\mathrm{L/R}}, \Sigma_2^{\uparrow/\downarrow}, \Sigma_3^{e/h}$.

Eq. (5.46) has two important consequences. First, we see that the CAR coefficient is proportional to the sum of the two lowest order processes, which means that the transmission probability will depend on the interference of both paths. Second, the closed loops affect both t_1 and t_2 in the exact same way, making interference between the two possible.

5.3.2 Implications for nonlocal currents

One can further analyze the decomposition of the CAR coefficient in order to see the consequences for the nonlocal charge current.

As a first step, notice that the loops $\Sigma_1^{\mathrm{L/R}}$ consist of all reflections and all four modes propagating through NL and NR, respectively. Hence, they should themselves be particle-hole symmetric and fulfill

$$\Sigma_1^{\mathrm{L/R}}(E) = \left(\Sigma_1^{\mathrm{L/R}}(-E)\right)^*, \tag{5.48a}$$

or, more specifically

$$\mathrm{Re}\left[\Sigma_1^{\mathrm{L/R}}(E)\right] = \mathrm{Re}\left[\Sigma_1^{\mathrm{L/R}}(-E)\right], \quad \mathrm{Im}\left[\Sigma_1^{\mathrm{L/R}}(E)\right] = -\,\mathrm{Im}\left[\Sigma_1^{\mathrm{L/R}}(-E)\right]. \tag{5.48b}$$

By the same logic, the terms $\Sigma_2^{\uparrow/\downarrow}$ and $\Sigma_3^{e/h}$ should be connected by particle-hole symmetry among themselves, such that

$$\Sigma_2^{\uparrow}(E) = \left(\Sigma_2^{\downarrow}(-E)\right)^*, \qquad \Sigma_3^{e}(E) = \left(\Sigma_3^{h}(-E)\right)^*, \tag{5.49}$$

and thus

$$\begin{aligned} \mathrm{Re}\left[\Sigma_2^{\uparrow}(E)\right] &= \mathrm{Re}\left[\Sigma_2^{\downarrow}(-E)\right], & \mathrm{Im}\left[\Sigma_2^{\uparrow}(E)\right] &= -\,\mathrm{Im}\left[\Sigma_2^{\downarrow}(-E)\right], \\ \mathrm{Re}\left[\Sigma_3^{e}(E)\right] &= \mathrm{Re}\left[\Sigma_3^{h}(-E)\right], & \mathrm{Im}\left[\Sigma_3^{e}(E)\right] &= -\,\mathrm{Im}\left[\Sigma_3^{h}(-E)\right]. \end{aligned} \tag{5.50}$$

As a next step, we define auxiliary complex functions $u(E), w(E), z(E)$ as

$$\begin{aligned} u(E) &= \Sigma_1^{\mathrm{L}}(E) + \Sigma_1^{\mathrm{R}}(E) - \Sigma_1^{\mathrm{L}}(E)\Sigma_1^{\mathrm{R}}(E), \\ w(E) &= \Sigma_2^{\uparrow}(E) + \Sigma_2^{\downarrow}(E) - \Sigma_2^{\uparrow}(E)\Sigma_2^{\downarrow}(E), \\ z(E) &= \Sigma_3^{\mathrm{e}}(E) + \Sigma_3^{h}(E), \end{aligned} \tag{5.51}$$

which implies $u + w + z = \boldsymbol{\Sigma}$. Importantly,

$$u^*(E) = u(-E), \quad w^*(E) = w(-E), \quad z^*(E) = z(-E), \tag{5.52}$$

due to Eqs. (5.48) and (5.49). Now Eq. (5.52) directly implies

$$[\boldsymbol{\Sigma}(E)]^* = \boldsymbol{\Sigma}(-E), \tag{5.53}$$

from which we immediately see that $|\boldsymbol{\Sigma}|$ is an even function of E.

To extract information about the full crossed Andreev reflection coefficient, we bring Eq. (5.46) in the form

$$t^{he}_{\mathrm{RL}} = (t_1 + t_2)\, \frac{1 - \boldsymbol{\Sigma}^*}{1 + |\boldsymbol{\Sigma}|^2 - \boldsymbol{\Sigma} - \boldsymbol{\Sigma}^*}, \tag{5.54}$$

where the denominator $d(E) = 1 + |\boldsymbol{\Sigma}(E)|^2 - \boldsymbol{\Sigma}(E) - (\boldsymbol{\Sigma}(E))^*$ is a real number with the properties

$$d^*(E) = d(-E) \qquad \Rightarrow \quad |d(E)|^2 = |d(-E)|^2. \tag{5.55}$$

Furthermore, the numerator of the second term in Eq. (5.54), *i.e.*, $n(E) = 1 - (\boldsymbol{\Sigma}(E))^*$, obeys

$$n^*(E) = n(-E) \qquad \Rightarrow \quad |n(E)|^2 = |n(-E)|^2. \tag{5.56}$$

Hence, the modulus of all higher order corrections represented by the term $1/(1 - \boldsymbol{\Sigma}) = d/n$ is an even function of energy. However, since the finite thermoelectric current is only possible if there is a finite antisymmetric contribution to the CAR coefficient, Eq. (5.46) implies that the asymmetry must be rooted in the interference of the two lowest-order paths.

To explicitly show this, we consider the first term in Eq. (5.54) responsible for the interference effect. Explicitly, we obtain

$$\begin{aligned} t_1 + t_2 = t^{ee}_{\mathrm{SL}(21)} t^{ee}_{\mathrm{NL}(32)} t^{hh}_{\mathrm{NR}(54)} t^{hh}_{\mathrm{SR}(65)} \Big(& r^{ee}_{\mathrm{F}(33)} t^{ee}_{\mathrm{NL}(23)} r^{he}_{\mathrm{SL}(22)} t^{hh}_{\mathrm{NL}(32)} t^{hh}_{\mathrm{F}(43)} \\ & + t^{ee}_{\mathrm{F}(43)} t^{ee}_{\mathrm{NR}(54)} r^{he}_{\mathrm{SR}(55)} t^{hh}_{\mathrm{NR}(45)} r^{hh}_{\mathrm{F}(44)} \Big). \end{aligned} \tag{5.57}$$

Taking advantage of the analytical expressions for the coefficients, we can write

$$\begin{gathered} t^{hh}_{\mathrm{F}(43)} = t^{ee}_{\mathrm{F}(43)}, \qquad r^{ee}_{\mathrm{F}(33)} = r^{hh}_{\mathrm{F}(44)}, \qquad r^{he}_{\mathrm{SR}(55)} = \mathrm{e}^{\mathrm{i}\varphi}\, r^{he}_{\mathrm{SL}(22)} \\ t^{ee}_{\mathrm{NL}(23)} = t^{hh}_{\mathrm{NL}(32)} = \mathrm{e}^{\mathrm{i}d_{\mathrm{NL}}E}, \qquad \text{and} \qquad t^{ee}_{\mathrm{NR}(54)} = t^{hh}_{\mathrm{NR}(45)} = \mathrm{e}^{\mathrm{i}d_{\mathrm{NR}}E}. \end{gathered} \tag{5.58}$$

Consequently, we can readily express Eq. (5.57) as

$$t_1 + t_2 = t^{ee}_{\mathrm{SL}(21)} t^{ee}_{\mathrm{NL}(32)} t^{hh}_{\mathrm{NR}(54)} t^{hh}_{\mathrm{SR}(65)} r^{ee}_{\mathrm{F}(33)} r^{he}_{\mathrm{SL}(22)} t^{ee}_{\mathrm{NR}(54)} \left(\mathrm{e}^{2\mathrm{i}d_{\mathrm{NL}}E} + \mathrm{e}^{2\mathrm{i}d_{\mathrm{NR}}E + \mathrm{i}\varphi} \right), \tag{5.59}$$

which has the form

$$t_1 + t_2 = 2|\tilde{t}(E)| \mathrm{e}^{\mathrm{i}\tau(E)} \cos(\Lambda/2). \tag{5.60}$$

In Eq. (5.60), we defined the phase difference between the two lowest order paths as

$$\Lambda = \varphi + 2(d_{\mathrm{NR}} - d_{\mathrm{NL}})E, \tag{5.61}$$

as well as included an unimportant global phase τ. The absolute value $\tilde{t}(E)$ is even in energy and thus fulfills $|\tilde{t}(E)| = |\tilde{t}(-E)|$ due to particle-hole symmetry.

Putting together the results from Eqs. (5.54)–(5.56) and (5.60), we arrive at the final expression for the squared modulus of the CAR coefficient, which reads

$$|t^{he}_{\mathrm{RL}}|^2 = T^{he}_{\mathrm{RL}}(E) = \gamma(E,\varphi)\cos^2\left[\varphi/2 + (d_{\mathrm{NR}} - d_{\mathrm{NL}})\,E\right]. \tag{5.62}$$

the function $\gamma(E,\varphi)$ is even in E and defined as

$$\gamma(E,\varphi) = \frac{4|\tilde{t}(E,\varphi)|^2|n(E,\varphi])|^2}{|d(E,\varphi)|^2}. \tag{5.63}$$

In conclusion, the antisymmetric contribution to the CAR amplitude is solely due to the interference of the two paths. The self-energies only lead to a correction which is even in energy, by influencing the factor $\gamma(E,\varphi)$. Interestingly, the contribution to the CAR amplitude which is odd in energy can be extracted using Eq. (5.62) and reads

$$T^{he}_{\mathrm{RL}}(-E) - T^{he}_{\mathrm{RL}}(E) = \gamma(E,\varphi)\,\sin\left[2E\,(d_{\mathrm{NR}} - d_{\mathrm{NL}})\right]\,\sin\left[\varphi\right]. \tag{5.64}$$

The compact relations in Eqs. (5.62) and (5.64) are enough to explain a lot of the features of the CAR amplitude and the nonlocal current in Fig. 5.3. In particular, for our standard set of parameters we have $\varphi = \pi/2$, $d_{\mathrm{NL}} = 0.4\xi_0$, $d_{\mathrm{NL}} = 0.9\xi_0$ and thus $d_{\mathrm{NR}} - d_{\mathrm{NL}} = 0.5\xi_0$. In Eq. (5.62) the cosine is zero if

$$\varphi/2 + (d_{\mathrm{NR}} - d_{\mathrm{NL}})\,E = \pi/2, \tag{5.65}$$

which happens at $E = \pi/2 \cdot \Delta_0$. Going back to Fig. 5.2, we see that at this energy the CAR amplitude is indeed suppressed.

5.4 Supercurrent

In the previous sections, we established that a temperature bias can be used to probe the CAR-amplitude in a heterostructure on the basis of helical edge states. Since CAR necessarily involves equal-spin triplet pairing, the nonlocal charge current can be interpreted as resulting from the creation/annihilation of equal-spin Cooper pairs. However, the current in the right lead itself is a standard charge current carried by particles. Thus, in this section we are going to explore how the supercurrent injected/extracted from the S regions is influenced by the thermoelectric effect we propose.

A good starting point for the discussion of the supercurrent is a setup with the same parameters as before, but without temperature gradient, *i.e.,* $\theta = 0$. Since in this case the nonlocal charge current is zero, the supercurrent as a function of the phase difference φ will provide a good baseline to compare to. Furthermore, it is helpful to consider the influence of the magnetic region as well, since varying the in-plane strength of the magnetic field $m_\parallel$ is a way to introduce CAR in a controlled fashion.

Accordingly, in Fig. 5.6, we show the supercurrent in both SL and SR as a function of the phase difference for multiple values of $m_\parallel$, without [(a)] and with [(b)] a temperature gradient $\theta = T_c/4$. Starting with the $\theta = 0$ case, the supercurrent

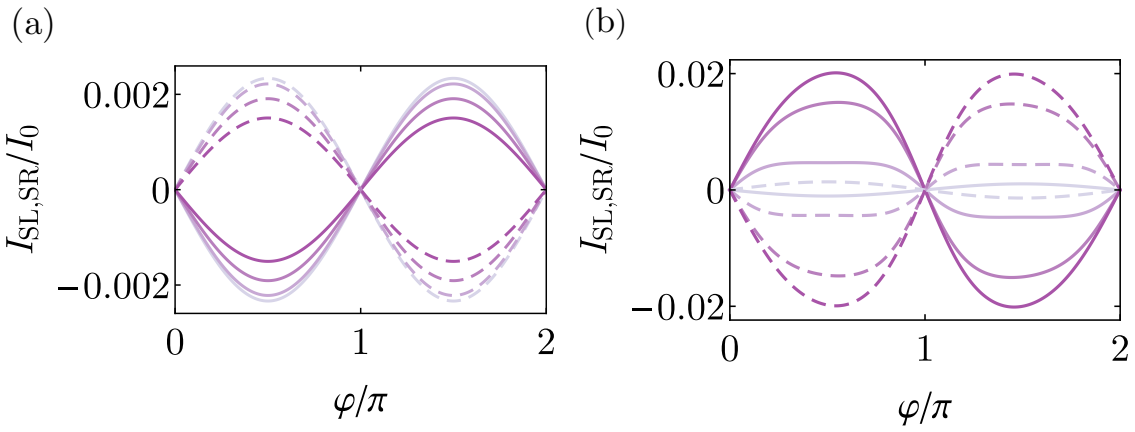

Figure 5.6: Plot of the phase dependence of the supercurrents I_{SL} (solid lines) and I_{SR} (dashed lines) for $\theta = 0$ [panel (a)] and $\theta = T_c/4$ [panel (b)]. In both cases, we show the supercurrents for different values of the magnetic field strength $m_{\parallel}$, where we vary from $m_{\parallel} = 0$ (gray line) to $m_{\parallel} = 1.5\Delta_0$ (purple line) in steps of $0.5\Delta_0$. The stronger the purple in the lines, the higher is the field strength.

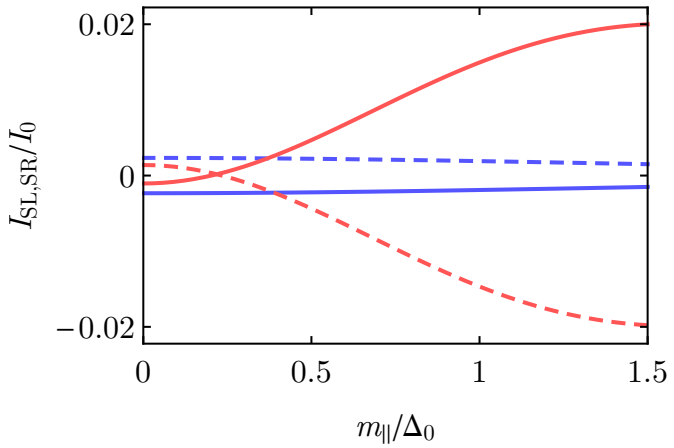

Figure 5.7: The supercurrent in SL and SR regions as a function of the magnetic field strength $m_{\parallel}$ for $\theta = 0$ (blue) and $\theta = T_c/4$ (red). Solid (dashed) lines correspond to I_{SL} (I_{SR}) as in Fig. 5.8 (a) and (b), respectively. Figure adapted from Ref. [136], copyright (2020) by The American Physical Society.

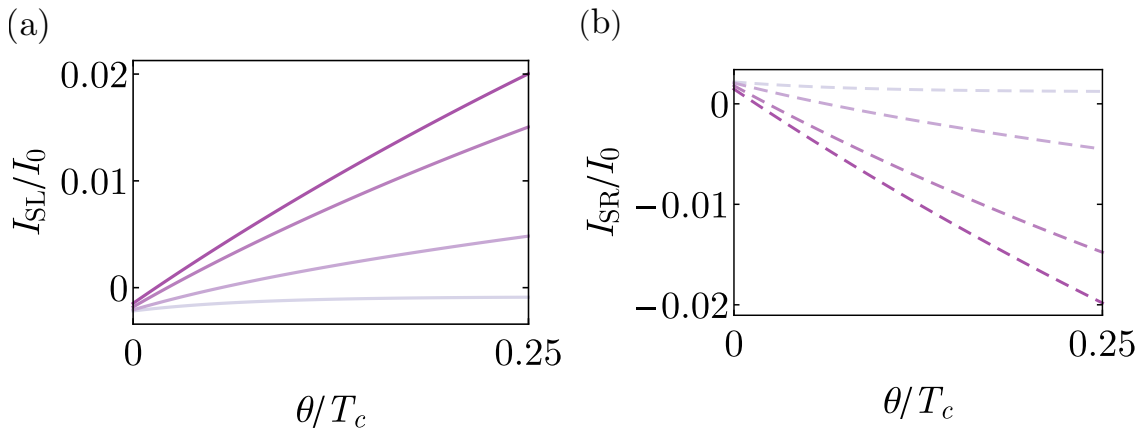

Figure 5.8: Plot of the supercurrent in the left superconductor SL (a) and the right superconductor SR (b) as a function of the temperature difference between the reservoirs θ and for different values of the in-plane magnetic field $m_\parallel$. We vary from $m_\parallel = 0$ (gray line) to $m_\parallel = 1.5\Delta_0$ (purple line) in steps of $0.5\Delta_0$ and the field strength increases with the intensity of purple.

is clearly sinusoidal and opposite in both S regions, which is the expected Josephson-like current-phase relation. The magnetic field suppresses the supercurrent slightly, which is due to the fact that the F region induces normal scattering processes. The picture changes completely for a finite thermal bias. While the supercurrent without magnetic field is roughly the same, its amplitude is greatly enhanced if a ferromagnet is present and grows with the in-plane field. Interestingly, upon turning on the temperature gradient the sign of the current switches, if the magnetic field is large enough. To illustrate this last point better, we show the supercurrents as a function of the in-plane field strength $m_\parallel$ for $\theta = 0$ and $\theta = T_c/4$ in Fig. 5.7, where we fix the phase difference $\varphi = \pi/2$.

Lastly, in order to emphasize that the temperature gradient indeed drives a supercurrent, in Fig. 5.8 we show $I_{\mathrm{SL,SR}}$ as a function of θ for different values of $m_\parallel$ and again at $\varphi = \pi/2$. Evidently, it is the interplay of a thermal bias and the presence of a ferromagnet what leads to a drastic change of the supercurrent.

The behavior of the supercurrent presented in this section serves as evidence that the Cooper pairs involved in the nonlocal CAR processes influence the current in the superconducting contacts. There is a strong influence of the magnetic field, which opens up the possibility for CAR itself as well as the interference in the first place. This hints at the interpretation that a temperature difference indeed drives spin-polarized Cooper pairs and consequently induces the supercurrent.

5.5 Thermoelectricity as a signature of odd-frequency superconductivity

We close this chapter by making a connection from the thermoelectric effect to the classification of nonlocal pairing amplitudes discussed in Chapter 4. The idea is actually very simple: since the thermally generated nonlocal current relies on the

CAR amplitude having a contribution which is odd in energy, it is only natural to ask whether there is a connection with nonlocal odd-frequency pairing. This has been explored in a quantum dot setting in Ref. [190].

To address this point, we make use of the analytical expression for the nonlocal pairings in Eq. (4.76). Adding even- and odd-frequency contributions straightforwardly yields

$$f_{+,+}(x_\mathrm{R}, x_\mathrm{L}, E) + f_{-,+}(x_\mathrm{R}, x_\mathrm{L}, E) = \frac{1}{\mathrm{i}v_\mathrm{F}} \mathrm{e}^{\mathrm{i}\mu(x_\mathrm{L}+x_\mathrm{R})} \mathrm{e}^{-\mathrm{i}E(x_\mathrm{L}-x_\mathrm{R})} s^{eh}_\mathrm{RL}(E). \tag{5.66}$$

Note that the notation for the scattering coefficients in the present chapter differs from Chapter 4, and recall that $s^{eh}_\mathrm{RL}(E)$ is the CAR coefficient associated with a hole from the left being transmitted as an electron into the right lead. In the language of Chapter 4, this corresponds to the coefficient t^e_2 associated with scattering state 2.

Solving for the transmission coefficient, we can bring Eq. (5.66) in the form

$$s^{eh}_\mathrm{RL}(E) = \mathrm{i}v_\mathrm{F} \mathrm{e}^{-\mathrm{i}\mu(x_\mathrm{L}+x_\mathrm{R})} \mathrm{e}^{\mathrm{i}E(x_\mathrm{L}-x_\mathrm{R})} \left(f_{+,+}(x_\mathrm{R}, x_\mathrm{L}, E) + f_{-,+}(x_\mathrm{R}, x_\mathrm{L}, E)\right). \tag{5.67}$$

We note that due to particle hole symmetry, this coefficient is related to the CAR process of an electron from the left being transmitted as a hole via $s^{eh}_\mathrm{RL}(E) = \left[s^{he}_\mathrm{RL}(-E)\right]^*$. Hence, we can rephrase Eq. (5.67) in terms of the scattering coefficient $s^{he}_\mathrm{RL}(E)$, which is more in line with the rest of the chapter. We find

$$\left[s^{he}_\mathrm{RL}(E)\right]^* = \mathrm{i}v_\mathrm{F} \mathrm{e}^{-\mathrm{i}\mu(x_\mathrm{L}+x_\mathrm{R})} \mathrm{e}^{-\mathrm{i}E(x_\mathrm{L}-x_\mathrm{R})} \left(-f_{+,+}(x_\mathrm{R}, x_\mathrm{L}, E) + f_{-,+}(x_\mathrm{R}, x_\mathrm{L}, E)\right), \tag{5.68}$$

where we used the even- and oddness in energy of the pairing amplitudes.

Eq. (5.68) has immediate consequences for our discussion of the nonlocal current, since the absolute square of it reads

$$\begin{aligned} |s^{he}_\mathrm{RL}(E)|^2 = |f_{+,+}(x_\mathrm{R}, x_\mathrm{L}, E)|^2 + |f_{-,+}(x_\mathrm{R}, x_\mathrm{L}, E)|^2 \\ -2\,\mathrm{Re}\left[\left(f_{+,+}(x_\mathrm{R}, x_\mathrm{L}, E)\right)^* f_{-,+}(x_\mathrm{R}, x_\mathrm{L}, E)\right]. \end{aligned} \tag{5.69}$$

The first two terms are trivially even and thus do not contribute to the thermoelectric current. Crucially, however, if there is both a finite even- *and* a finite odd-frequency pairing amplitude, the third term is *odd* in energy and thus results in a finite nonlocal charge current in the presence of a temperature bias. In conclusion, a nonlocal Andreev current generated by a temperature gradient is a smoking gun signature for coexisting ETO and OTE pairing.

6 Conclusion

A common feature of topological phases of matter as a part of modern condensed matter physics and the scope of this thesis is the enormous amount of connections they have to other branches of physics, or even other scientific fields. More specifically, the Kitaev chain discussed in Chapter 2, for instance, is a deceptively simple toy model which can be analyzed with rather simple tools. However, the identification of topologically distinct phases and the appearance of bound states at interfaces are at the heart of the study of topological systems, which, in turn, is one of the most active research areas in physics today. From there, topology as a subfield of mathematics is right around the corner, and the bulk-boundary correspondence is deeply related to field theory and mathematics in the form of index theorems. Furthermore, quite generally the quest for topological systems and materials is unthinkable without materials science, chemistry, and engineering. Physical realizations of the Kitaev chain are no exception, and close collaboration between both theoretical and experimental physicists and experts from the aforementioned disciplines is paramount for the progress made in condensed matter physics in recent years. Lastly, the potential use of Majorana fermions in quantum computation opened up a whole new connection to basic quantum mechanics, quantum information, and indirectly also to theoretical computer science. All these relations make for an incredibly versatile and fascinating research environment.

On the other hand, for a beginning master or PhD student this richness could sometimes be confusing and overwhelming. This was the target audience I had in mind while writing this thesis, and therefore my goal was to make it accessible by explaining the content in a quite detailed manner, rather than including as many different aspects as possible. This is especially true of Chapters 3–5, which roughly correspond to results of my own research.

Chapter 3 contains a detailed account of the Bogoliubov-de Gennes description of superconducting hybrids at the helical edge, including the solutions of the Hamiltonian, the treatment in scattering theory, and the formation of bound states. The connection of even small details in the formulas to the deep context of the underlying physics is fascinating me, which I hope the chapter conveys.

In Chapter 4, we touch upon superconductivity as a classic topic of condensed matter physics for basically the last century. However, through advances in nano-

technology and the proximity effect, physicists today have a wide range of tools available to create and study novel superconducting systems. Of course, this includes the edge states of quantum spin Hall insulators, which we identify to be an ideal candidate for unconventional superconductivity.

Picking up on one of the main results of Chapter 4 about the nature of nonlocal anomalous correlations, we discuss a potential device turning a temperature gradient into an electric current dominated by crossed Andreev reflection in Chapter 5. Not only does this connect to unconventional triplet *and* odd-frequency superconductivity, but it also provides an entry point into the interesting field of quantum thermodynamics.

As a final remark, I would like to point towards natural extensions of the material presented in this thesis. First, including interactions in one-dimensional systems is often both necessary and immensely interesting, and helical edge states of QSHI are no exception. Experimentally, there is growing evidence of interaction effects in edge states of both HgTe/CdTe quantum wells and in bismuthene [36,37,191]. Theoretically, upon introducing interactions Majorana bound states at the helical edge can generalize to parafermions [192–196], which show even more exotic exchange statistics and also hold potential for quantum computation [51,197,198]. However, in order to work towards utilizing parafermions in devices, a crucial first step would be to find strong experimental signatures for them.

Secondly, advances in nanotechnology have boosted the field of quantum thermodynamics, which we alluded to in Chapter 5. In the quest of developing powerful and efficient quantum technology, QSHI edge states provide an interesting platform for further research. While there have been efforts to study their utility for heat engines or refrigerators [199–203], a more recent development is the so-called *thermal shot noise*, or *delta-T noise*, *i.e.,* current fluctuations for a temperature bias. Experimental evidence has been reported in Refs. [204,205], while theoretical work started to appear on tunnel junctions [206] and fractional quantum Hall edge states [207]. Remarkably, in Ref. [207] the authors argue that thermal shot noise is a unique tool to study effects beyond the single-particle picture, *i.e.,* due to interactions or exotic exchange statistics. Hence, not only are helical edge states an interesting platform for quantum thermodynamics, maybe quantum thermodynamics, in turn, provides a way to access the remarkable interaction effects possible in such systems. As farfetched as it seems, it would provide a great deal of satisfaction and happiness to me if someone, someday, follows this path and ties those loose ends together.

Acknowledgements

Even though every thesis only has one name on the cover, it is always the work and effort of a number of people contributing to a PhD project and making its completion possible.

Above all, I am extremely grateful to my advisor Prof. Björn Trauzettel for his support and the opportunity to pursue a PhD at the University of Würzburg. His dedication and determination have been a great inspiration for me, and I thank him for his patience, for helping with my PostDoc application, and in particular for the opportunity to travel across Europe for numerous conferences and schools. The research environment he created at TP4 is extraordinary, and I am honored to have had the chance to work there.

I also want to thank Pablo Burset for guiding me from our collaboration for my Bachelor thesis to this very day. Thank you, Pablo, for every discussion, for answering my questions and for all your support over the years, and I will truly miss our Skype calls. I owe a large part of my physics career to our work together, and the thought that I maybe made a miniscule contribution to yours fills me with joy.

Furthermore, I thank every current and former member of TP4 for making my time as a PhD student memorable. In particular, thanks to Niccolò and Christoph for our nice little work on the invisible Majorana. I am also grateful to my office mates Daniel B., Daniel H., Benny, Gabriel and Masoud for discussions, riddles, support in all kinds of ways and for putting up with my bicycle related use of the office. A special thanks to Daniel H. for sharing a special pedantry with regard to LaTeX. Lastly, I want to explicitly thank Nelly for help with the pitfalls of administrative issues. It was always comforting to know that whatever happens, you would fight with us for advances for travel money and the like.

Of course, all my family and friends outside of physics helped me tremendously during the past years, by providing different perspectives, asking brilliant layman's questions, distracting me from frustration and continuing to believe in me when I didn't. Thanks for your support and your love, and thank you for being a part of my life.

The greatest thank you, however, belongs to Anna. I cannot even begin to list the ways you helped me, supported me, and motivated me. Thank you for always being there for me and for sharing frustration and success alike. You are the greatest source of inspiration for me and I am just whole-heartedly grateful, and lucky, to have you in my life. I can't wait to see what our future entails!

Lastly, I want to thank Ville, simply for being the greatest gift imaginable.

A

Helical edge states basics

In this appendix, we provide detailed expressions for the solutions of the BdG-Hamiltonian. As in the main text, we focus on the cases of a normal, free helical edge without magnetism or superconductivity, as well as superconducting and magnetic regions.

For completeness, we repeat the BdG-Hamiltonian here. Using the spinor $\Psi(x) = (\psi_\uparrow(x), \psi_\downarrow(x), \psi_\downarrow^\dagger(x), -\psi_\uparrow^\dagger(x))^\mathrm{T}$, it reads

$$H = \frac{1}{2}\int \mathrm{d}x\, \Psi(x)^\dagger\, \mathcal{H}_\mathrm{BdG}\, \Psi(x). \tag{A.1}$$

The BdG-Hamiltonian can be composed as

$$\mathcal{H}_\mathrm{BdG} = \mathcal{H}_0 + \mathcal{H}_\Delta + \mathcal{H}_m, \tag{A.2}$$

where

$$\mathcal{H}_0 = v_\mathrm{F}\hat{p}\,\hat{\tau}_3 \otimes \hat{\sigma}_3 - \mu\,\hat{\tau}_3 \otimes \hat{\sigma}_0 \tag{A.3}$$

describes the free helical edge,

$$\mathcal{H}_\Delta = [\Delta_1\,\hat{\tau}_1 + \Delta_2\,\hat{\tau}_2] \otimes \hat{\sigma}_0 = [\Delta\cos\varphi\,\hat{\tau}_1 + \Delta\sin\varphi\,\hat{\tau}_2] \otimes \hat{\sigma}_0 \tag{A.4}$$

accounts for the proximity induced superconducting order, and

$$\mathcal{H}_m = \hat{\tau}_0 \otimes \boldsymbol{m}(x)\cdot\hat{\boldsymbol{\sigma}} = \hat{\tau}_0 \otimes \left[m_\parallel \cos\lambda\,\hat{\sigma}_1 + m_\parallel \sin\lambda\,\hat{\sigma}_2 + m_z\,\hat{\sigma}_3\right] \tag{A.5}$$

describes the effect of the magnetic field.

In the following, we set $\hbar = v_\mathrm{F} = 1$. In normal regions, we model the system with the BdG-Hamiltonian $\mathcal{H}_0$. Its eigenstates read

$$\phi_{e+}^\mathrm{N} = \mathrm{e}^{\mathrm{i}k_e x}\,\phi_{e+}, \qquad \phi_{e-}^\mathrm{N} = \mathrm{e}^{-\mathrm{i}k_e x}\,\phi_{e-}, \qquad \phi_{h-}^\mathrm{N} = \mathrm{e}^{-\mathrm{i}k_h x}\,\phi_{h-}, \qquad \phi_{h+}^\mathrm{N} = \mathrm{e}^{\mathrm{i}k_h x}\,\phi_{h+}, \tag{A.6}$$

with the vectors

$$\phi_{e+} = (1,0,0,0)^\mathrm{T}, \qquad \phi_{e-} = (0,1,0,0)^\mathrm{T}, \quad \phi_{h-} = (0,0,1,0)^\mathrm{T}, \quad \phi_{h+} = (0,0,0,1)^\mathrm{T}, \tag{A.7}$$

and the momenta

$$k_{e/h} = E \pm \mu. \tag{A.8}$$

The subscript e (h) refers to electrons (holes), whereas + (−) indicates rightmovers (leftmovers). Notice that the rightmovers correspond to spin ↑ field operators in the spinor $\Psi(x)$.

Within the superconducting regions, the BdG-Hamiltonian is given by $\mathcal{H}_0 + \mathcal{H}_\Delta$. The structure of the eigenstates is more complicated, since we need to distinguish energies above ($|E| > 0$) and below ($|E| < \Delta$) the gap. Note that $\Delta > 0$ is the modulus of the pairing potential.

It is helpful to introduce the function

$$\Omega_{\mathrm{S}}(E,\Delta) = \begin{cases} \sqrt{E^2-\Delta^2} & E > \Delta \\ \mathrm{i}\sqrt{\Delta^2-E^2} & |E| < \Delta \\ -\sqrt{E^2-\Delta^2} & E < -\Delta. \end{cases} \tag{A.9}$$

In the main text, we furthermore abbreviate

$$\sqrt{\Delta^2-E^2} \equiv \Omega \tag{A.10}$$

for energies below the gap.

The eigenstates of the BdG-Hamiltonian are then given by (we drop the arguments of Ω_{S} for brevity)

$$\begin{aligned} \chi^{\mathrm{S}}_{e+} &= \mathrm{e}^{\mathrm{i}(\Omega_{\mathrm{S}}+\mu)x}\,\chi_{e+}, & \chi^{\mathrm{S}}_{e-} &= \mathrm{e}^{-\mathrm{i}(\Omega_{\mathrm{S}}+\mu)x}\,\chi_{e-}, \\ \chi^{\mathrm{S}}_{h-} &= \mathrm{e}^{-\mathrm{i}(\Omega_{\mathrm{S}}-\mu)x}\,\chi_{h-}, & \chi^{\mathrm{S}}_{h+} &= \mathrm{e}^{\mathrm{i}(\Omega_{\mathrm{S}}-\mu)x}\,\chi_{h+}, \end{aligned} \tag{A.11}$$

with the vectors

$$\begin{aligned} \chi_{e+} &= \frac{1}{N}\left(\mathrm{e}^{-\mathrm{i}\varphi}(E+\Omega_{\mathrm{S}}),0,\Delta,0\right)^{\mathrm{T}}, & \chi_{e-} &= \frac{1}{N}\left(0,\mathrm{e}^{-\mathrm{i}\varphi}(E+\Omega_{\mathrm{S}}),0,\Delta\right)^{\mathrm{T}} \\ \chi_{h-} &= \frac{1}{N}\left(\mathrm{e}^{-\mathrm{i}\varphi}\Delta,0,(E+\Omega_{\mathrm{S}}),0\right)^{\mathrm{T}}, & \chi_{h+} &= \frac{1}{N}\left(0,\mathrm{e}^{-\mathrm{i}\varphi}\Delta,0,(E+\Omega_{\mathrm{S}})\right)^{\mathrm{T}}. \end{aligned} \tag{A.12}$$

The normalization is given by $N = \sqrt{|E+\Omega_{\mathrm{S}}|^2+\Delta^2}$. Note that the modes $\chi^{\mathrm{S}}_{e+/h+}$ are rightmovers above the gap, and below the gap become evanescent modes decaying for growing x. Accordingly, the modes $\chi^{\mathrm{S}}_{e-/h-}$ are leftmovers above the gap and turn into evanescent waves decaying towards decreasing x. To make sure that this is true for positive as well as negative energies, the difference in sign between the first and third line in Eq. (A.9) is crucial.

A more convenient way of writing the eigenstates in superconducting regions is made possible by the identities

$$\mathrm{e}^{\operatorname{arccosh} x} = x \pm \sqrt{x^2-1} \qquad \text{for } x \gtrless \pm 1. \tag{A.13a}$$

and

$$\mathrm{e}^{\mathrm{i}\arccos x} = x + \mathrm{i}\sqrt{1-x^2} \qquad \text{for } |1| < 1. \tag{A.13b}$$

Observe that the square roots appearing in Eq. (A.13) match the definition of $\Omega_{\mathrm{S}}(E,\Delta)$ in Eq. (A.9).

Thus, above the gap the vectors $\chi_{e/h\pm}$ of the eigenstates within superconducting regions can be written as

$$\begin{aligned}\chi_{e+} &= \frac{1}{N'}\left(\mathrm{e}^{-\mathrm{i}\varphi}\,\mathrm{e}^{A(E)},0,1,0\right)^{\mathrm{T}}, \qquad \chi_{e-} = \frac{1}{N'}\left(0,\mathrm{e}^{-\mathrm{i}\varphi}\,\mathrm{e}^{A(E)},0,1\right)^{\mathrm{T}}\\ \chi_{h-} &= \frac{1}{N'}\left(\mathrm{e}^{-\mathrm{i}\varphi}\mathrm{e}^{-A(E)},0,1,0\right)^{\mathrm{T}}, \qquad \chi_{h+} = \frac{1}{N'}\left(0,\mathrm{e}^{-\mathrm{i}\varphi}\mathrm{e}^{-A(E)},0,1\right)^{\mathrm{T}},\end{aligned} \tag{A.14}$$

where we abbreviate $A(E) = \operatorname{arccosh}(E/\Delta)$. The normalization factor reads $N' = \sqrt{1+\mathrm{e}^{2A(E)}}$.

Below the gap, we find

$$\begin{aligned}\chi_{e+} &= \frac{1}{\sqrt{2}}\left(\mathrm{e}^{-\mathrm{i}\varphi}\,\mathrm{e}^{\mathrm{i}\eta(E)},0,1,0\right)^{\mathrm{T}}, \qquad \chi_{e-} = \frac{1}{\sqrt{2}}\left(0,\mathrm{e}^{-\mathrm{i}\varphi}\,\mathrm{e}^{\mathrm{i}\eta(E)},0,1\right)^{\mathrm{T}}\\ \chi_{h-} &= \frac{1}{\sqrt{2}}\left(\mathrm{e}^{-\mathrm{i}\varphi}\mathrm{e}^{-\mathrm{i}\eta(E)},0,1,0\right)^{\mathrm{T}}, \qquad \chi_{h+} = \frac{1}{\sqrt{2}}\left(0,\mathrm{e}^{-\mathrm{i}\varphi}\mathrm{e}^{-\mathrm{i}\eta(E)},0,1\right)^{\mathrm{T}},\end{aligned} \tag{A.15}$$

with the shorthand $\eta(E) = \arccos(E/\Delta)$. This is the form used in the main text to derive Andreev reflection coefficients below the gap.

The eigenstates in F regions described by the BdG-Hamiltonian $\mathcal{H}_0 + \mathcal{H}_m$ are very similar in structure to the ones in S regions. However, note that we need to distinguish electron- and hole-blocks, because they differ in their sign in front of the chemical potential. We define

$$\Omega_{\mathrm{F},e}(E,m_\parallel) = \begin{cases}\sqrt{(E+\mu)^2-\Delta^2} & E+\mu>\Delta\\ \mathrm{i}\sqrt{\Delta^2-(E+\mu)^2} & |E+\mu|<\Delta\\ -\sqrt{(E+\mu)^2-\Delta^2} & E+\mu<-\Delta\end{cases} \tag{A.16a}$$

and

$$\Omega_{\mathrm{F},h}(E,m_\parallel) = \begin{cases}\sqrt{(E-\mu)^2-\Delta^2} & E-\mu>\Delta\\ \mathrm{i}\sqrt{\Delta^2-(E-\mu)^2} & |E-\mu|<\Delta\\ -\sqrt{(E-\mu)^2-\Delta^2} & E-\mu<-\Delta,\end{cases} \tag{A.16b}$$

with the shorthands

$$\sqrt{\Delta^2-(E\pm\mu)^2} \equiv \kappa_{e/h} \tag{A.17}$$

used in the main text.

The eigenstates are then found to be

$$\begin{aligned}\zeta^{\mathrm{F}}_{e+} &= \mathrm{e}^{\mathrm{i}\Omega_{\mathrm{F},e}x - m_z x}\,\zeta_{e+}, \qquad \zeta^{\mathrm{F}}_{e-} = \mathrm{e}^{-\mathrm{i}\Omega_{\mathrm{F}}x - m_z x}\,\zeta_{e-},\\ \zeta^{\mathrm{F}}_{h-} &= \mathrm{e}^{-\mathrm{i}\Omega_{\mathrm{F},h}x + m_z x}\,\zeta_{h-}, \qquad \zeta^{\mathrm{F}}_{h+} = \mathrm{e}^{\mathrm{i}\Omega_{\mathrm{F},h}x + m_z x}\,\zeta_{h+}\end{aligned} \tag{A.18}$$

with the vectors

$$\begin{aligned}\zeta_{e+} &= \frac{1}{M_e}\left(\mathrm{e}^{-\mathrm{i}\lambda}(E+\mu+\Omega_{\mathrm{F},e}),m_\parallel,0,0\right)^{\mathrm{T}},\\ \zeta_{e-} &= \frac{1}{M_e}\left(\mathrm{e}^{-\mathrm{i}\lambda}m_\parallel,(E+\mu+\Omega_{\mathrm{F},e}),0,0\right)^{\mathrm{T}},\\ \zeta_{h-} &= \frac{1}{M_h}\left(0,0,\mathrm{e}^{-\mathrm{i}\varphi}(E-\mu+\Omega_{\mathrm{F},h}),m_\parallel\right)^{\mathrm{T}},\\ \zeta_{h+} &= \frac{1}{M_h}\left(0,0,\mathrm{e}^{-\mathrm{i}\varphi}m_\parallel,(E-\mu+\Omega_{\mathrm{F},h})\right)^{\mathrm{T}}.\end{aligned} \tag{A.19}$$

The normalization factors are $M_{e/h} = \sqrt{|E+\mu+\Omega_{mF,e/h}|^2 + m_\parallel^2}$.

Following the same procedure as in the S regions, the square roots can be replaced by exponentials. Above the gap we have the vectors

$$\begin{aligned} \zeta_{e+} &= \frac{1}{M'_e}\left(\mathrm{e}^{-\mathrm{i}\lambda}\,\mathrm{e}^{B_e(E)},1,0,0\right)^{\mathrm{T}}, \qquad \zeta_{e-} = \frac{1}{M'_e}\left(\mathrm{e}^{-\mathrm{i}\lambda}\,\mathrm{e}^{-B_e(E)},1,0,0\right)^{\mathrm{T}} \\ \zeta_{h-} &= \frac{1}{M_h}\left(0,0,\mathrm{e}^{-\mathrm{i}\varphi}\,\mathrm{e}^{B_h(E)},1\right)^{\mathrm{T}}, \qquad \zeta_{h+} = \frac{1}{M_h}\left(0,0,\mathrm{e}^{-\mathrm{i}\varphi}\,\mathrm{e}^{-B(E)},1\right)^{\mathrm{T}} \end{aligned} \tag{A.20}$$

with $B_{e/h}(E) = \operatorname{arccosh}(\frac{E\pm\mu)}{m_\parallel})$ and $M'_{e/h} = \sqrt{1+\mathrm{e}^{2B_{e/h}}}$.

Below the gap, the vectors can be written in the form

$$\begin{aligned} \zeta_{e+} &= \frac{1}{\sqrt{2}}\left(\mathrm{e}^{-\mathrm{i}\lambda}\,\mathrm{e}^{\mathrm{i}\rho_e(E)},1,0,0\right)^{\mathrm{T}}, \qquad \zeta_{e-} = \frac{1}{\sqrt{2}}\left(\mathrm{e}^{-\mathrm{i}\lambda}\,\mathrm{e}^{-\mathrm{i}\rho_e(E)},1,0,0\right)^{\mathrm{T}} \\ \zeta_{h-} &= \frac{1}{\sqrt{2}}\left(0,0,\mathrm{e}^{-\mathrm{i}\varphi}\,\mathrm{e}^{\mathrm{i}\rho_h(E)},1\right)^{\mathrm{T}}, \qquad \zeta_{h+} = \frac{1}{\sqrt{2}}\left(0,0,\mathrm{e}^{-\mathrm{i}\varphi}\,\mathrm{e}^{-\mathrm{i}\rho(E)},1\right)^{\mathrm{T}} \end{aligned} \tag{A.21}$$

where $\rho_{e/h}(E) = \arccos(\frac{E\pm\mu}{m_\parallel})$. As with the eigenstates in the S regions, Eq. (A.21) is the form we use in the main text.

Bibliography

[1] W. Hampson. "Improvements relating to the Progressive Refrigeration of Gases" (1895). *Patent Nr. GB189510165*.

[2] C. Linde. "Gasverflüssigungs-Maschine." (1895). *Patent Nr. CH10704*.

[3] H. Kamerlingh Onnes. "The liquefation of Helium". *KNAW Proceedings* **11**, 168–185 (1909).

[4] NobelPrize.org. "Heike Kamerlingh Onnes – Facts." (2020). https://www.nobelprize.org/prizes/physics/1913/onnes/facts/, Accessed Mar 30, 2020.

[5] A. Bergen, R. Andersen, M. Bauer, H. Boy, M. ter Brake, P. Brutsaert, C. Bührer, M. Dhallé, J. Hansen, H. ten Kate, J. Kellers, J. Krause, E. Krooshoop, C. Kruse, H. Kylling, M. Pilas, H. Pütz, A. Rebsdorf, M. Reckhard, E. Seitz, H. Springer, X. Song, N. Tzabar, S. Wessel, J. Wiezoreck, T. Winkler, and K. Yagotyntsev. "Design and in-field testing of the world's first ReBCO rotor for a 3.6 MW wind generator". *Superconductor Science and Technology* **32**, 125006 (2019).

[6] M. R. Islam, Y. Guo, and J. Zhu. "A review of offshore wind turbine nacelle: Technical challenges, and research and developmental trends". *Renewable and Sustainable Energy Reviews* **33**, 161–176 (2014).

[7] H. Thomas, A. Marian, A. Chervyakov, S. Stückrad, D. Salmieri, and C. Rubbia. "Superconducting transmission lines - Sustainable electric energy transfer with higher public acceptance?" *Renewable and Sustainable Energy Reviews* **55**, 59–72 (2016).

[8] L. Evans and P. Bryant. "LHC Machine". *Journal of Instrumentation* **3**, S08001 (2008).

[9] M. M. Waldrop. "The chips are down for Moore's law". *Nature* **530**, 144–147 (2016).

[10] E. Grumbling and M. Horowitz, editors. *Quantum Computing: Progress and Prospects*. The National Academies Press, Washington, DC (2019). ISBN 978-0-309-47969-1. https://www.nap.edu/catalog/25196/quantum-computing-progress-and-prospects.

[11] I. Žutić, J. Fabian, and S. Das Sarma. "Spintronics: Fundamentals and applications". *Reviews of Modern Physics* **76**, 323–410 (2004).

[12] J. Linder and J. W. Robinson. "Superconducting spintronics". *Nature Physics* **11**, 307–315 (2015).

[13] R. P. Feynman. "Simulating physics with computers". *International Journal of Theoretical Physics* **21**, 467–488 (1982).

[14] R. P. Feynman. "Quantum mechanical computers". *Foundations of Physics* **16**, 507–531 (1986).

[15] P. Shor. "Algorithms for quantum computation: discrete logarithms and factoring". *Proceedings 35th Annual Symposium on Foundations of Computer Science* pages 124–134 (1994).

[16] L. K. Grover. "A fast quantum mechanical algorithm for database search". In *Proceedings, 28th Annual ACM Symposium on the Theory of Computing (STOC)*, pages 212–219 (1996). http://arxiv.org/abs/quant-ph/9605043.

[17] F. Arute, K. Arya, R. Babbush, D. Bacon, J. C. Bardin, R. Barends, R. Biswas, S. Boixo, F. G. S. L. Brandao, D. A. Buell, B. Burkett, Y. Chen, Z. Chen, B. Chiaro, R. Collins, W. Courtney, A. Dunsworth, E. Farhi, B. Foxen, A. Fowler, C. Gidney, M. Giustina, R. Graff, K. Guerin, S. Habegger, M. P. Harrigan, M. J. Hartmann, A. Ho, M. Hoffmann, T. Huang, T. S. Humble, S. V. Isakov, E. Jeffrey, Z. Jiang, D. Kafri, K. Kechedzhi, J. Kelly, P. V. Klimov, S. Knysh, A. Korotkov, F. Kostritsa, D. Landhuis, M. Lindmark, E. Lucero, D. Lyakh, S. Mandrà, J. R. McClean, M. McEwen, A. Megrant, X. Mi, K. Michielsen, M. Mohseni, J. Mutus, O. Naaman, M. Neeley, C. Neill, M. Y. Niu, E. Ostby, A. Petukhov, J. C. Platt, C. Quintana, E. G. Rieffel, P. Roushan, N. C. Rubin, D. Sank, K. J. Satzinger, V. Smelyanskiy, K. J. Sung, M. D. Trevithick, A. Vainsencher, B. Villalonga, T. White, Z. J. Yao, P. Yeh, A. Zalcman, H. Neven, and J. M. Martinis. "Quantum supremacy using a programmable superconducting processor". *Nature* **574**, 505–510 (2019).

[18] J. M. Kosterlitz and D. J. Thouless. "Ordering, metastability and phase transitions in two-dimensional systems". *Journal of Physics C: Solid State Physics* **6**, 1181–1203 (1973).

[19] V. Berezinskii. "Destruction of Long-range Order in One-dimensional and Two-dimensional Systems having a Continuous Symmetry Group I. Classical Systems". *JETP Letters* **32**, 493 (1971).

[20] K. v. Klitzing, G. Dorda, and M. Pepper. "New Method for High-Accuracy Determination of the Fine-Structure Constant Based on Quantized Hall Resistance". *Physical Review Letters* **45**, 494–497 (1980).

[21] D. J. Thouless, M. Kohmoto, M. P. Nightingale, and M. den Nijs. "Quantized Hall Conductance in a Two-Dimensional Periodic Potential". *Physical Review Letters* **49**, 405–408 (1982).

[22] F. D. M. Haldane. "Model for a Quantum Hall Effect without Landau Levels: Condensed-Matter Realization of the "Parity Anomaly"". *Physical Review Letters* **61**, 2015–2018 (1988).

[23] C. L. Kane and E. J. Mele. "Quantum Spin Hall Effect in Graphene". *Physical Review Letters* **95**, 226801 (2005).

[24] C. L. Kane and E. J. Mele. "Z_2 topological order and the quantum spin hall effect". *Physical Review Letters* **95**, 146802 (2005).

[25] B. A. Bernevig, T. L. Hughes, and S.-C. Zhang. "Quantum Spin Hall Effect and Topological Phase Transition in HgTe Quantum Wells". *Science* **314**, 1757–1761 (2006).

[26] C. Wu, B. A. Bernevig, and S.-c. Zhang. "Helical Liquid and the Edge of Quantum Spin Hall Systems". *Physical Review Letters* **96**, 106401 (2006).

[27] M. Konig, S. Wiedmann, C. Brune, A. Roth, H. Buhmann, L. W. Molenkamp, X.-L. Qi, and S.-C. Zhang. "Quantum Spin Hall Insulator State in HgTe Quantum Wells". *Science* **318**, 766–770 (2007).

[28] C. Brüne, A. Roth, E. G. Novik, M. König, H. Buhmann, E. M. Hankiewicz, W. Hanke, J. Sinova, and L. W. Molenkamp. "Evidence for the ballistic intrinsic spin Hall effect in HgTe nanostructures". *Nature Physics* **6**, 448–454 (2010).

[29] A. Roth, C. Brüne, H. Buhmann, L. W. Molenkamp, J. Maciejko, X.-L. Qi, and S.-C. Zhang. "Nonlocal Transport in the Quantum Spin Hall State". *Science* **325**, 294–297 (2009).

[30] C. Brüne, A. Roth, H. Buhmann, E. M. Hankiewicz, L. W. Molenkamp, J. Maciejko, X.-L. Qi, and S.-C. Zhang. "Spin polarization of the quantum spin Hall edge states". *Nature Physics* **8**, 485–490 (2012).

[31] S. Hart, H. Ren, T. Wagner, P. Leubner, M. Mühlbauer, C. Brüne, H. Buhmann, L. W. Molenkamp, and A. Yacoby. "Induced superconductivity in the quantum spin Hall edge". *Nature Physics* **10**, 638–643 (2014).

[32] E. Bocquillon, R. S. Deacon, J. Wiedenmann, P. Leubner, T. M. Klapwijk, C. Brüne, K. Ishibashi, H. Buhmann, and L. W. Molenkamp. "Gapless Andreev bound states in the quantum spin Hall insulator HgTe". *Nature Nanotechnology* **12**, 137–143 (2017).

[33] J. Wiedenmann, E. Bocquillon, R. S. Deacon, S. Hartinger, O. Herrmann, T. M. Klapwijk, L. Maier, C. Ames, C. Brüne, C. Gould, A. Oiwa, K. Ishibashi, S. Tarucha, H. Buhmann, and L. W. Molenkamp. "4π-periodic Josephson supercurrent in HgTe-based topological Josephson junctions". *Nature Communications* **7**, 10303 (2016).

[34] V. S. Pribiag, A. J. A. Beukman, F. Qu, M. C. Cassidy, C. Charpentier, W. Wegscheider, and L. P. Kouwenhoven. "Edge-mode superconductivity in a two-dimensional topological insulator". *Nature Nanotechnology* **10**, 593–597 (2015).

[35] I. Knez, R.-R. Du, and G. Sullivan. "Evidence for helical edge modes in inverted InAs/GaSb quantum wells". *Physical Review Letters* **107**, 136603 (2011).

[36] F. Reis, G. Li, L. Dudy, M. Bauernfeind, S. Glass, W. Hanke, R. Thomale, J. Schäfer, and R. Claessen. "Bismuthene on a SiC substrate: A candidate for a high-temperature quantum spin Hall material". *Science* **357**, 287–290 (2017).

[37] R. Stühler, F. Reis, T. Müller, T. Helbig, T. Schwemmer, R. Thomale, J. Schäfer, and R. Claessen. "Tomonaga–Luttinger liquid in the edge channels of a quantum spin Hall insulator". *Nature Physics* **16**, 47–51 (2020).

[38] S. Wu, V. Fatemi, Q. D. Gibson, K. Watanabe, T. Taniguchi, R. J. Cava, and P. Jarillo-Herrero. "Observation of the quantum spin Hall effect up to 100 kelvin in a monolayer crystal". *Science* **359**, 76–79 (2018).

[39] I. Knez, R.-R. Du, and G. Sullivan. "Andreev reflection of helical edge modes in InAs/GaSb quantum spin hall insulator". *Physical Review Letters* **109**, 186603 (2012).

[40] E. Sajadi, T. Palomaki, Z. Fei, W. Zhao, P. Bement, C. Olsen, S. Lüscher, X. Xu, J. A. Folk, D. H. Cobden, S. Luescher, X. Xu, J. A. Folk, and D. H. Cobden. "Gate-induced superconductivity in a monolayer topological insulator". *Science* **362**, 922–925 (2018).

[41] V. Fatemi, S. Wu, Y. Cao, L. Bretheau, Q. D. Gibson, K. Watanabe, T. Taniguchi, R. J. Cava, and P. Jarillo-Herrero. "Electrically tunable low-density superconductivity in a monolayer topological insulator". *Science* **362**, 926–929 (2018).

[42] W. Zhao, Z. Fei, T. Song, H. K. Choi, T. Palomaki, B. Sun, P. Malinowski, M. A. McGuire, J.-H. Chu, X. Xu, and D. H. Cobden. "Magnetic proximity and nonreciprocal current switching in a monolayer WTe_2 helical edge". *Nature Materials* **19**, 503–507 (2020).

[43] L. Fu and C. L. Kane. "Superconducting Proximity Effect and Majorana Fermions at the Surface of a Topological Insulator". *Physical Review Letters* **100**, 096407 (2008).

[44] L. Fu and C. L. Kane. "Josephson current and noise at a superconductor/quantum-spin-Hall-insulator/superconductor junction". *Physical Review B* **79**, 161408 (2009).

[45] J. Alicea. "New directions in the pursuit of Majorana fermions in solid state systems". *Reports on Progress in Physics* **75**, 076501 (2012).

[46] E. Majorana. "Teoria simmetrica dell'elettrone e del positrone". *Il Nuovo Cimento* **14**, 171–184 (1937).

[47] A. Y. Kitaev. "Unpaired Majorana fermions in quantum wires". *Physics-Uspekhi* **44**, 131–136 (2001).

[48] A. Kitaev. "Fault-tolerant quantum computation by anyons". *Annals of Physics* **303**, 2–30 (2003).

[49] A. Kitaev. "Anyons in an exactly solved model and beyond". *Annals of Physics* **321**, 2–111 (2006).

[50] A. Stern. "Anyons and the quantum Hall effect—A pedagogical review". *Annals of Physics* **323**, 204–249 (2008).

[51] C. Nayak, S. H. Simon, A. Stern, M. Freedman, and S. Das Sarma. "Non-Abelian anyons and topological quantum computation". *Reviews of Modern Physics* **80**, 1083–1159 (2008).

[52] A. Stern. "Non-Abelian states of matter". *Nature* **464**, 187–193 (2010).

[53] B. A. Bernevig and T. L. Hughes. *Topological Insulators and Topological Superconductors*. Princeton University Press (2013). ISBN 9780691151755.

[54] F. von Oppen, Y. Peng, and F. Pientka. "Topological superconducting phases in one dimension". In *Topological Aspects of Condensed Matter Physics: Lecture Notes of the Les Houches Summer School: Volume 103, August 2014* (edited by C. Claudio, M. O. Goerbig, R. Moessner, and L. F. Cugliandolo), chapter 9, pages 387–450. Oxford University Press (2017).

[55] L. Herviou. *Topological phases and Majorana fermions*. Ph.D. thesis, Université Paris-Saclay, École Polytechnique (2017).

[56] S. R. Elliott and M. Franz. "Colloquium: Majorana fermions in nuclear, particle, and solid-state physics". *Rev. Mod. Phys.* **87**, 137–163 (2015).

[57] F. Wilczek. "Majorana returns". *Nature Physics* **5**, 614–618 (2009).

[58] C. W. J. Beenakker. "Search for Majorana fermions in superconductors". *Annual Review of Condensed Matter Physics* **4**, 15 (2013).

[59] M. Z. Hasan and C. L. Kane. "Colloquium: Topological insulators". *Reviews of Modern Physics* **82**, 3045–3067 (2010).

[60] X. L. Qi and S. C. Zhang. "Topological insulators and superconductors". *Reviews of Modern Physics* **83**, 1057–1110 (2011).

[61] M. Sato and Y. Ando. "Topological superconductors: a review". *Reports on Progress in Physics* **80**, 076501 (2017).

[62] J. Bardeen, L. N. Cooper, and J. R. Schrieffer. "Theory of superconductivity". *Physical Review* **108**, 1175–1204 (1957).

[63] J. Schrieffer. *Theory Of Superconductivity*. CRC Press (2018). ISBN 9780429975332.

[64] F. Hassler. "Majorana Qubits". In *Quantum information processing: lecture notes of the 44th IFF Spring School 2013, IFF Spring School; 44, Schriften des Forschungszentrums Jülich, Reihe Schlüsseltechnologien* (edited by D. DiVincenzo). Forschungszentrum Jülich (2013). ISBN 9783893368334.

[65] C. W. Beenakker. "Random-matrix theory of Majorana fermions and topological superconductors". *Reviews of Modern Physics* **87**, 1037–1066 (2015).

[66] P. W. Brouwer. "Enter the Majorana Fermion". *Science* **336**, 989–990 (2012).

[67] M. Leijnse and K. Flensberg. "Introduction to topological superconductivity and Majorana fermions". *Semiconductor Science and Technology* **27**, 124003 (2012).

[68] C. W. J. Beenakker. "Search for non-Abelian Majorana braiding statistics in superconductors". *SciPost Phys. Lect. Notes* page 15 (2020).

[69] N. Read and D. Green. "Paired states of fermions in two dimensions with breaking of parity and time-reversal symmetries and the fractional quantum Hall effect". *Physical Review B* **61**, 10267–10297 (2000).

[70] G. Moore and N. Read. "Nonabelions in the fractional quantum hall effect". *Nuclear Physics B* **360**, 362–396 (1991).

[71] S. Das Sarma, C. Nayak, and S. Tewari. "Proposal to stabilize and detect half-quantum vortices in strontium ruthenate thin films: Non-abelian braiding statistics of vortices in a $p_x + ip_y$ superconductor". *Physical Review B* **73**, 220502 (2006).

[72] S. Tewari, S. Das Sarma, C. Nayak, C. Zhang, and P. Zoller. "Quantum computation using vortices and majorana zero modes of a $p_x + ip_y$ superfluid of fermionic cold atoms". *Physical Review Letters* **98**, 010506 (2007).

[73] A. P. Mackenzie and Y. Maeno. "The superconductivity of Sr_2RuO_4 and the physics of spin-triplet pairing". *Rev. Mod. Phys.* **75**, 657–712 (2003).

[74] J. D. Sau, R. M. Lutchyn, S. Tewari, and S. Das Sarma. "Generic New Platform for Topological Quantum Computation Using Semiconductor Heterostructures". *Physical Review Letters* **104**, 040502 (2010).

[75] R. M. Lutchyn, J. D. Sau, and S. Das Sarma. "Majorana Fermions and a Topological Phase Transition in Semiconductor-Superconductor Heterostructures". *Physical Review Letters* **105**, 077001 (2010).

[76] Y. Oreg, G. Refael, and F. von Oppen. "Helical Liquids and Majorana Bound States in Quantum Wires". *Physical Review Letters* **105**, 177002 (2010).

[77] S. Nadj-Perge, I. K. Drozdov, J. Li, H. Chen, S. Jeon, J. Seo, A. H. MacDonald, B. A. Bernevig, and A. Yazdani. "Observation of majorana fermions in ferromagnetic atomic chains on a superconductor". *Science* **346**, 602–607 (2014).

[78] S. Jeon, Y. Xie, J. Li, Z. Wang, B. A. Bernevig, and A. Yazdani. "Distinguishing a majorana zero mode using spin-resolved measurements". *Science* **358**, 772–776 (2017).

[79] B. Jäck, Y. Xie, J. Li, S. Jeon, B. A. Bernevig, and A. Yazdani. "Observation of a Majorana zero mode in a topologically protected edge channel". *Science* **1444**, eaax1444 (2019).

[80] V. Mourik, K. Zuo, S. M. Frolov, S. R. Plissard, E. P. A. M. Bakkers, and L. P. Kouwenhoven. "Signatures of majorana fermions in hybrid superconductor-semiconductor nanowire devices". *Science* **336**, 1003–1007 (2012).

[81] L. P. Rokhinson, X. Liu, and J. K. Furdyna. "The fractional a.c. josephson effect in a semiconductor–superconductor nanowire as a signature of majorana particles". *Nature Physics* **8**, 795–799 (2012).

[82] M. T. Deng, C. L. Yu, G. Y. Huang, M. Larsson, P. Caroff, and H. Q. Xu. "Anomalous Zero-Bias Conductance Peak in a Nb–InSb Nanowire–Nb Hybrid Device". *Nano Letters* **12**, 6414–6419 (2012).

[83] A. Das, Y. Ronen, Y. Most, Y. Oreg, M. Heiblum, and H. Shtrikman. "Zero-bias peaks and splitting in an al–inas nanowire topological superconductor as a signature of majorana fermions". *Nature Physics* **8**, 887–895 (2012).

[84] A. P. Higginbotham, S. M. Albrecht, G. Kiršanskas, W. Chang, F. Kuemmeth, P. Krogstrup, T. S. Jespersen, J. Nygård, K. Flensberg, and C. M. Marcus. "Parity lifetime of bound states in a proximitized semiconductor nanowire". *Nature Physics* **11**, 1017–1021 (2015).

[85] M. T. Deng, S. Vaitiekenas, E. B. Hansen, J. Danon, M. Leijnse, K. Flensberg, J. Nygård, P. Krogstrup, and C. M. Marcus. "Majorana bound state in a coupled quantum-dot hybrid-nanowire system". *Science* **354**, 1557–1562 (2016).

[86] F. Nichele, A. C. C. Drachmann, A. M. Whiticar, E. C. T. O'Farrell, H. J. Suominen, A. Fornieri, T. Wang, G. C. Gardner, C. Thomas, A. T. Hatke, P. Krogstrup, M. J. Manfra, K. Flensberg, and C. M. Marcus. "Scaling of Majorana Zero-Bias Conductance Peaks". *Physical Review Letters* **119**, 136803 (2017).

[87] H. Zhang, C.-X. Liu, S. Gazibegovic, D. Xu, J. A. Logan, G. Wang, N. van Loo, J. D. S. Bommer, M. W. A. de Moor, D. Car, R. L. M. Op het Veld, P. J. van Veldhoven, S. Koelling, M. A. Verheijen, M. Pendharkar, D. J. Pennachio, B. Shojaei, J. S. Lee, C. J. Palmstrøm, E. P. A. M. Bakkers, S. D. Sarma, and L. P. Kouwenhoven. "Quantized Majorana conductance". *Nature* **556**, 74–79 (2018).

[88] Ö. Gül, H. Zhang, F. K. de Vries, J. van Veen, K. Zuo, V. Mourik, S. Conesa-Boj, M. Nowak, D. J. van Woerkom, M. Quintero-Pérez, M. C. Cassidy, A. Geresdi, S. Koelling, D. Car, S. R. Plissard, E. P. A. M. Bakkers, and L. P. Kouwenhoven. "Hard Superconducting Gap in InSb Nanowires". *Nano Letters* **17**, 2690–2696 (2017).

[89] H. J. H.-J. Kwon, K. Sengupta, V. M. Yakovenko, and K. Sengupta. "Fractional ac Josephson effect in unconventional superconductors". *Low Temperature Physics* **30**, 814–822 (2004).

[90] F. Domínguez, O. Kashuba, E. Bocquillon, J. Wiedenmann, R. S. Deacon, T. M. Klapwijk, G. Platero, L. W. Molenkamp, B. Trauzettel, and E. M.

Hankiewicz. "Josephson junction dynamics in the presence of 2π- and 4π-periodic supercurrents". *Physical Review B* **95**, 195430 (2017).

[91] R. S. Deacon, J. Wiedenmann, E. Bocquillon, F. Domínguez, T. M. Klapwijk, P. Leubner, C. Brüne, E. M. Hankiewicz, S. Tarucha, K. Ishibashi, H. Buhmann, and L. W. Molenkamp. "Josephson Radiation from Gapless Andreev Bound States in HgTe-Based Topological Junctions". *Physical Review X* **7**, 021011 (2017).

[92] E. Bocquillon, J. Wiedenmann, R. S. Deacon, T. M. Klapwijk, H. Buhmann, and L. W. Molenkamp. "Microwave Studies of the Fractional Josephson Effect in HgTe-Based Josephson Junctions". In *Topological Matter: Lectures from the Topological Matter School 2017* (edited by D. Bercioux, J. Cayssol, M. G. Vergniory, and M. Reyes Calvo), pages 115–148. Springer International Publishing, Cham (2018). ISBN 978-3-319-76388-0.

[93] D. Laroche, D. Bouman, D. J. van Woerkom, A. Proutski, C. Murthy, D. I. Pikulin, C. Nayak, R. J. J. van Gulik, J. Nygård, P. Krogstrup, L. P. Kouwenhoven, and A. Geresdi. "Observation of the 4π-periodic Josephson effect in indium arsenide nanowires". *Nature Communications* **10**, 245 (2019).

[94] R. Jackiw and C. Rebbi. "Solitons with fermion number". *Physical Review D* **13**, 3398–3409 (1976).

[95] F. Crépin, B. Trauzettel, and F. Dolcini. "Signatures of Majorana bound states in transport properties of hybrid structures based on helical liquids". *Physical Review B* **89**, 205115 (2014).

[96] E. J. Weinberg. "Index calculations for the fermion-vortex system". *Physical Review D* **24**, 2669–2673 (1981).

[97] M. F. Atiyah and I. M. Singer. "The index of elliptic operators on compact manifolds". *Bulletin of the American Mathematical Society* **69**, 422–434 (1963).

[98] A. Kitaev and C. Laumann. "Topological phases and quantum computation" *arXiv-ID* 0904.2771 (2009).

[99] J. K. Pachos. *Introduction to Topological Quantum Computation*. Cambridge University Press, Cambridge (2012). ISBN 9780511792908.

[100] V. Lahtinen and J. Pachos. "A Short Introduction to Topological Quantum Computation". *SciPost Physics* **3**, 021 (2017).

[101] J. Alicea, Y. Oreg, G. Refael, F. Von Oppen, and M. P. A. Fisher. "Non-Abelian statistics and topological quantum information processing in 1D wire networks". *Nature Physics* **7**, 412–417 (2011).

[102] M. A. Nielsen and I. L. Chuang. *Quantum Computation and Quantum Information*. Cambridge University Press, Cambridge (2010). ISBN 9780511976667. http://ebooks.cambridge.org/ref/id/CBO9780511976667.

[103] O. Zilberberg, B. Braunecker, and D. Loss. "Controlled-NOT gate for multiparticle qubits and topological quantum computation based on parity measurements". *Physical Review A* **77**, 012327 (2008).

[104] S. Bravyi and A. Kitaev. "Universal quantum computation with ideal clifford gates and noisy ancillas". *Physical Review A* **71**, 022316 (2005).

[105] S. Bravyi. "Universal quantum computation with the $\nu = 5/2$ fractional quantum hall state". *Physical Review A* **73**, 042313 (2006).

[106] B. van Heck, A. R. Akhmerov, F. Hassler, M. Burrello, and C. W. J. Beenakker. "Coulomb-assisted braiding of Majorana fermions in a Josephson junction array". *New Journal of Physics* **14**, 035019 (2012).

[107] T. Karzig, Y. Oreg, G. Refael, and M. H. Freedman. "Universal Geometric Path to a Robust Majorana Magic Gate". *Physical Review X* **6**, 031019 (2016).

[108] J. D. Sau, D. J. Clarke, and S. Tewari. "Controlling non-Abelian statistics of Majorana fermions in semiconductor nanowires". *Physical Review B* **84**, 094505 (2011).

[109] J. Nilsson, A. R. Akhmerov, and C. W. J. Beenakker. "Splitting of a Cooper Pair by a Pair of Majorana Bound States". *Physical Review Letters* **101**, 120403 (2008).

[110] A. M. Black-Schaffer and J. Linder. "Magnetization dynamics and majorana fermions in ferromagnetic josephson junctions along the quantum spin hall edge". *Physical Review B* **83**, 220511 (2011).

[111] L. Jiang, D. Pekker, J. Alicea, G. Refael, Y. Oreg, and F. von Oppen. "Unconventional josephson signatures of majorana bound states". *Physical Review Letters* **107**, 236401 (2011).

[112] S. Barbarino, R. Fazio, M. Sassetti, and F. Taddei. "Parity dependent josephson current through a helical luttinger liquid". *New Journal of Physics* **15**, 085025 (2013).

[113] L. Jiang, D. Pekker, J. Alicea, G. Refael, Y. Oreg, A. Brataas, and F. von Oppen. "Magneto-Josephson effects in junctions with Majorana bound states". *Physical Review B* **87**, 075438 (2013).

[114] C. W. J. Beenakker, D. I. Pikulin, T. Hyart, H. Schomerus, and J. P. Dahlhaus. "Fermion-parity anomaly of the critical supercurrent in the quantum spin-hall effect". *Physical Review Letters* **110**, 017003 (2013).

[115] S. Zhang, W. Zhu, and Q. Sun. "Josephson junction on one edge of a two dimensional topological insulator affected by magnetic impurity". *Journal of Physics: Condensed Matter* **25**, 295301 (2013).

[116] S. Mi, D. I. Pikulin, M. Wimmer, and C. W. J. Beenakker. "Proposal for the detection and braiding of majorana fermions in a quantum spin hall insulator". *Physical Review B* **87**, 241405 (2013).

[117] F. Crépin, P. Burset, and B. Trauzettel. "Odd-frequency triplet superconductivity at the helical edge of a topological insulator". *Physical Review B* **92**, 100507 (2015).

[118] F. Keidel, P. Burset, and B. Trauzettel. "Tunable hybridization of Majorana bound states at the quantum spin Hall edge". *Physical Review B* **97**, 075408 (2018).

[119] A. Calzona and B. Trauzettel. "Moving Majorana bound states between distinct helical edges across a quantum point contact". *Physical Review Research* **1**, 033212 (2019).

[120] Q. Meng, V. Shivamoggi, T. L. Hughes, M. J. Gilbert, and S. Vishveshwara. "Fractional spin josephson effect and electrically controlled magnetization in quantum spin hall edges". *Physical Review B* **86**, 165110 (2012).

[121] C. Malciu, L. Mazza, and C. Mora. "4π and 8π dual josephson effects induced by symmetry defects". *Physical Review B* **99**, 125153 (2019).

[122] E. Wigner. *Gruppentheorie und ihre Anwendung auf die Quantenmechanik der Atomspektren*. Vieweg+Teubner Verlag, Wiesbaden (1931). ISBN 978-3-663-00642-8.

[123] C. Chamon, R. Jackiw, Y. Nishida, S.-Y. Pi, and L. Santos. "Quantizing Majorana fermions in a superconductor". *Physical Review B* **81**, 224515 (2010).

[124] P. Adroguer, C. Grenier, D. Carpentier, J. Cayssol, P. Degiovanni, and E. Orignac. "Probing the helical edge states of a topological insulator by Cooper-pair injection". *Physical Review B* **82**, 081303 (2010).

[125] G. E. Blonder, M. Tinkham, and T. M. Klapwijk. "Transition from metallic to tunneling regimes in superconducting microconstrictions: Excess current, charge imbalance, and supercurrent conversion". *Physical Review B* **25**, 4515–4532 (1982).

[126] C. J. Lambert and R. Raimondi. "Phase-coherent transport in hybrid superconducting nanostructures". *Journal of Physics Condensed Matter* **10**, 901–941 (1998).

[127] Y. Blanter and M. Büttiker. "Shot noise in mesoscopic conductors". *Physics Reports* **336**, 1–166 (2000).

[128] F. Taddei, F. Giazotto, and R. Fazio. "Properties of Mesoscopic Hybrid Superconducting Systems". *Journal of Computational and Theoretical Nanoscience* **2**, 329–347 (2005).

[129] C. Fleckenstein, F. Keidel, B. Trauzettel, and N. Traverso Ziani. "The invisible Majorana bound state at the helical edge". *The European Physical Journal Special Topics* **227**, 1377–1386 (2018).

[130] C. Timm. "Transport through a quantum spin Hall quantum dot". *Physical Review B* **86**, 155456 (2012).

[131] Y. Peng, F. Pientka, E. Berg, Y. Oreg, and F. Von Oppen. "Signatures of topological Josephson junctions". *Physical Review B* **94**, 085409 (2016).

[132] Y. Peng, Y. Vinkler-Aviv, P. W. Brouwer, L. I. Glazman, and F. von Oppen. "Parity Anomaly and Spin Transmutation in Quantum Spin Hall Josephson Junctions". *Physical Review Letters* **117**, 267001 (2016).

[133] C. Fleckenstein, N. Traverso Ziani, and B. Trauzettel. "Detection of fractional solitons in quantum spin Hall systems". *EPL (Europhysics Letters)* **121**, 57003 (2018).

[134] C. Fleckenstein, N. T. Ziani, and B. Trauzettel. "Conductance signatures of odd-frequency superconductivity in quantum spin Hall systems using a quantum point contact". *Physical Review B* **97**, 134523 (2018).

[135] F. Dolcini, M. Houzet, and J. S. Meyer. "Topological Josephson ϕ_0 junctions". *Physical Review B* **92**, 035428 (2015).

[136] F. Keidel, S.-Y. Hwang, B. Trauzettel, B. Sothmann, and P. Burset. "On-demand thermoelectric generation of equal-spin Cooper pairs". *Physical Review Research* **2**, 022019 (2020).

[137] M. Sigrist. "Introduction to Unconventional Superconductivity". In *AIP Conference Proceedings*, volume 789, pages 165–243. AIP (2005).

[138] M. Sigrist and K. Ueda. "Phenomenological theory of unconventional superconductivity". *Reviews of Modern Physics* **63**, 239–311 (1991).

[139] P. Muzikar. "Unconventional superconductivity". *Journal of Physics: Condensed Matter* **9**, 1159–1179 (1997).

[140] M. R. Norman. "Unconventional Superconductivity". In *Novel superfluids*, volume 2, chapter 2. Oxford University Press (2014). ISBN 9780198719267.

[141] G. R. Stewart. "Unconventional superconductivity". *Advances in Physics* **66**, 75–196 (2017).

[142] A. J. Leggett. "A theoretical description of the new phases of liquid ^{3}He". *Rev. Mod. Phys.* **47**, 331–414 (1975).

[143] M. Eschrig. "Spin-polarized supercurrents for spintronics: a review of current progress". *Reports on Progress in Physics* **78**, 104501 (2015).

[144] Y. Tanaka, M. Sato, and N. Nagaosa. "Symmetry and Topology in Superconductors –Odd-Frequency Pairing and Edge States–". *Journal of the Physical Society of Japan* **81**, 011013 (2012).

[145] J. Linder and A. V. Balatsky. "Odd-frequency superconductivity". *Reviews of Modern Physics* **91**, 045005 (2019).

[146] P. Coleman. *Introduction to Many-Body Physics*. Cambridge University Press, Cambridge (2015). ISBN 9781139020916.

[147] V. L. Berezinskii. "New model of anisotropic phase of superfluid He-3". *JETP Letters* **20**, 287–289 (1974).

[148] F. S. Bergeret, A. F. Volkov, and K. B. Efetov. "Odd triplet superconductivity and related phenomena in superconductor-ferromagnet structures". *Rev. Mod. Phys.* **77**, 1321–1373 (2005).

[149] J. Cayao, C. Triola, and A. M. Black-Schaffer. "Odd-frequency superconducting pairing in one-dimensional systems". *The European Physical Journal Special Topics* **229**, 545–575 (2020).

[150] S. Kashiwaya and Y. Tanaka. "Tunnelling effects on surface bound states in unconventional superconductors". *Reports on Progress in Physics* **63**, 1641–1724 (2000).

[151] W. J. Herrera, P. Burset, and A. Levy Yeyati. "A Green function approach to graphene–superconductor junctions with well-defined edges". *Journal of Physics: Condensed Matter* **22**, 275304 (2010).

[152] P. Burset, B. Lu, G. Tkachov, Y. Tanaka, E. M. Hankiewicz, and B. Trauzettel. "Superconducting proximity effect in three-dimensional topological insulators in the presence of a magnetic field". *Physical Review B* **92**, 205424 (2015).

[153] D. S. Fisher and P. A. Lee. "Relation between conductivity and transmission matrix". *Physical Review B* **23**, 6851–6854 (1981).

[154] J. Cayao and A. M. Black-Schaffer. "Odd-frequency superconducting pairing and subgap density of states at the edge of a two-dimensional topological insulator without magnetism". *Physical Review B* **96**, 155426 (2017).

[155] Y. Tanaka and A. A. Golubov. "Theory of the proximity effect in junctions with unconventional superconductors". *Phys. Rev. Lett.* **98**, 037003 (2007).

[156] Y. Tanaka, Y. Tanuma, and A. A. Golubov. "Odd-frequency pairing in normal-metal/superconductor junctions". *Physical Review B* **76**, 054522 (2007).

[157] Y. Asano and Y. Tanaka. "Majorana fermions and odd-frequency Cooper pairs in a normal-metal nanowire proximity-coupled to a topological superconductor". *Physical Review B* **87**, 104513 (2013).

[158] Z. Huang, P. Wölfle, and A. V. Balatsky. "Odd-frequency pairing of interacting Majorana fermions". *Physical Review B* **92**, 121404 (2015).

[159] S.-P. Lee, R. M. Lutchyn, and J. Maciejko. "Odd-frequency superconductivity in a nanowire coupled to Majorana zero modes". *Physical Review B* **95**, 184506 (2017).

[160] O. Kashuba, B. Sothmann, P. Burset, and B. Trauzettel. "Majorana STM as a perfect detector of odd-frequency superconductivity". *Physical Review B* **95**, 174516 (2017).

[161] D. Takagi, S. Tamura, and Y. Tanaka. "Odd-frequency pairing and proximity effect in Kitaev chain systems including a topological critical point". *Physical Review B* **101**, 024509 (2020).

[162] M. Eschrig. "Spin-polarized supercurrents for spintronics". *Physics Today* **64**, 43–49 (2011).

[163] K. Ohnishi, S. Komori, G. Yang, K.-R. Jeon, L. A. B. Olde Olthof, X. Montiel, M. G. Blamire, and J. W. A. Robinson. "Spin-transport in superconductors". *Applied Physics Letters* **116**, 130501 (2020).

[164] S. Kawabata, A. Ozaeta, A. S. Vasenko, F. W. J. Hekking, and F. Sebastián Bergeret. "Efficient electron refrigeration using superconductor/spin-filter devices". *Applied Physics Letters* **103**, 032602 (2013).

[165] P. Machon, M. Eschrig, and W. Belzig. "Nonlocal Thermoelectric Effects and Nonlocal Onsager relations in a Three-Terminal Proximity-Coupled Superconductor-Ferromagnet Device". *Physical Review Letters* **110**, 047002 (2013).

[166] P. Machon, M. Eschrig, and W. Belzig. "Giant thermoelectric effects in a proximity-coupled superconductor–ferromagnet device". *New Journal of Physics* **16**, 073002 (2014).

[167] M. S. Kalenkov and A. D. Zaikin. "Electron-hole imbalance and large thermoelectric effect in superconducting hybrids with spin-active interfaces". *Physical Review B* **90**, 134502 (2014).

[168] F. Giazotto, T. T. Heikkilä, and F. S. Bergeret. "Very large thermophase in ferromagnetic josephson junctions". *Physical Review Letters* **114**, 067001 (2015).

[169] F. Giazotto, P. Solinas, A. Braggio, and F. S. Bergeret. "Ferromagnetic-insulator-based superconducting junctions as sensitive electron thermometers". *Physical Review Applied* **4**, 044016 (2015).

[170] S.-Y. Hwang, R. López, and D. Sánchez. "Large thermoelectric power and figure of merit in a ferromagnetic–quantum dot–superconducting device". *Physical Review B* **94**, 054506 (2016).

[171] C. D. Shelly, E. A. Matrozova, and V. T. Petrashov. "Resolving thermoelectric "paradox" in superconductors". *Science Advances* **2**, e1501250 (2016).

[172] S. Kolenda, M. J. Wolf, and D. Beckmann. "Observation of Thermoelectric Currents in High-Field Superconductor-Ferromagnet Tunnel Junctions". *Physical Review Letters* **116**, 097001 (2016).

[173] R. Beiranvand and H. Hamzehpour. "Spin-dependent thermoelectric effects in graphene-based superconductor junctions". *Journal of Applied Physics* **121**, 063903 (2017).

[174] A. Rezaei, A. Kamra, P. Machon, and W. Belzig. "Spin-flip enhanced thermoelectricity in superconductor-ferromagnet bilayers". *New Journal of Physics* **20**, 073034 (2018).

[175] F. S. Bergeret, M. Silaev, P. Virtanen, and T. T. Heikkilä. "Colloquium: Nonequilibrium effects in superconductors with a spin-splitting field". *Rev. Mod. Phys.* **90**, 041001 (2018).

[176] T. T. Heikkilä, M. Silaev, P. Virtanen, and F. S. Bergeret. "Thermal, electric and spin transport in superconductor/ferromagnetic-insulator structures". *Progress in Surface Science* **94**, 100540 (2019).

[177] M. S. Kalenkov and A. D. Zaikin. "Large thermoelectric effect in ballistic andreev interferometers". *Phys. Rev. B* **95**, 024518 (2017).

[178] P. E. Dolgirev, M. S. Kalenkov, and A. D. Zaikin. "Current-phase relation and flux-dependent thermoelectricity in Andreev interferometers". *Physical Review B* **97**, 054521 (2018).

[179] Z. Cao, T.-F. Fang, L. Li, and H.-G. Luo. "Thermoelectric-induced unitary Cooper pair splitting efficiency". *Applied Physics Letters* **107**, 212601 (2015).

[180] N. S. Kirsanov, Z. B. Tan, D. S. Golubev, P. J. Hakonen, and G. B. Lesovik. "Heat switch and thermoelectric effects based on Cooper-pair splitting and elastic cotunneling". *Physical Review B* **99**, 115127 (2019).

[181] R. Hussein, M. Governale, S. Kohler, W. Belzig, F. Giazotto, and A. Braggio. "Nonlocal thermoelectricity in a Cooper-pair splitter". *Physical Review B* **99**, 075429 (2019).

[182] R. Sánchez, P. Burset, and A. L. Yeyati. "Cooling by Cooper pair splitting". *Physical Review B* **98**, 241414 (2018).

[183] F. Giazotto, T. T. Heikkilä, A. Luukanen, A. M. Savin, and J. P. Pekola. "Opportunities for mesoscopics in thermometry and refrigeration: Physics and applications". *Reviews of Modern Physics* **78**, 217–274 (2006).

[184] J. T. Muhonen, M. Meschke, and J. P. Pekola. "Micrometre-scale refrigerators". *Reports on Progress in Physics* **75**, 046501 (2012).

[185] J. P. Pekola. "Towards quantum thermodynamics in electronic circuits". *Nature Physics* **11**, 118–123 (2015).

[186] G. Benenti, G. Casati, K. Saito, and R. S. Whitney. "Fundamental aspects of steady-state conversion of heat to work at the nanoscale". *Physics Reports* **694**, 1–124 (2017).

[187] P. P. Potts. "Introduction to Quantum Thermodynamics (Lecture Notes)" *arXiv-ID* 1906.07439 (2019).

[188] S. Kheradsoud, N. Dashti, M. Misiorny, P. P. Potts, J. Splettstoesser, and P. Samuelsson. "Power, efficiency and fluctuations in a quantum point contact as steady-state thermoelectric heat engine". *Entropy* **21**, 777 (2019).

[189] M. P. Anantram and S. Datta. "Current fluctuations in mesoscopic systems with Andreev scattering". *Physical Review B* **53**, 16390 (1996).

[190] S.-Y. Hwang, P. Burset, and B. Sothmann. "Odd-frequency superconductivity revealed by thermopower". *Physical Review B* **98**, 161408 (2018).

[191] J. Strunz, J. Wiedenmann, C. Fleckenstein, L. Lunczer, W. Beugeling, V. L. Müller, P. Shekhar, N. Traverso Ziani, S. Shamim, J. Kleinlein, H. Buhmann, B. Trauzettel, and L. W. Molenkamp. "Interacting topological edge channels". *Nature Physics* **16**, 83–88 (2020).

[192] F. Zhang and C. L. Kane. "Time-Reversal-Invariant $\mathbb{Z}_4$ Fractional Josephson Effect". *Physical Review Letters* **113**, 036401 (2014).

[193] C. P. Orth, R. P. Tiwari, T. Meng, and T. L. Schmidt. "Non-Abelian parafermions in time-reversal-invariant interacting helical systems". *Physical Review B* **91**, 081406 (2015).

[194] C. J. Pedder, T. Meng, R. P. Tiwari, and T. L. Schmidt. "Missing Shapiro steps and the 8π -periodic Josephson effect in interacting helical electron systems". *Physical Review B* **96**, 165429 (2017).

[195] Y. Vinkler-Aviv, P. W. Brouwer, and F. Von Oppen. "$\mathbb{Z}_4$ parafermions in an interacting quantum spin Hall Josephson junction coupled to an impurity spin". *Physical Review B* **96**, 195421 (2017).

[196] C. Fleckenstein, N. Traverso Ziani, and B. Trauzettel. "$\mathbb{Z}_4$ parafermions in weakly interacting superconducting constrictions at the helical edge of quantum spin Hall insulators". *Physical Review Letters* **122**, 066801 (2019).

[197] A. Hutter and D. Loss. "Quantum computing with parafermions". *Physical Review B* **93**, 125105 (2016).

[198] J. Alicea and P. Fendley. "Topological Phases with Parafermions: Theory and Blueprints". *Annual Review of Condensed Matter Physics* **7**, 119–139 (2016).

[199] D. Gresta, M. Real, and L. Arrachea. "Optimal Thermoelectricity with Quantum Spin Hall Edge States". *Physical Review Letters* **123**, 186801 (2019).

[200] F. Ronetti, L. Vannucci, G. Dolcetto, M. Carrega, and M. Sassetti. "Spin-thermoelectric transport induced by interactions and spin-flip processes in two-dimensional topological insulators". *Physical Review B* **93**, 165414 (2016).

[201] F. Ronetti, M. Carrega, D. Ferraro, J. Rech, T. Jonckheere, T. Martin, and M. Sassetti. "Polarized heat current generated by quantum pumping in two-dimensional topological insulators". *Physical Review B* **95**, 115412 (2017).

[202] L. Bours, B. Sothmann, M. Carrega, E. Strambini, E. M. Hankiewicz, L. W. Molenkamp, and F. Giazotto. "A Topological SQUIPT based on helical edge states in proximity to superconductors". *Physical Review Applied* **10**, 014027 (2018).

[203] G. Blasi, F. Taddei, L. Arrachea, M. Carrega, and A. Braggio. "Nonlocal thermoelectricity in a superconductor–topological-insulator–superconductor junction in contact with a normal-metal probe: Evidence for helical edge states". *Phys. Rev. Lett.* **124**, 227701 (2020).

[204] O. S. Lumbroso, L. Simine, A. Nitzan, D. Segal, and O. Tal. "Electronic noise due to temperature differences in atomic-scale junctions". *Nature* **562**, 240–244 (2018).

[205] E. Sivre, H. Duprez, A. Anthore, A. Aassime, F. D. Parmentier, A. Cavanna, A. Ouerghi, U. Gennser, and F. Pierre. "Electronic heat flow and thermal shot noise in quantum circuits". *Nature Communications* **10**, 5638 (2019).

[206] S. Larocque, E. Pinsolle, C. Lupien, and B. Reulet. "Shot noise of a temperature-biased tunnel junction". *Phys. Rev. Lett.* **125**, 106801 (2020).

[207] J. Rech, T. Jonckheere, B. Grémaud, and T. Martin. "Negative delta-t noise in the fractional quantum hall effect". *Phys. Rev. Lett.* **125**, 086801 (2020).